Design & Optimization of Organic Rankine Cycle Solar-Thermal Powerplants

by

ANDREW C. MCMAHAN

A thesis submitted in partial fulfillment of
The requirements for the degree of

MASTER OF SCIENCE
(MECHANICAL ENGINEERING)

at the

UNIVERSITY OF WISCONSIN-MADISON

2006

Approved by

Professor Sanford A. Klein

August 10, 2006

Abstract

Solar-thermal powerplants have enjoyed limited success in the energy market to date. The ability to better characterize the performance of existing solar-thermal technologies as well as investigate the potential of new technologies is a crucial step in developing more economically viable designs. To this end, computer models and simulation capability are developed in this thesis to predict the performance of several emerging solar-thermal powerplant technologies. Specifically, models of organic Rankine cycles and packed-bed stratified (thermocline) thermal energy storage systems are developed. These models provide a low-cost context for analyzing the design and optimization (both economic and engineering) of solar-thermal technologies that show tremendous unrealized potential.

Organic Rankine cycles have unique properties that are well suited to solar power generation. The thermodynamic potential of a variety organic Rankine cycle working fluids and configurations are analyzed. In addition, a general economic optimization methodology for solar-thermal organic Rankine cycle powerplants is developed and presented. The methodology is applied to an existing plant design which demonstrates opportunities for further optimization in current design practice.

Thermal energy storage enables powerplant output to be tailored to meet end-user demands. The design and integration of thermal energy storage systems is discussed. Plant operating and control strategies for a variety of utility pricing schedules are developed and analyzed. The potential for thermal energy storage to impact the economic attractiveness of solar power generation is shown to be heavily dependent on energy market structure and utility pricing strategies.

Acknowledgements

This work would not have been possible without the guidance and experience of my principle advisors, Sandy Klein and Doug Reindl. The respect and freedom they gave me as a researcher, from the very beginning, made me feel like a respected colleague rather than the neophyte I more likely resembled. I am truly grateful for their mentoring and partnership, and as a result I will depart the solar lab a far more confident and skilled problem-solver than I entered.

Greg Nellis, Bill Beckman, Tim Shedd and the other Solar Lab regulars, with their universal interest in student projects and development, created a research environment that was profoundly beneficial to my development and progress, in addition to being a true pleasure to participate in.

Hank Price and Nate Blair of the National Renewable Energy Lab proved invaluable in providing unrivaled flexibility to give me the creative freedom to play a large part in determining the direction of this research.

Thanks are due also to my wife, Mical, who with great love and patience endured countless discussions of the most boring and esoteric academic variety.

Table of Contents

List of Tables

List of Figures

Nomenclature

A	Area [m^2]
A_c	Cross-sectional Area [m^2]
A_s	Surface Area Exposed to Heat Transfer [m^2]
A_{SF}	Solar field area [m^2]
$\dot{A}_{destruction}$	Availability Destruction rate [kW]
A_{PC}	Power cycle heat transfer surface area [m^2]
$A_{PC,REF}$	Power cycle reference heat transfer surface area [m^2]
A_{total}	Total fluid-solid heat transfer surface area in a packed-bed storage tank [m^2]
Bi	Biot Number [-]
C	specific heat [kJ/kg-K]
C_R	Solar collector concentration ratio [-]
C_{SF}	Specific solar field cost [$/$m^2$]
ED	Energy Density [kW/m^3]
k	Thermal Conductivity [W/m-K]
F_R	Solar collector performance factor
h	heat transfer coefficient [W/m^2-K]
h_v	volumetric heat transfer coefficient [W/m^3-K]
IR	Investment Ratio [$/kW]
$\dot{m}$	mass flow rate [kg/s]
m	mass [kg]
n_{crit}	Critical mesh size for the simplified explicit model [-]
n_{rec}	Recommended mesh size for the simplified explicit model [-]
NIR	Normalized Investment Ratio
NTU_{fluid}	Storage fluid heat transfer parameter [-]
NTU_{solid}	Storage solid heat transfer parameter [-]
NTU	Short-hand for NTU_{fluid}, storage system heat transfer parameter [-]
$NTUsum$	Total fluid-solid nodal heat transfer parameter [-]
Pr	Prandtl Number [-]
Q	Energy Transferred [kJ]
$\dot{Q}$	Energy Transfer Rate [kW]
Q_u	Useful Energy Gain [kW]
R	Fluid-solid storage system capacitance ratio [-]
Re	Reynolds' Number [-]
$R_{f\text{-}s}$	Resistance to fluid-solid heat transfer [K/W]
$R_{axial\ conduction}$	Resistance to axial conduction [K/W]
R_{losses}	Resistance to environmental losses [K/W]
r_{axial}	ratio of resistance to fluid-solid heat transfer and axial conduction [-]
r_{loss}	ratio of resistance to fluid-solid heat transfer and environmental losses [-]
S	Absorbed solar radiation [W/m^2]
T	Temperature [C]
T_o	Dead State Temperature [C]
T_L	Low temperature thermal resource [C]

T_H	High temperature thermal resource [C]
t	time [s]
UA	Total power cycle heat exchanger conductance [W/K]
U_L	Loss Coefficient [W/m^2-K]
U_{SF}	Solar Field Utilization [kW/m^2]
U	Storage system Utilization [-]
v	velocity (or specific volume by context)
V	Volume [m^3]
$V``$	Volume flux [m^3/m^2-s]
W	work [kJ]
$\dot{W}$	Power output [kW]
X	axial distance [m]
y	dimensionless parameter from equation 5.3.18
z	dimensionless parameter from equation 5.3.19

Greek Letters:

α	Overall heat addition coefficient from finite-time analysis [W/K]
β	Overall heat rejection coefficient from finite-time analysis [W/K]
Ψ	Total availability of a resource stream (kW)
ε	void fraction
ρ	density (kg/ m^3)
η_{cycle}	first-law cycle efficiency
$\eta_{2nd\ Law}$	second-law cycle efficiency
η_{CNCA}	Chambadal-Novikov-Curzon-Ahlborn Efficiency [-]
$\Delta T_{Boiler,Inlet}$	HTF-Working Fluid Temperature difference at the Boiler inlet
Δx	numerical distance step [m]
Δt	numerical time step [s]
τ	Thermal resource temperature ratio [-]
θ	Power cycle temperature ratio [-]

Subscripts:

a	ambient
$CNCA$	Chambadal-Novikov-Curzon-Ahlborn efficiency and power
i	initial or inlet
In	in
Out	out
s	solid
f	fluid
g	gaseous
HTF	Heat transfer fluid
MP	Maximum power from a finite resource
sf	solid-fluid
SF	solar field
b	packed bed

o	initial
v	volumetric
0	Dead state
ref	reference or design state
WF	Working fluid

Acronyms:

PTORC	Parabolic Trough Organic Rankine Cycle Powerplant
ORC	Organic Rankine Cycle
WF	Working Fluid
HTF	Heat Transfer Fluid

1 Introduction

1.1 Background

The global demand for energy continues to increase while traditional energy resources are becoming scarcer. Exacerbating the situation is the growing realization that the use of traditional fuels carries a significant environmental burden. Adoption of environmentally benign and renewable energy conversion technologies is essential if our society is to retain its advanced lifestyle in the face of global development.

Economic opportunity drives the energy market just as it drives every market. Maximizing the economic opportunity associated with safe and renewable energy technologies is an essential step towards increasing their use. Taxes, penalties, incentives, public awareness and government mandates can all influence the economic opportunity associated with renewable energy technology. The principle focus of this thesis, however, is improving economic opportunity by providing tools for the evaluation and optimization of several specific renewable technologies: Organic Rankine power cycles and thermal energy storage.

Parabolic trough solar-thermal power generation is a proven technology, with several utility scale plants in operation for nearly 20 years. Current large-scale systems rely on

traditional steam-based Rankine cycles for power production. Organic Rankine cycle powerplants are more compact and less costly than traditional steam cycle powerplants and are able to better exploit lower temperature thermal resources. Utilizing organic Rankine cycles allows solar-thermal power generation to become a more modular and versatile means of supplanting traditional fuels. While they have great potential, organic Rankine cycles have received relatively little attention from the solar energy community.

While solar-thermal power generation has the potential to play an important role in future energy markets, it is fundamentally limited by its energy source: the sun. The ability to store large amounts of high-temperature thermal energy enables the delivery of solar-thermal power independent of variation in insolation. Storage can be used to make output mimic grid demand, compensate for variation in radiation levels throughout the day, or provide 24-hour on-demand solar-thermal power. This flexibility, if achieved both efficiently and at low-cost, has the potential to increase the economic viability and overall market potential of solar power generation.

1.2 Objectives

Together organic Rankine cycle solar-thermal powerplants and thermal energy storage represent a complete and versatile renewable energy technology with great potential. The focus of this thesis is maximizing that potential using computer simulation and modeling capability to optimize their performance in a variety of applications.

Chapter 2 presents a technical background on organic Rankine cycles. It focuses on the unique design considerations of organic Rankine cycles which are essential to the model development and optimization work done in later chapters.

Chapter 3 goes through the development of two organic Rankine cycle computer models. The first is developed for the rapid-screening of potential cycle designs and configurations. The second is designed to capture power cycle part-load performance for use in long-term simulation and optimization.

Chapter 4 uses the rapid-screening model developed in chapter three to examine the thermodynamic merit of a variety of organic Rankine cycle configurations. In addition, the rapid-screening model is used to compare steam and organic Rankine cycles operating within the same thermal boundary conditions.

Chapter 5 develops a methodology for optimizing parabolic-trough solar-thermal powerplants. Finite-time thermodynamics is used to provide a theoretical context for understanding the fundamental differences between a solar-thermal powerplant and one that uses more traditional fuel sources. The methodology is then applied to the APS Saguaro powerplant, a recently completed Organic Rankine cycle solar-thermal powerplant.

Chapter 6 provides background on proposed thermal-energy storage technologies for solar-thermal powerplant applications. Packed-bed stratified storage tanks are identified as a storage technology of particular interest. Detailed numerical models of these systems are then developed. Different numerical modeling techniques are considered and compared, both with one another and data taken from real-world systems.

Chapter 7 presents a series of analyses based on the storage models developed in chapter six. Storage system control and operating strategies are considered based on two common utility pricing models. Design considerations related to storage system-powerplant integration are discussed.

Chapter 8 offers a summary of the most significant results identified in the preceding chapters. It also features recommendations for further developments of the current work.

2 ORGANIC RANKINE CYCLE BACKGROUND

2.1 Introduction

Organic Rankine cycle (ORC) powerplants are of interest for solar electricity generation due to their versatility and simplicity. They are most often used when exploiting low-temperature thermal resources for power generation, or small-scale applications (typically <5 MW). The most common uses are for geothermal and solar power generation, waste-heat recovery, and remote-power. This chapter provides general background on the history and variety of ORC systems with particular emphasis on solar energy applications. The details of ORC operation that make them advantageous for small systems are discussed along with the important design considerations that accompany their unique design.

2.2 Background and General Design Considerations

Organic Rankine cycles are analogous to traditional steam Rankine cycles with an organic fluid as the working fluid in place of water. Many different organic fluids have been proposed and utilized as ORC working fluids, and fluids of particular interest for solar power applications will be discussed in detail in later sections. The following is a

brief list of fluids that have been used or proposed for use in Rankine cycles:

- Toluene
- Xylene
- n-pentane
- n-butane
- R-11,R-22
- R-248fa

Organic Rankine Cycles are not new technology. They have been used in large numbers for various purposes since the first-half of the 20th century, nearly as long as the steam Rankine cycle [Curran, 1981]. Interest in ORCs as a means for converting solar radiation into useful work is a more recent development. Several small demonstration plants were built and successfully operated in the early 1980's [Fenton, 1984 & Larson, 1987]. After the success of high-temperature steam Rankine cycle solar powerplants (SEGS [Cable, 1998]) the ORC related publication rate in the solar community waned and most ORC research was performed by the geothermal and waste heat recovery communities. A recent resurgence of interest in ORCs as a viable option for small-scale solar electricity generation has been spurred by the construction of the 1 MW APS Saguaro parabolic trough ORC powerplant.

The following sections will offer a general technical background for organic Rankine cycles. In many cases organic fluids will be considered in contrast to steam because it is precisely the differences between steam and organic fluids that make ORCs useful. In section 2.2.1 a description of the cycle configuration of most commercially available ORCs is provided as a point of reference for further discussions. Section 2.2.2 examines the fundamental thermodynamic differences between water and organic fluids for power cycle applications. Section 2.2.3 will show the factors that are involved in selecting an appropriate organic fluid for ORC applications. Section 2.2.4 details the significance of superheating organic working fluids in cycle design. Section 2.2.5 offers an analysis of the effect of system operating pressures. Observations made in this chapter will establish boundaries and ground rules for analyses and studies performed later in this thesis.

2.2.1 Typical ORC configuration

There are many possible organic Rankine cycle configurations, several of which will be considered in this thesis. There is, however, a particular design that is by far the most commonly observed in commercial applications. It is important to take note of this configuration as many of the technical issues discussed are directly related to it. Figure 2.1 shows a general process flow for a typical commercially available ORC:

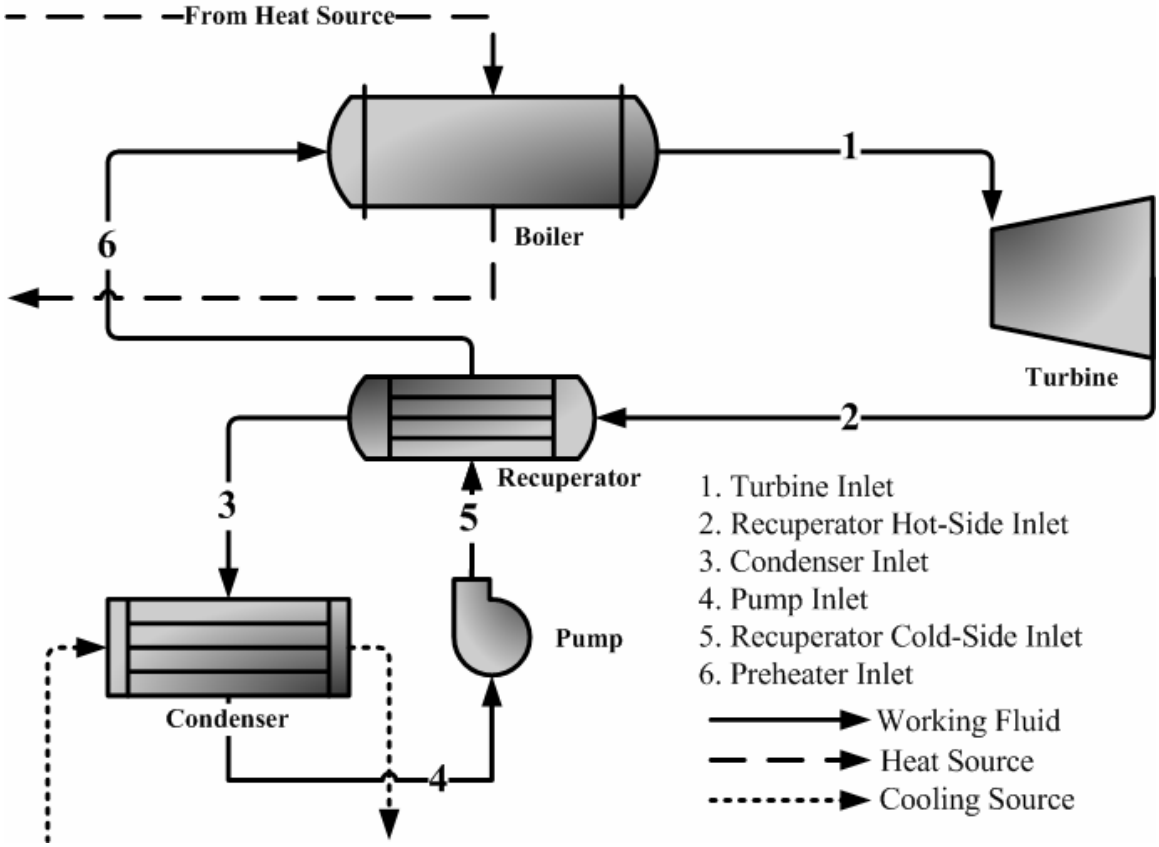

Figure 2.1: Process flow for a typical solar driven ORC

The component processes that occur between the state-points labeled in Figure 2.1 are as follows:

1-2: The working fluid is expanded through a turbine
2-3: The turbine exhaust is used to preheat the working fluid exiting the pump
3-4: The working fluid is condensed
4-5: The working fluid is pumped from to high pressure
5-6: The working fluid is heated by the turbine exhaust
6-1: Heat is added to the working fluid

Figure 2.2 shows the general shape of a T-s diagram corresponding to the typical ORC configuration just described.

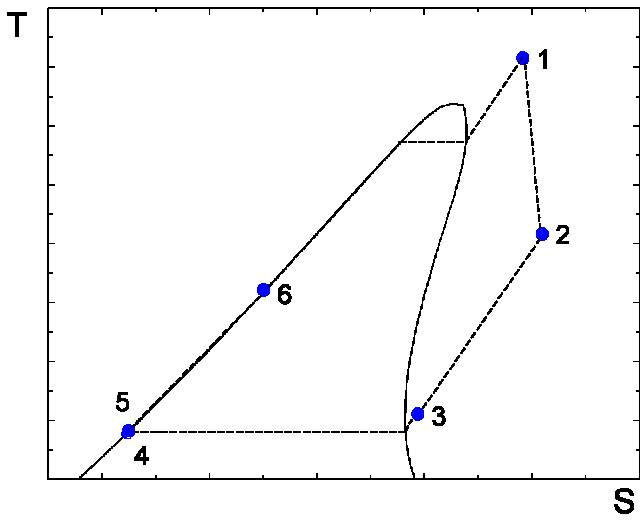

Figure 2.2: T-S Diagram for water showing the state points corresponding to a typical commercial organic Rankine cycle configuration

The only departure from a steam Rankine cycle in the system shown in Figure 2.1 is the presence of the recuperator which utilizes available energy in the turbine exhaust to preheat the working fluid stream. It is only necessary at this stage to recognize that ORCs often utilize recuperators and steam Rankine cycles do not; the thermodynamic basis for this will become apparent in the following sections. It should also be indicated that there are no feedwater heaters in this configuration; feedwater heaters are common in steam Rankine cycle systems.

2.2.2 A Thermodynamic Comparison of Water and Organic Fluids

Water is the working fluid of choice for the vast majority of large scale fossil-fired Rankine cycle powerplants. Water is well-suited for those high-temperature applications, but it has its limitations that become more significant during lower temperature operation. It is the unique properties of organic fluids that allow them to excel where water falters.

The principle difference between organic fluids and water is their behavior when expanding from a saturated or superheated state through a turbine at low to moderate

temperature (200-400ºC). This behavior is best observed by examining turbine expansion in this temperature regime.

Figure 2.3 shows a T-s diagram for water with two isobaric heat additions to 300ºC followed by isentropic expansions. In the absence of superheat the isentropic expansion of water results in a relatively low-quality two-phase mixture (<80%). A low quality flow through a turbine is unacceptable as it can result in significant equipment damage. Design practice for steam Rankine cycles dictates reheated and superheated cycles to avoid low-quality flow through the turbine. There are other means to mitigate low-quality flow, such as mechanical separation of the liquid and vapor at intermediate expansion stages, but they are complex and expensive. Referring again to Figure 2.3, the preferred cycle would be the dashed line which boils at a lower pressure and superheats to the desired temperature resulting in a higher quality turbine exhaust. This cycle ensures high quality flow through the turbine.

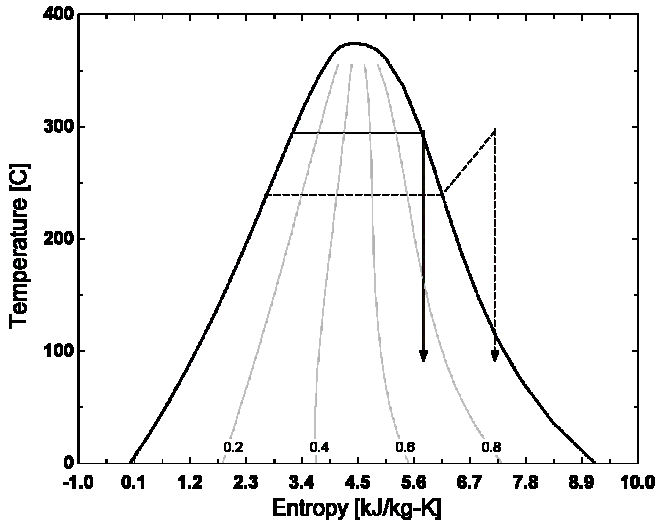

Figure 2.3: T-S Diagram for water showing results of performing an isentropic expansion for a single temperature and different pressures

Organic fluids show a much different behavior than that seen with water in the T-s plane. Toluene, as seen in Figure 2.4 has a vapor saturation curve with a positive slope in the T-s plane. Figure 2.4 shows an isentropic expansion from a saturated vapor state resulting in a superheated vapor, rather than the two-phase mixture seen with water. The positive slope of toluene's saturated vapor line (shared with most other candidate working fluids)

eliminates the possibility of low-quality turbine flows and the associated complications to cycle design.

The increasing degree of superheat with expansion also creates an opportunity for energy recovery not present in a steam Rankine cycle. Organic fluids like toluene exit the turbine at the condensing pressure but at a temperature higher than the condensing temperature. The available energy in this superheated turbine exhaust can be recovered, in part, with a recuperator used to preheat the working fluid on its way to the boiler, as seen in section 2.2.1.

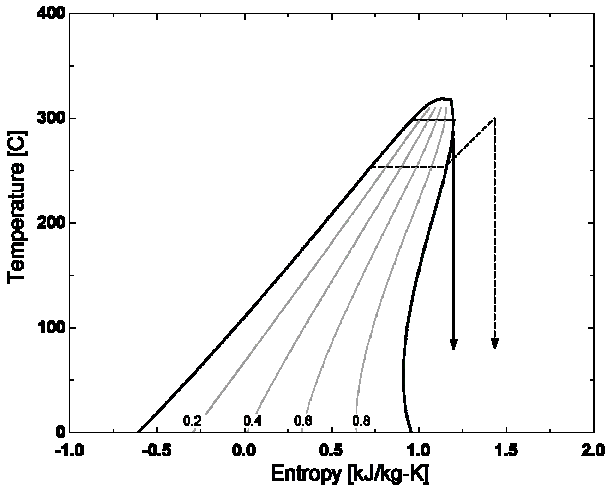

Figure 2.4: T-S Diagram for toluene (a typical organic working fluid) showing results of performing an isentropic expansion for a single temperature and different pressures

The vapor saturation curve behavior seen in organic fluids and water is described in the literature as *wetting* and *drying* [Curran, 1981, Hung, 1997]. Water is a wetting fluid because its vapor saturation curve has a negative slope ($\delta T/\delta s < 0$), resulting in a two-phase mixture upon isentropic expansion. Most organic fluids show, to varying degrees, drying behavior resulting in a superheated vapor upon isentropic expansion. The degree to which organic fluids are drying is generally related to their molecular weight (or molecular complexity) as shown in Figure 2.5. It is the *drying* behavior of organic working fluids that make them superior to water for the utilization of low-temperature thermal resource (solar, geothermal, waste-heat recovery).

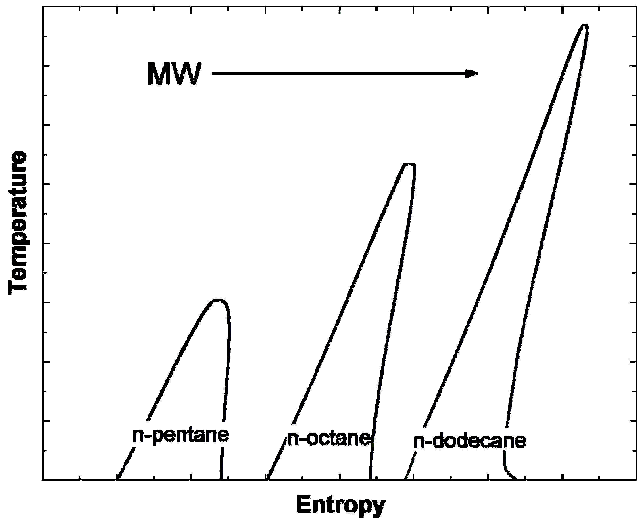

Figure 2.5: Showing the trend in the shape of the liquid-vapor dome in the T-S plane for organic fluids of increasing molecular weight (MW)

Steam Rankine cycles, operate with sub-atmospheric condensing pressures, typically close to 1 psia (7 kPa), in order to achieve high efficiencies. The inevitable result of sub-atmospheric condensation is the infiltration of non-condensable gases into the working-fluid flow requiring the addition of de-aeration equipment or de-aerating feedwater heaters. The variety of organic working fluids available enables the tailoring of system operating pressures to what is appropriate for particular applications. Many organic fluids have saturation pressures well above atmospheric pressure for temperatures that are typically achievable in air and water-cooled condensers. Super-atmospheric condensation enables the design of low or no-maintenance power cycles. This attribute is highly-desirable in remote and low-output applications where a full-time maintenance staff is not a reasonable expectation.

One of the most challenging and expensive obstacles to an efficient steam Rankine cycle is the turbine. Steam turbines are complex and expensive, consisting of many stages. These stages are also used as intermediate extraction points for a complex system of feedwater heaters which serve to increase cycle efficiency and remove non-condensable gases. The turbines in organic Rankine cycles are often very simple; many designs involve only a single stage. The size and complexity advantage of organic fluid turbines is driven by higher fluid density at typical turbine operating conditions as well as much

smaller expansion pressure ratios (inlet/outlet). Simplified turbine design is then another advantage associated with high condensing pressures.

2.2.3 Organic Working Fluid Selection

With some of the general differences between water and organic fluids established, it is possible to examine the properties that drive organic fluid selection for particular applications. There are a number of practical issues that take precedence over thermodynamic considerations, including: thermal stability, toxicity, flammability and cost. Any of these can eliminate a fluid from contention regardless of its thermodynamic merit. Thermal stability and thermodynamic considerations are discussed here. The others are indirectly considered by examining only working fluids with a history of successful use in ORC applications.

Thermal Stability

The purpose of this research is to investigate organic Rankine cycles for power generation, so high operating temperatures are a priority. Thermal stability at elevated temperature is thus a principle consideration in working fluid selection.

The high temperature thermal resource range considered is 300ºC-400ºC. This range is chosen because it is the approximate range in which the current parabolic trough concentrating collectors are designed to operate. The thermal resource temperature refers to the maximum temperature in the solar field, not necessarily in the power cycle. 300ºC-400ºC is well above the operating limit for most organic fluids, narrowing the field of candidate fluids considerably. Cold temperature resources ranging from 15ºC-40ºC will be considered, depending on the cooling technique that is employed.

A recent study was performed showing straight-chain alkanes, in particular n-pentane, possess good thermal stability at 315ºC [Andersen, 2005]. Toluene also performed well at 315ºC. These published results are consistent with current design practice which favors n-pentane and toluene [Larsen, 1987, Price, 2006]. As a result of these studies and

historical precedent this research focuses on the straight-chain alkanes and toluene as potential working fluids.

Thermal stability data for candidate organic working fluids are limited, forcing approximate operational maximum temperatures to be chosen somewhat arbitrarily. The testing conditions of 315ºC will be used as an upper bound for the straight chain alkanes, and 385ºC for toluene based on previous successful installations [Curran, 1981].

Thermodynamic Considerations

Working fluids are selected to allow operation between two available temperature boundary conditions at reasonable pressures. Particular consideration is given to condensing pressure and volume as they are directly related to cycle O&M and equipment size.

Figures 2.6 and 2.7 show vapor specific volume and saturation pressure as a function of saturation temperature for several organic fluids as well as water. Vapor specific volume at saturation (condensing) conditions gives an indication of condensing equipment size. Noticing that organic fluid vapor volume varies by three orders-of-magnitude between n-pentane and n-dodecane highlights the importance of this information in making a working fluid selection. Organic fluids with low saturation volumes, like n-pentane, require smaller condensing equipment and contribute to the choice of these working fluids for applications where minimizing size and complexity are a priority. By contrast, N-dodecane is not a reasonable working fluid candidate for any application due to the massive condensing equipment it would require.

Figure 2.7 shows the operating pressures corresponding to the saturation temperatures considered in Figure 2.6. Note that n-pentane operates at super-atmospheric pressures over a wide range of condensing conditions. Super-atmospheric operation is beneficial for small-scale applications by eliminated the infiltration of non-condensable gases as well as simplifying turbine design by creating small expansion pressure ratios. Toluene, like water, condenses at sub-atmospheric pressures over a realistic condensing

temperature range. This introduces additional O&M considerations and costs, but toluene's unsurpassed thermal stability makes it a good choice for higher temperature and higher output organic Rankine cycle applications. These observations reinforce the selection of n-pentane and toluene as the working fluids considered in this thesis.

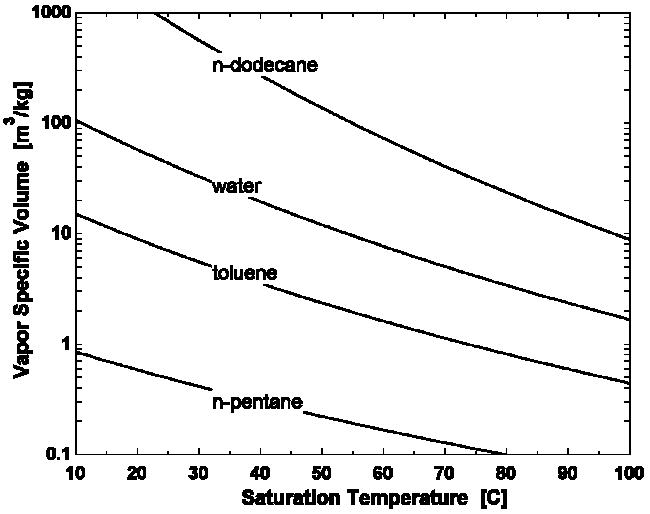

Figure 2.6: Saturated vapor specific volume for organic fluids as a function of saturation temperature, with water as a reference.

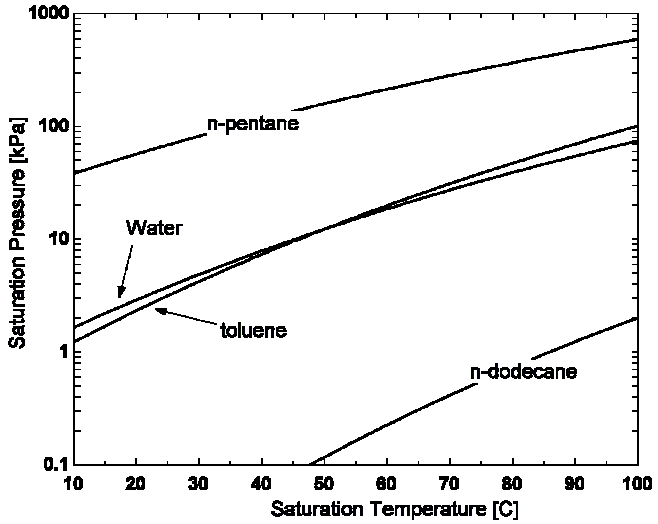

Figure 2.7: Saturation pressure as a function of saturation temperature.

2.2.4 The Impact of Superheat on ORC Performance

A large degree of superheat is employed in traditional steam Rankine plants for several reasons. The first is to prevent low-quality steam from being sent through the turbine as discussed in section 2.2.2. The second reason is thermodynamic. First-Law thermodynamic efficiency in a steam Rankine cycle increases as the degree of superheat increases at a fixed pressure (increasing temperature), where the degree of superheat is defined as:

$$T_{sh} = \left.\frac{T}{T_{sat}}\right|_{p} \qquad [2.2.1]$$

The increase in efficiency is most often explained using the Carnot analogy whereby increasing the average temperature of heat addition the cycle efficiency is increased. This behavior can be related to the shape of constant pressure lines in the h-s plane. Constant pressure lines diverge for all fluids in the superheat regime. It is the rate at which these lines diverge that determines the impact of cycle efficiency. For a given incremental increase in the degree of superheat from some reference state (in general this would be the saturated vapor state) an incremental efficiency can be defined as the ratio of incremental work and heat, shown in equation [2.2.2] and Figure 2.8. In order for the cycle efficiency to increase with the degree of superheat at a particular temperature, the incremental efficiency must be greater than the efficiency at the reference state.

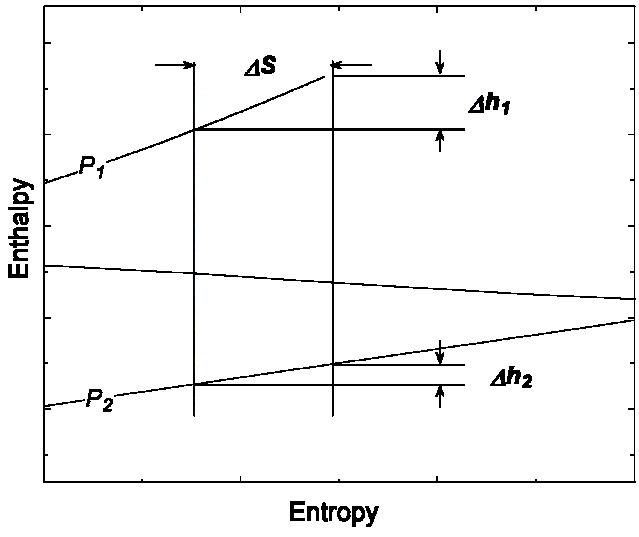

Figure 2.8: Enthalpy-Entropy diagram for water to aid development of equation [2.2.2].

$$\Delta\eta = \frac{\Delta w}{\Delta q} = \frac{\Delta h_1 - \Delta h_2}{\Delta h_2} \qquad [2.2.2]$$

Constant pressure lines for water diverge rapidly, leading to increased efficiency as superheat increases. Constant pressure lines for most organic working fluids are nearly parallel, leading to decreased, unchanged or marginally improved cycle efficiencies as superheat increases [Hung et al, 1997]. In other words, the *drying* behavior of most organics causes the average temperature a heat rejection to increase along with the average temperature of heat addition, negating efficiency gains associated with increased temperature. Note that ORC efficiency only degrades in the absence of any form of recuperation or energy recovery. As the degree of superheat increases for an organic working fluid, the amount of available energy at the turbine exit also increases.

Figure 2.9 shows cycle efficiency for both water and toluene as a function of the degree of superheat. The pressure for each working fluid is chosen such that the saturation temperature is 300ºC, typical for a solar-thermal powerplant. The expansion is treated as isentropic, pump work is neglected and the working fluid is condensed at 20ºC. Toluene is indicative of many organic fluids showing decreasing cycle efficiency with increasing superheat.

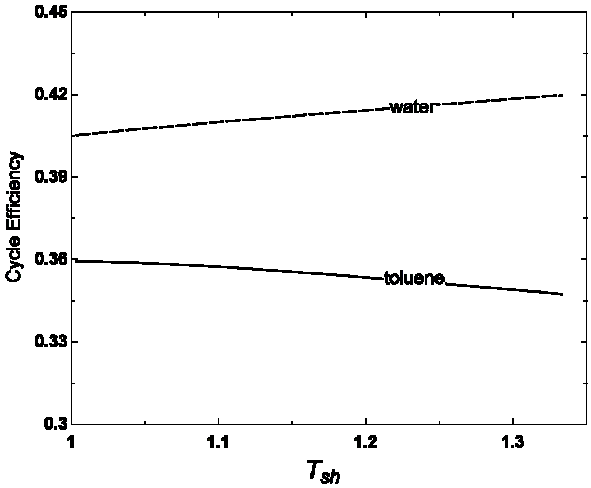

Figure 2.9: The effect of added superheat on cycle efficiency for a steam cycle and an organic fluid cycle without recuperation

The observation that organic Rankine cycle efficiency can degrade as the degree of superheat increases emphasizes the importance of energy recovery in ORC design. Efforts to increase the average temperature of heat addition must always be considered along with energy recovery in order to optimize cycle efficiency.

2.2.5 The impact of turbine inlet pressure on ORC performance

Most thermodynamic texts will show that steam Rankine cycle efficiency shows a small, but positive improvement with increased turbine inlet pressure. The relationship between turbine inlet pressure and cycle efficiency is more complicated for organic Rankine cycles as the presence of recuperation can upset the trend seen with traditional Rankine cycles.

In order to characterize the relationship between turbine inlet pressure and cycle efficiency for ORCs a series of analyses were performed. The test case is an ORC using toluene as the working fluid operating between 360ºC and 40ºC thermal boundary conditions with an isentropic pump and turbine as well as a recuperator of defined effectiveness.

The general shape of this cycle at three discrete pressures with a 90% effective recuperator was examined. Figures 2.10 and 2.11 show T-s and h-s diagrams for this cycle. Note 7500 kPa is supercritical for toluene. In general, as turbine inlet pressure increases at constant temperature, turbine inlet enthalpy and turbine exit enthalpy decrease. At lower pressures the amount of heat addition to the power cycle increases while the amount of recoverable heat in the turbine exhaust also increases.

To see the effect of turbine inlet pressure on turbine work it is helpful to refer to Figure 2.12 which is a zoomed-in view of the expansion shown in Figure 2.11. Here it can be seen that, over the range of pressures, turbine work per unit mass goes through a maximum. For toluence, this maximum occurs at 3700 kPa.

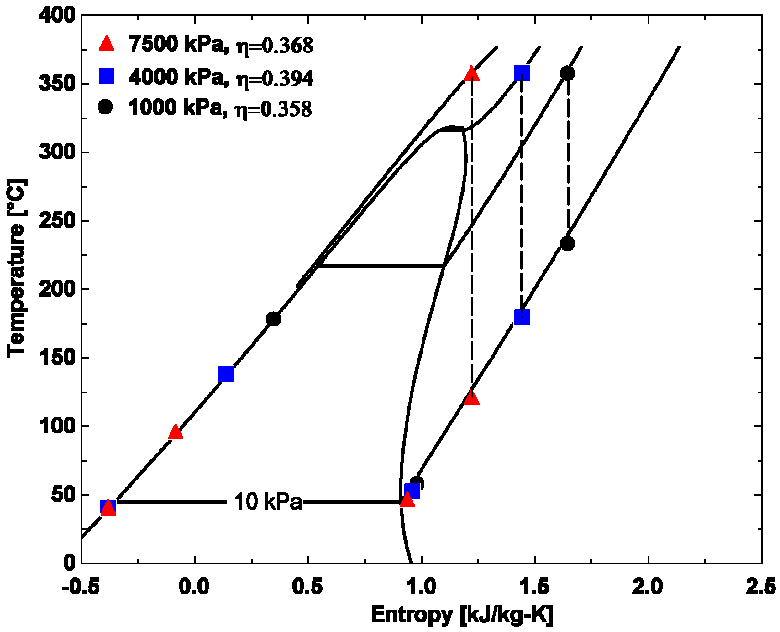

Figure 2.10: T-s diagram for a 90% recuperated ORC with toluene as the working fluid operating at three discrete pressures.

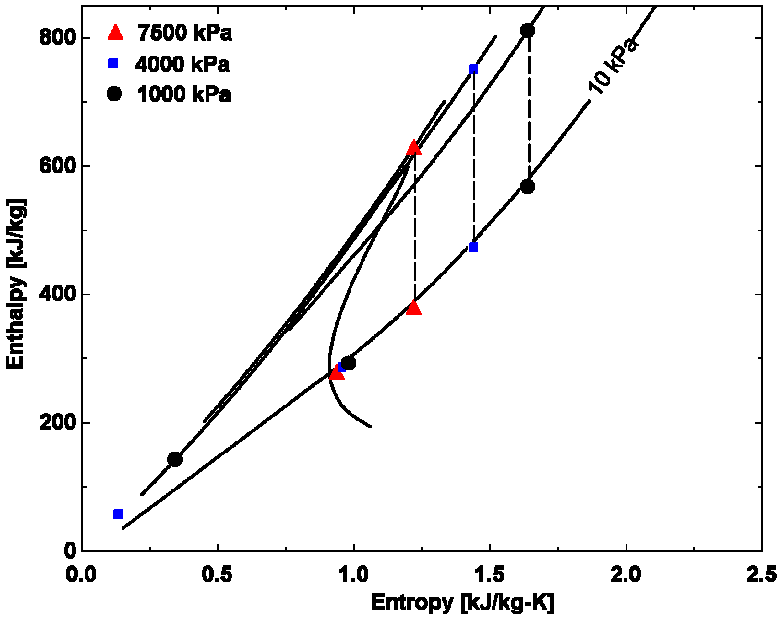

Figure 2.11: h-s diagram for a 90% recuperated ORC with toluene as the working fluid operating at three discrete pressures.

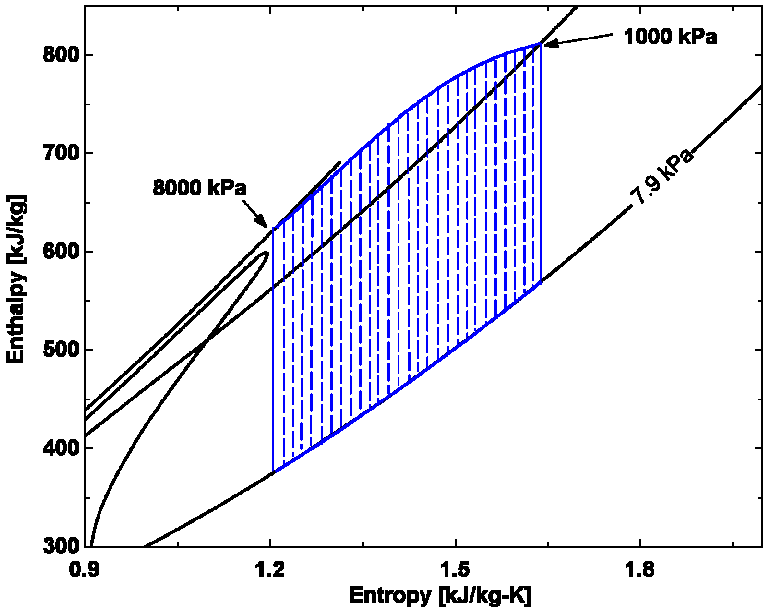

Figure 2.12: Variation in isentropic turbine work as a function of inlet pressure.

In order to understand all the interactions that effect cycle efficiency, it is helpful to first examine a cycle that has no recuperation. Figure 2.13 shows how work per unit mass, heat addition and cycle efficiency vary as a function of turbine inlet pressure. For a cycle with no recuperation, cycle efficiency asymptotes to a value as turbine inlet pressure increases. This behavior occurs because the turbine work is *relatively* constant when compared to the rate at which heat addition decreases with increasing pressure.

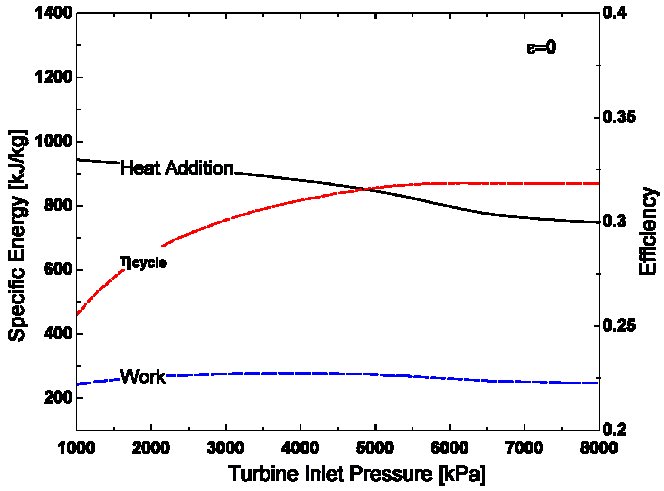

Figure 2.13: Isentropic turbine work, Heat addition and cycle efficiency as a function of turbine inlet pressure.

Now consider Figure 2.14 which shows performance of the same system seen in Figure 2.13 but with the addition of recuperation at 90% effectiveness. Specific work as a function of pressure is unchanged, as it should be since the expansion is independent of the presence of recuperation (assuming recuperation induces no pressure drops). Cycle efficiency now passes through a very clear maximum.

Energy recovered by the recuperator decreases with increasing turbine inlet pressure, shown in Figure 2.14. Heat addition shows less of a discernable trend when compared to the case with no recuperation because the presence of the recuperator roughly compensates for the change in heat addition as a function of pressure. As a result, the maximum in efficiency is driven by the maximum in work identified in Figure 2.15. This is an interesting result because that same maximum had no discernable effect on cycle efficiency in the non-recuperated case.

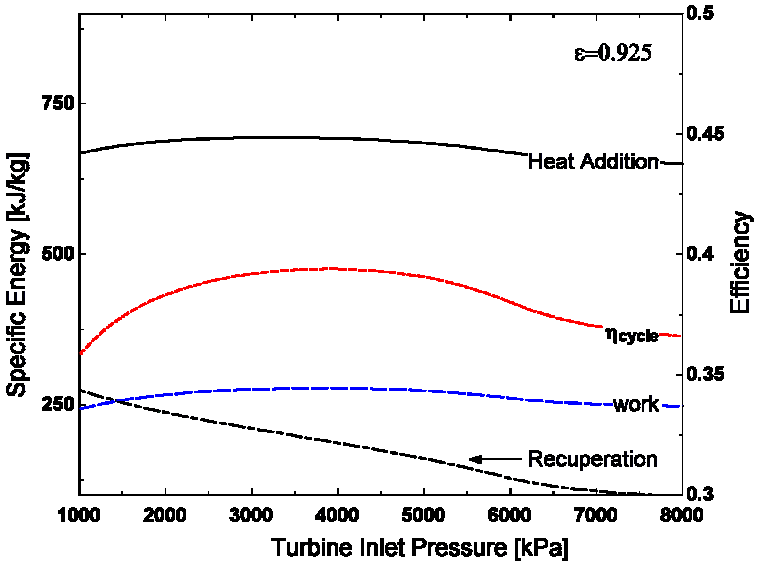

Figure 2.14: Isentropic turbine work, heat addition and cycle efficiency as a function of turbine inlet pressure for a recuperated ORC.

Figure 2.15 and Figure 2.16 show cycle efficiency as a function of turbine inlet pressure and recuperator effectiveness for two cycle configurations. Figure 2.15 is the case studied in the previous examples, with no pressure drop across the recuperator. Figure 2.16 is identical except for the addition of a 100 kPa pressure drop across the recuperator. The efficiency trends at various levels of effectiveness are identical for the two cases,

only shifted down in 2.17 due to the pressure drop.

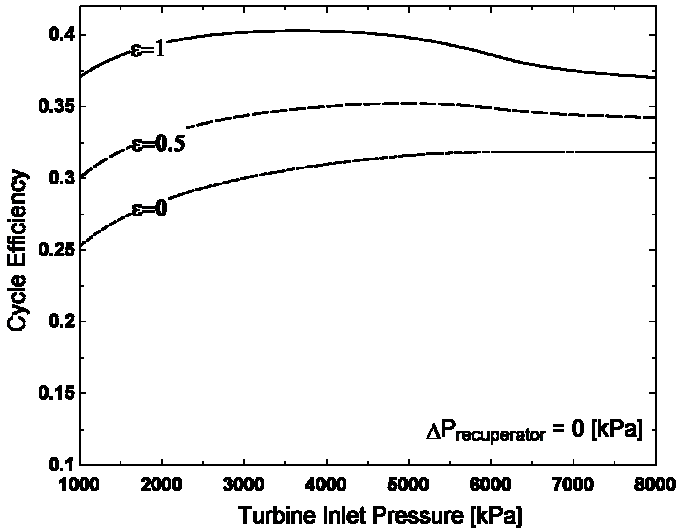

Figure 2.15: Cycle efficiency as a function of turbine inlet pressure for different values of recuperator effectiveness.

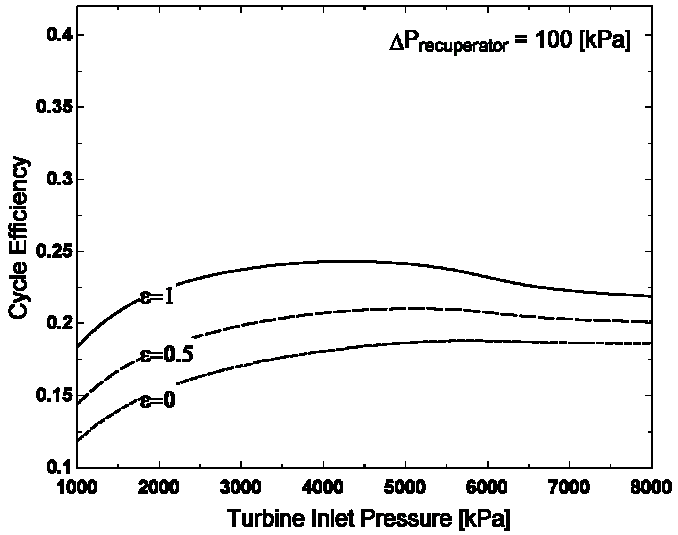

Figure 2.16: Cycle efficiency as a function of turbine inlet pressure for different values of recuperator effectiveness.

Optimal boiler pressure varies with recuperator effectiveness. In general, as recuperator effectiveness increases, optimal operating pressure is reduced. This behavior is due to the fact that at lower pressures there is more energy that can be recovered in the recuperator, thus the recuperator has a larger impact on efficiency at lower pressures.

2.3 Summary and conclusions

Rankine cycles using organic working fluids have some distinct practical and thermodynamic advantages over steam for applications that depend on low-moderate temperature thermal resources or demand simplicity.

In general organic working fluids display a *drying* behavior which results in a superheated turbine exhaust rather than the two-phase mixture common with steam. This dramatically simplifies cycle design at low temperature. A further simplification to cycle design is afforded by the relatively small turbine pressure ratios (working fluid dependent). Small pressure ratios and the high saturation densities of candidate organic working fluids simplify turbine design.

High temperature thermal stability is a principle consideration when selecting an organic working fluid for power generation. Identifying the approximate condensing pressure for an organic Rankine cycle design is of particular importance, as a sub-atmospheric condensing pressure requires added maintenance.

The addition of superheat at constant pressure expectedly increases steam cycle performance. However, in the absence of recuperation the addition of superheat can lead to a decrease in organic Rankine cycle efficiency. The relationship between superheat and efficiency is an important organic Rankine cycle design consideration.

Steam cycles show a diminishing benefit to cycle efficiency with the increase of turbine inlet pressure. In organic Rankine cycles this relationship is complicated by the presence of a recuperator showing that for ORCs an optimal boiler pressure does exist.

Understanding the fundamental thermodynamic distinctions between steam and organic fluids can help inform the intelligent design of simple powerplants for the utilization of low-moderate temperature thermal resources.

3 Organic Rankine Cycle Models

Two mathematical models of organic Rankine cycles are developed for simulation and analysis. The first model is designed for rapid screening of potential power cycle configurations and the second for detailed part-load simulation, optimization and analysis.

3.1 Rapid Screening Cycle Analysis Model

The rapid screening cycle analysis model is designed to compare and evaluate potential organic Rankine cycle configurations. Equations that describe the performance of each cycle component are developed and the coupled equations are solved to provide a steady-state operating point that can be analyzed to determine the performance potential of a particular cycle. The model described first in this section is the most common ORC configuration, a single-stage expansion with recuperation. This cycle configuration will be referred to as the 'reference cycle.' The modeling of alternate cycle configurations (reheat, feedwater heating, etc…) is treated the end of this section.

Figure 3.1 shows the individually modeled cycle components of the rapid screening model and the corresponding working fluid state points.

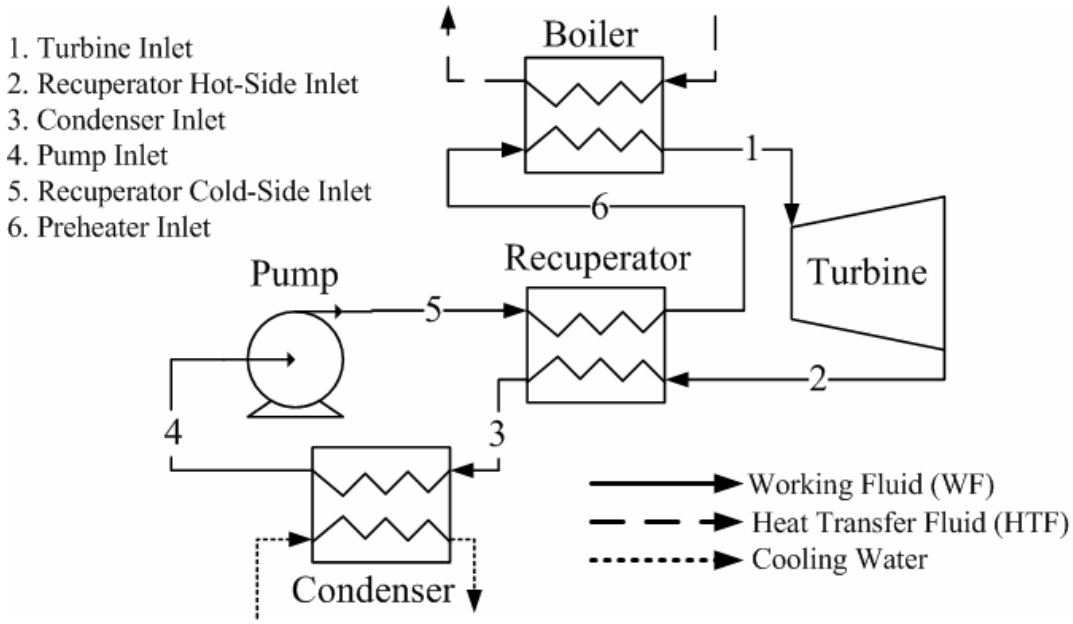

Figure 3.1: Modeled components in an ORC with single-stage expansion and recuperation

This model requires the following parameters to identify a steady-state operating point:

- Boiler approach temperature (pinch-point)
- Condenser approach temperature (pinch-point)
- Working fluid mass flow rate
- Recuperator effectiveness
- Component pressure drops
- Pump, turbine and generator efficiencies
- Cooling water supply temp
- Heat Transfer Fluid supply temp

Organic working fluid property data is obtained using EES [Klein, 2006]. EES uses the Fundamental Equation of State [Jacobsen et al, 1997] for n-pentane and toluene. Cooling water property data are also obtained using EES.

Detailed property data are not available for most of the proposed heat transfer fluids, typically only specific heat correlated as a function of temperature is provided by manufacturers. In order to simplify the formulation of component energy balances, the enthalpy of the heat transfer fluid is calculated as a function of temperature in the following manner (with 0ºC as the reference temperature) [Moran & Shapiro, 2002]:

$$h_{HTF} = \int_{0^\circ C}^{T} C_{p,HTF}\, dT \qquad [3.1.1]$$

Boiler

The boiler is modeled such that all power cycle heat addition (preheating, evaporation and superheating) takes place in a single adiabatic counter-flow heat exchanger. Figure 3.2 shows the flows through the boiler, where *h* refers to fluid enthalpy and the subscript refers to the state point shown in Figure 3.1.

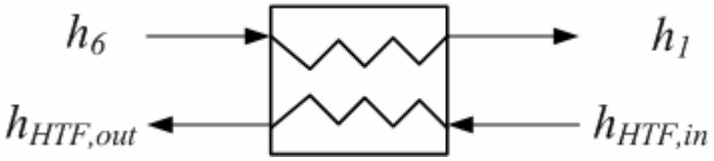

Figure 3.2: Flow directions of HTF and WF through the boiler

The performance of the boiler is constrained by the boiler pinch-point parameter, where the pinch-point temperature is defined as the minimum temperature difference occurring in the heat exchanger, demonstrated in Figure 3.3. In most cycles this occurs at the working fluid liquid saturation point, as shown in Figure 3.3, or at the working fluid exit.

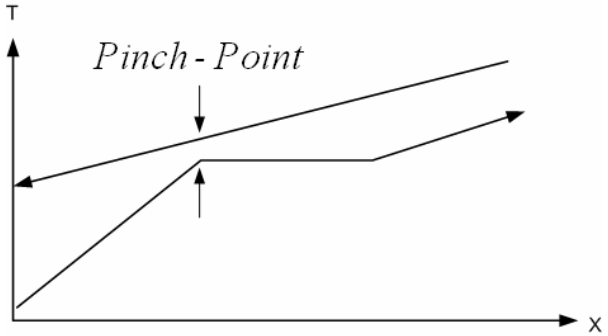

Figure 3.3: Heat exchanger pinch-point temperature

An energy balance on the boiler reduces to the following form yielding the heat transfer fluid exit temperature:

$$\dot{Q}_{boiler} = \dot{m}_{WF}(h_1 - h_6) = \dot{m}_{HTF}(h_{HTF,in} - h_{HTF,out}) \qquad [3.1.2]$$

Working fluid enthalpy (h_1, h_6) is constrained by the pinch-point temperature and defined operating pressure.

Turbine/Generator

The turbine and generator are modeled using an isentropic efficiency for the turbine and a mechanical-electrical efficiency for the generator. Figure 3.4 shows the turbine generator and related working fluid enthalpies.

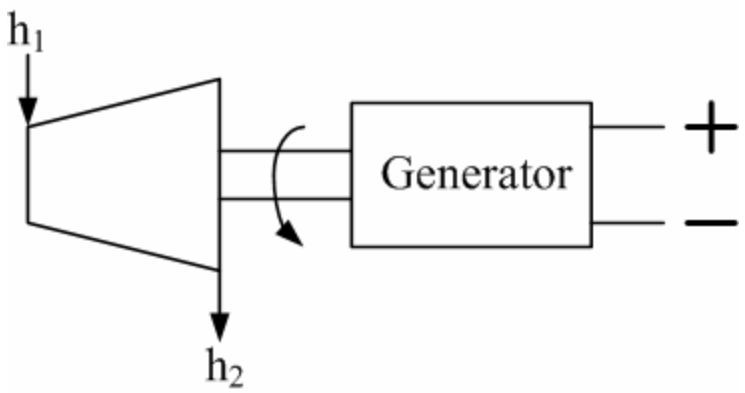

Figure 3.4: Turbine Generator process flow

The turbine isentropic efficiency is defined as follows [Moran & Shapiro, 2002]:

$$\eta_{Turbine} = \frac{h_1 - h_2}{h_1 - h_{2,s}} \qquad [3.1.3]$$

where $h_{2,s}$ is the working fluid enthalpy at the turbine exit after an isentropic expansion.

Turbine power is then:

$$W_{turbine} = \dot{m}_{WF}(h_1 - h_2) \qquad [3.1.4]$$

Generator efficiency is defined as follows:

$$\eta_{generator} = \frac{\dot{W}_{electric}}{\dot{W}_{mechanical}} \qquad [3.1.5]$$

Unless otherwise stated, generator efficiency is assumed to be 100%.

Recuperator

The performance of the recuperator, assumed to be adiabatic, is constrained by the defined effectiveness. Figure 3.5 shows the working fluid enthalpies associated with the recuperator.

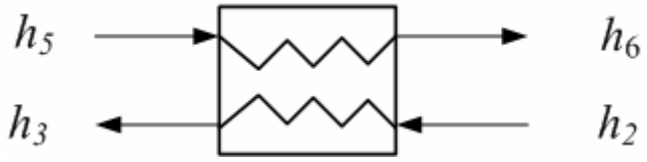

Figure 3.5: Flow directions of the hot (*2-3*) and cold (*5-6*) working fluid streams in the recuperator

Recuperator effectiveness is defined as:

$$\varepsilon = \frac{h_{in} - h_{out}}{h_{in} - h_{out,min}} \quad [3.1.6]$$

where h_{in} and h_{out} correspond to the inlet and outlet states of the minimum capacitance working fluid stream. In most organic Rankine cycle recuperators, the stream with the minimum capacitance rate will be the turbine exhaust (h_2 and h_3). $h_{out,min}$ represents the minimum possible exit enthalpy for the smaller capacitance rate stream. Thus, in most cases, as ε approaches 1, the hot fluid exiting the recuperator (turbine exhaust) approaches the cold fluid inlet temperature.

As with the boiler, the energy balance reduces to the following form allowing state 6 to be constrained:

$$\dot{Q}_{recuperator} = \dot{m}_{WF}(h_2 - h_3) = \dot{m}_{WF}(h_6 - h_5) \quad [3.1.7]$$

Condenser

Like the boiler, the condenser is governed by a pinch-point temperature parameter. The pressure at state 4 is the saturation pressure corresponding to the condensing temperature. Figure 3.6 shows the flows associated with the condenser.

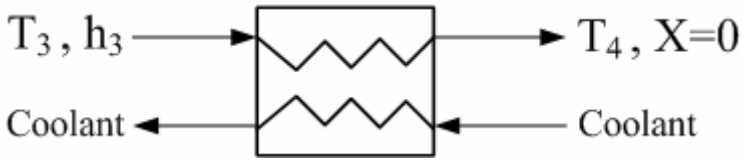

Figure 3.6: Flow directions in the condenser

Total heat rejection and coolant exit conditions are again calculated with an energy balance around the condenser:

$$\dot{Q}_{condenser} = \dot{m}_{WF}(h_3 - h_4) = \dot{m}_{coolant}(h_{coolant,out} - h_{coolant,in}) \quad [3.1.8]$$

Pump

Pump performance is governed by an isentropic efficiency. Figure 3.7 shows the fluid flows associated with the pump.

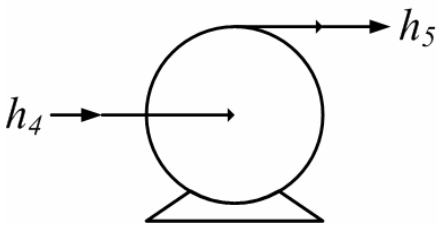

Figure 3.7: Pump fluid flows

The pump efficiency is defined as follows:

$$\eta_{pump} = \frac{h_{5,s} - h_4}{h_5 - h_4} \qquad [3.1.9]$$

where $h_{5,s}$ is the enthalpy at state 5 if the compression were isentropic. Power required by the pump is then:

$$\dot{W}_{pump} = m_{WF}(h_5 - h_4) \qquad [3.1.10]$$

Figures of merit

Equations [3.1.1] – [3.1.9] constrain all the state points for the working fluid, heat transfer fluid and cooling water in the power cycle. Together they identify a single steady-state operating point for the power cycle. Using this operating point, figures of merit useful for comparing power cycles can be calculated. They are as follows:

- Thermal (first-law) efficiency, which is the ratio of net work done by the power cycle to the amount of heat input to the cycle:

$$\eta_{cycle} = \frac{\eta_{generator}\dot{W}_{turbine} - \dot{W}_{pump}}{\dot{Q}_{boiler}} \qquad [3.1.11]$$

- Energy Density (*ED*), which relates the work done by the power cycle and the maximum fluid specific volume in the power cycle. V_{max} generally occurs at the turbine exit:

$$ED = \frac{\eta_{generator}\dot{W}_{turbine} - \dot{W}_{pump}}{\dot{m}_{WF} v_{\max}} \qquad [3.1.12]$$

- Second Law efficiency, which is the ratio of work done by the power cycle to the theoretical maximum amount of work [Moran & Shapiro, 2002]:

$$\eta_{2nd\,law} = \frac{\eta_{generator}\dot{W}_{turbine} - \dot{W}_{pump}}{\dot{m}_{HTF,in}(\Psi_{HTF,in} - \Psi_{HTF,out})} \qquad [3.1.13]$$

  Where Ψ is the specific availability of the HTF and is defined as (neglecting kinetic and potential energy effects):

$$\Psi_x = (h_x - h_0) - T_0(s_x - s_0) \qquad [3.1.14]$$

- Component Availability Destruction (steady-state, adiabatic), which is the resource availability that was not successfully converted into useful work:

$$\dot{A}_{destruction} = \sum \dot{m}_{in}\Psi_{in} - \sum \dot{m}_{out}\Psi_{out} - \dot{A}_{work} \qquad [3.1.15]$$

3.1.1 Alternate cycle configurations

The model presented in the preceding section is specifically formulated for the reference cycle. The unique modeling details of each alternative configurations of interest are discussed below:

Reference cycle without recuperation

No modifications to the model are required to accommodate this change, the effectiveness of the recuperator is simply set to zero.

Reference cycle with turbine reheat

In this cycle two turbine stages are used. The working fluid is expanded to an intermediate pressure, reheated, and then extracted to the condensing pressure. The intermediate pressure is a design parameter. Figure 3.8 shows a schematic of such a system.

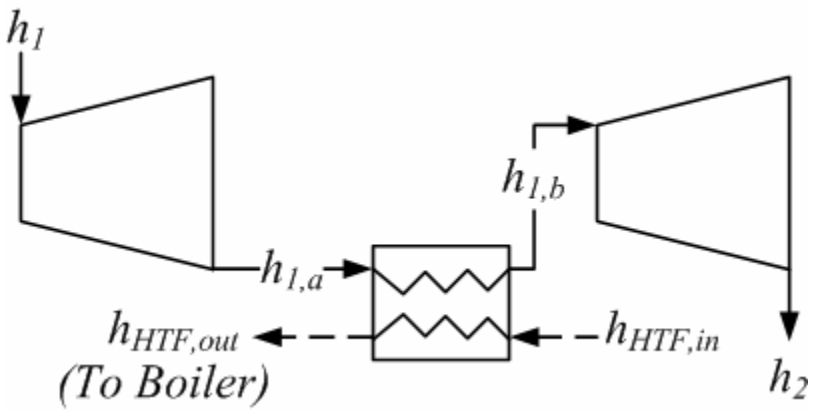

Figure 3.8: Turbine reheat system flow directions

The two turbine stages are analyzed separately just as the single stage turbine was, using equation [3.1.3]. Their efficiencies need not be the same. The reheater is constrained using a pinch-point temperature, analogous to the boiler. The reheater receives heat transfer fluid directly from the solar field making $h_{HTF,out}$ in Figure 3.8 the new inlet to the boiler.

Reference cycle with feedwater heating in place of recuperation

The feedwater heater, like the recuperator, preheats the working fluid before it enters the boiler. In a feedwater heater system, hot vapor is extracted from the turbine at an intermediate pressure (requiring a two-stage turbine) and heat exchanged with the cold working fluid on its way to the boiler. This configuration is shown in Figure 3.9. In this case no recuperator is used and only the feedwater heater preheats the working fluid prior to the boiler.

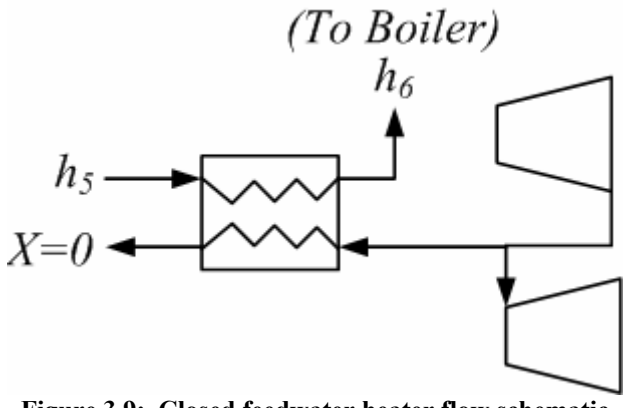

Figure 3.9: Closed feedwater heater flow schematic

As shown in Figure 3.9 the hot vapor extracted from the turbine is assumed to be fully

condensed at the exit of the feedwater heat exchanger. The extraction pressure or extraction mass flow can be specified while the other is varied to achieve a defined pinch-point temperature.

A second heat exchanger can be added to the feedwater heater where the saturated liquid is sub-cooled. This heat exchanger would use the previously described approach temperature methodology.

Reference cycle with feedwater heating

This cycle incorporates the feedwater heating system just described to the reference cycle.

3.1.2 Heating Curve Generation

Heating curves show the temperature profile of both the hot and cold fluids in a heat exchanger as a function heat transfer rate (duty). These curves offer insight into power cycle design. Temperature as a function of heat transfer rate for both hot and cold fluid is formulated using a finite-difference approach as follows:

$$\Delta h = \frac{\dot{Q}}{i_n \dot{m}} \qquad [3.1.16]$$

$$h_{i+1} = h_i + \Delta h \quad for\, i = 0, n-1 \qquad [3.1.17]$$

$$T_{i+1} = f(P, h_{i+1}) \quad for\, i = 0, n-1 \qquad [3.1.18]$$

where n is the number of data points in the heating curve representation, P is a constant or average pressure in the heat exchanger and i is a placeholder.

3.2 Simulation and Part-Load Performance Model

The simulation model is structured in much the same way as the rapid screening model with emphasis shifted to simulation and optimization of a particular design rather than

screening many different designs. The model presented here is general, but it has been tailored specifically to represent the APS Saguaro plant [Price, 2006]. It could be readily modified to represent other designs of similar configuration.

The configuration for the APS plant is the reference cycle, but unlike the rapid screening model each heat transfer process is independently modeled in order to capture part-load performance. The general process flow for the simulation model is shown in Figure 3.10.

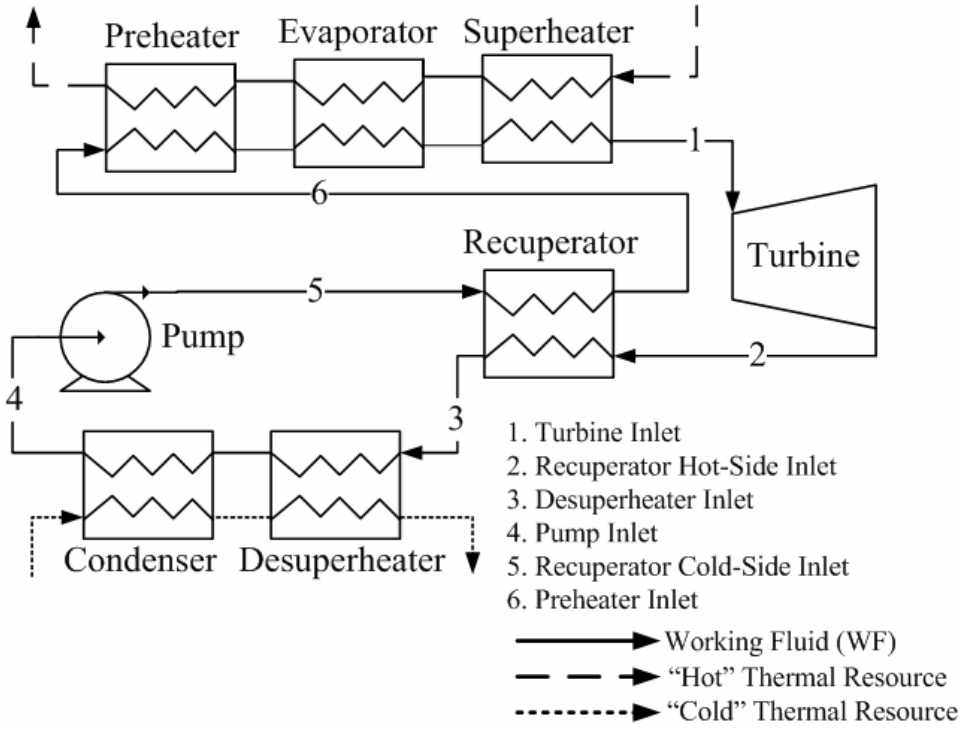

Figure 3.10: process flow for simulation and optimization power cycle model

This model is designed to integrate with other "balance of system" component models to allow analysis of entire solar power generation systems. Figure 3.11 shows the macroscopic information flow in to and out of this power cycle model.

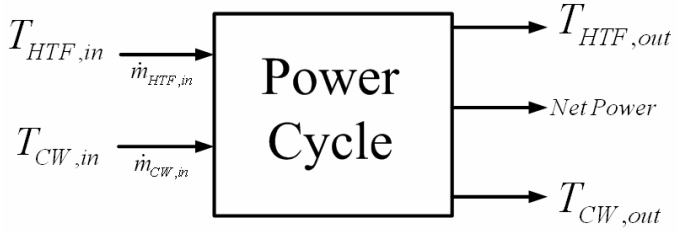

Figure 3.11: Power cycle simulation data flow

In addition to the cycle inputs shown in figure 3.29, the following quantities are design parameters or equipment performance factors required for simulation:

- Heat exchanger areas
- Turbine/Pump efficiencies
- Turbine Inlet pressure

The simulation model determines hot-side component operating pressures based on a design (turbine inlet) pressure and component pressure drops. Cold-side operating pressures are based on calculated heat exchanger performance. In the case of the APS design the part-load boiler pressure control is approximated in as follows:

$$P_1 = P_{1,ref}\left(\frac{\dot{m}}{\dot{m}_{ref}}\right) \qquad [3.1.19]$$

As load varies, so will component pressure drops. This variation must be accounted for if part-load performance is to be closely approximated. The Moody friction factor is typically used to determine pipe-flow pressure drops [White, 2003]:

$$\Delta P = f\frac{L}{D}\frac{\rho\vec{v}^2}{2} = 8\cdot f\frac{L\dot{m}^2}{\rho\pi^2 D^5} \qquad [3.1.20]$$

f, the Moody friction factor is a very weak function of Re at high values of Re so it is assumed to be constant in the expected operating range. If density variation is taken to be minor, part-load pressure drop variation is then only a function of mass flow rate and can be formulated as follows:

$$\Delta P = \Delta P_{ref}\left(\frac{\dot{m}}{\dot{m}_{ref}}\right)^2 \qquad [3.1.21]$$

where ΔP_{ref} is the manufacturer-specified or design pressure drop for the given component at the reference mass flow rate.

Heat Exchanger Modeling

In order to predict part-load heat exchanger performance in the simulation model a log-mean temperature difference approach is used such that:

$$\dot{Q} = UA\Delta T_{LM} \qquad [3.1.22]$$

where *UA* is the heat transfer coefficient-heat exchanger area product and ΔT_{LM} is the log-mean temperature difference defined as [Incropera, 2002]:

$$\Delta T_{LM} = \frac{(T_{H,in} - T_{C,out}) - (T_{H,out} - T_{C,in})}{LN\left(\frac{T_{H,in} - T_{C,out}}{T_{H,out} - T_{C,in}}\right)} \qquad [3.1.23]$$

Where the temperatures are as shown in Figure 3.12:

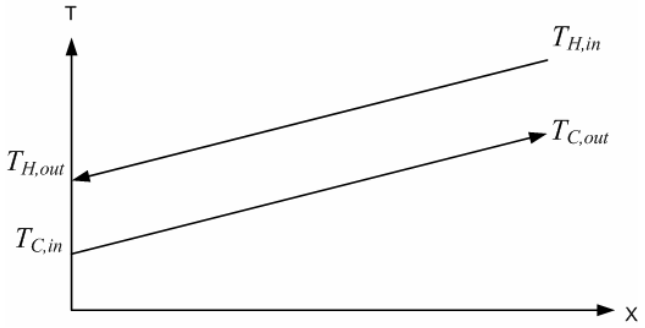

Figure 3.12: Temperature as a function of distance through a counter-flow heat exchanger

The log-mean temperature difference approach assumes constant fluid specific heat. In any of the modeled heat exchangers (preheater, evaporator, etc…) fluid thermal capacitance is roughly constant allowing the log-mean temperature difference technique to be employed.

U in equation [3.1.22] is the overall heat transfer coefficient for the heat exchanger. Predicting heat transfer coefficients normally depends on detailed fluid property data and geometry information as well as an appropriate correlation. For this generalized model it is inappropriate to assume knowledge of either. However, it is still desirable to know the approximate physical sizes of the heat exchangers relative to one another. In order to account for this the relative full-load heat transfer coefficients for each heat transfer process were estimated.

The overall heat transfer coefficient in each case is calculated as a counter-flow heat exchanger neglecting tube thermal conductivity [Incropera, 2002]:

$$\frac{1}{U} = \frac{1}{h_x} + \frac{1}{h_y} + R_w + R_f(t) \qquad [3.1.24]$$

Where h_x and h_y are the convective heat transfer coefficients of the two fluids in the heat exchanger. R_w and $R_f(t)$ represent the tube-wall resistance and time-dependent fouling resistance respectively. R_w and $R_f(t)$ are generally neglected for general models but can be integrated as design-specific data is available. The following order-of-magnitude values were used for single fluid heat transfer coefficients [Incropera, 2002]:

$$h_{liquid} = 1{,}000 \frac{W}{m^2}$$
$$h_{vapor} = 140 \frac{W}{m^2} \qquad [3.1.25]$$
$$h_{two-phase} = 10{,}000 \frac{W}{m^2}$$

The overall heat transfer coefficient calculated using this technique will not remain constant during off-design operation. The variation in U as a function of system load is determined as follows:

Single phase convective heat transfer correlations are often formulated in the following manner [Incropera, 2002]:

$$h = \frac{k}{d} \cdot a \cdot \mathrm{Re}^{0.8} \mathrm{Pr}^{0.3,0.4} = \frac{k}{d} \cdot a \cdot \left(\frac{4\dot{m}}{\pi D \mu} \right)^{0.8} \left(\frac{C_p \mu}{k} \right)^{0.3,0.4} \qquad [3.1.26]$$

where the exponent on the Prandtl number is 0.3 when the fluid is being cooled and 0.4 when the fluid is being heated. Based on the reference value determined by equation [3.1.24] the part-load overall heat transfer coefficient can be calculated for each heat exchange process in the following manner:

$$\frac{U}{U_{ref}} = \frac{k}{k_{ref}} \left(\frac{\dot{m} \mu_{ref}}{\dot{m}_{ref} \mu} \right)^{0.8} \left(\frac{C \mu k_{ref}}{C_{ref} \mu_{ref} k} \right)^{0.3,0.4} \qquad [3.1.27]$$

Correlations of the form of equation [3.1.26] do not capture all of the effects occurring in the two-phase heat exchangers (evaporator and condenser). Two-phase heat transfer correlations are often formulated as a liquid phase heat transfer enhancement of the form

[Rohsenow, 1998]:

$$\frac{h_{two-phase}}{h_{liquid}} = f(x, \rho_{liquid}, \rho_{vapor}, \sigma, ...) \neq f(\dot{m}) \qquad [3.1.28]$$

where h_{liquid} is of the form of equation [3.1.26]. As seen in equation [3.1.28] two-phase heat transfer enhancement is generally formulated in terms of mixture quality and liquid-vapor properties, not mass flow – which is the dominant force in single-phase heat transfer variation. In addition, in the two-phase heat exchangers the dominant resistance to heat transfer lies on the liquid side limiting the effect of variation in two-phase heat transfer coefficient. As a result, and for the sake of simplicity, the off-design correction factor in equation [3.1.27] is also used for the two-phase heat exchange processes.

Boiler

The boiler is modeled as three separate heat exchangers: a preheater, evaporator and superheater. Figure 3.13 shows the flow directions through the heat exchangers along with a corresponding temperature profile.

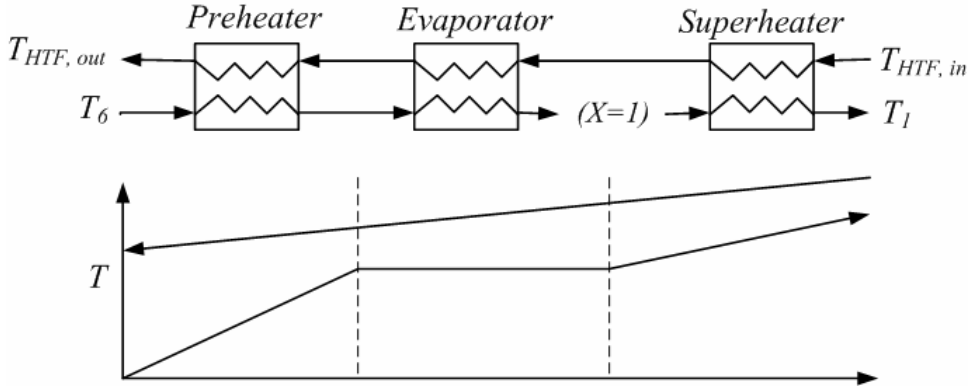

Figure 3.13: Flow directions for hot side heat exchangers in the simulation model

The preheater and evaporator are coupled by a shared surface area. Working fluid mass flow rate is calculated such that only saturated vapor exits the evaporator, a constraint consistent with typical power cycle design [El-Wakil, 1984]. The following system of equations is employed to describe boiler and preheater performance:

$$\dot{Q}_{preheater} = \dot{m}_{WF}(h_1 - h_6) = \dot{m}_{HTF}(h_{HTF,in,preheater} - h_{HTF,out}) \qquad [3.1.29]$$

$$\dot{Q}_{evaporator} = \dot{m}_{WF}(h_v - h_l) = \dot{m}_{HTF}(h_{HTF,in,evaporator} - h_{HTF,in,preheater}) \quad [3.1.30]$$

$$\dot{Q}_{preheater} = U_{preheater} A_{preheater} \Delta T_{LM,preheater} \quad [3.1.31]$$

$$\dot{Q}_{evaporator} = U_{evaporator} A_{evaporator} \Delta T_{LM,evaporator} \quad [3.1.32]$$

$$A_{preheater+evaporator} = A_{preheater} + A_{evaporator} \quad [3.1.33]$$

The preheater and evaporator are coupled by a combined area, $A_{preheater+evaporator}$, as seen in equation [3.1.33]. This combined area becomes a design variable and the solution to the set of equations yields the relative area required for each process. The superheater is assigned an independent heat exchanger area and also solved using a log-mean temperature difference technique.

Turbine

The turbine in the simulation model uses an isentropic efficiency (equation [3.1.3]) to describe its performance. Turbine efficiency, in general, is strongly dependent on how the operating flow relates to the design flow rate [Bartlett, 1958]. A second order polynomial was fit to a series of turbine design points from the APS plant to approximate turbine performance, as shown in equation [3.1.34]. The functional form of the fit is based on correlations developed for steam-turbines [Bartlett, 1958].

$$\eta_{turbine} = -0.1423 \cdot \left(\frac{\dot{m}}{\dot{m}_{ref}}\right)^2 + 0.2981 \cdot \left(\frac{\dot{m}}{\dot{m}_{ref}}\right) + 0.6127 \quad [3.1.34]$$

Recuperator and Condenser

The "cold" side heat exchangers (recuperator, desuperheater and condenser) are a mirror image of the boiler. Figure 3.14 shows the fluid flows in the condenser, recuperator and desuperheater.

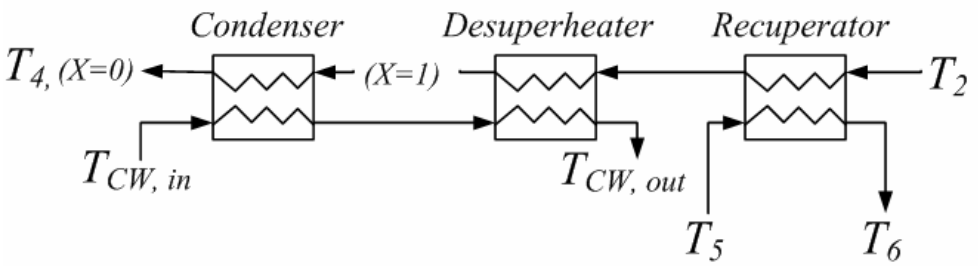

Figure 3.14: Cold side heat exchanger orientation and process flow for the simulation model

The technique used to compute performance for the preheater and evaporator is employed here with the condenser and desuperheater. The only difference is the constrained variables. In the boiler, pressure is a design variable and mass flow is a function of the heat exchanger performance. In the condensing section, mass flow rate is known (determined in boiler) and pressure is a function of the heat exchanger performance. The recuperator, like the superheater is assigned an independent heat exchange surface area.

Pump

Isentropic pump efficiency (equation [3.1.9]) is used to describe pump performance. Part-load pump efficiency is approximated as a function of mass flow using a relationship presented by Lippke [1998]:

$$\eta_{pump} = 2 \cdot \eta_{ref} \cdot \left(\frac{\dot{m}}{\dot{m}_{ref}} \right) - \eta_{ref} \left(\frac{\dot{m}}{\dot{m}_{ref}} \right)^2 \qquad [3.1.35]$$

where *ref* values represent design conditions.

3.3 Model Calibration and Validation

3.3.1 Plant Description

The Arizona public service (APS) has sponsored the construction of a 1 MW parabolic trough organic Rankine cycle (PTORC) powerplant by SolarGenix and ORMAT. The APS plant uses n-pentane as the power cycle working fluid and Radco Industries XCELTHERM®600 as the solar field heat transfer fluid. Figure 3.15 shows a flow

diagram for the plant.

All plant heat exchangers are a shell-in-tube design. Boiling and superheating take place in the same shell-in-tube heat exchanger as shown in Figure 3.15. Heat transfer fluid flows through the tube side, and the working fluid on the shell side. Likewise, in the water-cooled condenser the water occupies the tube side. In the recuperator the liquid working fluid occupies the tube side and the turbine exhaust occupies the shell side. The source of cooling water is a single induced draft cross-flow cooling tower.

The turbine is a specially designed impulse type turbine designed to rotate at 3630 rpm.

The solar field is composed of three parallel HTF flow loops. Each loop has eight independently controlled parabolic-trough reflectors connected in series. In total the solar field collector area is 10,340 $m^{2.}$ The solar field was sized to meet the design heat-input specifications of the power cycle [Price, 2006].

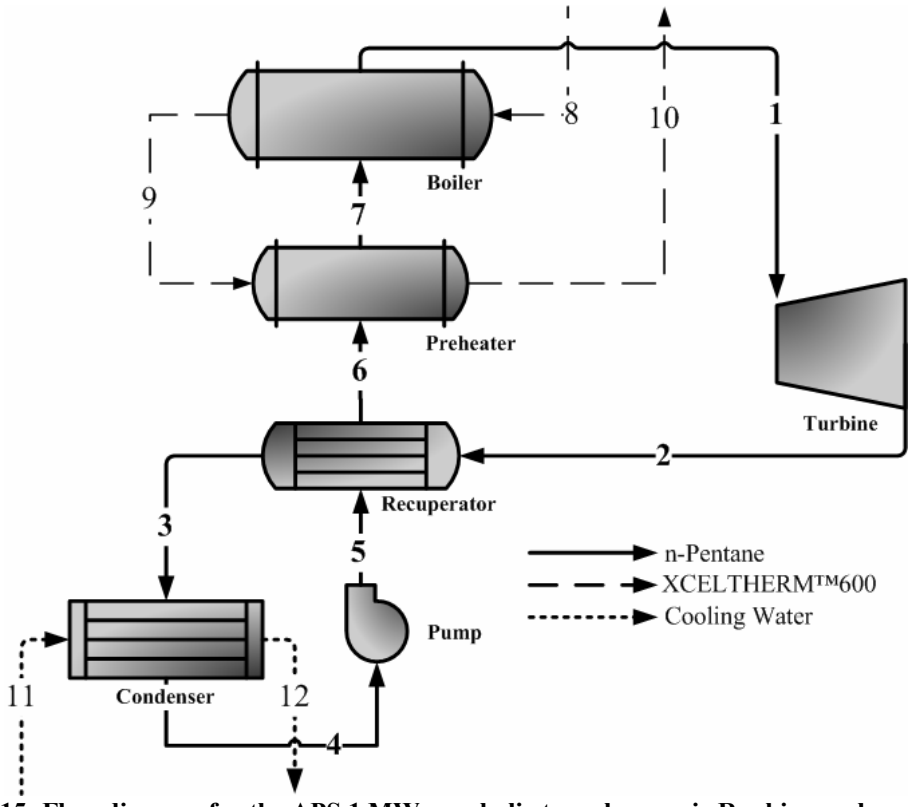

Figure 3.15: Flow diagram for the APS 1 MW parabolic trough organic Rankine cycle powerplant

3.3.2 Model Calibration Based on Manufacturer Predictions

The plant was modeled using the techniques described in section 3.2 along with projected performance data provided by the manufacturer using EES [Klein, 2006]. Table 3.1 provides a detailed breakdown of the state points shown in Figure 3.15. Both manufacturer and model output temperatures and pressures for full-load operation are reported. The model correlates well with the manufacturers' data at 100% load. The only discrepancies occur at state points 7 and 9, which are the intermediate states between the boiler and preheater. These discrepancies do not reflect a limitation in the model but rather they are a function of how the hot-side heat exchangers were modeled as explained in section 3.2.

The model outputs in table 3.1 were achieved by calculating the required heat exchanger area (and corresponding *UA*) to develop the pinch point temperatures in the boiler, condenser and recuperator predicted by the manufacturer at design conditions. Pump and turbine efficiencies were extracted from manufacturer's documents [Price, 2006]. All cycle state-points not based on manufacturer data are functions of the component performance models.

Table 3.1 APS plant 100% load state point summary

State #	State Name	Fluid	Manufacturer		Model	
			[C]	[kPa]	[C]	[kPa]
1	Turbine Inlet	n-Pentane	204.4	2227	204.5	2227
2	Recuperator Inlet	n-Pentane	133.3	81	133.3	81
3	Condenser Inlet	n-Pentane	57.7	74	57.7	74
4	Pump Inlet	n-Pentane	-	-	23.3	62
5	Recuperator Inlet	n-Pentane	24.4	2289	24.4	2289
6	Preheater Inlet	n-Pentane	86.9	2268	85.6	2268
7	Boiler Inlet	n-Pentane	148.9	2227	169.7	2227
8	HTF inlet	XCELTHERM®600	300	313	300	-
9	HTF preheater inlet	XCELTHERM®600	186.2	263	211	-
10	HTF return	XCELTHERM®600	120	104	119.9	-
11	CW inlet	Water	20	203	20	-
12	CW return	Water	24.3	143	24.3	-

Part-Load Performance

Data were available from the manufacturer predicting the facility's part-load performance. Figure 3.16 shows a comparison between the part-load performance predictions of the manufacturer and the model developed in this thesis. There is good agreement between the two simulations.

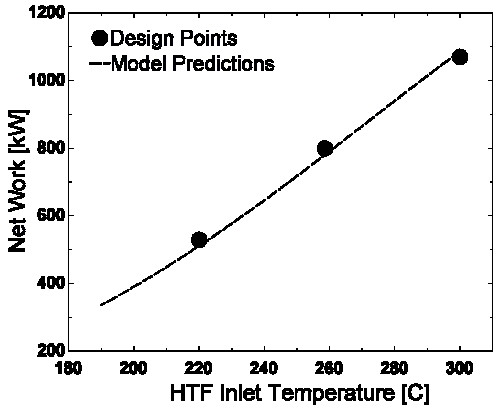

Figure 3.16: Comparison between APS plant designed part-load operating points and model predictions

3.4 TRNSYS Model Implementation

Implementing the model described in section 3.2 in EES [Klein, 2006] is ideal for performing parametric studies such as generating the part-load performance curve shown in Figure 3.16. However, it is not well suited for long-term simulation. That is, using local weather data to drive the simulation over long periods (years).

The TRNSYS [Klein et al, 2006] simulation environment is ideally suited to this task. TRNSYS is a program that controls the simulation of an array of interconnected components. For instance, in the case of the APS plant TRNSYS would read a weather data file which would serve as input to a solar field model which would then in turn be connected to the APS plant power cycle model.

The structure of TRNSYS requires that models be formulated as FORTRAN libraries (subroutines). In this environment it becomes a difficult programming task to

reformulate the non-linear APS plant model in FORTRAN where there is no intrinsic capability for handling such a problem. In addition, property data is not readily accessible like it is in EES, furthering the challenge. To make implementation of the APS plant model tractable in TRNSYS a linear regression was performed to correlate model outputs and inputs. The correlation parameters are the temperature and flow rate of the heat transfer fluid and the minimum working fluid temperature (condensing temperature). Heat transfer fluid temperature and mass flow rate will vary based on weather and solar field performance. Minimum working fluid temperature will vary based on ambient conditions as well as the cooling technique employed. The outputs of interest are the net power produced by the cycle, as well as temperature of the heat transfer fluid as it returns to the solar field.

Net power produced by the power cycle is correlated in the following manner:

$$\begin{aligned}\dot{W}_{NET} = {} & a_0 + a_1 \cdot T_{HTF,in} + a_2 \cdot T_{HTF,in}{}^2 + a_3 \cdot \dot{m}_{HTF} + a_4 \cdot \dot{m}_{HTF}{}^2 + a_5 \cdot T_{WF,min} \\ & + a_6 \cdot T_{WF,min}{}^2 + a_7 \cdot T_{HTF,in} \cdot \dot{m}_{HTF} + a_8 \cdot T_{HTF,in} \cdot T_{WF,min} + a_9 \cdot \dot{m}_{HTF} \cdot T_{WF,min}\end{aligned} \qquad [3.1.36]$$

where a_0-a_9 are determined using the linear regression capability built into EES [Klein, 2006].

Table 3.2 coefficients for net power correlation

coefficient	value
a_0	-1321
a_1	-3.401
a_2	0.008
a_3	-61.97
a_4	-1.507
a_5	152.75
a_6	-3.219
a_7	0.641
a_8	-0.037
a_9	-0.468

Figure 3.17 shows the output of equation [3.1.36] for different values of heat transfer fluid temperature, flow rate and a minimum working fluid temperature fixed to the design value. There is no perceivable error in between the full model and the linear regression (R^2=99.9).

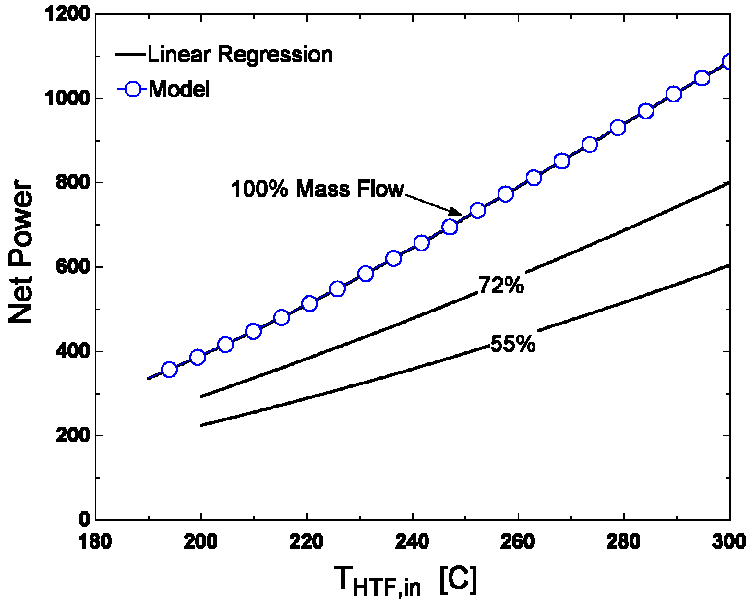

Figure 3.17: Linear regression of net power as a function of heat transfer fluid inlet temperature for 3 different heat transfer fluid flow rates. Also shown are the full model results for the design flow rate.

Heat transfer fluid return temperature is correlated similarly:

$$T_{HTF,out} = b_0 + b_1 \cdot T_{HTF,in} + b_2 \cdot T_{HTF,in}^{\ 2} + b_3 \cdot \dot{m}_{HTF} + b_4 \cdot \dot{m}_{HTF}^{\ 2} + b_5 \cdot T_{WF,min} + b_6 \cdot T_{WF,min}^{\ 2} + b_7 \cdot T_{HTF,in} \cdot \dot{m}_{HTF} + b_8 \cdot T_{HTF,in} \cdot T_{WF,min} + b_9 \cdot \dot{m}_{HTF} \cdot T_{WF,min} \quad [3.1.37]$$

where b_0-b_9 are determined using EES [Klein, 2006]

Table 3.3 coefficients for heat transfer fluid return temperature correlation

coefficient	value
b_0	-416.2
b_1	0.463
b_2	-0.001
b_3	7.326
b_4	-0.063
b_5	34.45
b_6	-0.688
b_7	-0.011
b_8	0.002
b_9	-0.012

To prevent erroneous simulation results the TRNSYS model is bounded so that it will

only produce power for a range of inputs that are consistent with its design parameters. A further detailed description of the TRNSYS implementation and its parameters is available in Appendix A.

4 ORGANIC RANKINE CYCLE ANALYSIS

4.1 Introduction

The rapid screening model developed in Chapter three allows the evaluation of organic Rankine cycles with specified boundary conditions and component performance criteria. This model enables the exploration of the practical limits for ORC performance as well as the comparison of alternative configurations from within a single, consistent, framework.

In this chapter, two such studies are presented. The first considers the thermodynamic potential of alternative organic Rankine cycle configurations. There is little discussion in the literature regarding ORC configurations that deviate from the reference configuration presented in section 2.2.1. This study will consider the efficiency benefit of alternative cycle configurations based on a realistic baseline design. The second study compares the performance of steam and organic Rankine cycles operating within similar thermal and component performance boundary conditions.

4.2 Evaluation of Alternative Organic Rankine Cycle Configurations

The recuperated cycle presented in section 2.2.1 is the most commercially available organic Rankine cycle configuration. While this configuration offers great simplicity, it is unclear whether it represents the limit of achievable efficiency. This section considers a variety of common power cycle modifications in the context of an actual ORC design in an attempt to identify potential for improving cycle efficiency.

The Coolidge solar-thermal powerplant is used here as the baseline for comparison. It was one of four plants built to demonstrate alternative means for producing irrigation pumping power [Larson, 1987]. It used 2140 m^2 of parabolic trough collectors to heat Caloria™ HT-43 HTF from 200^{o}C to 288^{o}C. The Caloria™ delivered thermal energy to an ORC with toluene as the working fluid. The plant was designed to generate 200 kW of electricity. The plant also included a HTF storage tank to provide on-demand power in periods of low insolation.

The operating conditions and component performance criteria obtained from the Coolidge plant are used here as a baseline for considering alternate cycle configurations with the rapid-screening model. In total, five ORC plants are modeled based on the Coolidge design criteria, where the reference cycle refers to the Coolidge plant's design configuration:

1. Reference cycle
2. Reference cycle without recuperation
4. Reference cycle with reheat
4. Reference cycle with feedwater heating in place of recuperation
5. Reference cycle with feedwater heating and recuperation

Table 4.1 shows the design specifications from the Coolidge plant used to determine the model input parameters for the reference case [Larson, 1987].

Table 4.1 Coolidge ORC Design Specifications

Specification		
Solar Field Inlet Temperature	200	°C
Solar Field Exit Temperature	288	°C
Caloria HT-43 Flow Rate	15,740	kg/h
Toluene Flow Rate	6305	kg/h
Turbine Inlet Temperature	268	°C
Turbine Inlet Pressure	1034	kPa
Parasitic Power	24	kW
Cycle Efficiency	20.4	%
Condensing Temperature	41	°C
Boiler Approach Temperature	20	°C

These design specifications are not sufficient to constrain the rapid screening model. Data were unavailable for recuperator and condenser pressure drops, turbine and pump efficiencies, and recuperator effectiveness. Unconstrained performance parameters were approximated using engineering judgment in order for model outputs to approach the reported performance of the Coolidge plant. While this does not capture the precise performance of the Coolidge plant, it is sufficient for establishing a base case for comparison. Note that for consistent power cycle comparison the maximum working fluid temperature is constrained to 268°C in all cases.

4.2.1 Coolidge Reference Cycle

The reference Coolidge plant cycle is a textbook Rankine cycle with the addition of turbine-exhaust recuperation for feedwater heating, analogous to the standard design described in section 2.2.1. Figure 4.1 shows a schematic of the power cycle with state points labeled that correspond to the T-s diagram in Fig. 4.2.

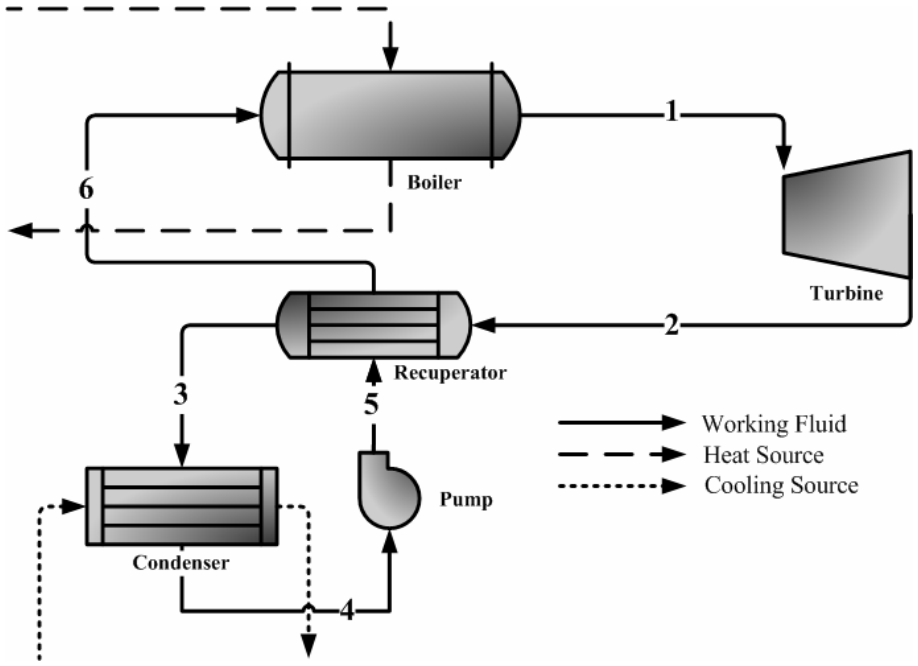

Figure 4.1: Coolidge Solar Thermal Power Plant reference cycle schematic, consisting of a organic Rankine Cycle with recuperation.

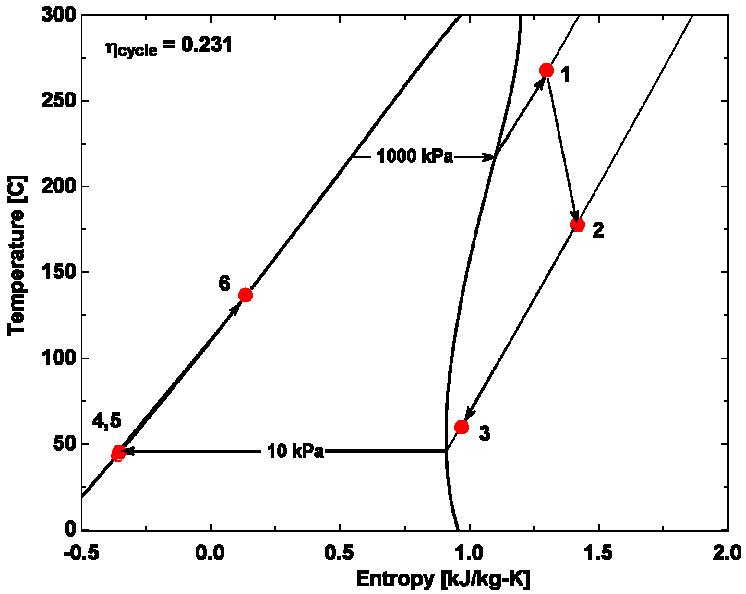

Figure 4.2: T-S Diagram for the Coolidge reference cycle. Numbered state points correspond with state points in Figure 4.1.

For the reference case, and all other cases, system pressure drops were neglected. A recuperator effectiveness of 90%, an isentropic turbine efficiency of 75% and pump efficiency of 65% were chosen to estimate the base-case performance. The efficiency of

the reference cycle is calculated as 23.1% using the rapid screening model described in Chapter 3.

4.2.2 Reference Cycle without Recuperation

This cycle is identical to the reference cycle with the elimination of recuperation. Analysis of this cycle provides an indication of the significance of recuperation on cycle performance. Figure 4.3 shows a schematic of the Coolidge cycle without recuperation. Figure 4.4 shows the T-s diagram for this cycle. Cycle efficiency in the absence of recuperation case dropped substantially, from 23.1% to 17.6%.

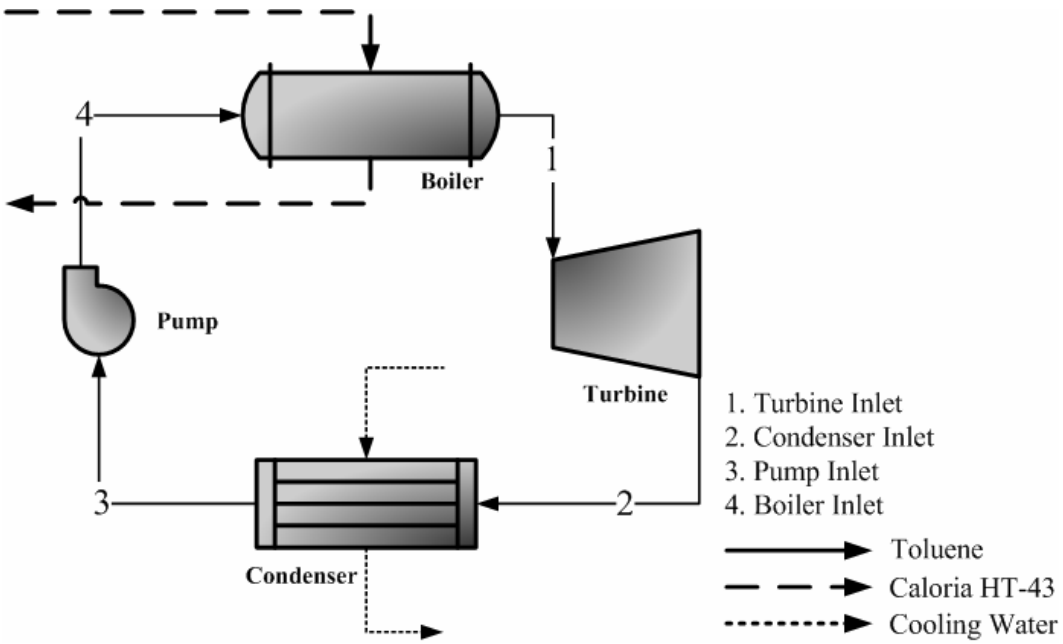

Figure 4.3: Power cycle schematic for the Coolidge plant with turbine exhaust recuperation eliminated.

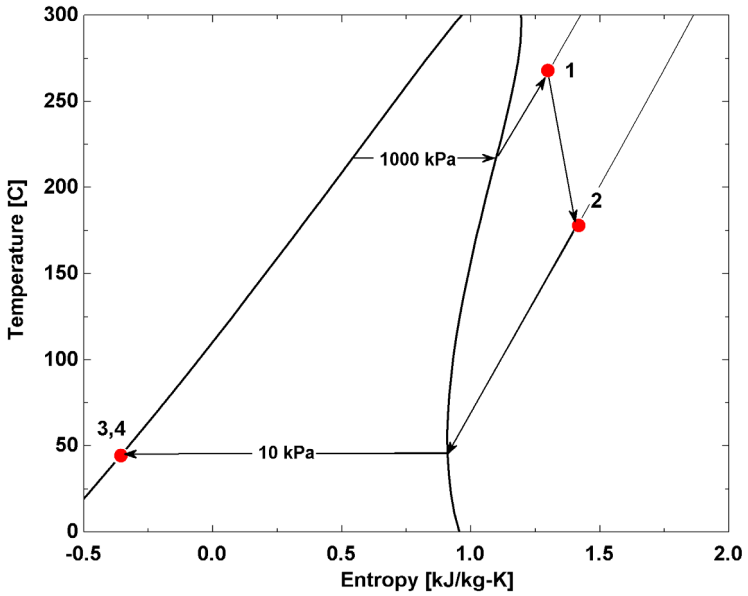

Figure 4.4: T-S diagram for the Coolidge plant without recuperation.

4.2.3 Reference Cycle with Turbine Reheat

Turbine reheat, described in section 3.1.1, is often employed in steam cycle power plants in order to take advantage of the higher efficiency that results with higher temperature boiler operation and to avoid low-quality steam at the turbine exit.

Figure 4.5 shows the schematic for the reference cycle with the addition of turbine reheat. Note the second (reheated) turbine expansion takes advantage of the highest temperature Caloria™. For this model the maximum working fluid temperature was achieved in the reheat stage, while an approach temperature of 20^{o}C was used in the boiler.

The reheat extraction pressure was chosen based on a parametric optimization of cycle efficiency, shown in Figure 4.7. The addition of a turbine-reheat stage results in a cycle efficiency of 24.1% or 1% higher than the reference case.

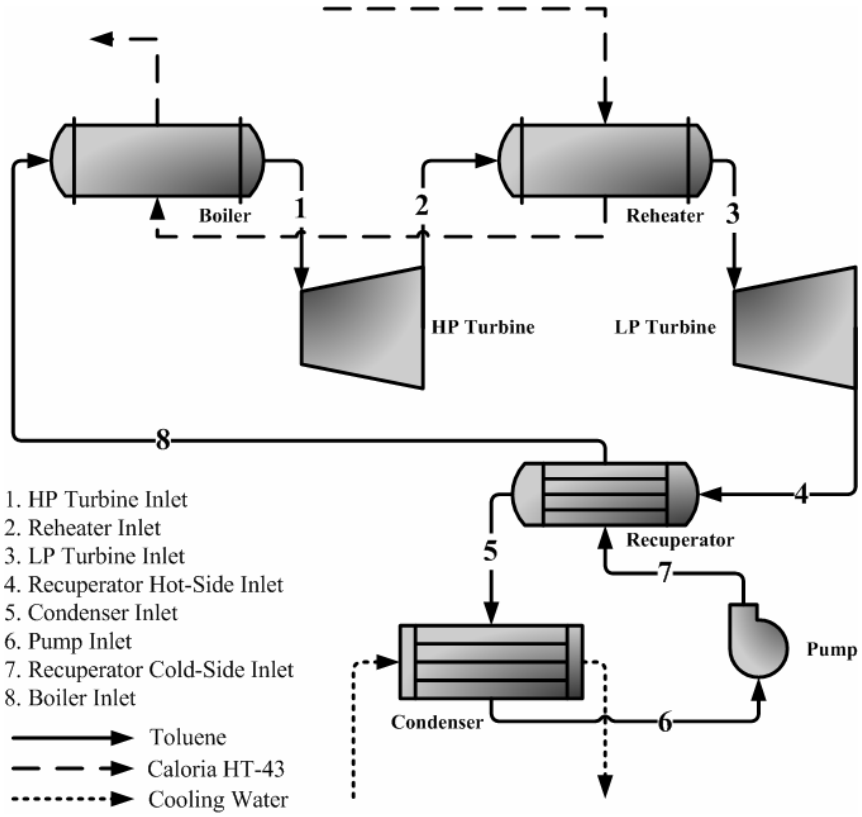

Figure 4.5: Power cycle schematic for the Coolidge reference cycle with the addition of turbine reheat.

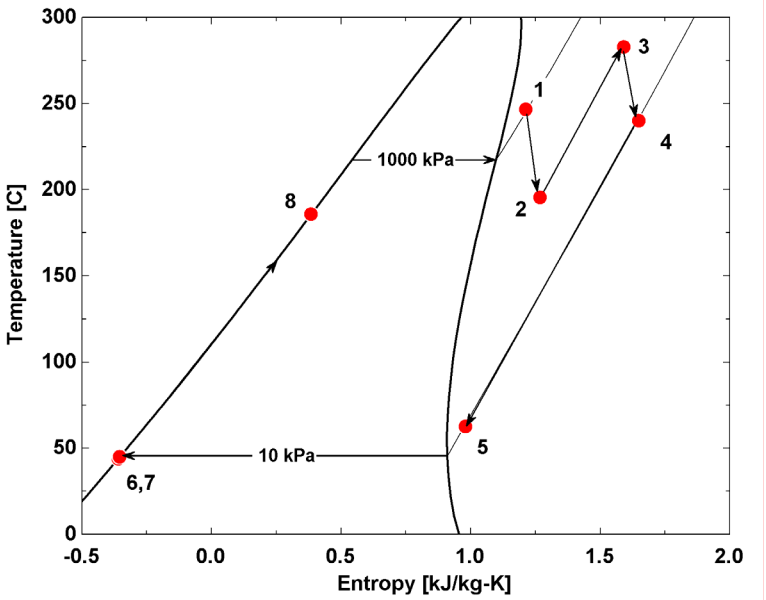

Figure 4.6: T-S diagram for the Coolidge cycle with the addition of turbine reheat.

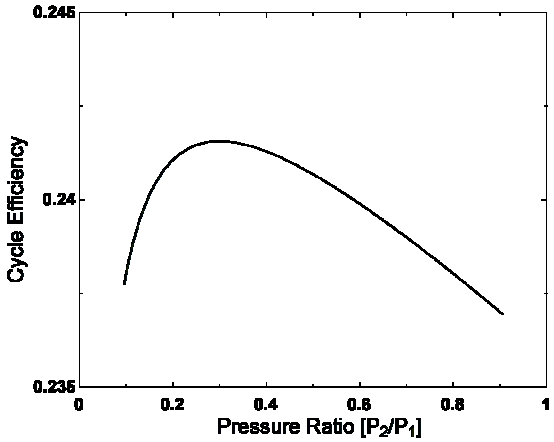

Figure 4.7: Cycle efficiency as a function of reheat extraction pressure where the extraction pressure is normalized to the initial turbine inlet pressure.

4.2.4 Reference Cycle with a Closed Feedwater Heater in Place of Recuperation

Feedwater heating, described in section 3.1.1, is a technique used in virtually every fossil fuel plant to de-aerate feedwater, as well as improve cycle efficiency by increasing the average heat addition temperature. Unlike recuperation, feedwater heating increases efficiency at the cost of mass flow rate through the low pressure turbine, decreasing turbine output.

The Coolidge plant has been modeled with a closed feedwater heater[1] in place of recuperation. The steam extraction pressure and mass flow rate were chosen based on maximizing efficiency and maintaining a 10°C pinch point in the heater. The feedwater heater was modeled such that the extraction steam would be fully condensed in the heater and then expanded to the condenser pressure and reincorporated into the working fluid stream. Figure 4.8 shows the system schematic and Figure 4.9 shows the cycle represented in a T-s diagram.

Like recuperation, feedwater heating increases efficiency to 19.1% relative to the case with no energy recovery, but to a lesser degree than recuperation.

[1] A "closed" feedwater heater indicates there is no physical contact between the hot and cold working fluid streams.

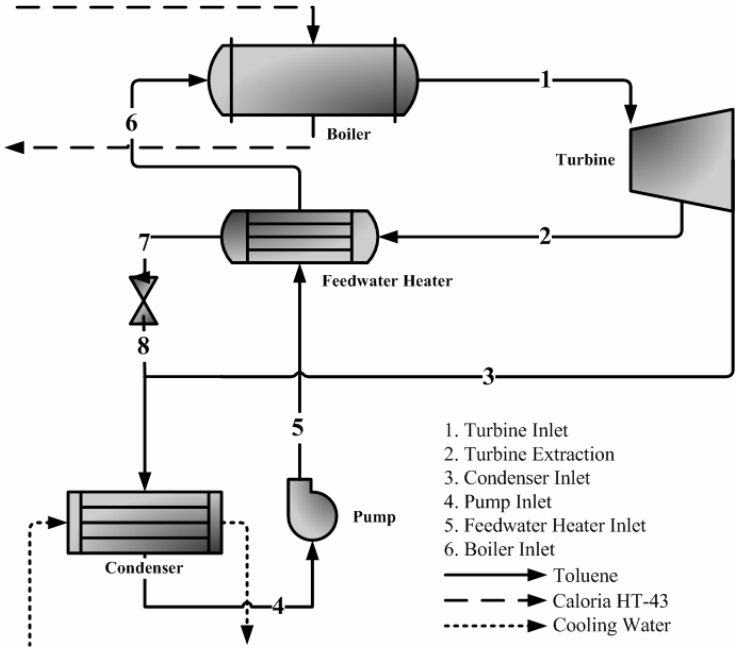

Figure 4.8: Power cycle schematic for the Coolidge reference plant with the addition of a single closed feedwater heater instead of recuperation

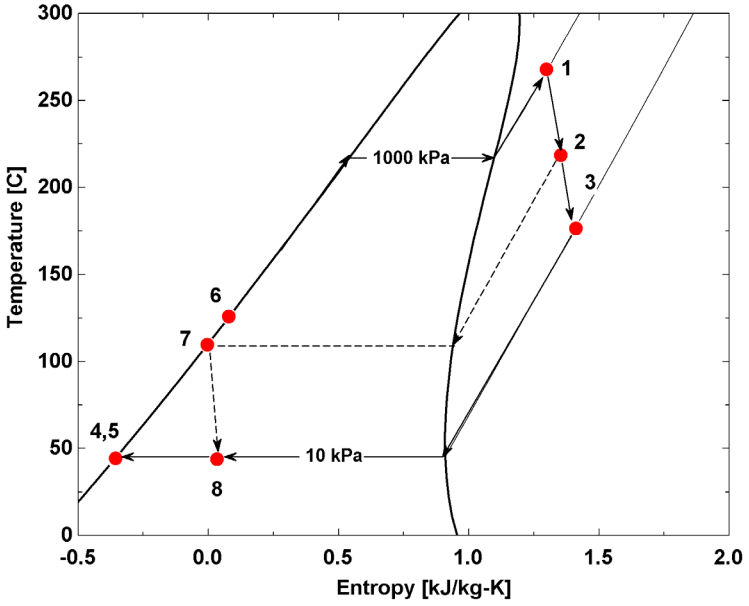

Figure 4.9: T-S Diagram for the Coolidge reference cycle with the addition of a single closed feedwater heater.

4.2.5 Reference Cycle with Feedwater Heating

This cycle incorporates both a closed feedwater heater and recuperator to improve efficiency. The recuperator from the reference cycle is coupled with a closed feedwater heater from the previous configuration. Figure 4.10 shows a schematic of this cycle with labeled state points that correspond to the T-s diagram in Figure 4.11. Before entering the boiler, the working fluid passes first through the recuperator then the closed feedwater heater. The heat exchangers were sequenced in this fashion due to the flexibility in the closed feedwater heater. The temperature of the turbine exhaust is fixed and thus so is the potential outlet temperature of the recuperator. The feedwater heater extraction pressure can be altered to change the hot-side inlet conditions and can thus be tailored to match the outlet of the recuperator.

The feedwater heater extraction pressure and mass flow were then set to achieve a pinch point of 10°C. Adding a closed feedwater heater to the reference cycle improves efficiency only slightly, to 23.6%.

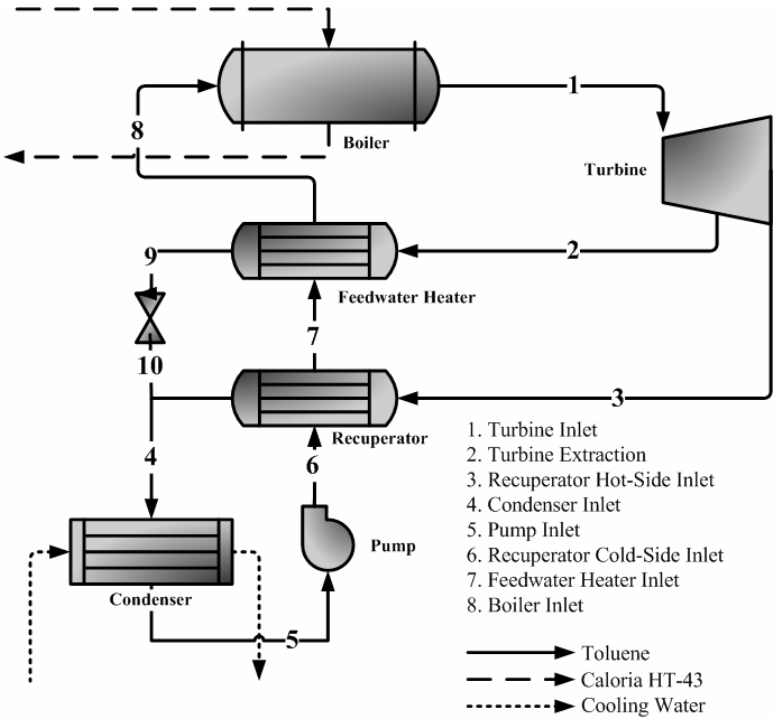

Figure 4.10: Power cycle schematic for the Coolidge reference plant with the addition of a single closed feedwater heater.

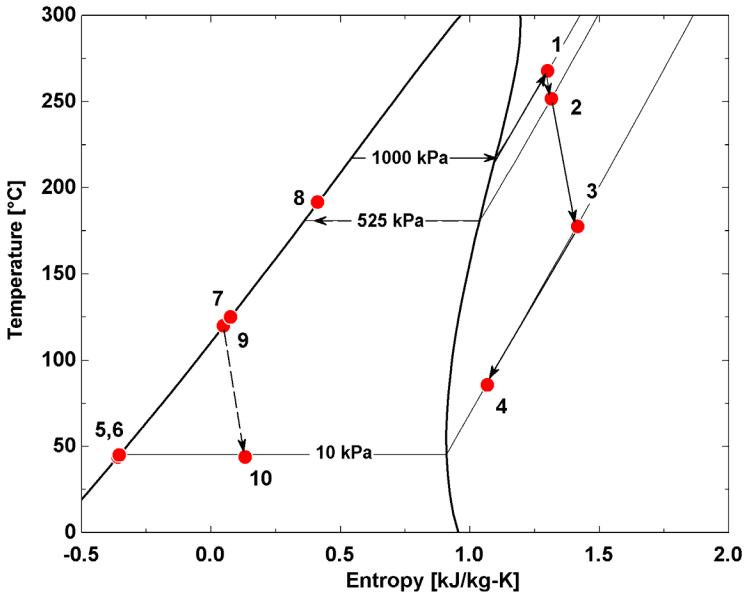

Figure 4.11: T-S Diagram for a reference cycle with the addition of a single closed feedwater heater.

4.2.6 Summary and Conclusions

The Coolidge plant has been modeled based on design specifications. Several cycle configurations were similarly modeled to evaluate their performance operating with similar thermal and component performance boundary conditions. Included in this study were: turbine reheat, turbine-exhaust recuperation, and closed feedwater heating. Table 4.2 summarizes the results.

Table 4.2 ORC Performance Summary

Cycle	Thermal Efficiency
Reference	23.1%
Reference without recuperation	17.6%
Reference with Turbine Reheat	24.1%
Feedwater Heating	19.1%
Reference with Feedwater Heating	23.6%

The highest efficiency cycle utilized turbine reheat. The addition of reheat resulted in an increase in the average heat addition temperature, increasing cycle efficiency. This benefit comes at the cost of an additional turbine and heat exchanger. In addition, reheat creates an added discontinuity in the heating curve of the working fluid making it more

difficult to match the thermal resource and working fluid capacitance rates. Matching resource and working fluid capacitance rates is of great importance for system optimization and is discussed at length in chapter five.

Removing recuperation from the reference cycle reduced efficiency 5.5% indicating the importance of energy recovery in maintaining organic Rankine cycle efficiency. Feedwater heating in an organic Rankine cycle proved a lackluster performer relative to recuperation and turbine reheat.

The current market niche for organic Rankine cycles depends on simplicity and affordability. The additional equipment and marginal benefit of the technologies discussed in this section demonstrate why the basic Rankine cycle with recuperation is the favored organic Rankine cycle configuration. It is this configuration which will be the focus of all further investigations and analyses appearing in this thesis.

4.3 A Comparison of Steam and Organic Rankine Cycles

The SEGS (Solar Electricity Generation System) are successful solar-thermal powerplants. They have operated continuously for nearly 20 years employing a steam Rankine cycle for power generation. Due to the operational advantages of organic Rankine cycles, it is of interest to compare their theoretical performance potential with steam cycles operating between the same thermal boundary conditions. In this section the SEGS VI powerplant is compared with an organic Rankine cycle using three different working fluids.

4.3.1 SEGS VI Plant Description

The SEGS VI facility is a solar-driven steam cycle powerplant located in the Mojave Desert. A synthetic oil, Therminol™ VP-1, is used as the heat transfer fluid to collect

solar energy as it circulates through an array of parabolic trough solar collector field. The concentrating, single-axis tracking collectors heat the Therminol™ to nearly 400ºC (depending on the plant). The Therminol™ is then used to vaporize the steam in a series of heat exchangers at the power plant. SEGS VI is a hybrid plant, meaning that it has the ability to draw on natural-gas fired boilers to supplement the solar field in periods of peak demand and insufficient solar radiation [Patnode, 2006].

Figure 4.12 shows the T-s diagram for the SEGS VI power cycle at sample operating conditions. It is similar in design to most fossil fired Rankine cycle plants with one exception; it operates at a considerably lower maximum temperature and pressure. The cycle includes five closed feedwater heaters, one open feedwater heater, and a single stage of turbine reheat with a typical maximum steam temperature of 358ºC.

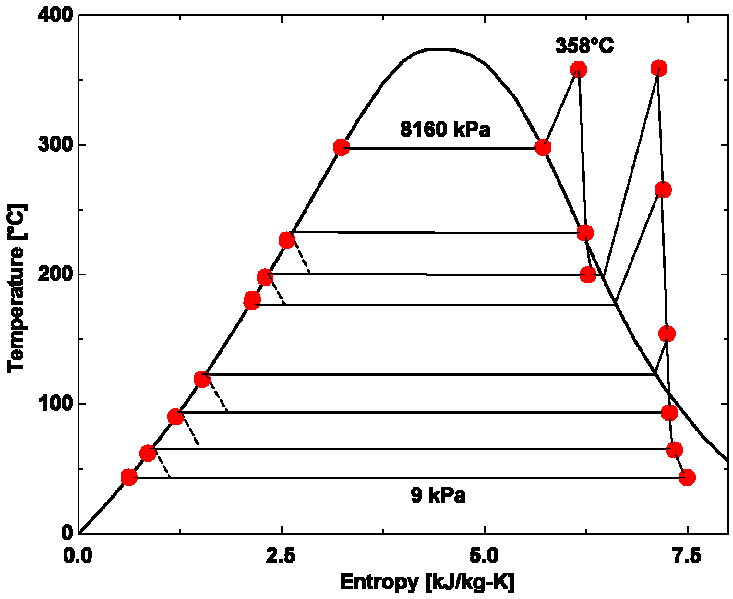

Figure 4.12: T-S Diagram of sample SEGS power plant operation [Patnode, 2006].

4.3.2 Organic Rankine Cycle Performance Comparison

The performance of the SEGS plants has been well documented [e.g., Cable 1998, Patnode 2006]. The analysis presented here compares the performance of SEGS and a theoretical organic Rankine cycle system operating between the same temperature

boundary conditions and possessing identical turbine and pump performance.

Most commonly used organic fluids are not suitable for operation in the temperature range of SEGS VI because of thermal stability limitations [Andersen et al, 2005]. With this in mind, only three potential power cycle working fluids are investigated: toluene, n-octane and n-dodecane. Toluene is the only organic fluid with a service record in this temperature range; the others are unproven and included only for comparison. N-pentane is not included because reliable property data in this temperature range is not presently available. These working fluids will be considered in two cycle configurations. The configurations considered are the reference and turbine reheat cycles discussed in the previous section. The pump and turbine efficiencies are taken from full-load SEGS data [Patnode, 2006] and recuperator pressure drop is neglected. The ORC turbine efficiencies are taken to be the average stage efficiency of the SEGS VI turbines. A list of relevant rapid-screening model inputs is given in Table 4.3.

Table 4.3 Model Inputs

Parameter	Value
Operating Pressure	Optimal
Turbine Efficiency	0.91
Pump Efficiency	0.6
Recuperator Effectiveness	0.9
Maximum WF Temperature	358ºC
Minimum WF Temperature	41ºC

Reference Configuration

Figure 4.13 shows the T-s diagram for the reference configuration with toluene as the working fluid.

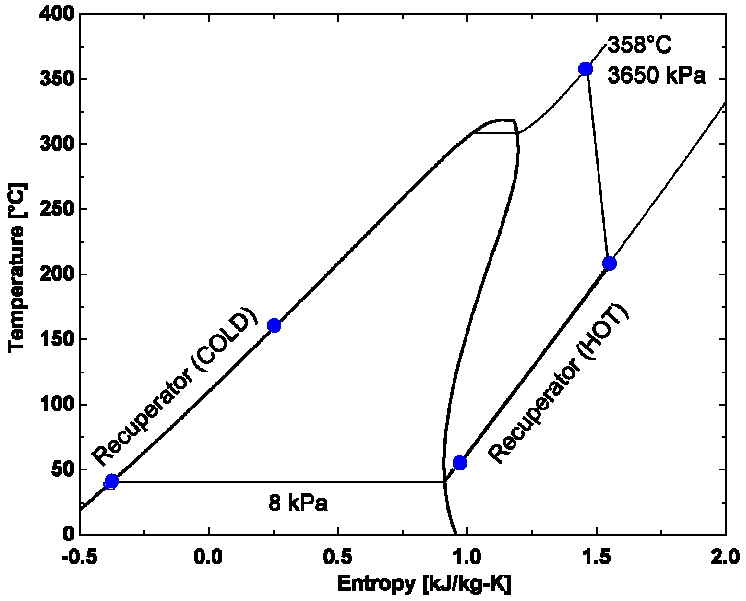

Figure 4.13: T-S Diagram for an ORC with Toluene as the working fluid and operating temperatures approximating those in the SEGS VI plant.

The turbine inlet pressure was chosen based on an efficiency optimization for each working fluid given the temperature limits. Table 4.4 shows optimized operating pressure and critical pressure for each fluid[2]. Note that n-octane optimally operates at supercritical pressures. Recuperator effectiveness was assumed to be 90%, a number based on manufacturer claims [Price, 2006].

Table 4.4 Properties of Candidate Fluids

Working Fluid	Critical Pressure [kPa]	Operating Pressure [kPa]
Toluene	4126	3700
n-octane	2497	3290
n-dodecane	1817	1200

Figure 4.14 offers a summary of simulation results using the rapid screening model. The theoretical n-dodecane cycle exceeds the net efficiency of the steam cycle. Toluene and n-octane are close behind, both within 1% of the SEGS VI performance. It appears from Figure 4.14 alone that n-dodecane is the best performer of the organics.

[2] Refer to chapter 2 for a detailed discussion of the origins of this optimal operating pressure

Figure 4.15 shows the energy density for each theoretical organic Rankine cycle and SEGS VI. The Steam cycle has the highest energy density, with toluene a close second and the best performing organic fluid. N-dodecane has an extremely low energy density, eliminating it from practical consideration and helping to explain why it has no history of use in ORC applications.

A negligible pressure drop across the recuperator is a not a realistic assumption. A sensitivity analysis was performed to evaluate the implications of this assumption. Figure 4.16 shows that the effect of recuperator pressure drop varies widely between the candidate working fluids. This variation is related to saturation pressure, as turbine performance is related to the expansion pressure ratio (inlet/outlet). A fixed pressure drop will have a larger impact on turbine pressure ratio for cycles with very low condensing pressures. It follows, then, that n-dodecane has both the lowest energy density and largest sensitivity to recuperator pressure-drop.

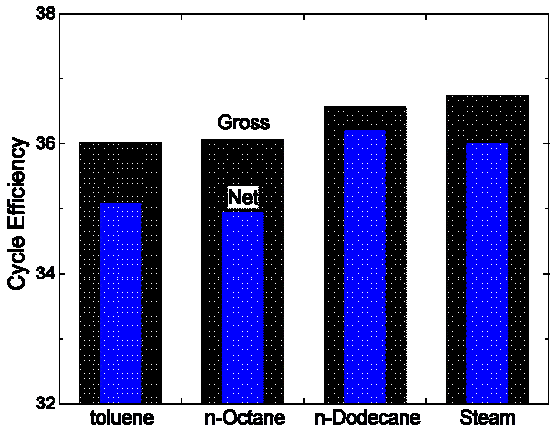

Figure 4.14: Gross and net efficiency for the three ORC working fluids and the SEGS VI plant

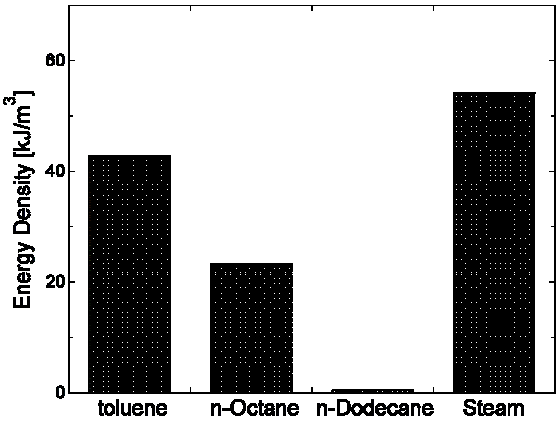

Figure 4.15: Energy density for the three ORC working fluids and the SEGS VI plant

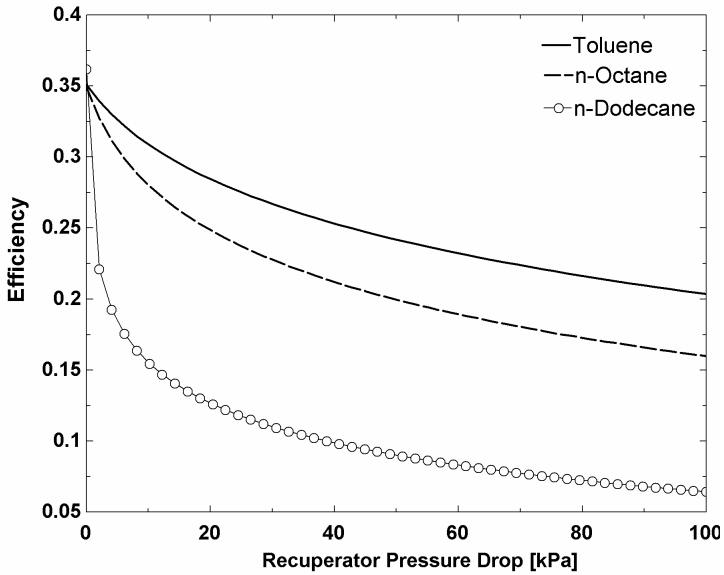

Figure 4.16: ORC efficiency dependence on pressure drop across the recuperator.

Turbine-Reheat Configuration

Figure 4.13 shows the T-s diagram for the reference configuration with toluene as the working fluid. The turbine-reheat ORC is a more authentic comparison to SEGS VI as it also has a turbine-reheat stage and the efficiency benefits that come with it.

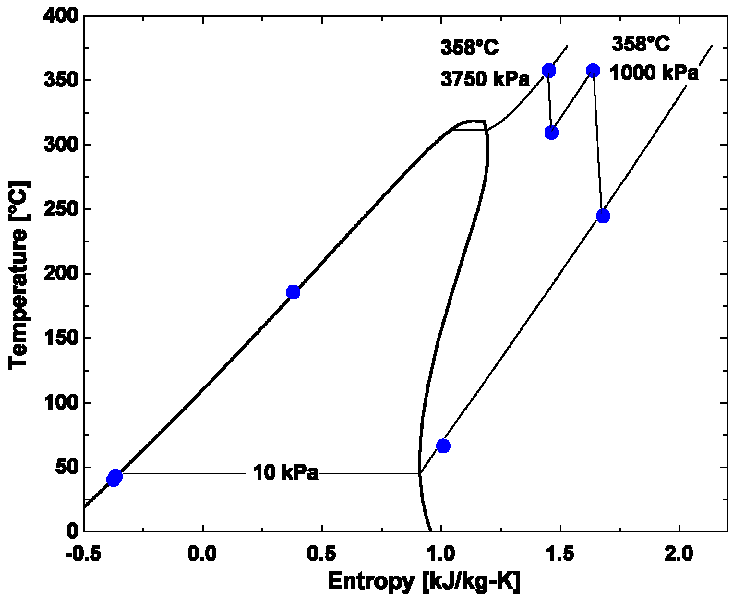

Figure 4.17: T-S Diagram for a turbine-reheat ORC with Toluene as the working fluid and operating temperatures approximating those in the SEGS VI plant.

Due to the impractically strong sensitivity to recuperator pressure drop observed with the reference configuration using n-octane and n-dodecane, only toluene is considered in the reheat case. As seen in section 4.2.3 the turbine inlet pressure for both turbines was chosen such that an optimum efficiency was achieved, with values shown in Figure 4.17. The toluene turbine-reheat cycle achieved a gross efficiency of 38.8% and a net efficiency of 37.7%, besting SEGS VI in both categories. The addition of turbine-reheat improved toluene energy density to 50 kJ/m^3, roughly equivalent to the SEGS VI value.

4.3.3 Summary and Conclusions

Aggressive recuperation of superheated turbine exhaust gases make it theoretically possible for organic Rankine cycles to match the efficiency seen in traditional steam cycles operating between the same thermal boundary conditions.

Based on efficiency, sensitivity to recuperator pressure drop and established thermal stability toluene is the clear favorite organic working fluid for realistic power generation in the 350-400ºC temperature range. A theoretical toluene cycle can nearly match the predicted performance of SEGS VI in the reference configuration and exceed it with the

addition of turbine-reheat. Although pressure drops will exist in a real system, it is conceivable that with careful recuperator design a toluene ORC could remain close to the performance of SEGS VI steam cycle.

While organic Rankine cycles using toluene can approach the efficiency of the SEGS VI steam cycle, they do so while sacrificing some of their fundamental advantages. Condenser operating pressures corresponding to 40ºC operation are sub-atmospheric (10 kPa). In addition to added O&M, these low condensing pressures correspond to larger turbine pressure ratios, potentially complicating turbine design. Despite the sacrifices necessitated by this operating range, the organic Rankine cycle still represents a reduction in overall powerplant complexity as there is no extensive feedwater heating system.

The high operational efficiency and established market of the steam Rankine cycle makes it unlikely that organic Rankine cycles will compete for large-scale electricity generation. In addition, advances in concentrating solar collector design and operation could allow cycle operation at temperatures wholly unattainable by existing organic fluids [Kearney et al, 2003]. However, the comparable thermodynamic performance and simplicity of organic Rankine cycles makes high-efficiency, low-output, and low-maintenance solar power generation a more attractive investment. If an organic Working fluid was developed that retained all the advantages of a low-temperature n-pentane cycle during higher temperature operation organic Rankine cycles would be an even more attractive option for solar power generation.

5 ORGANIC RANKINE CYCLE SOLAR POWERPLANT OPTIMIZATION

5.1 Introduction

Optimal design methods of Rankine cycles for traditional powerplants using high temperature heat sources (derived from fossil or nuclear fuels) are well established; however, the design rules for these high temperature heat sources are not directly applicable for lower source temperature parabolic trough solar-thermal powerplants. That is, using a cycle optimized for coal-fired power generation in a solar-thermal powerplant would not result in optimal performance. To maximize the economic competitiveness of solar-thermal powerplants it is essential to understand how their optimal design is distinct from traditional powerplant design.

In this chapter the fundamental principles of both traditional and solar powerplant optimization are discussed in the context of finite-time thermodynamic analysis. The finite-time analysis is used as a backdrop for developing a generalized solar-thermal powerplant optimization methodology. The method is then applied to the APS Saguaro 1MW organic Rankine cycle solar powerplant. The results of the optimization are discussed in an effort to elucidate the key issues in solar powerplant optimization.

5.2 A General Powerplant Optimization Framework

5.2.1 Finite-Time Thermodynamic Analysis

Finite-time thermodynamics is a method of analysis that couples power-cycle thermodynamics with realistic heat transfer rates [Curzon & Ahlborn, 1975]. It provides a useful framework for considering the relationship between capital investment (heat exchanger size and performance, thermal resource) and power cycle performance.

It is important to mention before the analysis is presented, that finite-time thermodynamics is being employed as a conceptual framework. It is derived for cases which are wholly disconnected from the engineering realities of powerplant operation. In spite of this fact, it is of great conceptual value as it identifies in a very general way, the relationship between powerplant size, investment and performance. There has been a substantial debate in the literature over finite-time thermodynamics, most of it over-stating or under-stating its real usefulness [Chen, 2001 & Gyftopoulos, 2002]. It is herein acknowledged that the results of the finite-time analysis may not be an accurate reflection of reality but a none-the-less important tool for understanding powerplant optimization.

In this section several finite-time analyses are presented to serve as a framework for a discussion of powerplant optimization. The first is an idealized analytical study of a Carnot cycle operating between constant-temperature thermal reservoirs. This is the "original" finite-time analysis that has been famously derived by a number of individuals [Chambadal, 1958, Novikov, 1958, Curzon, Ahlborn, 1975]. The Carnot cycle analysis is extended to real power cycles by considering a reversible Rankine cycle operating between finite thermal resources. To round out the discussion of finite-time thermodynamics, an "ideal" cycle for extracting power from finite thermal resources is presented and analyzed from a finite-time perspective to establish an upper-bound on power production from a resource of finite capacitance-rate.

Carnot Cycle

Consider a Carnot cycle operating between two constant-temperature thermal resources as shown in Figure 5.1.

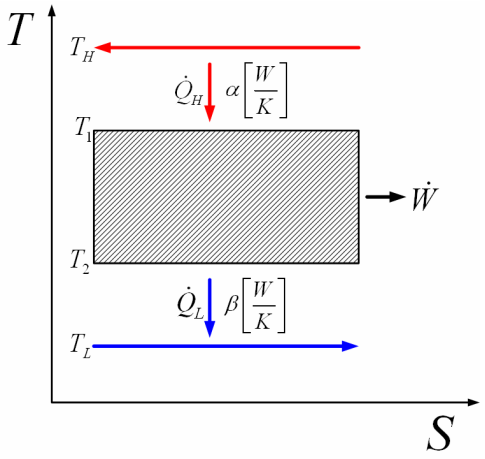

Figure 5.1: T-S diagram describing the bases of finite-time thermodynamic analysis

The power (work per unit time) produced by the Carnot cycle is equal to the difference between the heat addition and rejection rates:

$$\dot{W} = \dot{Q}_H - \dot{Q}_L \qquad [5.2.1]$$

The heat addition and rejection rates are related to the thermal resource and power cycle by a first order temperature difference (Newton's law of cooling). Let α and β be defined as constant overall heat transfer coefficients between the power cycle and the thermal resources such that the heat addition and rejection rates can be written as follows:

$$\dot{Q}_L = \beta(T_2 - T_L) \qquad [5.2.2]$$

$$\dot{Q}_H = \alpha(T_H - T_1) \qquad [5.2.3]$$

The efficiency of the Carnot cycle is a function of the maximum and minimum cycle temperatures, T_1 and T_2:

$$\eta = 1 - \frac{T_2}{T_1} \qquad [5.2.4]$$

Note that T_1 must be lower than T_H in order to drive thermal energy from the resource to the cycle at a finite rate. The cycle efficiency can also be written in terms of the heat addition and rejection rates:

$$\eta = \frac{\dot{W}}{\dot{Q}_H} = \frac{\dot{Q}_H - \dot{Q}_L}{\dot{Q}_H} \quad [5.2.5]$$

In practice, α and β are functions of physical heat exchanger size and performance. If heat exchanger performance is approximately constant then physical heat exchanger size scales with α and β. In addition, as heat exchanger size increases it follows that related plant equipment must also scale up to accommodate larger fluid flow rates and power outputs. α and β are then representative of total power cycle size, defined here as *UA*, the total overall heat transfer coefficient:

$$UA = \alpha + \beta \quad [5.2.6]$$

α, β, T_H, and T_L are arbitrarily defined parameters. Equations [5.2.1] through [5.2.5] make up a system of 5 equations with 6 unknown variables. Consider that T_H and T_L are fixed boundary conditions that the cycle must operate within. Consider also that the power output is a salable product. Finite-time thermodynamics then suggests that the optimal power cycle design would extract the maximum possible power from the thermal resources. This observation is used as the impetus to derive the efficiency at which maximum power is produced in terms of the thermal resource temperatures.

Equations [5.2.1] through [5.2.5] are used to obtain an expression for cycle power output in terms of thermal resource and power cycle temperature ratios, $\tau = T_L/T_H$ and $\theta = T_2/T_1$ [Yilmaz, 2006]:

$$\dot{W} = \frac{T_H(\theta - \tau)(1 - \theta)}{\theta\left(\frac{1}{\alpha} + \frac{1}{\beta}\right)} \quad [5.2.7]$$

The maximum power point is found by setting the derivative of work with respect to θ to zero:

$$\theta\Big|_{\frac{d\dot{W}}{d\theta}=0} = \sqrt{\tau} = \sqrt{\frac{T_L}{T_H}} \quad [5.2.8]$$

The maximum power, and the corresponding efficiency are identified by substituting equation [5.2.8] into equation [5.2.7] and equation [5.2.8] into equation [5.2.4], respectively:

$$\eta_{CNCA} = 1 - \sqrt{\tau} = 1 - \sqrt{\frac{T_L}{T_H}} \qquad [5.2.9]$$

$$\dot{W}_{CNCA} = \frac{T_H \alpha \beta (1 - \sqrt{\tau})^2}{\alpha + \beta} \qquad [5.2.10]$$

Where the subscript CNCA gives credit to Chambadal, [1958], Novikov, [1958], and Curzon & Ahlborn [1975] who first showed this result. For a visual appreciation of equation [5.2.9] equations [5.2.1] through [5.2.6] can be solved for efficiencies ranging between 0 and the Carnot efficiency (defined by the ratio of the thermal resource temperatures). Doing this reveals a parabolic relationship between power and cycle thermal efficiency. The parabolic relationship implies that, as a power cycle approaches its maximum efficiency, its power output will approach zero. Figure 5.2 shows this analysis applied to a Carnot cycle operating between thermal resources of 20ºC and 300ºC to be indicative of typical ORC operating conditions. Figure 5.2 shows the power output of this cycle as a function of Carnot cycle efficiency for a range of plant sizes (expressed in terms of *UA*). Maximum power increases with increasing *UA*.

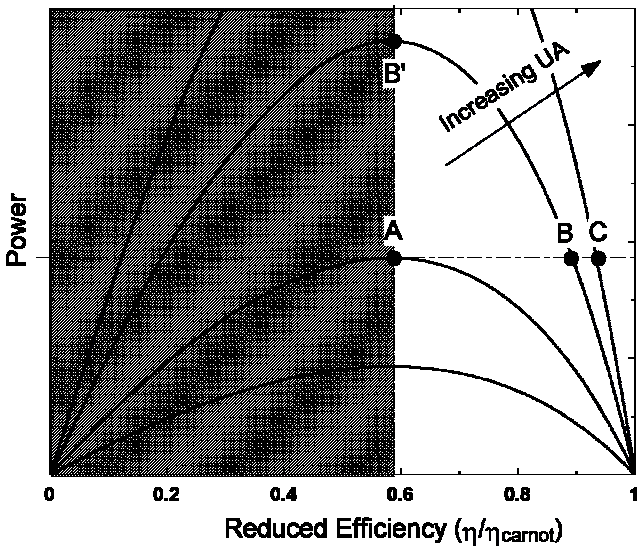

Figure 5.2: Results of a finite-time analysis of a Carnot cycle operating between 20ºC and 300ºC showing a parabolic relation between first-law efficiency and power at constant UA. Each line is for constant (evenly-spaced, linearly-increasing) UA.

Figure 5.2 shows that in order to increase cycle efficiency while maintaining a constant power output, the power cycle size (*UA*) must increase, as indicated by points A, B, and

C. The opposite behavior occurs in the shaded region of the plot, however this region represents non-economical cycle designs and is not useful to consider. The change in power cycle size (*UA*) from point A to B and point B to C is the same, although the efficiency gains differ demonstrating a diminishing return on cycle efficiency gain with increasing *UA*.

Real Power Cycles

Finite-time analysis performed on a Carnot cycle operating between constant-temperature thermal reservoirs is a useful academic exercise, but is disconnected from the reality of powerplant operation. Powerplants depend on finite fuel sources and real power cycles. To demonstrate the significance of the Carnot cycle result, Leff (1987) has shown that a nearly identical relationship between power, efficiency and heat exchanger conductance (UA) is obtained for the Brayton, Otto, Diesel, and Atkinson cycles operating between thermal resources of finite capacitance-rate; all of which generate maximum power at the CNCA efficiency. Not covered by Leff (1987), and of principle interest to solar-thermal power generation, is the Rankine cycle. Consider, then, two thermal resources having finite capacitance rates with an internally-reversible single-stage steam Rankine cycle operating between them, shown in Figure 5.3.

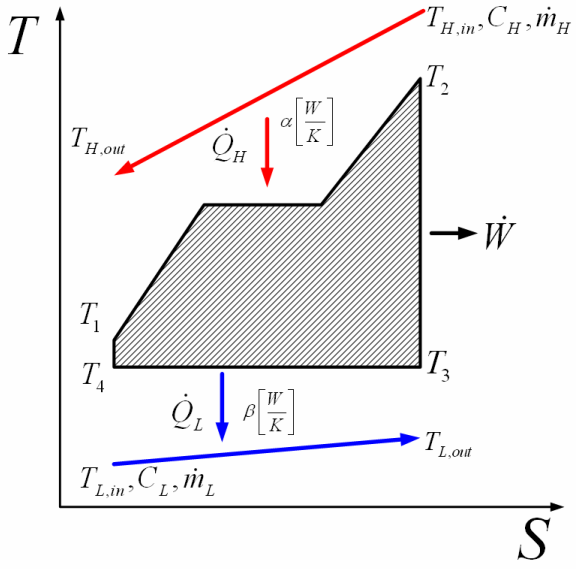

Figure 5.3: T-S diagram describing a internally-reversible Rankine cycle operating between two finite thermal resources.

A Rankine cycle requires that the working fluid (steam is considered in this case) go through a phase change. The liquid-vapor phase change results in a highly varying working fluid capacitance rate, as seen in Figure 5.3. In order to accommodate this variation, the "hot" side of the Rankine cycle is considered as three separate heat transfer processes: preheating, evaporation and superheating. During each of these processes working fluid capacitance rate is approximately constant enabling each heat transfer process to be described using an effectiveness-*NTU* technique [Incropera, 2002]. Total Rankine cycle heat addition can then be expressed as:

$$\dot{Q}_H = \dot{Q}_{preheat} + \dot{Q}_{evaporation} + \dot{Q}_{superheat} \quad [5.2.11]$$

$$\dot{Q}_H = \dot{m}_H C_H (T_{H,in} - T_{H,out}) \quad [5.2.12]$$

$$\dot{Q}_H = \dot{m}_{ST} (h_2 - h_1) \quad [5.2.13]$$

The subscript *ST* refers to steam, the Rankine cycle working fluid and *h* is the specific enthalpy at a given state. To maintain the heat exchanger conductance constraint, the sum of the conductance in all three heat addition processes must equal α. Rankine cycle heat rejection is similarly expressed:

$$\dot{Q}_L = \dot{m}_L C_L (T_{L,out} - T_{L,in}) \quad [5.2.14]$$

$$\dot{Q}_H = \dot{m}_{ST} (h_3 - h_4) \quad [5.2.15]$$

Cycle power production and efficiency are again constrained with equations [5.2.5] and [5.2.1].

The Rankine cycle model results in a set of equations with two free parameters. In varying these parameters to maximize power production, the Rankine cycle shows behavior similar to the Carnot cycle. Rankine cycle behavior in the power-efficiency plane is shown in Figure 5.4. The efficiency at which maximum power is achieved for the Rankine cycle departs slightly from the CNCA efficiency, due most likely to the more complicated shape of the Rankine cycle as compared to the Carnot cycle or the cycles considered by Leff (1987).

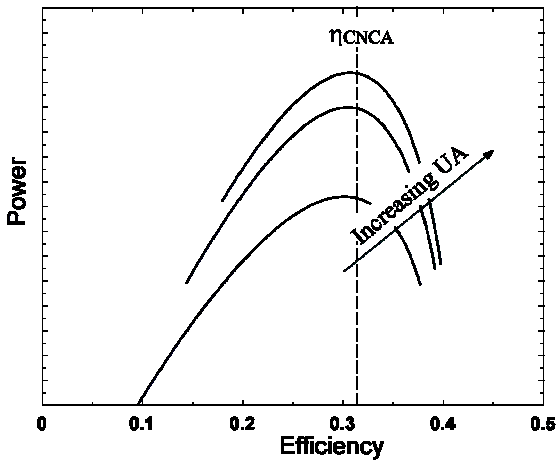

Figure 5.4: Maximum power behavior of a single-stage Rankine cycle operating between finite thermal resources having inlet temperatures of 20°C and 300°C, respectively.

"Ideal" Power Cycle

Ibrahim, et al. [1995] have shown that the power cycle capable of the maximum power production operating between finite resource streams is one in which the power cycle working fluid is able to match the capacitance rates of the thermal resources during both the heat addition and rejection processes. Figure 5.5 shows the ideal power cycle. Analysis of this cycle in the context of finite-time thermodynamics is of interest in order to establish an absolute upper-bound for theoretical power extraction from a finite resource.

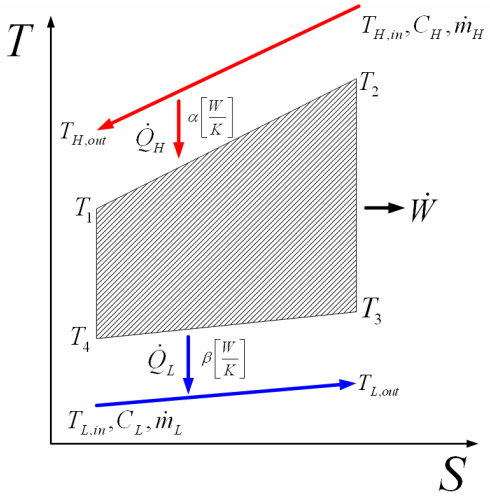

Figure 5.5: T-S diagram describing the ideal reversible power cycle operating between two finite thermal resources.

The analysis of this cycle is identical to the Rankine cycle case with the added simplicity of only a single heat addition and rejection process modeled using an effectiveness-*NTU* technique. The efficiency of the ideal power producing cycle can be described by an internally-reversible power cycle efficiency analogous to the Carnot efficiency:

$$\eta = 1 - \frac{Q_L}{Q_H} = 1 - \frac{\int_1^2 Tds}{\int_3^4 Tds} = 1 - \frac{\overline{T}_{1-2}\Delta S}{\overline{T}_{3-4}\Delta S} = \boxed{1 - \frac{\overline{T}_{1-2}}{\overline{T}_{3-4}}} \qquad [5.2.16]$$

where $\overline{T}_{1-2}$ and $\overline{T}_{3-4}$ are the average temperatures of heat addition and heat rejection in the power cycle working fluid.

The interest in analyzing this cycle is to establish the limits of theoretical powerplant performance. As such, a "cold" resource capacitance rate that is much larger $\left(\dot{m}_H C_H << \dot{m}_L C_L\right)$ than the "hot" resource capacitance rate is considered. This arrangement is not an unreasonable approximation of reality as high capacitance rates in power cycle cooling improve performance and have little cost relative to the "hot" resource (fuel). The results of the analysis of each case are shown in Figure 5.6 in the same power-efficiency variable space that the Carnot and Rankine cycle results were presented. Note that the fundamental relationship between power, power cycle efficiency, and *UA* is unchanged. However, as *UA* increases, a lower bound on achievable cycle efficiency emerges. As *UA* becomes very large cycle efficiency is limited to values larger than the CNCA efficiency. The shape of the curves remains unchanged, indicating that maximum power production occurs at the minimum achievable cycle efficiency. The efficiency that is approached as *UA* goes to infinity is here defined as η_{MP}:

$$\eta_{MP} = 1 - \frac{2T_{L,in}}{T_{H,in} + T_{L,in}} \qquad [5.2.17]$$

and the corresponding power at η_{MP}:

$$\dot{W}_{MP} = \dot{m}_H C_H \frac{\left(T_{H,in} - T_{L,in}\right)^2}{T_{H,in} + T_{L,in}} \qquad [5.2.18]$$

η_{MP} and $\dot{W}_{MP}$ are derived assuming that the "cold" resource has an infinite capacitance rate and that energy is removed from the "hot" resource until it reaches the "cold" resource temperature. Based on the results of the finite-time analysis $\dot{W}_{MP}$ represents a true practical engineering limit for the power produced from a resource of constant specific heat and finite capacitance rate.

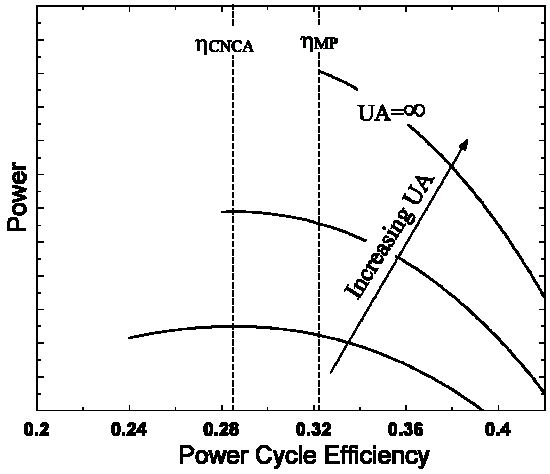

Figure 5.6: Results of the finite capacitance-rate finite-time analysis for an internally reversible power cycle operating between 20ºC and 300ºC for the case where the "cold" capacitance rate is much larger than the "hot" capacitance rate.

5.2.2 Optimizing Traditional Powerplants

A *traditional* powerplant is defined here as one in which the temperature of the thermal resource (combustion gases, geothermal brine) is independent of power cycle operation. The optimal operating point of such a power plant, for a given investment, is the point at which maximum power is generated. If it is assumed that total powerplant cost is some function of its physical size (*UA*), then an optimally designed traditional plant will always operate at the maximum power condition predicted by a finite-time analysis (revealed in the previous section as or near the CNCA efficiency for most common power cycles) [Ibrahim, 1991, Leff, 1987]. To demonstrate this, consider the analysis of the Carnot cycle in Figure 5.2. Points A, B and C produce the same power from the same thermal resource, but they do so at different efficiencies requiring different *UA*s. Point A represents the optimal design because it achieves the desired power output with the minimum investment, i.e., the smallest *UA*. There is no economic benefit to operating

above the maximum power efficiency for a traditional power cycle (that is, sacrificing output for efficiency). If the investment in *UA* were made to operate at point B it would be preferable to reallocate the heat exchanger areas so that the cycle operated at point B′, generating more power from the same *UA* investment. While points A and B' represent the optimum operating points for their respective levels of *UA* investment, it is fuel cost that dictates the optimum level of *UA* investment. As fuel cost increases, the incentive to invest in more *UA* and extract more power from the purchased fuel increases. Alternatively, increasing *UA* investment can generate the same power from less fuel.

The presence of internal irreversibilities, restrictions on thermal resource exhaust temperatures and equipment operating limits place additional boundary conditions on powerplant performance. These more complicated boundary conditions cause the optimum cycle efficiency of real plants to diverge from the CNCA and MP efficiencies (in most cases well below), but the basic behavior is unchanged and it is still the identification of maximum power operation (and fuel cost) for a given set of operating conditions that drives optimization of a traditional powerplant.

5.2.3 Optimizing Parabolic Trough Solar-Thermal Powerplants

Solar-thermal powerplants are distinct from traditional powerplants in that there are two major components to the total capital cost: the power cycle and the solar field. That is, rather than a recurring fuel cost, the "fuel" for a solar-thermal powerplant is principally a capital cost reflected in the solar field. In addition, the performance of the solar field is coupled to the performance of the power cycle – the thermal resource is no longer independent of power cycle operation as it was in the traditional case. The outlet of the power cycle is the inlet to the solar field, and the outlet of the solar field is the inlet to the power cycle. A finite-time analysis of a solar-thermal powerplant must consider this distinction.

The treatment of the power cycle component of a solar-thermal powerplants is identical to the treatment presented for traditional powerplants; powerplant behavior does not

change on account of the origin of the thermal resource it utilizes. It is the solar field, and its performance coupling to the power cycle that complicates the analysis. In order to be consistent with the other analyses, a constant solar field outlet temperature and mass flow rate (thermal resource) is assumed and the solar field size necessary to provide this resource determined. In addition, a constant solar field mass flow rate eliminates the complication of variations in pumping loads. Based on finite-time power cycle analysis, it is possible to determine the size of the solar field that would be necessary to drive a power cycle operating at a specific point in the power-efficiency plane. Figure 5.7 shows results of the ideal power cycle analysis in which the power cycle heat addition is assumed to be directly proportional to solar field size (dashed lines). Solar field thermal losses are typically small enough such that this approximation captures basic solar field performance. The ideal cycle case is shown here for graphical clarity, but recall all real power cycles demonstrate the same fundamental relationship between power output, efficiency and heat exchanger conductance (UA).

Figure 5.7 shows that the required size of the solar field for a fixed power depends on the efficiency of the power cycle. Operating the power cycle at the CNCA efficiency requires a larger solar field than that required for a cycle operating at a higher efficiency and the same power (points A and B in Figure 5.7). Investing in a more efficient power cycle reduces the required solar field expenditure for a fixed power. However, as the maximum efficiency for a given power is approached, increasing power cycle size (UA) returns strongly diminishing gains in efficiency for a given power output.

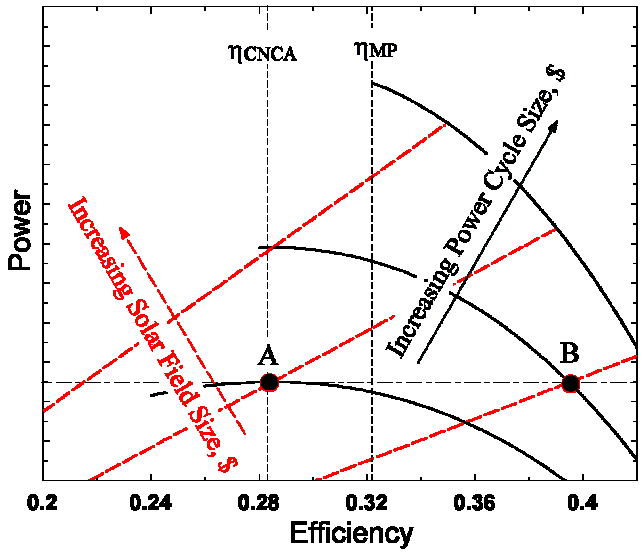

Figure 5.7: Finite-time analysis of a parabolic trough solar powerplant with constant HTF inlet conditions. Dashed lines indicate constant solar field size; solid lines are of constant power cycle size.

In order to capture the relationship between system cost and performance in a manner consistent with Figure 5.2 (the traditional case), it is helpful to plot lines of total system cost which include both the solar field and power cycle. In order to determine total system cost at a given operating point in the power-efficiency plane, there must be functions that relate the relative weighting of solar field and power cycle cost. As an example, Figure 5.8 shows the case where the solar field and power cycle account for equal parts of the total system cost.

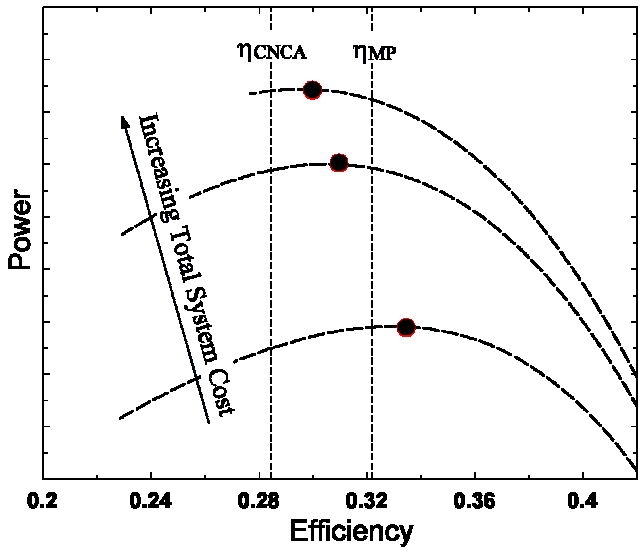

Figure 5.8: Finite-time analysis of a parabolic trough solar powerplant with constant HTF inlet conditions. Lines of constant total system cost shown.

Following the same logic presented for the traditional powerplant, that is identifying the operating point that generates maximum power for a given capital investment, the optimum operating point for a solar-thermal powerplant is indicated by the maximum power point for a line of total system (combined solar field and power cycle) cost. Or alternatively, the optimal configuration is one that requires the minimum investment in order to achieve a desired power output. Unlike the traditional case, there is no recurring fuel cost to complicate optimization, so these maximum power points reflect true optimums for the defined operating conditions. Figure 5.8 shows that the solar field contribution to total system cost has shifted maximum power per unit capital investment away from the CNCA efficiency and towards the Carnot efficiency. The precise location of this maximum power point is determined by the functions that govern power cycle and solar field cost. Note that as power increases, optimum power cycle operating efficiency approaches the CNCA efficiency. This is due to the fact that as power output becomes large, gains in efficiency require proportionately greater amounts of UA. The diminishing return on UA investment at high operating power outputs encourages lower operating efficiencies and correspondingly larger solar fields.

5.2.4 An Optimization Methodology for Solar-Thermal Powerplants

In order to formulate an objective function for optimizing PTSPs, parameters that capture both the plant's thermodynamic performance and associated economic costs must be identified. The principle considerations in PTSP investment are the solar field and power cycle. For capital optimization it is necessary to quantify the costs of both these system components as functions of the quantities that characterize their thermodynamic performance. These parameters are chosen as the solar field collector area, A_{SF}, total power cycle heat exchanger area, A_{PC}, and power cycle output, W.

Projections of near-term parabolic trough steam Rankine cycle plant cost developed by SunLab [Sargent & Lundy, 2003] are used to create cost functions for the solar field and power cycle. These cost functions are used here only to capture the basic scaling of solar

field and power cycle costs, more representative functions could be used in their place if more detailed data was available.

SunLab predicts that the solar field collector system will represent approximately 75% of the total project capital cost with the remainder accounting for power cycle and balance-of-plant equipment. This information is used to formulate the following cost functions that relate relative solar field and power cycle investment in terms of solar field area, power cycle heat exchanger area and power cycle output:

$$Solar\ Field\ Cost = \frac{3}{4}\left(\frac{A_{SF}}{A_{SF,REF}}\right)^{1} \qquad [5.2.19]$$

$$Power\ Cycle\ Cost = \frac{1}{4}\left[\frac{1}{2}\left(\frac{\dot{W}}{\dot{W}_{REF}}\right)^{0.67} + \frac{1}{2}\left(\frac{A_{PC}}{A_{PC,REF}}\right)^{0.59}\right] \qquad [5.2.20]$$

The functional form of equations [5.2.19] and [5.2.20] is based on models presented by Boehm [1987]. The power cycle cost is divided into two components, power output and heat exchanger area. Heat exchanger area is related to heat exchanger and cooling system cost. Plant output is related to turbine, generator, piping and auxiliary system cost. The equal weighting is based on a break-down of power cycle costs at the SEGS VI parabolic trough plant reported by Pilkington [2000]. The cost scaling factors for heat exchanger area and power are obtained from data compiled by Boehm [1987]. Solar field unit cost is expected to reduce over time as global production increases, however current production capacity is insufficient to create economies of scale [5.2.19] [Sargent & Lundy, 2003]. $A_{PC,REF}$, and $A_{SF,REF}$ are defined in terms of a baseline case consistent with current parabolic-trough plant design practice.

The cost models (Eqns [5.2.19] and [5.2.20]) include only capital expenses and neglect O&M costs. Inclusion of O&M costs would favor smaller solar fields because the solar field is responsible for the majority of the planned O&M costs in PTSPs [Price, 1999].

The investment ratio (IR) is defined as the ratio of total plant capital cost to design point

power output:

$$IR = \frac{Solar\ Field\ Cost + Power\ Cycle\ Cost}{Net\ Power\ Output} \qquad [5.2.21]$$

IR is minimized to find the optimum system configuration. The net power output is generally considered a design constraint and held constant during optimization. Power cycle performance is constrained by heat exchanger allocation and system operating pressure (an optimization parameter). The allocation of heat exchanger area refers to the amount of total heat exchanger area used for each heat exchange process (evaporation, superheating, etc.). Varying the allocation of heat exchanger area allows the design power output to be achieved as total heat exchanger area varies, in effect moving along a line of constant power seen in Figure 5.2. By considering only the total heat exchanger area in equation [5.2.20], it is implicitly assumed that all heat exchanger area is of equivalent unit cost. It would be possible to include specific costs for heat exchanger allocation into the cost functions if these data were available.

A dimensionless normalized investment ratio, *NIR*, is defined as follows in order to compare different designs:

$$NIR = \frac{IR}{IR_{ref}} \cdot 100 \qquad [5.2.22]$$

The working fluids and solar field heat transfer fluids that are currently being used or proposed for use in PTSPs have limited temperature operating ranges. In order to ensure the optimization routines do not violate these physical limits, the solar field outlet temperature is fixed at the lowest maximum stable operating point for the HTF and WF. This temperature is chosen because maximizing thermal resource temperature is necessary to maximize opportunity for cycle efficiency improvement. Fixing solar field outlet temperature requires the solar collector area to vary as solar field inlet conditions vary. Solar field size for each power cycle configuration is computed using a version of the Hottel-Whillier equation, which incorporates estimated thermal losses and the relation between inlet and outlet temperatures [Beckman and Duffie, 1992]:

$$Q_u = F_R A_{SF}\left[S - \frac{U_L}{C_R}(T_i - T_a)\right] = \dot{m}_{HTF}\int_{T_i}^{T_o} C_{HTF}\,dT \qquad [5.2.23]$$

where U_L/C_R is the ratio of receiver tube loss coefficient and concentration ratio and S is insolation. F_R is a dimensionless collector performance parameter.

5.3 Optimizing the APS Saguaro Plant

The methodology described in the previous section is applied here to the APS Saguaro organic Rankine power cycle, which was designed specifically for use in a parabolic-trough solar powerplant. This will demonstrate both the power of the optimization methodology to reveal optimized design parameters, and also inform general observations about PTSP optimization. For this study the performance of the plant is characterized by the full-load model described in sections 2.3.3 and 2.5. Pressure drops and component efficiencies provided by the manufacturer were treated as "typical" and remained constant for all optimization cases.

5.3.1 APS Optimization Results & Discussion

The design case for the APS plant is used as the reference for optimization. The working fluid was not changed and solar field outlet temperature was fixed to the reference 300ºC and flow of 11.75 kg/s.

Table 5.1 presents a summary of performance metrics for the optimization. Table 5.2 shows the heat exchanger allocation corresponding to the optimization.

Table 5.1 Optimization Results

Metric	Reference	Optimized
Heat Exchanger Area, m^2	2540	2670
Solar Field Area, m^2	6606	5045
NIR	100	83
Availability Destruction, kW	925	571
Cycle Efficiency	19.3	25.3
Net Power, kW	1081	1081

Table 5.2 Heat exchanger allocation, %

Heat Exchanger	Reference	Optimized
Preheater	5.6	7.2
Evaporator	1.3	1.8
Superheater	3.7	22.0
Recuperator	12.6	41.0
Desuperheater	14.0	3.0
Condenser	62.8	25.0

NIR was improved 17% as a result of the optimization at the cost of a 5% increase in power cycle heat exchanger size. The increase in gross cycle efficiency and subsequent decrease in required solar field size is the driving force for the improved *NIR*. This result demonstrates that cycle efficiency, achieved at the cost of additional power cycle heat exchanger area, results in substantially improved *NIR*. Efficiency could be further increased by additional power cycle investment, but the reduction in solar field size would be insufficient to account for the added power cycle cost.

Figure 5.9 and 5.10 show heating and cooling curves for the reference case and the optimized cycle. The optimized case dramatically improves the heat addition process by reducing approach temperatures at both the inlet and exit as well as improving capacitance rate matching, approaching the ideal cycle shown in Figure 5.5. This improvement in heat addition is responsible for the nearly 50% reduction in availability destruction seen in the optimized cycle design.

The optimized cycle design operates within 10% of the theoretical maximum efficiency for the component efficiencies and thermal boundary conditions of the APS plant, 27.7%. Where the theoretical efficiency is computed at the limit where all heat exchanger approach temperatures go to zero, recuperator effectiveness goes to one and the cycle operates at optimal pressure. This result demonstrates in very real terms that the dominance of solar field costs require running solar-thermal power cycles at the practical limits of efficiency.

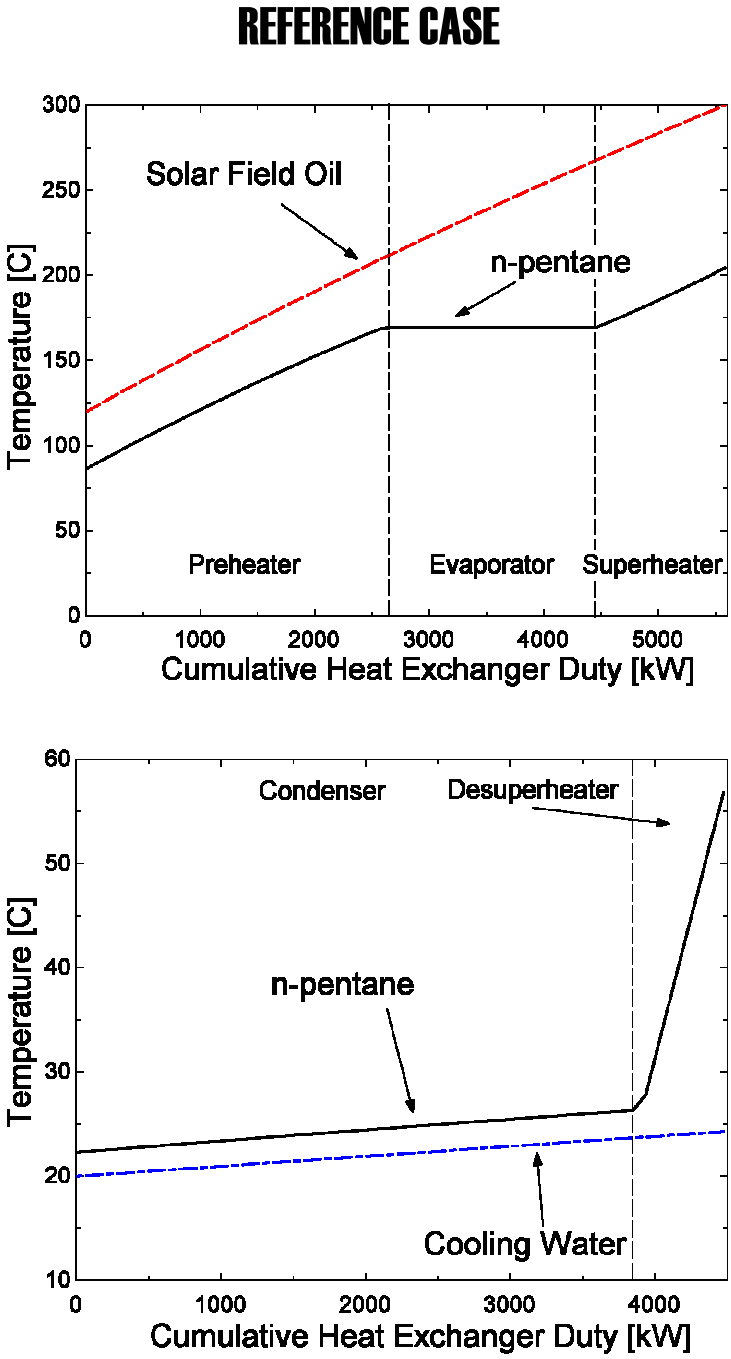

Figure 5.9: Heating and cooling curves for the reference APS PTSP

OPTIMIZED CASE

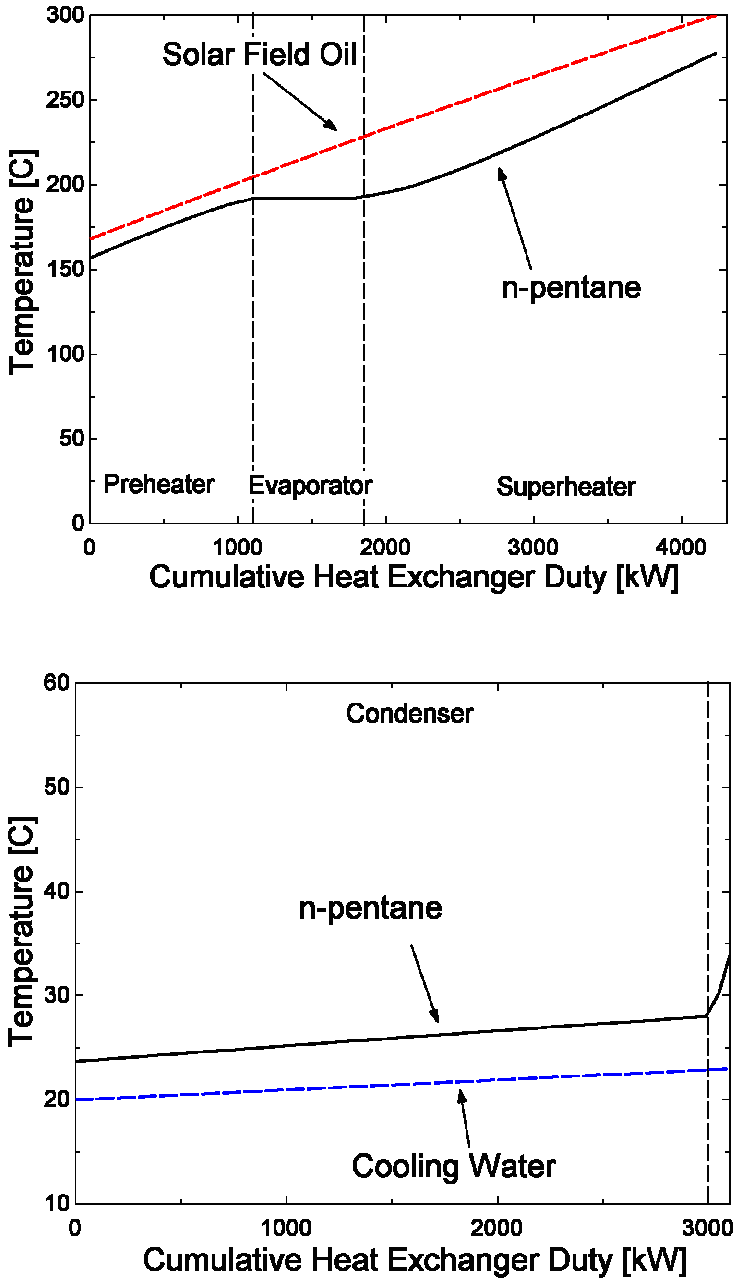

Figure 5.10: Heating and cooling curves for the optimized APS PTSP

Cost Function Analysis

The optimized design presented in section 5.3.2 is heavily dependent on the cost functions presented in section 5.2.5. It is useful to understand the significance of the scaling and proportionality factors used in equations [5.2.19] and [5.2.20]. The optimization in section 5.3.2 does not alter system output, indicating that the only sources of variation in *NIR* are the portion of plant cost represented by the solar field and the scaling exponents for heat exchanger and solar field size. Table 5.3 shows the contribution of each parameter, assuming equal uncertainty for each parameter, to total uncertainty.

Table 5.3 Uncertainty Contribution, %

Parameter	% of Uncertainty
Solar Field Cost Fraction	71%
Solar Field Scaling Exponent	28%
Heat Exchanger Scaling Exponent	1%

From Table 5.3 it is apparent that the plant cost distribution (between solar field and power cycle) is the most significant factor in determining *NIR*. In addition, it is likely the most speculative parameter in the cost functions.

Figure 5.11 shows *NIR* as a function of solar field cost fraction. Note in equation [5.2.19] the solar field cost fraction is 75%.

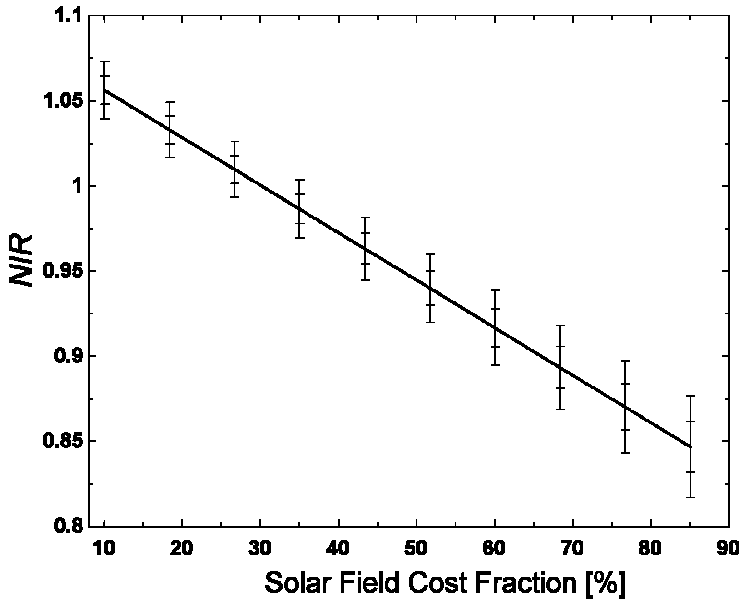

Figure 5.11: NIR as a function of solar field cost fraction for the optimized case showing variation corresponding to 10 and 20% relative error in all scaling exponents

Variation in *NIR* due to uncertainty in the cost function scaling exponents is not sufficient to dramatically alter the optimized APS design. Only a major shift in the total capital cost distribution between power cycle and solar field would cause a major shift in optimization results. According to Figure 5.11 the solar field cost fraction would need to reduce below 30% in order for the benefits of the optimized cycle design to be negated. Thus, for any cost scenario where the solar field cost dominates total powerplant cost there is substantial room for improvement in the APS design. As the solar field cost fraction reduces, optimum cycle design will shift away from maximum efficiency operation and towards maximum power operation.

Evaluation of Other Solar Designs

While the performance of the APS plant could be improved by applying the optimization methodology, it is of interest to compare it with other designs for solar powerplants. Figure 5.12 shows heating curves for two parabolic trough solar-thermal powerplant designs using a similar (300ºC) HTF temperature and toluene as the working fluid.

Based on the general rules developed in the previous sections for evaluating optimal

power cycle design for solar applications it is clear that neither of these designs are thoroughly optimized. The approach temperature in both superheaters is relatively large. In addition, they both suffer severe pinch-points where the working fluid begins to boil. These pinch-points result in very poorly matched capacitance rates in the HTF and WF. These observations indicate that toluene was a poor working fluid choice for a 300ºC thermal resource. The large latent-heat of toluene in the temperature and pressure ranges achievable with a 300ºC resource prohibit capacitance rate matching to the degree seen in Figure 5.12. Working fluid selection is an important part of optimal solar power cycle design as it enables fully optimized cycle configurations. Powerplant designers must consider the ability of their working fluid to conform to their thermal resource.

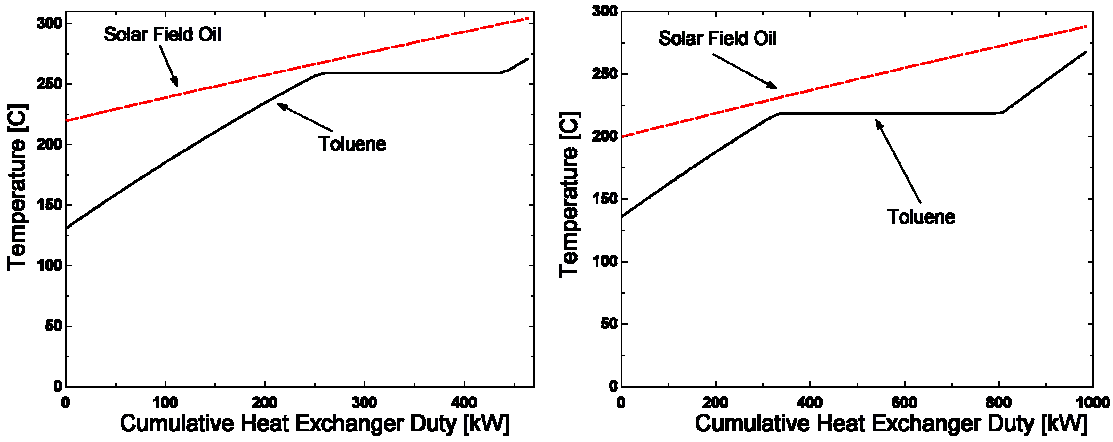

Figure 5.12: Heating and cooling curves for two parabolic trough solar powerplant designs using Toluene as the working fluid and a 300ºC thermal resource.

5.4 Conclusions

Finite-time thermodynamics offers a versatile framework for evaluating generalized optimization strategies for traditional powerplants. When properly modified for the consideration of solar-thermal powerplants it provides a convenient way of estimating the optimum design of these plants that considers the fundamentally coupled performance of the solar field and power cycle. This analysis demonstrates why traditional powerplant design favors maximum power operation and solar-thermal powerplant design favors maximum efficiency operation. It is important to understand the relative weighting of

solar field and power cycle costs in a solar powerplant as this weighting determines how far towards maximum efficiency operation the optimum design exists.

The specific design considerations for optimally designing a solar-thermal powerplant are: maximizing heat addition temperature and matching working fluid and heat transfer fluid capacitance rates. This results in a cycle of the maximum practical efficiency while minimizing heat transfer fluid return temperature which aids solar field efficiency.

The APS Saguaro powerplant, as well as other solar-thermal powerplants do not appear to be optimized for solar-thermal operation. Utilizing the methodology developed in this chapter it was possible to improve the plant's *NIR* 17%, a substantial improvement. This result indicates that special consideration is necessary for optimal solar-thermal powerplant design. Increasing power cycle size adds a diminishing benefit as its costs become significant, and eventually completely mitigates efficiency gains. Inclusion of O&M costs in the cost models would favor still larger power cycle investment.

6 THERMAL ENERGY STORAGE FOR SOLAR POWER GENERATION

6.1 Introduction

The ability to store large amounts of high-temperature thermal energy both efficiently and at low-cost has the potential to increase the economic viability of solar power generation. Without storage or conventional fuel sources as backup, solar power generation is subject to the regular and irregular variations in insolation. This variation in insolation results in a generated energy profile that may or may not be consistent with end-user demands. Thermal energy storage enables the delivery of solar-thermal power to be tailored to meet end-user demands.

This chapter begins by providing an overview of thermal energy storage technologies and research progress to-date, followed by a detailed discussion of the design and modeling of packed-bed storage intended for use in parabolic trough solar powerplants. The strengths and weaknesses of various modeling techniques are analyzed in order to determine the best models for long-term simulation.

6.2. Background and Literature Review

Most energy storage systems proposed for solar electricity generation systems seek to accomplish one of three tasks:

1. Compensate for the normal diurnal variation in solar radiation
2. Shift electricity output to match the utility peak period
3. Extend powerplant operation past sunset

Many different energy storage concepts have been proposed. Energy can be stored readily in many forms: kinetic, potential, electric, thermal and chemical. Thermal energy storage is the most common choice for solar-thermal power generation. In solar-thermal power generation solar radiation is captured as thermal energy in a heat transfer fluid before conversion to electricity. Using thermal energy storage in solar-thermal applications prevents conversion losses associated with using another form of energy storage as well as eliminating added system complexity. Of the thermal storage concepts, sensible (vs. phase-change or chemical reaction) thermal energy storage is accepted as the near-term option for parabolic trough solar powerplants [Herrmann, 2002]. The storage systems of principle interest in this category are two-tank storage, single-tank stratified (thermocline) storage and concrete (packed bed) storage.

When thermal storage systems are discussed herein, *direct* indicates the solar field heat transfer fluid is also used as the storage medium. In an *indirect* storage system the solar field heat transfer fluid is separated from the storage medium via a heat exchanger. Direct storage systems eliminate losses associated with the heat exchanger used in indirect systems. However, some solar field heat transfer fluids have pressurization requirements that would make direct storage systems prohibitively expensive. In addition, indirect systems have the added design flexibility of using different fluids in the solar field and storage system.

6.2.1 Storage Concepts

Two-Tank

Two-tank thermal energy storage systems use two reservoirs, a "hot tank" and "cold tank" to store thermal energy. Both *direct* and *indirect* versions of a two-tank storage system are shown in Figure 6.1. To charge the direct system (Figure 6.1(b)), high temperature fluid exiting the solar field is allowed to accumulate in the "hot tank" while low temperature fluid is pumped from the cold tank to supply the solar field. When discharging, the fluid in the "hot tank" is pumped to provide thermal energy to the power cycle and before returning to the "cold tank" as it is diverted away from the solar field. In the case of the indirect system (Figure 6.1(a)) the system is charged by diverting solar field fluid flow from the power cycle through the heat exchanger while the storage fluid is heated as it is pumped to from the "cold tank" to the "hot tank." When discharging, the flow directions through the heat exchanger are reversed and solar field fluid flow is diverted away from the solar field. The indirect two-tank system can also be configured so that the storage fluid provides thermal energy to the power cycle instead of the solar field fluid.

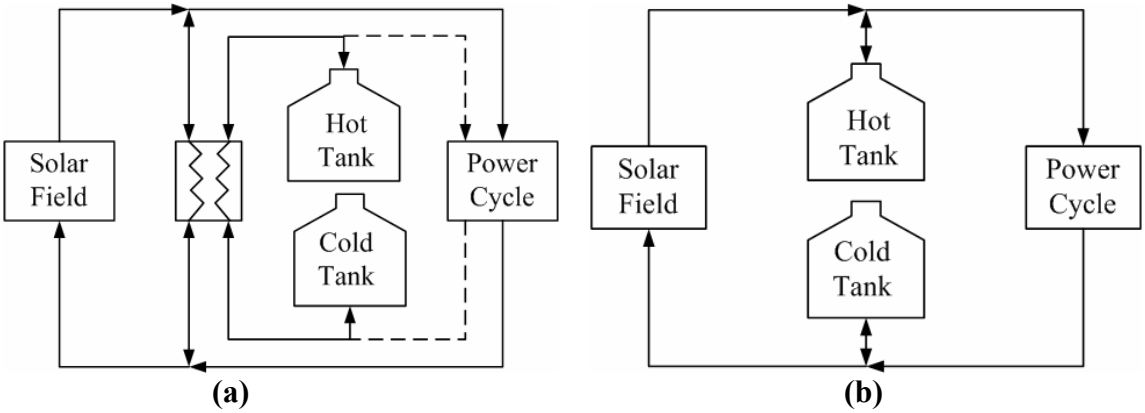

Figure 6.1: Two-tank thermal energy storage systems, (a) Indirect, and (b) Direct

Stratified (Thermocline)

The term *thermocline* refers to the sharp fluid temperature gradient (stratification) that develops between high and low temperature fluid in a storage tank. Stratification is caused by fluid buoyancy resulting from the variation in fluid density with temperature

(in which density typically decreases with temperature). Careful tank design will minimize macroscopic mixing allowing hot and cold fluid to naturally stratify – with hot fluid "floating" on top of the cold fluid.

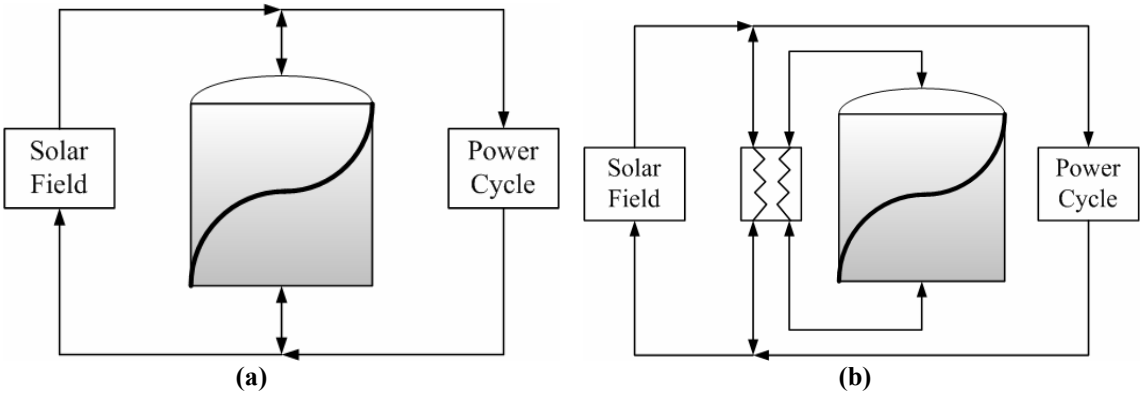

Figure 6.2: Stratified (Thermocline) energy storage systems, (a) Direct and (b) Indirect.

The thermocline is exploited as a storage system by drawing from or adding to the high temperature side of the tank. If designed properly, such that fluid stratification is maximized, stratified storage offers similar performance to a 2-tank system. When charging, cold fluid is drawn from the bottom of the tank and circulated through the solar field for heating then added to the top of the tank. During discharging, the stored hot fluid is drawn from the top of the tank and cooled through the power cycle then returned to the bottom of the tank. Figure 6.2 shows both direct and indirect flows for a single tank stratified thermal storage system.

The stratified thermal energy storage concept can be augmented by adding a solid storage medium to the storage tank. The purpose of the solid medium is to maintain thermal mass while reducing the required fluid volume for a given storage capacity. A temperature gradient forms in the solid as well as the liquid so the fundamental behavior of the system is similar.

Concrete

Concrete, or packed-bed, storage is essentially the same as the stratified storage tank with added filler material. Figure 6.3 shows how a proposed concrete storage unit would be coupled to the solar field and power cycle. Two versions of this storage system have

been proposed. The first utilizes a packed "bed" of rocks, sand or some other filler material. The second, and more recently proposed [Tamme, 2004], involves configuring a series of horizontal concrete tubes through which the storage fluid would flow. The packed bed offers lower capital cost, while the second offers a smaller pressure drop and thus reduced parasitic pumping load.

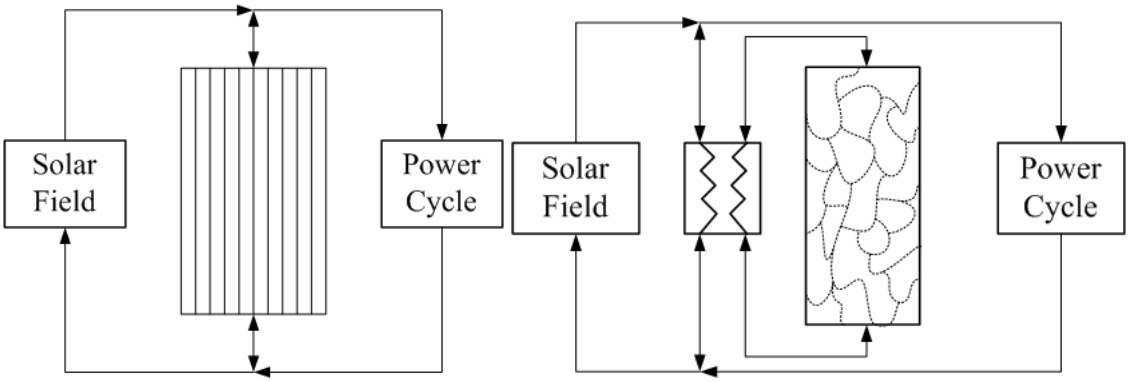

Figure 6.3: Packed-Bed energy storage concepts, (a) direct (potentially pressurized) caste concrete tubes for use with solar field fluid, and (b) indirect rock bed for use with a molten salt

6.2.2 Research Progress

Two-tank and stratified storage tank designs are the two technologies that have been implemented in high-temperature large-scale solar electricity generation plants. Direct two-tank systems were used in both the SEGS I and Solar Two plants [Herrmann, 2004]. The SEGS I system used a mineral oil and the Solar Two system used molten salt both in the receiver and for storage. The Solar One plant had an indirect single-tank stratified storage system using rock and sand as a filler material [Faas, 1986]. All three of these large-scale systems operated as expected, proving the fundamental feasibility of the two-tank and packed-bed stratified storage concepts [Herrmann, 2004].

Indirect systems are currently being proposed to overcome problems associated with the synthetic heat transfer oils used in the most modern SEGS plants. Therminol™VP-1 and similar high-temperature heat transfer fluids have relatively high vapor pressures at required operating temperatures. As a result storage tanks require pressurization (~1700 kPa) which dramatically increases storage tank cost and complexity. As a result, systems

using Therminol™VP-1 or a similar synthetic heat transfer oil in the solar field generally require an indirect system for tank storage concepts. Molten salts are the current class of fluids most commonly considered as the indirect storage medium.

Molten salts offer the advantages of a much lower vapor pressure and are significantly less expensive than Therminol™VP-1, but they have the disadvantage of high freezing temperatures (100ºC-220ºC) [Herrmann, 2004]. Freezing is a design issue that must be considered with salts. Using molten salts as the parabolic trough solar field heat transfer fluid in addition to the storage medium has also been proposed [Kearney, 2003], but all current parabolic trough plants use oil in the solar field. If molten salts were used in this way, all of the indirect storage concepts discussed here could be made direct. Table 6.1 shows a list of commonly considered liquid storage media.

Table 6.1 Liquid Storage Media*

Liquid Media	Min Temp [ºC]	Max Temp [ºC]	Density [kg/m^3]	Thermal Conductivity [W/m-K]	Specific Heat [kJ/kg-K]
Mineral Oil	-	300	770	0.12	2.6
Synthetic Oil	-	350	900	0.11	2.3
Silicone Oil	-	400	900	0.1	2.1
Nitrite Salts	250	450	1825	0.57	1.5
Nitrate Salts	265	565	1870	0.52	1.6
Carbonate Salts	450	850	2100	2.0	1.8
Liquid Sodium	270	530	850	71	1.3

*Hermann, 2004

Molten salts are the only currently available and realistic option for use as both a storage medium and solar field fluid. There is an effort, still in its early stages, to develop a high-temperature, low vapor pressure, low melting point heat transfer fluid that would eliminate the weaknesses of both the synthetic oils and molten salts. The current focus is on ‘room temperature ionic liquids’ [Moens, et al, 2003].

The indirect two-tank system is considered by some to be the most promising near-term candidate for parabolic trough plant thermal storage [Herrmann, 2002]. However, Pacheco [Pacheco et al, 2002] has suggested using a filler material in an indirect single-

tank thermocline would be 35% less expensive than an indirect two-tank system. This proposal was followed up with work by Brosseau, et al. [2005] showing that quartzite rock and silica sand offer an inexpensive filler material which was shown not to deteriorate from prolonged exposure to the molten salt environment. In addition, quartzite has a higher thermal conductivity than most other rocks making it an even more attractive candidate [Incropera, 2002].

Tamme [2004] has suggested concrete tubes as a direct storage medium. This alternative eliminates the heat exchanger necessary for an indirect molten salt rock bed storage system, which would improve storage system performance and reduce cost. However, it adds the cost of an organized rather than randomly packed bed. In addition, some questions have been raised about the long-term structural stability of the caste concrete structures following multiple thermal cycles [Tamme, 2004].

Phase-change materials (PCMs) have been investigated as a storage medium for parabolic trough powerplants. The most current conceptual PCM work for parabolic troughs was performed in by Michels in 1996 [Hermann, 2002]. He suggested that a 5-stage cascade of PCMs (nitrates) operating at different temperatures showed promise as the predicted capital cost was lower and storage density higher than sensible storage of equivalent capacity. However, Hermann concludes that although further research in this area could prove "rewarding," that the technology is not sufficiently mature for PCMs to be considered as a near-term, large-scale thermal storage option for parabolic trough solar powerplants [2002].

Chemical reaction energy storage has also been considered as a low-cost storage system for use with parabolic trough systems. Systems based on a reaction between CaO and H_2O as well as ammonia dissociation have been considered. Similar to PCM storage it is generally considered as a long-term option and not yet ready for large-scale application [Hermann, 2002].

Conclusions

Single-tank stratified systems and concrete systems have obvious cost advantages over the two-tank systems. They offer both a reduction in equipment size (number of tanks) and the use of an inexpensive packing material allows heat transfer fluid (HTF) inventory to be decreased. As a result of these advantages, direct and indirect single-tank systems utilizing a secondary filler material will the primary focus of the further investigations included in this thesis.

6.3 Packed-Bed Thermal Storage Modeling

The heat-transfer modeling techniques described in this section are discussed in terms of a single-tank system with a secondary storage medium. These techniques also describe the heat transfer performance of concrete storage systems.

6.3.1 Analytical solution to the Packed-Bed Heat Transfer Problem

Modeling of packed-bed heat transfer can be a problem of immense complexity, in some cases requiring the use of 3-D finite-element techniques to understand the dynamics of stratification and fluid-solid interaction during different modes of operation. In this thesis the interest is in characterizing the performance of storage systems over long periods of time. That is, daily charge-discharge cycles of storage systems simulated for long periods (years). From the outset this modeling constraint places a premium on the computational overhead of modeling techniques that are considered. The goal of this section is to identify and solve a set of governing equations that economically and accurately characterize the dominant energy transfer mechanisms in a charging or discharging packed-bed storage tank over long time periods that include multiple cycles.

To begin, consider a tank with diameter D, filled with coarsely-packed solid material and fluid flowing through the free space, characterized by a void fraction ε:

$$\varepsilon = \frac{V_f}{V_f + V_s} \qquad [6.3.1]$$

where V_f and V_s are the solid and fluid volumes.

Now consider a differential segment of this tank of length dx, shown in Figure 6.4:

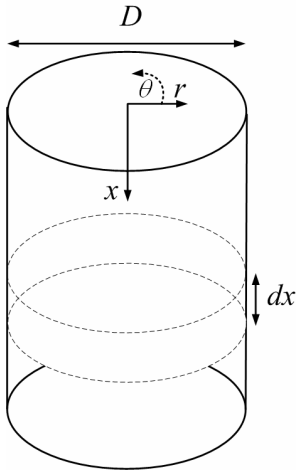

Figure 6.4: Storage tank coordinate system and differential control volume

Figure 6.5 shows one-dimensional fluid and solid energy balances corresponding to the differential tank segment shown in Figure 6.4. Axial conduction, viscous dissipation and losses to the environment are neglected. The energy balances are written in one-dimension assuming that significant temperature variations occur only in the axial (x) direction. This formulation of the one-dimensional packed-bed heat transfer problem is popular and credited to Schumann [1929].

It is appropriate to neglect environmental losses due to the large volume to surface area ratio for storage units designed for power production system. The thermal losses to the environment will be negligible compared to energy transfer in the tank during a charge or discharge cycle in a well-designed unit. In the event the tank lies idle for long periods shell losses become significant. This scenario is considered in section 6.3.6; the current section is focused only on storage system charging and discharging. Likewise, for well-designed storage systems axial conduction will be negligible. Limiting axial conduction is essential to maintaining stratification in the fluid. One way to mitigate axial conduction effects is the presence of low-conductivity "plates" at various heights in the

tank which allow fluid flow but limit dynamic conductive effects as well as any conduction through the solid material. Maintaining stratification requires prevention of large-scale mixing, accomplished by limiting fluid velocity in the tank. Low fluid velocities correspond to a negligible viscous dissipation effect.

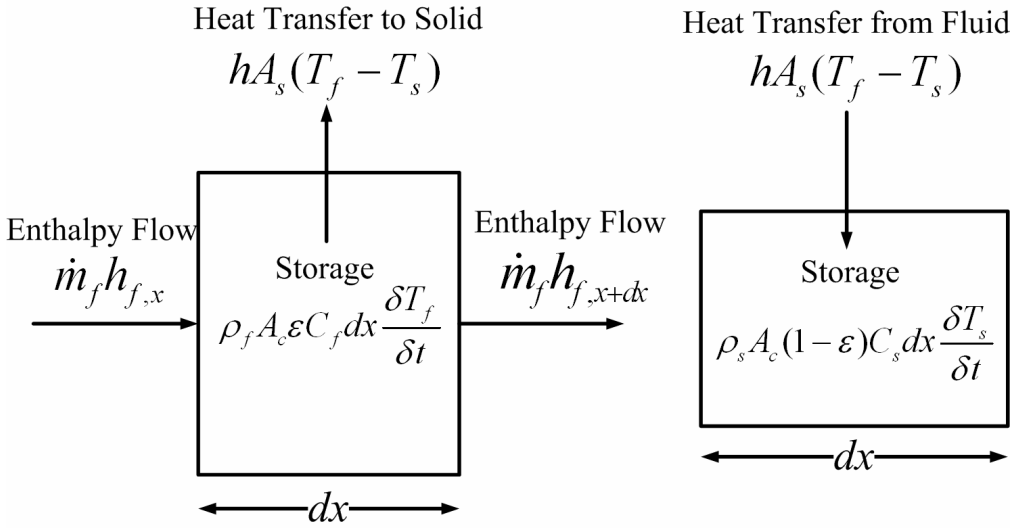

Figure 6.5: Energy balance on the fluid (left) and solid (right) components of the differential element of the storage tank

A one-dimensional energy balance performed on the control volumes shown in Figure 6.5 results in governing partial differential equations for the fluid and solid, respectively:

$$\dot{m}_f C_f \frac{dT_f}{dx} + \rho_f \varepsilon A_c C_f dx \frac{dT_f}{dt} = -hA_s(T_f - T_s) \qquad [6.3.2]$$

$$\rho_s (1-\varepsilon) A_c C_s dx \frac{dT_s}{dt} = hA_s(T_f - T_s) \qquad [6.3.3]$$

In equations [6.3.2] and [6.3.3], A_s is the solid-fluid interface surface area available for heat transfer. A_s can be determined in terms of average particle diameter (d_p) for the differential control volume if the particles are assumed to be spheres of uniform size:

$$A_s = \frac{6A_c(1-\varepsilon)dx}{d_p} \qquad [6.3.4]$$

A_{node} and A_{total} are used in section 6.3.3 when describing numerical methods and are defined analogously to A_s. A_c is tank cross-sectional area. If packing material particle size varies dramatically a technique that considered particle size variation (equation

[6.3.4] does not) would be required to determine A_s.

It is important to make note of several additional assumptions implicit in the formulation of equations [6.3.2] and [6.3.3]:

- Material and transport properties are constant
- Solid material is thermally lumped (internal conductivity is ~infinite, no temperature gradients within solid particles)

Analytical Solution

Prior to exploring numerical techniques it is desirable to develop an analytical solution to equations [6.3.2] and [6.3.3]. This solution will provide a limiting case against which numerical techniques can be tested, in addition to facilitating the understanding of basic system performance. Shitzer [1993] offers a solution to equations [6.3.2] and [6.3.3] and the following boundary conditions:

$$T_f(0,t) = T_o$$
$$T_s(x,0) = 0 \qquad [6.3.5]$$

The solution is presented as a double infinite series which typically converges at 10-50 terms depending on system parameters:

$$\frac{T_s}{T_o} = e^{-y-z}\sum_{n=1}^{\infty}\sum_{m=0}^{\infty}\frac{y^m z^{m+n}}{m!(m+n)!} \qquad [6.3.6]$$

$$\frac{T_f}{T_o} = e^{-y-z}\sum_{n=0}^{\infty}\sum_{m=0}^{\infty}\frac{y^m z^{m+n}}{m!(m+n)!} \qquad [6.3.7]$$

where

$$y = \frac{h_v}{\rho_f C_f \varepsilon}\left(\frac{x}{v}\right) \qquad [6.3.8]$$

$$z = \frac{h_v}{\rho_s C_s (1-\varepsilon)}\left(t - \frac{x}{v}\right) \qquad [6.3.9]$$

$$v = \frac{V''}{\varepsilon_b} \qquad [6.3.10]$$

Assumption Relaxation

The assumptions made in the formulation of equations [6.3.2] and [6.3.3], as well as the subsequent analytical solution place some limitations on simulation accuracy using the Schumann equations. Of principle concern are material and transport property variation and the assumption of infinite solid conductivity. Properties can vary dramatically with temperature and the solid materials under consideration have relatively low conductivity indicating the likely presence of significant temperature gradients within solid particles.

Variable properties are readily managed in the context of the numerical solutions that will be used to solve the governing equations.

The treatment of the solid as a lumped capacitance (infinite conductivity) requires more consideration. The solid materials (quartzite rock, silica sand, etc...) under consideration for powerplant thermal storage possess relatively low thermal conductivities, calling into question the universal validity of the lumped-capacitance assumption. Jeffreson [1972] proposes a heat transfer coefficient correction factor that accounts for temperature gradients within solid particles without adding dimensions to the computational domain. Jeffreson's correction factor is formulated in terms of the Biot number, shown below:

$$\frac{h_{corrected}}{h} = \frac{1}{1 + Bi/5} \qquad [6.3.11]$$

The Biot number is a ratio of convective heat transfer with the fluid and conduction within the solid. As the Biot number becomes large convective heat transfer from fluid to solid dominates conduction within the solid, indicating significant temperature gradients within the solid. The Jeffreson factor estimates the degradation of fluid-solid overall heat transfer coefficient resulting from these temperature gradients. A more advanced correction factor that includes both the Biot and Fourier numbers is proposed by Engelbrecht, et al [2006].

6.3.2 General System Performance

The Schmuann equations presented in section 6.3.1 have general applicability to packed-bed heat transfer problems. It is useful to introduce a "test case" in order to provide a realistic framework for the thermal energy storage systems being considered.

The packed-bed stratified tank test conditions are based on the system built for Solar One consisting of Caloria™ HT-43 heat transfer oil and a rock-sand packing material [Faas, 1986]. Approximate system parameters are listed in Table 6.2. Note that the bed material is treated as spheres with average diameter d_p. The fluid-solid heat transfer coefficient, h, is calculated using a correlation developed by Ranz and Marshall [Rohsenow, 1998].

$$Nu_p = 2 + 1.8\,\mathrm{Re}_p^{1/2}\,\mathrm{Pr}^{1/3} \qquad [6.3.12]$$

where Re_p and Nu_p are defined in terms of the particle diameter and axial fluid velocity (fluid velocity within the packed bed). This correlation was developed for a multi-particle system incorporating heat transfer enhancement related to dynamic particle-fluid interaction. As bed void fraction decreases, linear velocity increases thus increasing dynamic heat transfer enhancement.

The test case considers a single charge period of one-hour with a HTF mass flow rate of 720 kg/s and the following temperature boundary conditions:

$$T_f(x=0,t) = 400[C] \qquad [6.3.13]$$

$$T_s(x,t=0) = 300[C] \qquad [6.3.14]$$

Table 6.2 Storage System Test Case Parameters based on Solar One*

Parameter		
C_f	2400	J/kg-K
C_s	1000	J/kg-K
ρ_f	1000	kg/m^3
ρ_s	2400	kg/m^3
h	183	w/m^2-K
T_o	300	C

T_i	400	C
d_p	0.01	m
ε	0.23	-
A_c	729	m^2
L	14	m

*Faas, 1986

Using the analytical solution to the Schumann model and the test conditions it is possible to explore the parameters that govern packed-bed storage system performance. Understanding the dominant parameters will provide design information for future storage systems for solar power applications in addition to providing a framework for interpreting the results of more complex simulation and modeling efforts.

It is helpful to characterize system performance in terms of dimensionless quantities. The first group examined here is defined as:

$$U = \frac{C_f \int_0^t \dot{m}_f dt}{m_{s,total} C_s + m_{f,total} C_f} \qquad [6.3.15]$$

U is the ratio of the thermal capacitance of the fluid that flows through the system during some period of time, t, and the total static thermal capacitance of the system (solid + entrained fluid). U is sometimes referred to as the *utilization* of the storage system and can be usefully thought of as a dimensionless thermocline penetration depth [Nellis and Klein, 2006]. Figure 6.6 shows the relationship between the location of the fluid thermocline during a charge cycle and U. U can also be thought of an average normalized penetration depth (δ_{conv}/L). That is, if $U=1$ and the heat transfer coefficient were infinite then the solid and fluid would be uniformly at the fluid inlet temperature.

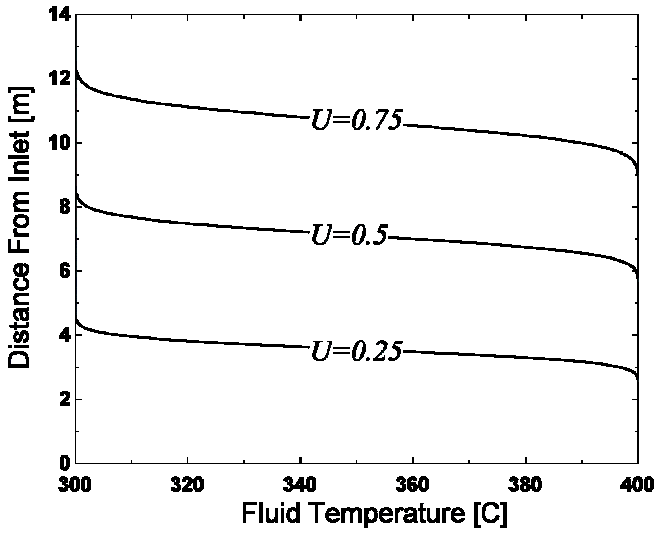

Figure 6.6: The relationship between the utilization (*U*) and thermocline penetration depth.

There is a related dimensionless group that can be defined, *R*, as the static thermal capacitance ratio of the solid and entrained fluid:

$$R = \frac{m_{f,total} C_f}{m_{s,total} C_s} \qquad [6.3.16]$$

R provides an indication of how significant the thermal capacitance of the fluid entrained in the system is relative to the thermal capacitance of the solid material. The value of *R* depends on the bed void fraction as well as fluid and solid heat capacity and density. In the test case, *R=0.32*. This value indicates the fluid capacitance is a significant component of the total system capacitance. This is an important observation, because it is common in the heat transfer community to neglect the thermal capacitance of the fluid when modeling gas-solid systems [Nellis and Klein, 2006]. The majority of packed-bed literature concerns gas-solid systems, including the models designed for TRNSYS [Klein et al, 2006], thus the results that are applied to packed-bed thermal storage systems must be carefully examined. Equations [6.3.2] and [6.3.3] consider the thermal capacitance of both the fluid and solid components of the bed. The implications of incorrectly neglecting thermal capacitance are discussed in section 6.3.4.

The performance of a packed-bed thermal storage system is related to the heat transfer performance between the solid and fluid tank constituents. To describe the fluid-solid heat transfer performance NTU_{fluid} is defined in a manner analogous to the *NTU* used in

heat exchanger analysis:

$$NTU_{fluid} = \frac{hA_{total}}{\dot{m}_f C_f} \qquad [6.3.17]$$

NTU_{fluid} is related to the shape of the thermocline (temperature gradient) in the fluid. Thermocline shape for different values of NTU_{fluid} is shown for a 1-hour charge cycle of the test case in Figure 6.7. NTU_{fluid} was varied for the test case by increasing the fluid-solid heat transfer coefficient.

The effectiveness of a storage system for power generation requires the maintenance of a sharp (large NTU_{fluid}) thermocline. As the thermocline becomes poorly defined (smears) the average outlet temperature delivered to the power cycle will decrease limiting powerplant performance and thus overall storage system efficiency. The relationship between storage system effectiveness and NTU_{fluid} can be quantified specifically for power-cycle applications by using a second law efficiency defined as follows:

$$\eta_{2nd\,law} = \frac{\int_{t_0}^{t} (\psi_{out,discharge} - \psi_{in,discharge})dt}{\int_{t_0}^{t} (\psi_{in,charge} - \psi_{out,charge})dt} \qquad [6.3.18]$$

where Ψ is the specific availability (exergy) of the fluid defined as:

$$\psi = \dot{m}_f \left[C_f (T_f - T_o) - T_o C_f LN\left(\frac{T_f}{T_o}\right) \right] \qquad [6.3.19]$$

where T_o represents the dead-state temperature.

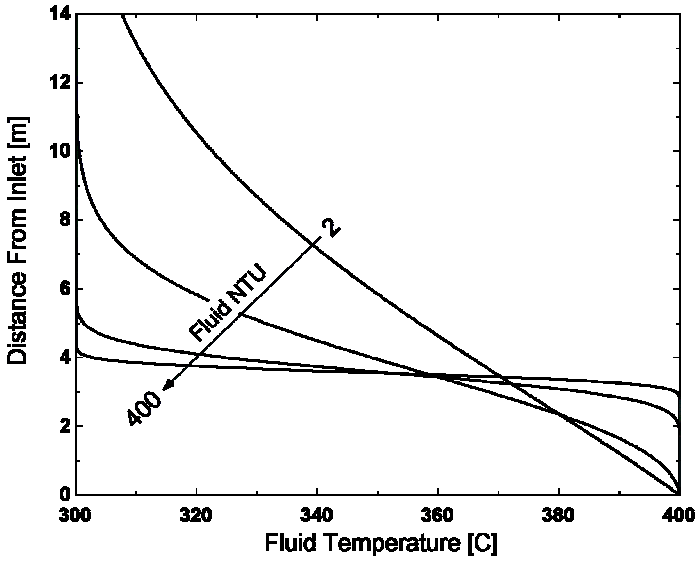

Figure 6.7: The relationship between NTU_{fluid} and the slope of the thermocline. Higher values of NTU_{fluid} result in steeper thermoclines and thus more efficient thermal storage systems.

The Second Law efficiency here represents the ratio of the availability retrieved and stored from the system during charge and discharge cycles of equivalent length. Figure 6.8 shows the relationship between system Second Law efficiency and NTU_{fluid} for the test case with a sufficient number of charge and discharge cycles to reach a cyclic steady-state. Cyclic steady-state is defined when, for some periodic forcing functions, the second law efficiency approaches a constant value for consecutive charge-discharge cycles. The cyclic steady-state Second Law efficiency is not obtained from the initial cycles because of transient behavior imposed by the system's initial conditions.

The NTU_{fluid} values encountered in thermal storage applications here are much larger than NTU values typically seen in heat exchanger because of the massive amount of fluid-solid interfacial surface area. The Second Law efficiency approaches one as NTU_{fluid} becomes large provided the storage tank capacity is not exceeded.

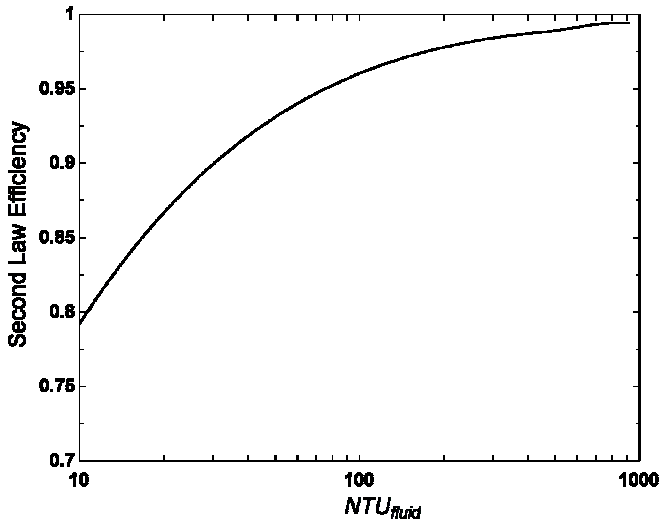

Figure 6.8: Storage system exergetic (second law) efficiency as defined in equation [6.3.18].

6.3.3 Numerical Modeling Techniques

Useful long-term simulation of packed-bed storage systems requires efficiency and accuracy. In this section several numerical approaches to equations [6.3.2] and [6.3.3] are presented.

General explicit model

A single-step explicit approach is considered as a starting point for ease of numerical modeling. Figure 6.9 shows the 1-D fluid and solid energy balances corresponding to equations [6.3.2] and [6.3.3].

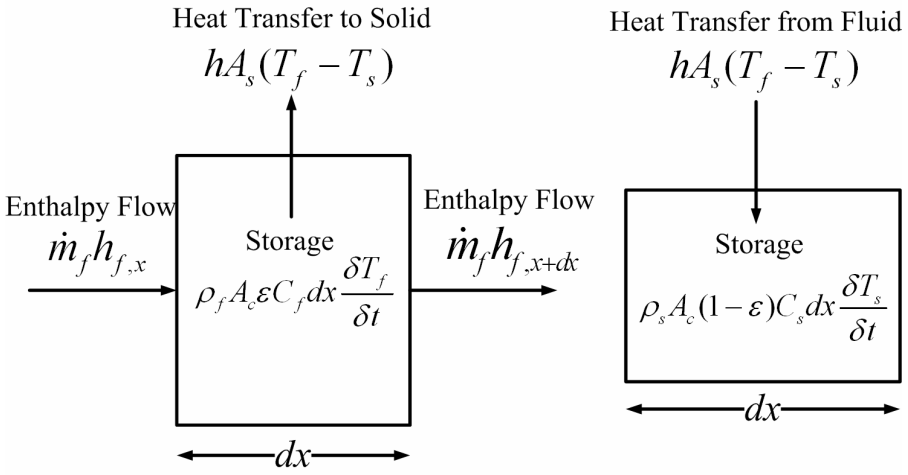

Figure 6.9: Energy balance on the fluid (left) and solid (right) components of the differential element of the storage tank

Figure 6.10 shows the numerical grid that is used for this explicit scheme and all other numerical models discussed in these sections. Note that both fluid and solid temperature nodes are located at the center of the numerical control volumes. Temperature node location was chosen to simplify expression of the fluid-solid heat transfer term. The only coupling effect between the two governing energy equations is the convective heat transfer term.

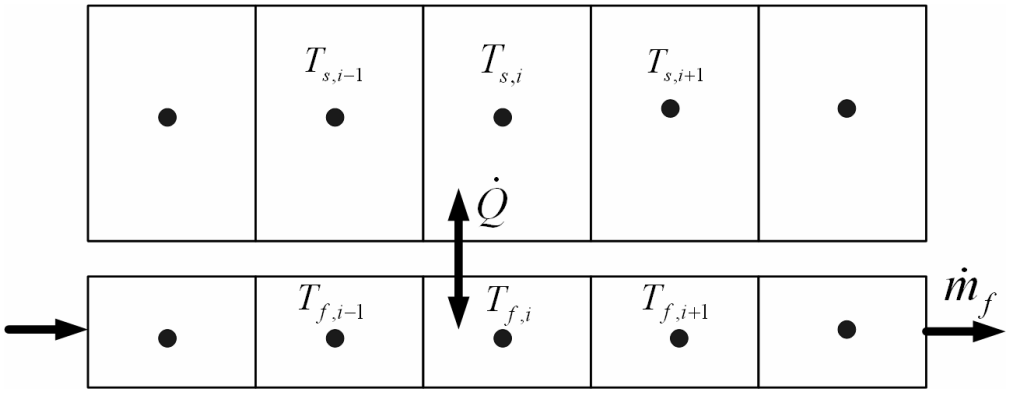

Figure 6.10: Numerical grid used for finite-difference numerical modeling techniques

Explicitly approximating the differential fluid energy balance in Figure 6.6 using a linear relation yields the following nodal energy balance:

$$\dot{m}_f C_f \left(\frac{T_{f,(i-1,t)} + T_{f,(i,t)}}{2} \right) = \dot{m}_f C_f \left(\frac{T_{f,(i,t)} + T_{f,(i+1,t)}}{2} \right) + hA_{node}(T_{f,(i,t)} - T_{s,(i,t)}) + \frac{\rho_f A_c (1-\varepsilon)\Delta x C_f}{\Delta t}(T_{f,(i,t+\Delta t)} - T_{f,(i,t)}) \quad [6.3.20]$$

where

$$T_{f,(i,t)} = T_{fluid,(node,time)} \quad [6.3.21]$$

Likewise the solid energy balance becomes:

$$\rho_s A_c \Delta x C_s (T_{s,(i,t+\Delta t)} - T_{s,(i,t)}) = hA_{node}\Delta t (T_{f,(i,t)} - T_{s,(i,t)}) \quad [6.3.22]$$

To accommodate the nodal locations chosen in Figure 6.10 the average fluid temperature between nodes is the basis for calculating the convective energy transport across the nodal boundary during a given timestep. Discretized in this way the equations are explicit in both time and space.

Simplified explicit formulation

The relationship between the discretized energy balance and fluid flow rate can be exploited to simplify the fluid energy balance. The simplification starts by making the following substitution into equation [6.3.20]:

$$\Delta t = \frac{\rho_f A_c \varepsilon \Delta x}{\dot{m}_f} = \frac{m_f}{\dot{m}_f} \qquad [6.3.23]$$

where Δt is the time required for the fluid to move an axial distance that is exactly equal to Δx and m_f is the amount of fluid that occupies one node. If the timestep used to solve equations [6.3.20] and [6.3.22] is selected to be Δt, then the nodal temperatures represent the average temperature of the entire mass of fluid in each respective node. In this case, the convective transport across nodal boundaries during a timestep is precisely equal to a single nodal temperature, rather than the average temperature used in equation [6.3.20]. Figure 6.11 shows this effect graphically: the distance a plug of fluid flows during a single timestep is exactly equal to the size of the control volume.

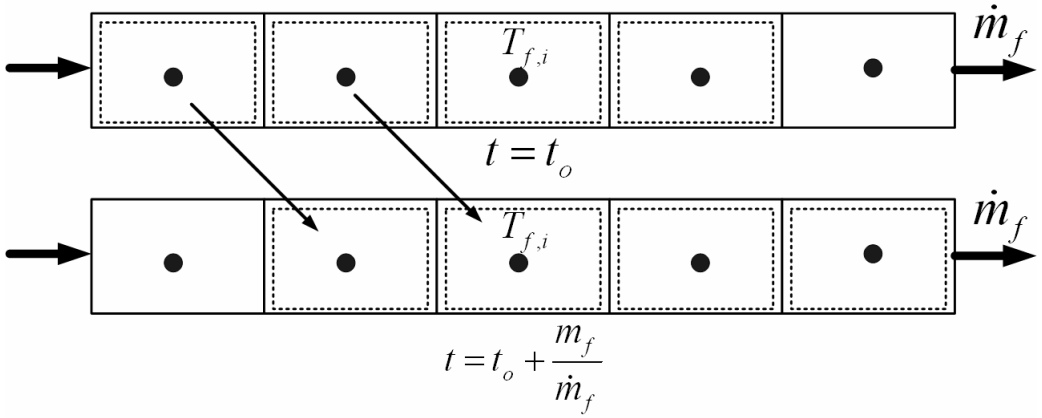

Figure 6.11: Flow of fluid plugs in porous bed demonstrating the simplifying assumption which defines fluid plugs to have the same dimension as the control volumes

An order of operations for each timestep is necessarily established to ensure consistent formulation of the coupled energy balances. In this case fluid motion is considered first, followed by heat transfer with the solid. The driving force for heat transfer in a node can then be defined in terms of the fluid temperature entering that nodal control volume rather than the nodal temperature because the entering fluid temperature occupies the entire node. Applying the above substitutions to equation [6.3.20] yields:

$$\dot{m}_f C_f \left(T_{f,(i-1,t)}\right) = \dot{m}_f C_f \left(T_{f,(i,t)}\right) + hA_{node}(T_{f,(i-1,t)} - T_{s,(i,t)}) + \dot{m}_f C_f (T_{f,(i,t+\Delta t)} - T_{f,(i,t)}) \quad [6.3.24]$$

Grouping $\dot{m}_f C_f$ terms:

$$\dot{m}_f C_f \left(T_{f,(i-1,t)} - \cancel{T_{f,i,t}} + \cancel{T_{f,i,t}} - T_{f,(i,t+\Delta t)}\right) = hA_s (T_{f,(i-1,t)} - T_{s,(i,t)}) \quad [6.3.25]$$

Finally solving for the ith nodal temperature at the beginning of the next timestep:

$$T_{f,(i,t+\Delta t)} = T_{f,(i-1,t)} - \frac{hA_{node}(T_{f,(i-1,t)} - T_{s,(i,t)})}{\dot{m}_f C_f} \quad [6.3.26]$$

The solid energy balance is unchanged with the exception of the temperature driving heat transfer:

$$T_{s,(i,t+\Delta t)} = T_{s,(i,t)} + \frac{hA_{node}\Delta t(T_{f,(i-1,t)} - T_{s,(i,t)})}{m_s C_s} \quad [6.3.27]$$

The net result is a dramatically simplified fluid energy balance based on the timestep constraint described in equation [6.3.23]. In effect, the timestep required to solve the equations is now linked to the size of the nodes. If more nodes are used to represent the temperature distribution, the corresponding timestep is reduced.

Figure 6.12 shows the simplified explicit solution converging on the analytical solution to the Schumann equations for the test conditions. Equation [6.3.23] dictates that as the node count increases, the timestep will decrease, resulting in a more precise solution in both time and distance.

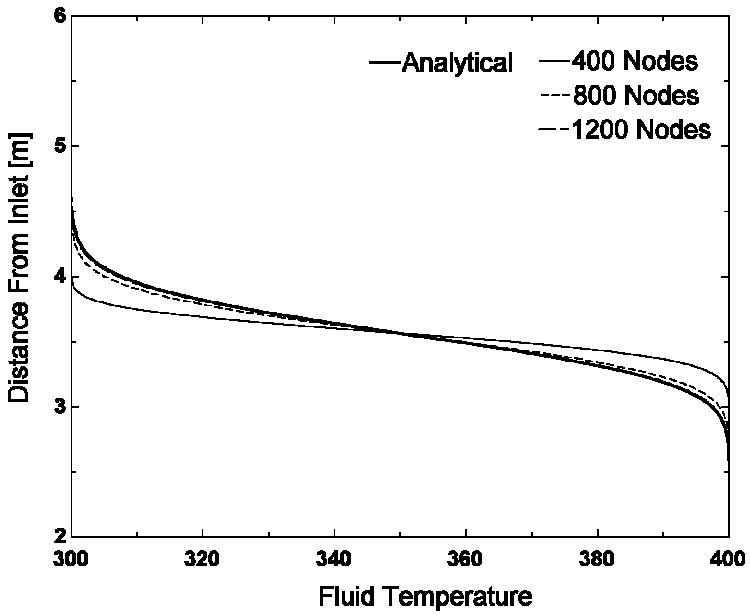

Figure 6.12: Comparison of the analytical solution to the Schumann equations with the explicit numerical solution

Solution Stability

When the simplified explicit solution is used with an insufficient number of nodes, the solution becomes unstable because the time and distance steps are coupled. In the interest of minimizing computational overhead with the explicit model, a method for predicting both the stability and accuracy of the solution is investigated. This method can help to choose appropriate mesh and timestep sizes for rapid and accurate simulation.

Two dimensionless groups are related to the stability of this explicit numerical solution. They are defined here as:

$$NTU_{fluid,node} = \frac{hA_{node}}{\dot{m}_f C_f} \qquad [6.3.28]$$

$$NTU_{solid,node} = \frac{hA_{node}\Delta t}{m_s C_s} \qquad [6.3.29]$$

Notice that $NTU_{fluid,node}$ is simply a nodal version of the previously defined NTU_{fluid}. In the context of solution stability it is most useful to think of both nodal *NTU* values as "sensitivity" parameters to temperature change. Defining these terms allows equations [6.3.26] and [6.3.27] to be reformulated as follows:

$$T_{f,(i,t+\Delta t)} - T_{f,(i-1,t)} = -NTU_{fluid,node}(T_{f,(i-1,t)} - T_{s,(i,t)}) \quad [6.3.30]$$

$$T_{s,(i,t+\Delta t)} - T_{s,(i,t)} = NTU_{solid,node}(T_{f,(i-1,t)} - T_{s,(i,t)}) \quad [6.3.31]$$

Solution instability arises when the calculated temperature difference between solid and fluid increases. Increasing temperature differences result in the uncontrolled, geometric change in predicted fluid and solid temperatures. Based on this understanding a very simple stability criterion can be considered: if the temperature difference between solid and fluid is decreasing from timestep to timestep then the temperature profile that develops will be stable (although not necessarily accurate). This criterion is satisfied for any initial fluid and solid temperatures if the sum of the two nodal *NTU* values (NTU_{sum}) is less than or equal to two:

$$NTU_{sum} = \frac{hA_{node}\Delta t}{m_s C_s} + \frac{hA_{node}}{\dot{m}_f C_f} \leq 2 \quad [6.3.32]$$

If NTU_{sum} is greater than two, equations [6.3.30] and [6.3.31] dictate that the nodal temperature difference at the end of a timestep will be larger than the temperature difference at the beginning of the timestep, causing the solution to become unstable.

Equation [6.3.32] can be used to derive a critical node count for achieving solution stability by recognizing:

$$A_{node} = \frac{A_{total}}{n} \quad [6.3.33]$$

Then substituting equations [6.3.23] and [6.3.33] into [6.3.32] and solving for the critical number of nodes to ensure solution stability:

$$n_{crit} = \frac{hA_{total}}{2\dot{m}_f}\left(\frac{1}{C_f} + \frac{m_{f,node}}{m_s C_s}\right) \quad [6.3.34]$$

Criterion [6.3.34] ensures only solution stability; it does not guarantee agreement with the Second Law. If n_{crit} nodes are used the predicted solid and fluid temperatures can exceed what would be their equilibrium temperature given infinite time for heat transfer. To ensure both solution stability and the agreement with the second law NTU_{sum} must not exceed one, implying that the sum of the solid and fluid temperature changes during the timestep does not exceed the temperature difference at the beginning of the timestep.

Setting NTU_{sum} to one results in the following recommended node count:

$$n_{rec} = \frac{hA_{total}}{\dot{m}_f}\left(\frac{1}{C_f} + \frac{m_{f,node}}{m_s C_s}\right) \qquad [6.3.35]$$

Figure 6.13 shows a progression of temperature profiles as the NTU sum passes through the recommended and critical node criteria. Figure 6.13(a) shows a temperature profile with the recommended node count, producing a stable and well-behaved temperature profile. Figure 6.13(b) shows that stable, but oscillatory, temperature profiles arise for node counts between the recommended and critical node counts. While stable, the profile in Figure 6.13(b) violates the second law as fluid temperature is shown dropping below the initial rock temperature. Figure 6.13(c) shows complete solution instability when there are fewer nodes than the n_{crit}.

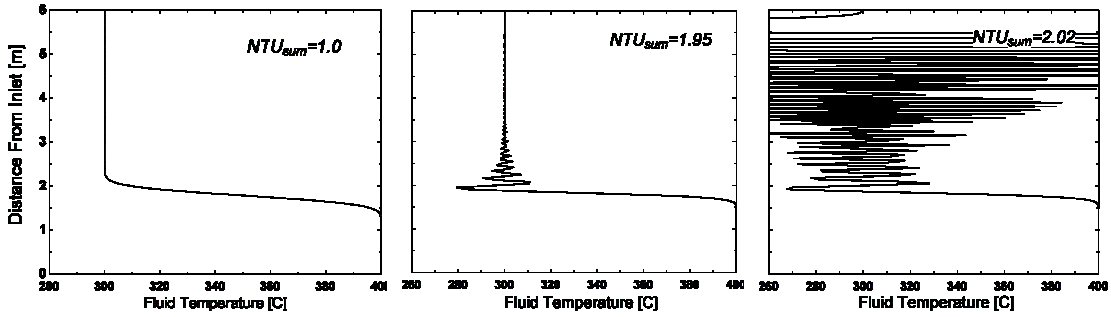

(a) **(b)** **(c)**

Figure 6.13: The simplified explicit solution approaching instability as NTU_{sum} approaches and exceeds 2.

Implicit Numerical Model

The stability issues experienced with the explicit model motivate the development of an analogous implicit model. Implicit models guarantee solution stability. In an implicit model, the values of fluid temperature and solid temperature are calculated based on their values at the end of a timestep or distance step rather than the beginning (as in an explicit model). The implicit finite-difference equations are formulated as follows based on equations [6.3.26] and [6.3.27]:

$$T_{f,(i,t+\Delta t)} = T_{f,(i-1,t)} - \frac{hA_{node}(T_{f,(i,t+\Delta t)} - T_{s,(i,t+\Delta t)})}{\dot{m}_f C_f} \qquad [6.3.36]$$

$$T_{s,(i,t+\Delta t)} = T_{s,(i,t)} + \frac{hA_{node}\Delta t(T_{f,(i,t+\Delta t)} - T_{s,(i,t+\Delta t)})}{m_s C_s} \qquad [6.3.37]$$

This implicit model is derived from the simplified explicit model so it requires inclusion of the same timestep constraint (equation [6.3.23]).

In the explicit model every calculation depends only on previously known values, so calculating forward in time and distance is trivial. In the case of the implicit model equations [6.3.36] and [6.3.37] result in a system of equations for each node and each timestep. Writing the system of equations for a single timestep and organizing them in matrix form yields the following tri-diagonal matrix equation of the standard form $Ax=B$:

$$\begin{array}{c} \\ node\,1,f \\ node\,1,s \\ \vdots \\ \vdots \\ node\,n,f \\ node\,n,s \end{array}\begin{array}{c} \begin{array}{cccccc} T^+_{f,1} & T^+_{s,1} & \cdots & \cdots & T^+_{f,n} & T^+_{s,n} \end{array} \\ \begin{bmatrix} 1+A_1\Delta t & -A_1\Delta t & 0 & 0 & 0 & 0 \\ -B\Delta t & 1+B\Delta t & 0 & 0 & 0 & 0 \\ 0 & 0 & \ddots & \ddots & 0 & 0 \\ 0 & 0 & \ddots & \ddots & 0 & 0 \\ 0 & 0 & 0 & 0 & 1+A_n\Delta t & -A_n\Delta t \\ 0 & 0 & 0 & 0 & -B\Delta t & 1+B\Delta t \end{bmatrix} \end{array} \begin{Bmatrix} T^+_{f,1} \\ T^+_{s,1} \\ \vdots \\ \vdots \\ T_{f,n} \\ T^+_{s,n} \end{Bmatrix} = \begin{bmatrix} T_{f,in} \\ T_{s,1} \\ \vdots \\ \vdots \\ T_{f,n-1} \\ T_{s,n} \end{bmatrix}$$

Figure 6.14: The tridiagonal matrix that results from implementation of equations [6.3.36] **and** [6.3.37]**.**

In Figure 6.14, $A_n = \dfrac{hA_{node}}{\dot{m}_f C_{f,n}\Delta t}$ and $B = \dfrac{hA_{node}}{m_s C_s}$

If the full explicit energy balance in equation [6.3.20] were used the matrix necessary to solve each timestep implicitly would be tridiagonal with each diagonal fully populated. That is, the system of equations would be fully coupled. In this case each node is represented by a discrete set of equations (*n* sets of two equations each with two unknowns) where equation [6.3.20] would yield a fully populated tri-diagonal matrix (*2n* equations with *2n* unknowns).

Figure 6.15 shows the implicit solution converging on the analytical solution reported in section 6.3.1 as the number of nodes increases (using equation [6.3.23] to constrain the solution timestep).

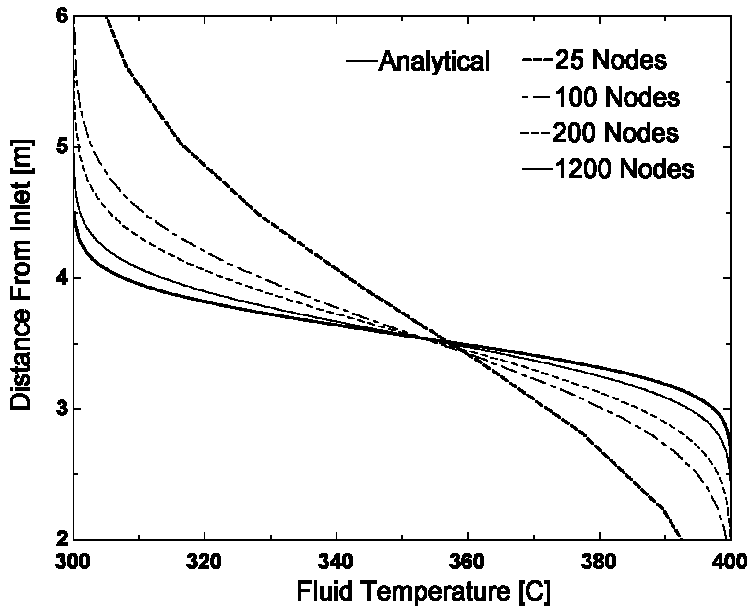

Figure 6.15: Comparison of the analytical solution to the Schumann equations with the implicit numerical solution

The implicit model requires additional computational overhead, but the guarantee of solution stability makes the implicit model conducive to either coarse or detailed simulation runs.

The Infinite-*NTU* Model

The infinite-*NTU* model adds an additional assumption to the Schumann equations that offers unsurpassed computational efficiency and guaranteed stability. These attributes are achieved by assuming the overall heat transfer coefficient in each node of the finite-difference approximation is effectively infinite. The result is that at the end of every time and distance step the temperature of the solid and the temperature of the fluid are in equilibrium.

The finite-difference equations for the infinite-*NTU* model are derived starting with equations [6.3.26] and [6.3.27] while assuming $T_{f,(i+1,t+\Delta t)} = T_{s,(i,t+\Delta t)}$. This simplification yields the following single equation:

$$T_{f,(i,t+\Delta t)} = T_{s,(i-1,t+\Delta t)} = \frac{T_{f,(i-1,t)}\dot{m}_f C_{p,f}\Delta t + T_{s,(i,t)} m_s C_{p,s}}{\dot{m}_f C_{p,f}\Delta t + m_s C_{p,s}} \qquad [6.3.38]$$

This model retains stability despite its explicit formulation due to the assumed solid-fluid equilibrium. The cause of instability in the simplified explicit formulation was variation in fluid and solid temperatures and the terms that governed heat transfer between them. This mechanism is entirely absent in the infinite-*NTU* formulation as the fluid and solid are always in thermal equilibrium.

Note that this infinite-*NTU* model could also be formulated implicitly. It is not developed here because an implicit formulation only adds computational complexity to an already efficient and stable method.

Figure 6.16 shows that the infinite-*NTU* solution converges on a temperature profile that is sharper than the analytical solution for the test conditions. This behavior is explained by the fact that thermocline slope is related to NTU_{fluid} (discussed in section 6.3.2). The analytical solution for the test case considers a finite fluid-solid heat transfer coefficient, thus the infinite-*NTU* solution overestimates the sharpness of the thermocline. As the precision of the infinite-*NTU* solution decreases the predicted thermocline becomes less and less sharp. Thus, as the resolution of the infinite-NTU solution decreases it first passes through the analytical solution, and then fully diverges. When used with systems having appropriately large values of NTU_{fluid} the error incurred by using this approach will be minimal.

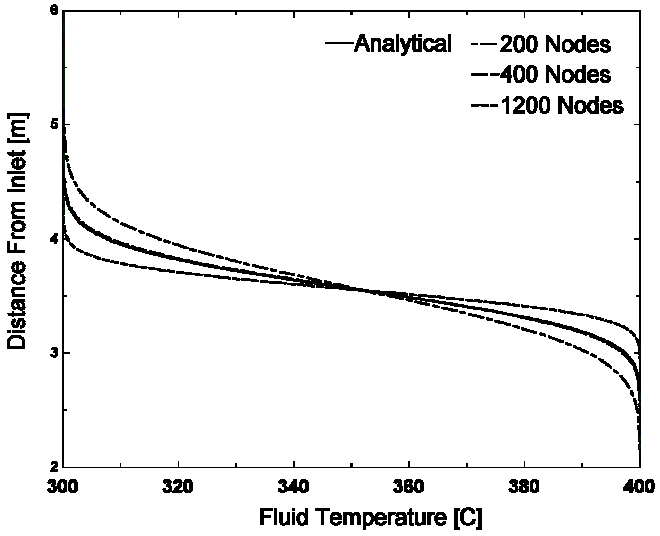

Figure 6.16: Comparison of the analytical solution to the Schumann equations with the infinite-*NTU* numerical solution

Effect of Fluid Capacitance

The models in this chapter were developed specifically with thermal energy storage systems in mind. However, much of the existing simulation capability was developed to evaluate gas-solid packed-bed heat transfer performance. In these gas-solid models the fluid thermal capacitance is often neglected. A numerical model that neglects fluid capacitance is presented here in order to quantify the impact of making this assumption with packed-bed thermal storage systems where the fluids have much higher thermal capacitances.

The finite-difference equations are developed explicitly from the fluid energy balance shown in Figure 6.9 by neglecting the thermal capacitance term. For convenience, the temperature nodes are defined at the axial nodal interfaces. The fluid energy balance is then:

$$T_{f,(i+1,t)} = T_{f,(i,t)} - \frac{hA_{node}}{\dot{m}_f C_f}\left(\frac{T_{f,(i,t)} + T_{f,(i+1,t)}}{2} - T_{s,(i,t)}\right) \qquad [6.3.39]$$

And the solid energy balance becomes:

$$T_{s,(i,t+\Delta t)} = T_{s,(i,t)} + \frac{hA_{node}\Delta t}{m_s C_s}\left(\frac{T_{f,(i,t)} + T_{f,(i+1,t)}}{2} - T_{s,(i,t)}\right) \qquad [6.3.40]$$

Figure 6.17 shows the simplified explicit model (equations [6.3.26] and [6.3.27]) converging on the no-capacitance model (equations [6.3.39] and [6.3.40]) for a storage system where R (capacitance ratio)~0, demonstrating that for systems where the fluid capacitance truly is negligible, these two models are equivalent. This model will be used in section 6.3.4 to compare predicted performance in systems where fluid capacitance is not negligible, as is expected in thermal-storage systems.

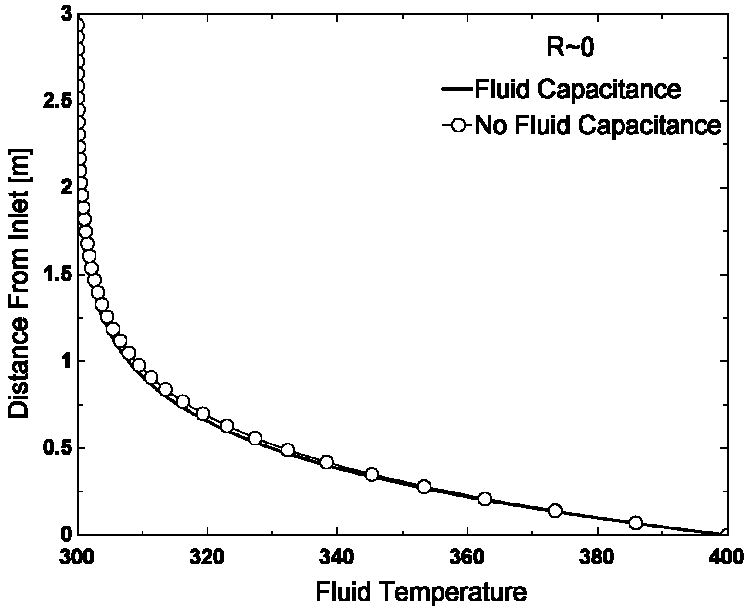

Figure 6.17: The simplified explicit model converging on the no-capacitance model for the limiting case where R~0

6.3.4 Numerical Model Performance Comparison

The focus on computational speed necessitates an analysis of the relative speed and accuracy of the models developed in the previous section. This analysis will help inform model selection for long-term simulation. In this section the speed and accuracy of the infinite-NTU, implicit and simplified explicit models are compared. In addition, the error associated with incorrectly neglecting fluid thermal capacitance as described in section 6.3.3 is quantified. Error in determination of steady state efficiency is defined in this section as $Error = \left|(\eta_{ref} - \eta)/\eta_{ref}\right|$.

Numerical Model Performance: Cyclic Steady-State

The infinite-*NTU*, simplified explicit and implicit models all provide useful solutions of the Schumann model for packed-bed heat transfer. Given the computational efficiency and guaranteed stability of the infinite-*NTU* model, determining the conditions under which its use is appropriate is of principle interest. To evaluate these conditions the same cyclic steady-state simulation described in section 6.3.2 is run using the infinite-*NTU*

model and the explicit finite-*NTU* model at various values of *NTU* with sufficient numerical resolution to negate numerical error along with the time step constraint in equation [6.3.23]. Numerical error is defined here as the discrepancy between predicted system performance at a given resolution and the system performance predicted if the number of nodes goes to infinity. Figure 6.18 shows the results of this simulation, indicating the error incurred by using the infinite-*NTU* model as a function of system *NTU*.

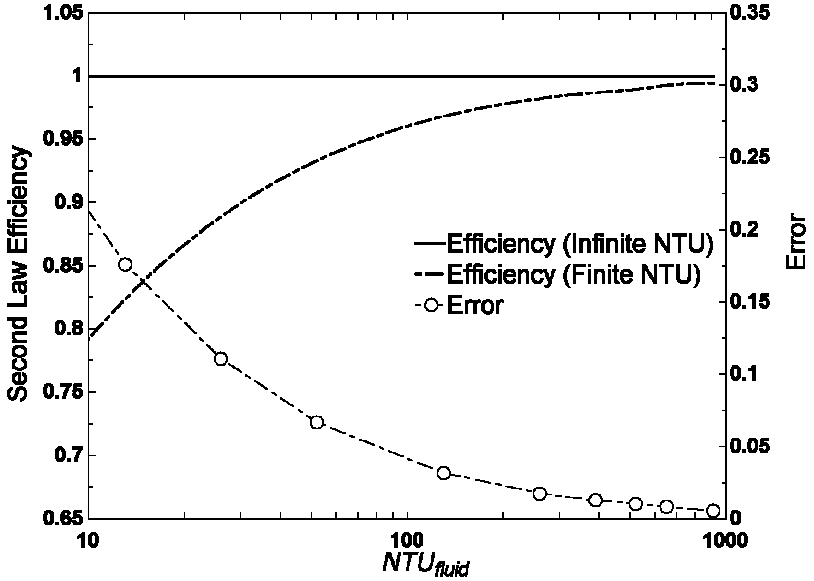

Figure 6.18: The performance of the infinite-NTU model relative to the simplified explicit model for various values of fluid NTU

For values of *NTU* > ~100 the error incurred by using the infinite-*NTU* model is less than ~3%. An *NTU* of 100 corresponds to h~25 W/m^2-K for the test conditions. By comparison, equation [6.3.12] and the Jeffreson correlation predict h~180 W/m^2-K and *NTU*~500 for the test conditions. For an *NTU* of 500 the infinite-*NTU* model imposes error of less than 1% indicating it would be appropriate for the test conditions. The test case represents a realistic storage design indicating that for most solar-thermal powerplant storage simulation the infinite-*NTU* model represents a valid assumption.

It is necessary to understand the relationship between mesh precision and solution accuracy. This relationship will determine the maximum speed (minimum mesh size) at which the models can be run while maintaining accuracy. Figure 6.19 shows cyclic

steady-state second law efficiency for the implicit and infinite-*NTU* models for a system with *NTU*~500. In this case both the Infinite-*NTU* and implicit models have less than ~3% error with meshes as coarse as 100 Nodes. Note that the infinite-*NTU* model converges at nearly zero error indicating at *NTU*~500 the infinite-*NTU* assumption is an excellent approximation. The explicit model results are not included in Figure 6.18 because of stability issues encountered at relatively fine mesh sizes for the test conditions.

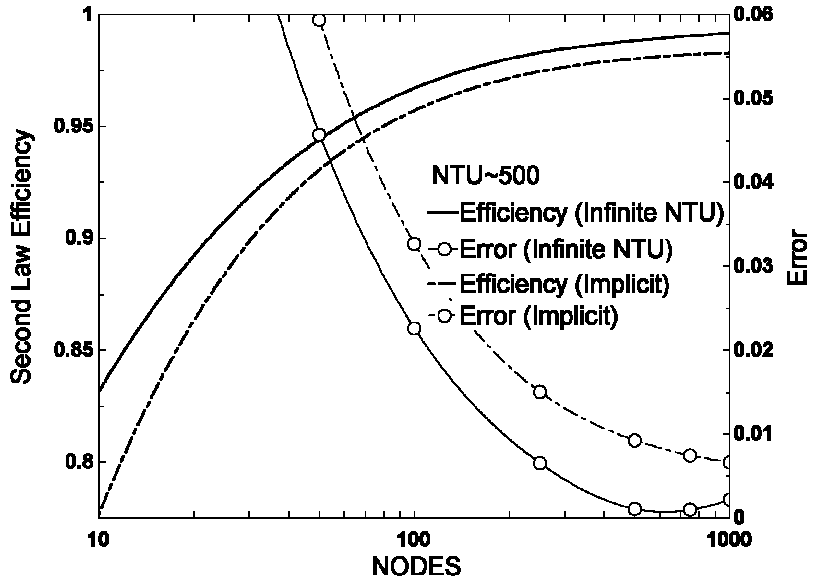

Figure 6.19: Model accuracy sensitivity to node count for a large *NTU* system (*NTU*~500)

While the implicit model and infinite-*NTU* models return results of comparable accuracy, the implicit model comes with a significantly larger computational cost. If the explicit model remains stable it returns very accurate results, but its stability requires very fine meshes and corresponding computation time. The stability requirements of the simplified explicit model incur too large a time penalty for it to be considered further for long-term simulation.

Figure 6.20 shows a case analogous to Figure 6.19 but with a lower *NTU* value of 100. In this case the performance of the implicit model is virtually the same as the *NTU*~500 case, with error approaching zero as the mesh size increases. The error of the infinite-*NTU* model decreases as the node count decreases, it then becomes large as the node

count becomes small. The behavior is explained by Figure 6.16. As the node count decreases the infinite-*NTU* model approaches, and then passes through, the actual solution. The amount of error incurred as the infinite-NTU model converges depends on the value of NTU_{fluid} for the system. As NTU_{fluid} becomes smaller the error incurred at convergence becomes larger.

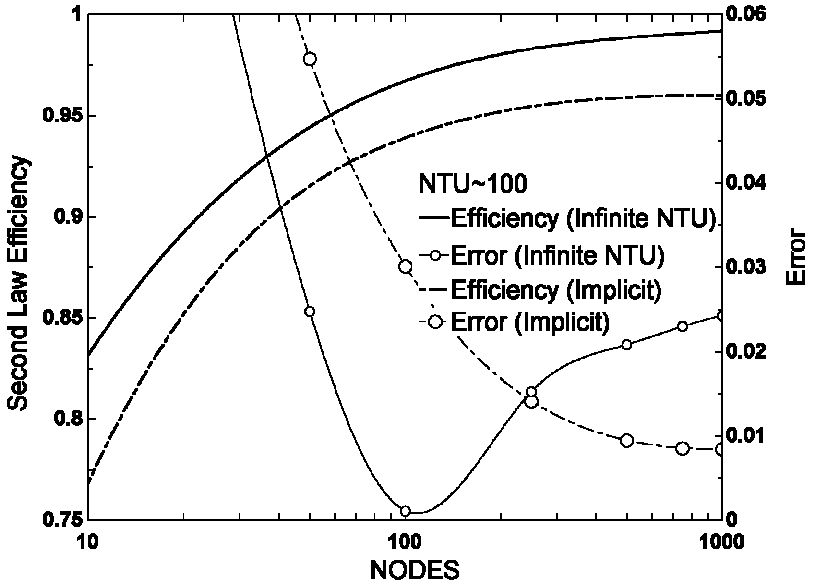

Figure 6.20: Model accuracy sensitivity to node count for a large NTU system (NTU~100)

For systems *NTU*>~100 the infinite-*NTU* or implicit models are both viable choices. The infinite-*NTU* model has the obvious computational advantage, while the implicit model guarantees accuracy as the node count becomes large. Despite the low-*NTU* value of the system the error at convergence for the infinite-*NTU* model is relatively small, 2.5%. In general, systems with a low *NTU* (*NTU*<~100) should be simulated with the implicit model for its more predictable error.

Computation time is proportional to the number of nodes since the time step is also fixed by the number of nodes according to equation [6.3.23]. Table 6.3 shows the relative computation time required for the implicit and infinite-*NTU* models. The simplified explicit model is not included because, as previously discussed, its stability requirements necessitate the use of many more nodes for simulation than the infinite-*NTU* or implicit models.

Table 6.3 Relative solution times for each numerical model

Model	Relative Time
Infinite-NTU	1
Implicit	2.9

Numerical Model Performance: Variable Input Simulation

Cyclic steady-state Second-Law efficiency computing with constant forcing functions is a consistent means for evaluating numerical model performance. It does not, however, accurately reflect the conditions under which the numerical models will be used in predicting the performance of storage systems used in solar-thermal power systems. Variation in solar radiation levels, power cycle performance and storage system operating strategies will result in varying storage system inputs. In this section model accuracy is quantified in the context of a "typical" long-term simulation using weather data as the forcing function.

For the cyclic steady-state case, the error incurred by the infinite-*NTU* and implicit models was less than 3% for numerical meshes as coarse as 100 nodes.

To better evaluate storage model performance under variable conditions, the infinite-*NTU* and implicit numerical models were tested for 30 day operating periods in TRNSYS with a full charge-discharge cycle occurring diurnally with varying numbers of nodes. The charge times were roughly analogous to those used in the previous cyclic steady-state tests. The solar field model, developed by Patnode [2006], was set to deliver fluid at constant temperature and variable flow rate throughout the day using weather data for July in Daggett, CA as input. During hours with sufficient solar radiation for the solar field to achieve the specified outlet temperature (400ºC), the storage tank was charged. During hours with insufficient solar radiation for the solar field to operate, the storage system discharged until empty to a model of the SEGS VI steam Rankine power cycle [Patnode, 2006]. These tests were again performed with each model for two cases, a "large-*NTU*" (*NTU*~500) tank and a "small-*NTU*" (*NTU*~100) tank.

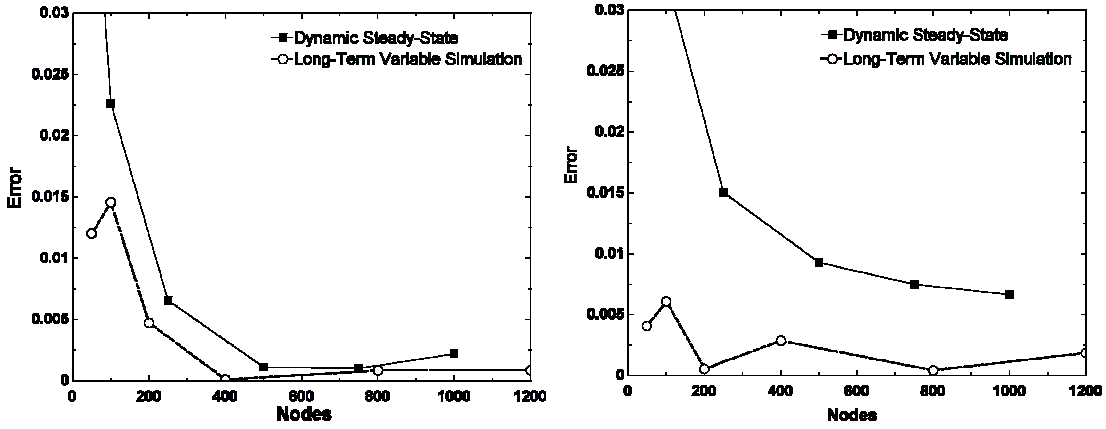

(a) (b)

Figure 6.21: Error comparison between dynamic steady-state testing and variable data driven simulation for the NTU~500 case. (a) Implicit Model (b) Infinite-NTU model

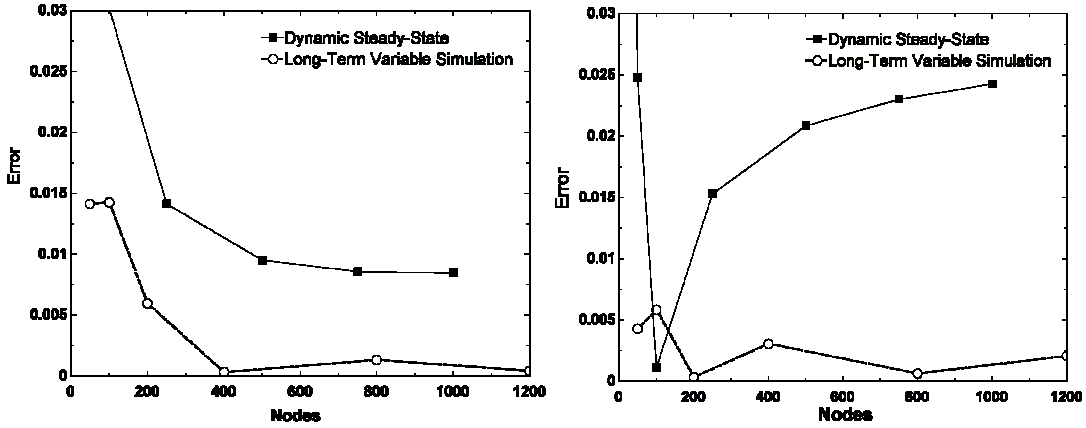

(a) (b)

Figure 6.22: Error comparison between dynamic steady-state testing and variable data driven simulation for the NTU~100 case. (a) Implicit Model (b) Infinite-NTU model

Figures 6.21 and 6.22 show the results of these tests with the absolute error, in terms of total power cycle output, plotted as a function of mesh size. Also shown are the errors in second-law efficiency incurred during the previously performed cyclic steady-state experiments. With both models, the variable input simulation produces significantly less error (defined for the variable-input test in terms of integrated power cycle output) at a given mesh size than the dynamic steady-state test (with error defined in terms of second-law efficiency). The lone exception to this trend is shown in Figure 6.22(b) where the dynamic steady-state error dips below the variable value with the infinite-*NTU* model. This point results from an artifact of the infinite-*NTU* model showing that as its mesh becomes coarser it approaches, and then passes through the real solution, as seen in

Figure 6.16.

These results indicate that the overall significance of numerical error is reduced when considering an entire solar powerplant utilizing thermal storage and realistically varying inputs.

Error Incurred by Neglecting Fluid Capacitance

As mentioned in section 6.3.3, it is common in the modeling of packed bed heat transfer to neglect the thermal capacitance of the fluid [Nellis and Klein, 2006]. A large number of packed bed applications discussed in the literature involve a gaseous fluid whose thermal capacitance is insignificant relative to the bed material. In these cases, neglecting fluid capacitance is a good assumption. However, the fluid storage media under consideration for solar power applications have heat capacities and densities on the same order as the solid material. The fluid then makes a non-trivial contribution to the total system capacitance (typically R=0.3-0.6). It has been shown for other applications of similar systems that inappropriately neglecting fluid capacitance can lead to significant underestimates of system performance [Nellis and Klein, 2006].

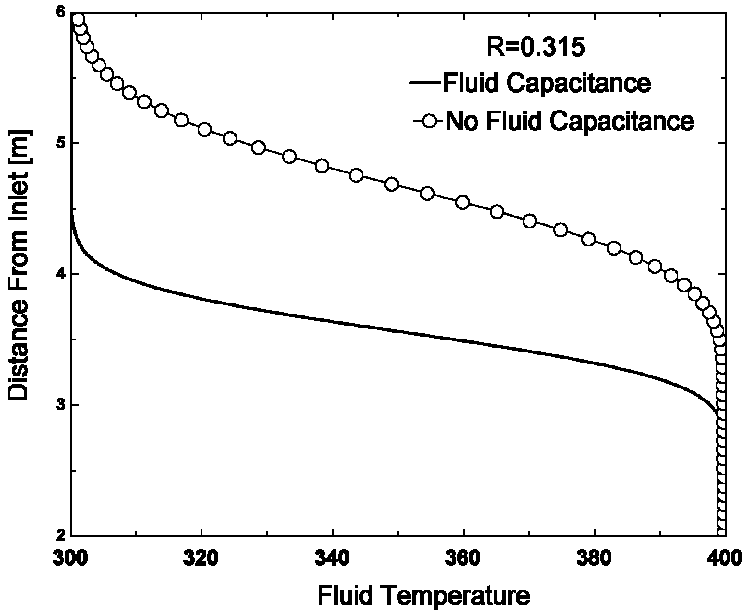

Figure 6.23: Fluid temperature profiles for the test case using the Schumann model and the no-capacitance model

Figure 6.23 shows a comparison between the analytical Schumann solution (which considers fluid capacitance) and the numerical solution for the test conditions which fully neglects fluid capacitance (*R=0.32*). The no-capacitance model diverges significantly from the Schumann solution. More importantly, it predicts a more poorly defined thermocline which is associated with reduced storage system performance.

Diverging from the Schumann solution over a single charge cycle is not sufficient to condemn the no-capacitance assumption for long-term simulation since the errors in the model may cancel over an extended operation time. To investigate this possibility, the previously described 20-cycle second law efficiency simulation was performed with the no-capacitance model. Figure 6.24 shows the results of this simulation, analogous to Figure 6.18 but also showing the error incurred from using the infinite-*NTU* model. The no-capacitance model underestimates system efficiency, as predicted by observing the more poorly defined thermocline. This result is also consistent with the results obtained by Nellis and Klein for magnetic refrigeration regenerators [2006]. The TRNSYS TYPE 10 Rock Bed model employs the no-capacitance assumption and is subject to the errors incurred when attempting to simulate high *R*-value systems.

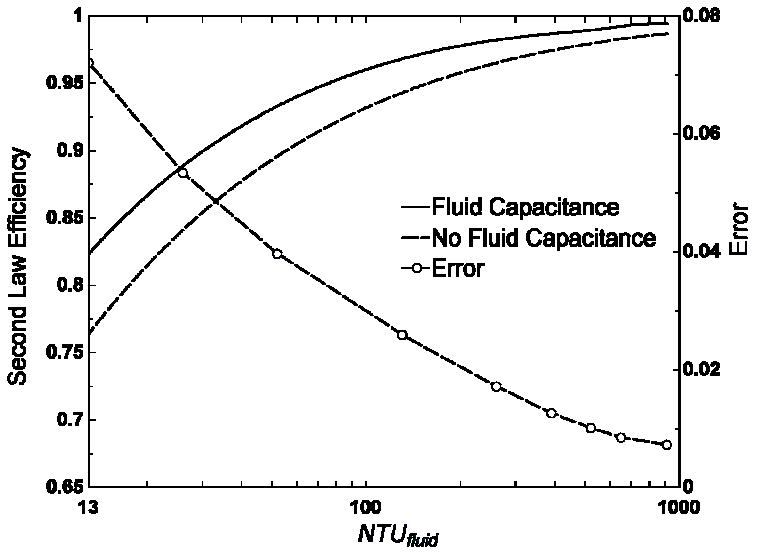

Figure 6.24: Second law storage system efficiency as a function of fluid NTU for the models that include and neglect the capacitance of the fluid.

The error associated with the no-capacitance model decreases with fluid *NTU* because second law efficiency asymptotes at one for both models. It is tempting to conclude that considering thermal capacitance is not important for large-*NTU* systems. While the second-law efficiency does approach one in both cases, neglecting fluid capacitance will result in an incorrect estimate of system capacity (as seen by the over-estimated thermocline penetration). If simulations are run where the full-capacity of the storage system is utilized, the failure to consider fluid capacitance in the numerical model will induce additional error.

The error calculated from figure 6.24 is for the test system, $R=0.315$. Since the no-capacitance and Schumann models converge as $R \rightarrow 0$ it is reasonable to presume that as R gets larger the accuracy penalty will increase and R values greater than 0.5 are likely with molten-salt based storage systems. It is sufficient for this thesis to recognize that the errors associated with neglecting thermal capacitance can be large for large R-value systems.

Rather than develop new models, some existing models that neglect fluid capacitance have been augmented for use with thermal storage systems [Kolb and Hassani, 2006]. Kolb and Hassani [2006] used the TRNSYS type 10 packed-bed heat transfer model [Klein et al, 2006] which neglects fluid thermal capacitance and makes the infinite-*NTU* assumption, to simulate a thermal storage system for a solar power application. The fluid capacitance was accommodated by adding it to the solid capacitance, which is considered. Figure 6.25 shows the results of this "combined-capacitance" augmentation for both the finite-*NTU* and infinite-*NTU* case. Each plot of Figure 6.25 shows temperature profiles for the case where fluid capacitance is considered independently of solid capacitance, and the case where fluid capacitance is neglected then combined with solid capacitance. In the finite-*NTU* case the combined-capacitance assumption corrects the penetration depth (storage capacity) error seen in Figure 6.23, but still incorrectly predicts the shape of the thermocline. In the limiting infinite-*NTU* case storage capacity is again correctly predicted and the thermocline slope error has been removed. Thus, for

a system where the limiting infinite-*NTU* assumption is appropriate using the combined-capacitance augmentation with models that neglect fluid capacitance yields accurate results.

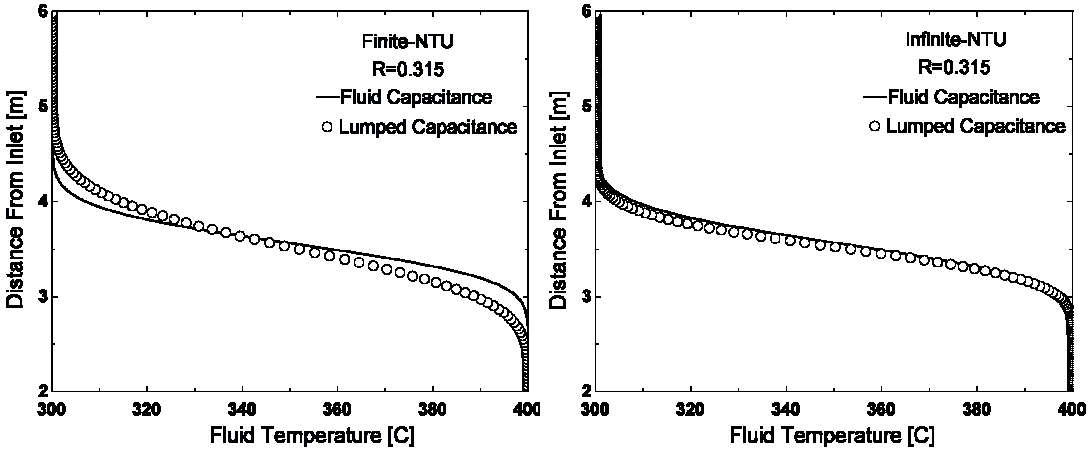

Figure 6.25: The result of augmenting models that neglect fluid capacitance by lumping fluid capacitance in with solid capacitance in the finite-*NTU* and infinite-*NTU* cases.

6.3.5 Comparison with Data from Solar One

The numerical models developed in the section 6.3.3 are one-dimensional and simplified using engineering judgment in order to meet the computational demands of long-term simulation. It is of interest how well the simplified models correspond to reality. In this section test data from a packed-bed storage tank are compared with the numerical models.

A packed-bed storage tank, with a capacity of 187MWh$_{th}$, was built for the Solar One central receiver concentrating solar powerplant in the early 1980's [Faas, 1986]. The Solar One storage system was designed to store sufficient thermal energy to run the power cycle at full load, 7 MW$_e$, for a period of 4 hours. The solid material used in the tank was rock and sand yielding an average void fraction measured as ε=0.23 [Faas, 1986]. Caloria™ HT-43 was the heat transfer fluid. Figure 6.26 shows a schematic of the system [Faas, 1986].

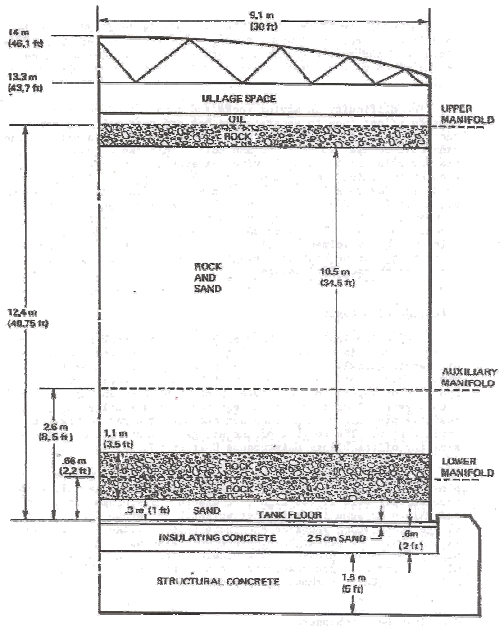

Figure 6.26: Schematic of the rock-sand packed thermocline installed at Solar One.

The storage system was put through a series of tests before it went into regular operation [Faas, 1986]. These tests included a low flow-rate discharge test [MDAC, 1986]. Available data include tank temperature profiles at the start of the test as well as two subsequent profiles after 4 and 8 hours of discharging. Fluid flow rate data are also available. However, based on a heat exchanger energy balance the investigators concluded that the Caloria™ flow rate data was over-stated by 15%-25% [MDAC, 1986].

Figures 6.27 through 6.30 compare the Solar One discharge data with the numerical models described in section 6.3.3.

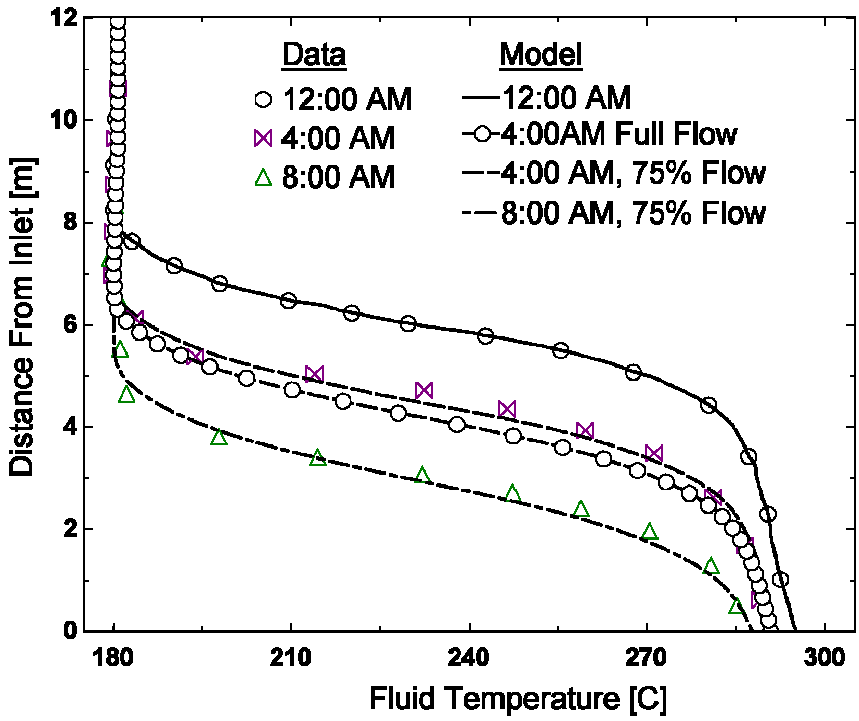

Figure 6.27: Comparison of the implicit model with the Solar One discharge test data.

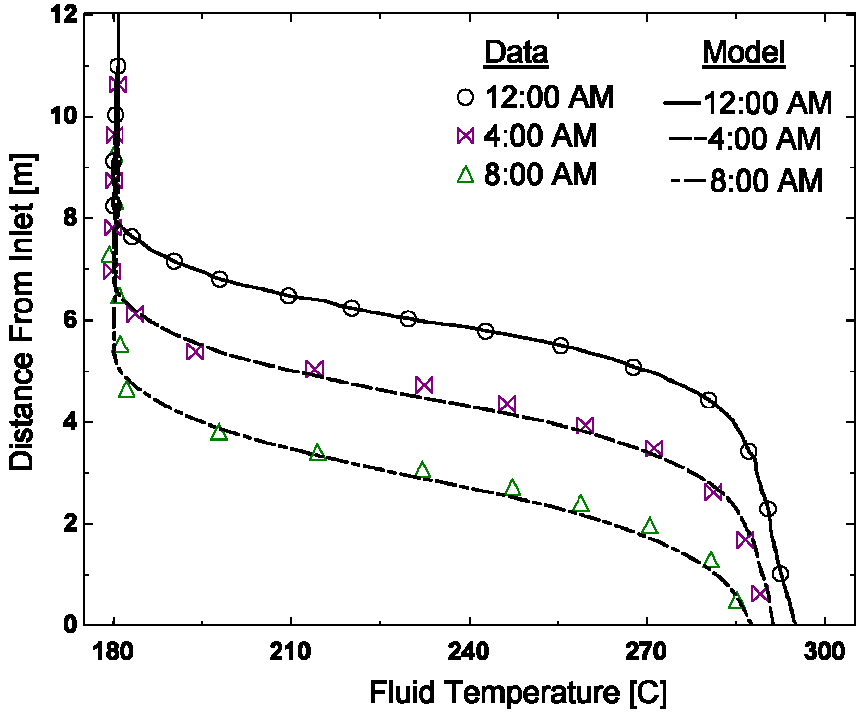

Figure 6.28: Comparison of the infinite-NTU model with Solar One discharge test data.

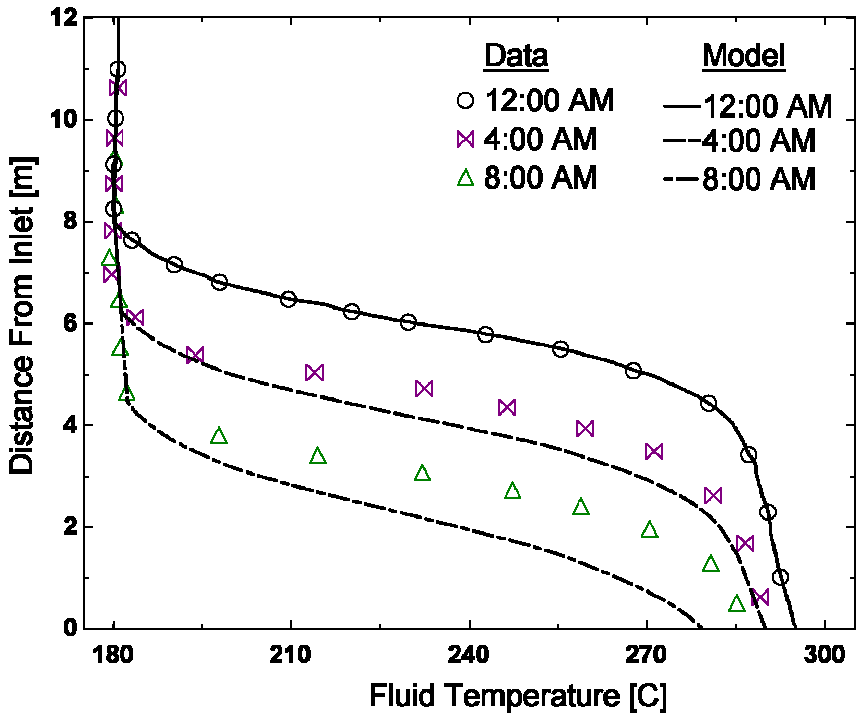

Figure 6.29: Comparison of the infinite-NTU model that neglects fluid thermal capacitance (TRNSYS Type10) with Solar One discharge test data.

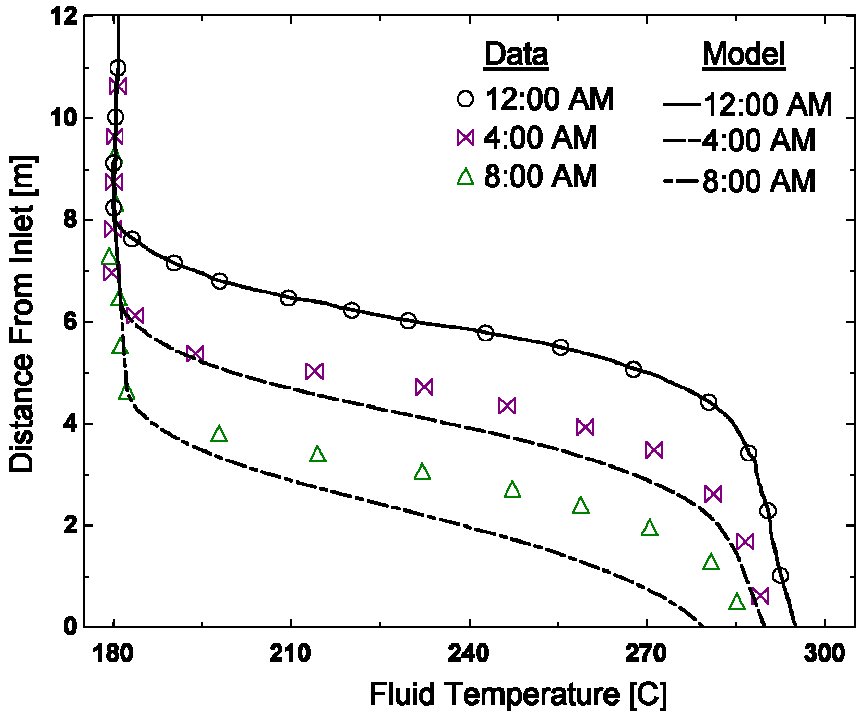

Figure 6.30: Comparison of the explicit model (finite-NTU) that neglects fluid thermal capacitance with the Solar One discharge test data.

Figure 6.27 shows both the measured flow rate and estimated flow rate from the report. The implicit model does an excellent job of matching both the slope and penetration depth of the Solar One data using the investigator's estimated fluid flow rate. The agreement is not as good using the direct flow meter values, but again these values are believed to be 25% high according to the investigators [MDAC, 1986]. Figures 6.28 through 6.30 show only the results for the estimated flow rate.

The infinite-*NTU*, as with the implicit model, predicts the Solar One data very well. The accuracy of the infinite-*NTU* model in this case is due to the extremely high *NTU* value of this system, resulting from the tremendous amount of heat transfer surface area provided by the rock-sand bed. NTU_{fluid} is also enhanced by relatively low fluid mass flow rate. The excellent performance of the infinite-*NTU* model in this discharge test aides the confirmation of the assumption that realistic thermal storage systems will have large values of NTU_{fluid}. The inherent computational advantages of the infinite-*NTU* model make it the preferred default for the long-term simulation for packed-bed stratified storage systems, like the one built for Solar One. Recall that using the combined fluid-solid capacitance augmentation to the model that neglects fluid capacitance along with the infinite-*NTU* assumption yields results equivalent to the full infinite-*NTU* model that considers fluid capacitance.

Figures 6.29 and 6.30 show how both the explicit and infinite-*NTU* models perform when neglecting the thermal capacitance of the fluid (and *without* making the combined capacitance augmentation). As discussed in section 6.3.4, the failure to consider the thermal capacitance of the fluid results in an overestimate of both the penetration and slope of the thermocline. The net effect is an underestimate of system thermal storage capacity and performance.

Comparison with the Solar One discharge data shows that neglecting axial conduction, viscous dissipation and tank shell losses in the numerical models were well-founded assumptions. These observations support the selection of the Schumann model (equations [6.3.2] and [6.3.3]) with the infinite-*NTU* assumption for simulating the

behavior of packed-bed storage systems during charging and discharging.

6.3.6 Long-Term Storage Modeling

The model developed in section 6.3.1, the Schumann model, neglects axial conduction and losses to the environment. Neglecting those effects was appropriate for a packed-bed tank during charging or discharging operation as the convective energy transport between the flowing fluid and solid dominates all other energy transfer mechanisms. These assumptions were further confirmed when model predictions were compared with data from Solar One. These same assumptions, however, become inappropriate if the storage tank lies idle (no fluid flow) for long periods of time. In the absence of the dominant fluid energy flow, axial conduction and losses to the surroundings must be considered. In this section a second storage system model is developed for use during long storage system idle periods.

Both modeling predictions and data from Solar One suggest that the infinite-*NTU* assumption is appropriate for packed-bed thermal storage systems. Recognizing the dominance of the fluid-solid interaction in the charge-discharge case invites the treatment of the fluid-solid mass as a continuous medium during idle periods. The validity of this assumption can be considered in terms of resistances to heat transfer. The relevant resistances are: convection between fluid and solid, axial conduction through the tank, and losses to the surroundings.

$$R_{f-s} = \frac{1}{(2k_f / d_p)A_{total}} \qquad [6.3.41]$$

$$R_{axial\,conduction} = \frac{L}{k_{eff} A_c} \qquad [6.3.42]$$

$$R_{losses} = \frac{1}{h_{loss,w}A_w + h_{loss,bot}A_{bot} + h_{loss,top}A_{top}} \qquad [6.3.43]$$

where R_{losses} includes losses from the walls, top and bottom of the tank. The individual loss coefficients were estimated at 1 W/m^2-K (for typical system losses see section 6.3.7). $R_{axial\,conduction}$ is computing using the effective packed-bed thermal conductivity calculated

in section 6.3.1. $R_{f\text{-}s}$ is based on a Nusselt number of two, the no-flow limit in equation [6.3.12]. The magnitude of axial conduction and environmental losses compared with fluid-solid convection is evaluated in the following ratios:

$$r_{axial} = \frac{R_{f-s}}{R_{axial\,conduction}} \qquad [6.3.44]$$

$$r_{loss} = \frac{R_{f-s}}{R_{losses}} \qquad [6.3.45]$$

For the test conditions (section 6.3.1) r_{axial} and r_{loss} were both computed to be less than 0.001 indicating that in the absence of fluid flow, fluid-solid interaction still dominates axial conduction and losses to the surroundings. It is then appropriate to treat the fluid-solid tank as a continuous medium for the simulation of an idle storage tank.

The consideration of convective losses, absent in the charge-discharge case, introduces a modeling dilemma. For the charge/discharge models, temperature gradients in the radial direction of the tank are not an issue as the fluid is presumed to be introduced uniformly (in temperature and flow) across the cross-section of the bed and shell losses were ignored. When considering convective losses, the relatively low effective conductivity in the bed will likely introduce temperature gradients in the radial direction (from the core of the tank to the wall). The significance of these temperature gradients is usually considered by examining the Biot number. The Biot number represents the ratio of resistance to conductive heat transfer from the core of the tank to the wall and the resistance to convective heat transfer from the tank's surface. It is defined for this case as follows:

$$Bi = \frac{R_{conduction}}{R_{convection}} = \frac{h_{loss,w} r_{tank}}{k_{eff}} \qquad [6.3.46]$$

Traditionally temperature gradients are negligible if the Biot number is less than 0.1, for the test case the Biot number for radial temperature gradients is well above this threshold (>1.0). Generally, the radial temperature gradient would be accommodated by expanding the heat transfer model to two dimensions. However, the computational requirements of long-term simulations are a 2-dimensional heat transfer model is not practical. In order to approximate the impact of the radial temperature gradients while retaining

computational efficiency, the Jeffreson correlation [1972] (described in section 6.3.1) can be applied to the model wall loss parameter.

Model Description

Figure 6.31 shows the lumped fluid-solid differential control volume describing the no-flow long-term storage operating condition with associated assumptions:

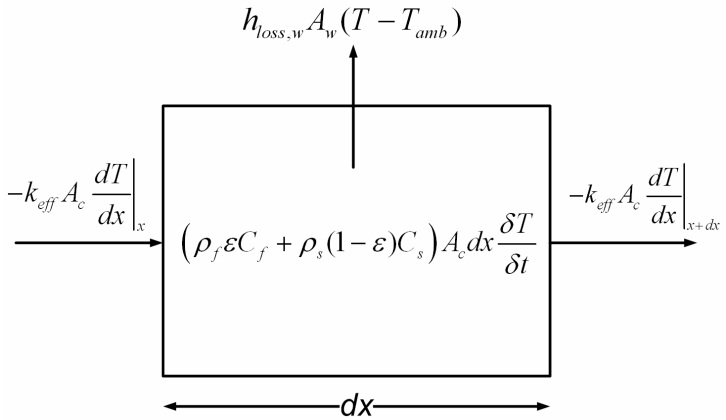

Figure 6.31: Differential control volume for the long-term simulation of packed-bed stratified storage systems

The governing partial differential equation that corresponds to Figure 6.30 is:

$$(\rho_f\varepsilon C_f+\rho_s(1-\varepsilon)C_s)A_c\frac{dT}{dt}=k_{eff}A_c\frac{\partial^2 T}{\partial x^2}-h_{loss,w}A_w(T-T_{amb}) \qquad [6.3.47]$$

with the following boundary conditions:

$$-k_{eff}A_c\left.\frac{dT}{dx}\right|_{x=0}=h_{loss,top}A_{top}(T|_{x=o}-T_{amb}) \qquad [6.3.48]$$

$$-k_{eff}A_c\left.\frac{dT}{dx}\right|_{x=L}=h_{loss,bot}A_{bot}(T|_{x=L}-T_{amb}) \qquad [6.3.49]$$

To solve equation [6.3.47] numerically the storage tank is divided into a one-dimensional numerical grid shown in Figure 6.32.

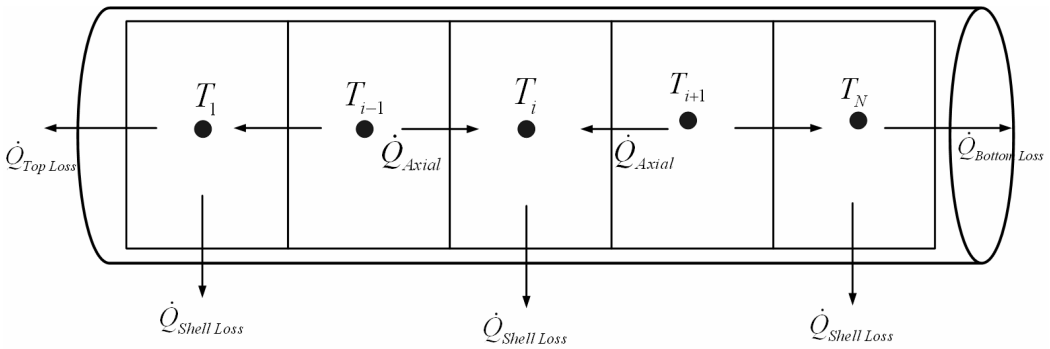

Figure 6.32: Numerical grid used for the long-term simulation of packed-bed stratified storage systems

For convenience a total nodal thermal capacitance is defined as follows:

$$(mC)_T = \left(\rho_f C_f \varepsilon + \rho_s C_s (1-\varepsilon)\right) A_c \Delta x \qquad [6.3.50]$$

Fluid specific heat and thermal conductivity are computed at every node as functions of temperature, as with the charge/discharge models. Fluid-solid mass in each node are assumed to be constant for the duration of the simulation period.

Equation [6.3.47] is discretized implicitly for all internal tank nodes:

$$(mC)_T \left[\frac{T_{i,t+\Delta t} - T_{i,t}}{\Delta t}\right] = \frac{k_{eff} A_c}{\Delta x}\left(T_{i-1,t+\Delta t} - T_{i,t+\Delta t}\right) + \frac{k_{eff} A_c}{\Delta x}\left(T_{i+1,t+\Delta t} - T_{i,t+\Delta t}\right) - h_{loss,w} A_w (T_{i,t+\Delta t} - T_{amb}) \qquad [6.3.51]$$

Likewise for the bottom of the tank:

$$(mC)_T \left[\frac{T_{n,t+\Delta t} - T_{n,t}}{\Delta t}\right] = \frac{k_{eff} A_c}{\Delta x}\left(T_{n-1,t+\Delta t} - T_{n,t+\Delta t}\right) - h_{loss,w} A_w (T_{n,t+\Delta t} - T_{amb}) - h_{loss,bot} A_{bot} (T_{n,t+\Delta t} - T_{amb}) \qquad [6.3.52]$$

And for the top of the tank:

$$(mC)_T \left[\frac{T_{1,t+\Delta t} - T_{1,t}}{\Delta t}\right] = \frac{k_{eff} A_c}{\Delta x}\left(T_{2,t+\Delta t} - T_{1,t+\Delta t}\right) - h_{loss,w} A_w (T_{1,t+\Delta t} - T_{amb}) - h_{loss,top} A_{top} (T_{1,t+\Delta t} - T_{amb}) \qquad [6.3.53]$$

Equations [6.3.51] through [6.3.53] form a tri-diagonal system of equations of the form $Ax=B$ where A has the dimensions NxN and B is $Nx1$. The system of equations is solved at each time step and then integrated forward in time.

6.3.7 Comparison with Data from Solar One

During the experiments performed on the Solar One packed-bed storage tank (section 6.3.5) an idle tank cool-down test was performed. The investigators reported an overall resistance to heat loss of 2474ºC/MW with an average ambient temperature of 12ºC. These values were obtained for a discharge test which lasted ~16.5 days (382.5 hours) [Faas, 1986]. Only the overall resistance to heat loss is available, and no specific consideration was made for specific regions (top, sides, and bottom). In addition to the overall heat loss coefficient, temperature profiles were recorded at the beginning and end of the test, shown in Figure 6.33.

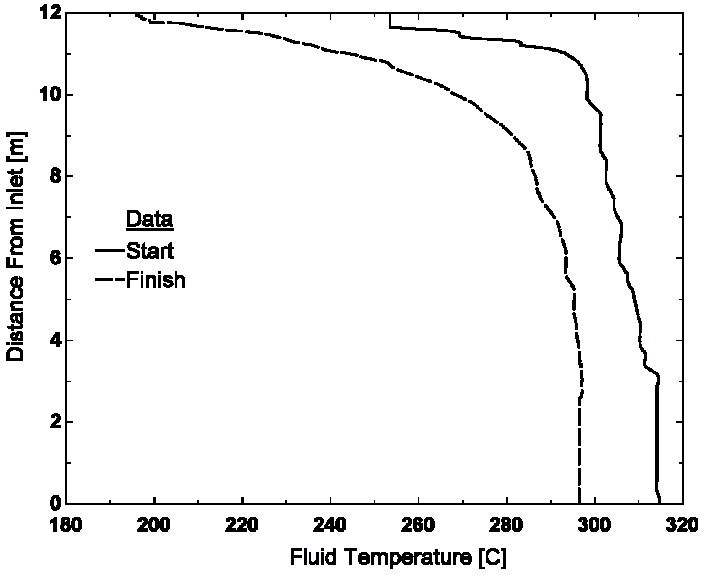

Figure 6.33: Temperature profiles in the Solar One storage tank before and after the "cool-down" test performed in 1983.

The data available from the Solar One cool-down test are not alone sufficient to constrain the model presented in the previous section. To enhance flexibility, the model requires separate loss coefficients for the walls, top and bottom. By the resistance analogy this allows the following constraint to be imposed on the long-term storage model:

$$\sum R_{Loss} = 2474\left[\frac{^\circ C}{MW}\right] = \frac{1}{h_{loss,w}A_w + h_{loss,top}A_{top} + h_{loss,bot}A_{bot}} \qquad [6.3.54]$$

The Jeffreson correlation is not used in this case to modify $h_{loss,w}$ as suggested in the previous section because the overall loss coefficient in this case was calculated in terms

of packed-bed temperature data taken from within the tank rather than the surface.

Examination of Figure 6.32 indicates that losses from the bottom of the tank are much more significant than from the top, as evident by the increase in temperature change from the top of the tank to the bottom. Considering the significant airspace at the top of tank, acting as insulation shown in Figure 6.26, this observation is not unreasonable. The constraint of equation [6.3.54] in combination with the fact that $h_{loss,top} << h_{loss,bot}$ was used to select approximate loss coefficients for the numerical model. Fluid property data for Caloria™ HT-43 are available and were used in this simulation. Properties of the rock-sand mixture at Solar One, particularly thermal conductivity, are more difficult to determine. Typical solid rock thermal conductivities are in the range of 2-5 W/m-K, with the majority of species favoring the lower bound [Incropera, 2005]. There was no specific information on the type of rock used in the Solar One system. As an approximation an "average" rock-sand thermal conductivity of 2.5 W/m-K was used for simulation of the Solar One cool-down test. Using the numerical model described in the previous section, Figure 6.34 was generated using the parameters appearing in Table 6.4.

Table 6.4 Long-term storage model inputs

Variable	Value
ρ_f	700*
ρ_s	2643*
k_f	*f(T)*
k_s	2.5
C_f	*f(T)*
C_s	1000*
$h_{loss,w}$	0.350
$h_{loss,top}$	0.005
$h_{loss,bot}$	0.595

*Faas, 1986

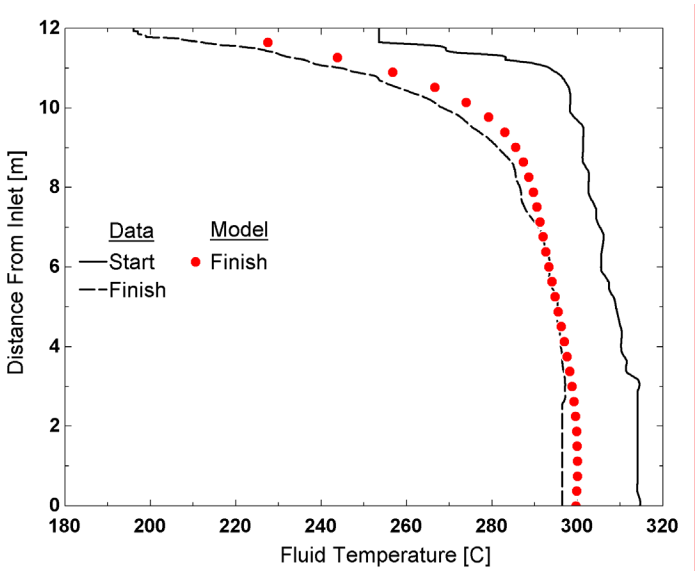

Figure 6.34: Comparison of numerical model and Solar One cool-down data.

The cool-down model shows good agreement with the data taken at Solar One. It is important to note that the data available from Solar One were not sufficient to provide well-defined boundary conditions for the model. However, the general compliance between the parameters of the cool-down model and the trends observed in the Solar One data instills confidence that the correct energy transfer mechanisms have been identified and accounted for in the model.

6.4 Summary and Conclusions

Long-term simulation of packed-bed storage systems necessitates the use of efficient modeling techniques. The one-dimensional Schumann model offers the best balance of accuracy and simplicity during charging and discharging.

Several numerical schemes are developed to solve the governing equations in the Schumann model. The infinite-*NTU* simplification offers the fastest solution and the added benefit of guaranteed solution stability. It is extremely accurate for storage systems with $NTU_{fluid}>500$. The implicit formulation of the solution offers the most accurate solution for any value of NTU_{fluid} at the cost of substantial computation time. Explicit schemes are not acceptable for long-term simulation due to significant stability

issues.

A model characterizing tank performance in the absence of fluid flow was developed for use with operating strategies that involve long-term idle periods.

Data from experiments performed on a packed-bed storage system built for the Solar One central receiver powerplant were compared with both the charging-discharging and heat-loss models. The numerical models performed well in both cases, indicating that appropriate simplifications were made during model development. The infinite-*NTU* assumption performed very well when compared to the Solar One data, indicating that real packed-bed storage systems will have very large values of *NTU*. This performance, in addition to the computational advantages of the infinite-*NTU* model makes it the ideal choice for long-term storage system simulation.

7 Storage System Analyses

Chapter 6 examined specific thermal-energy storage concepts, as well as their design and simulated performance. This chapter continues to examine thermal-energy storage but with a broader focus. Section 7.1 examines some of the unique design considerations associated with integrating an indirect storage system into a solar-thermal powerplant. Section 7.2 considers storage operating and control strategies derived from plant performance characteristics and utility pricing structures. Section 7.3 presents results of TRNSYS simulations that demonstrate application of some of the concepts discussed in sections 7.1 and 7.2.

7.1 Indirect Storage Design Considerations

Storage System Integration

There are a variety of ways in which an indirect storage system can be integrated into a solar-thermal powerplant. Because storage system integration affects powerplant performance, each option should be evaluated during the plant design phase. Figure 7.1 presents the two indirect storage arrangement schemes considered here. These arrangements are referred to as *fully-indirect* and *semi-indirect*. A fully-indirect storage

system is configured such that the solar field heat transfer fluid always provides thermal energy to the power cycle with an option to bypass fluid to/from the storage system. A semi-indirect storage system uses the storage fluid to deliver thermal energy to the power cycle.

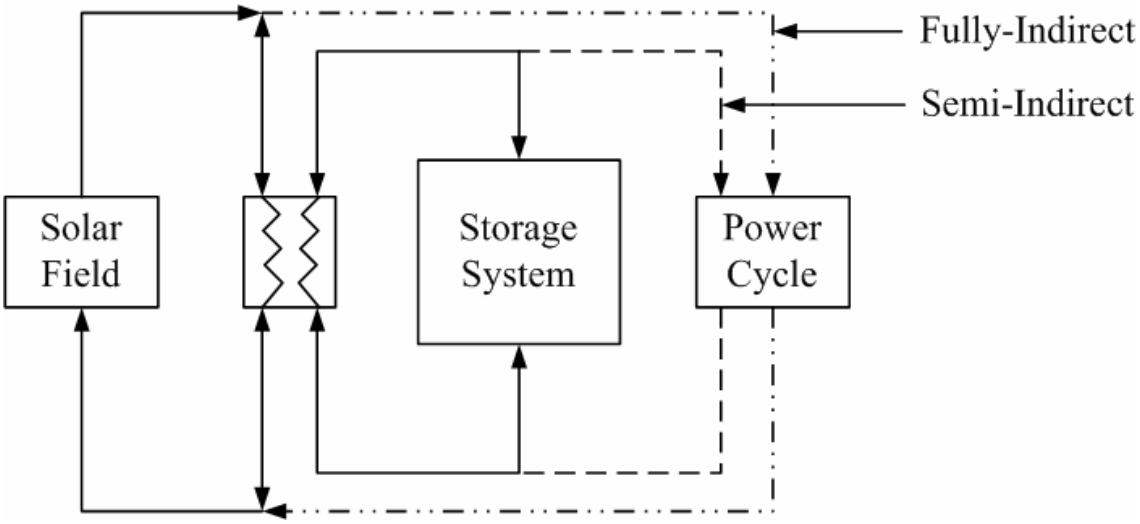

Figure 7.1: System flow configuration for semi-indirect and fully-indirect thermal energy storage.

The effect of indirect storage system integration is best understood by examining the heat exchanger that interfaces the storage and solar field fluid systems (shown in Figure 7.1). The use of a heat exchanger results in an availability destruction and thus reduced system efficiency. In the fully-indirect system, fluid passes through the heat exchanger during both charging and discharging, but not when the storage system is bypassed. Similarly, in the semi-indirect case fluid passes through the heat exchanger both during charging and during periods when the storage system is bypassed, but not during discharging. To quantify these effects on total system performance Second Law efficiency is considered for the storage system:

$$\eta_{2nd\,Law} = \frac{\sum m_{out}\psi_{out}}{\sum m_{in}\psi_{in}} \qquad [7.1.1]$$

where;

$$\psi = C(T - T_0) - T_0 C \cdot LN\left(\frac{T}{T_0}\right) \qquad [7.1.2]$$

$m_{out}\psi_{out}$ and $m_{in}\psi_{in}$ are the availability flows out of a in to the indirect storage system heat exchanger during a given mode of storage system operation. This efficiency definition conveniently captures availability destruction that occurs as a result of indirect storage system integration. Fluid specific heats are assumed constant, fluid was delivered from the solar field at 400ºC and cold stream inlet temperatures were assumed to be 300ºC (both from storage and from the power cycle). Mass flow rates are calculated such that the capacitance rates of both fluids are matched. Only heat exchanger irreversibilities are considered, the storage tank itself is "perfect."

Figures 7.2 and 7.3 show the results of applying equation [7.1.1] to fully-indirect storage and semi-indirect storage for both charge-discharge and storage bypass operation. Second law efficiency is displayed as a function of heat exchanger *NTU*. Semi-indirect storage provides better overall storage system performance during charge-discharge operation as the heat exchanger is utilized only once where fully-indirect storage must use the heat exchanger both while charging and discharging. Similarly, Fully-indirect storage provides better performance during storage bypass operation, as the heat exchanger is bypassed completely where the semi-indirect configuration still utilizes the heat exchanger once.

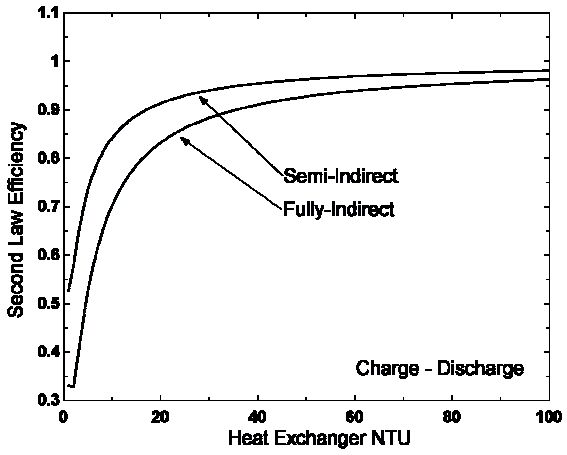

Figure 7.2: Net Second Law heat exchanger efficiency as a function of heat exchanger *NTU* for a charge cycle followed by a discharge cycle assuming perfect storage.

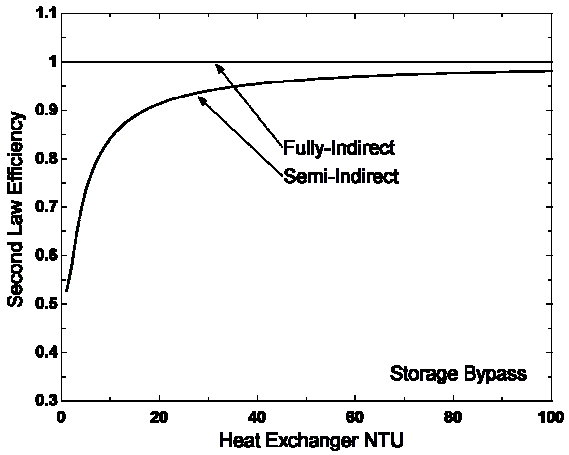

Figure 7.3: Net Second Law heat exchanger efficiency as a function of heat exchanger *NTU* when storage is bypassed in favor of power generation.

The fact that neither the fully-indirect or semi-indirect storage configuration is always more efficient implies that a compromise must be made during design. Requiring such a compromise assumes that it is not practical to have a power cycle which could receive thermal energy from both the heat transfer fluid and storage fluid. Were such a cycle possible, the better performing configuration could be utilized during both charge-discharge and bypass operation. Assuming again that either fully-indirect or semi-indirect storage are the only practical considerations, it follows that plant design must consider operating strategies when determining storage system integration.

Storage Fluid Selection – Pumping Loads

Indirect storage implies the presence of a secondary storage fluid and flow loop. As part of evaluating candidate storage fluids, it is essential to consider the parasitic pumping associated with them.

The parasitic load for a thermal storage system can be considered by comparing the pumping load relative to the amount of thermal energy stored. Consider R_{store}, the ratio of parasitic energy loss to energy stored:

$$R_{store} = \frac{\dot{E}_{parasitic}}{\dot{E}_{store}} \qquad [7.1.3]$$

where $\dot{E}_{parasitic}$ is the ideal pump work and $\dot{E}_{store}$ is the change in thermal energy of the

fluid as it passes through the storage loop:

$$\dot{E}_{parasitic} = \dot{m} v \Delta P = \dot{V}\left(f \frac{L}{D} \frac{\rho \vec{v}^2}{2} \right) \quad [7.1.4]$$

$$\dot{E}_{store} = \dot{m} C (\Delta T) \quad [7.1.5]$$

To formulate a simple and general metric for the comparison of storage fluids, laminar flow through a circular pipe is considered. In the case of laminar flow, the friction factor (*f*) associated with flow through a circular pipe is 64/Re. Making this substation into equation [7.1.4] allows R_{store} to be written:

$$R_{store} = \frac{128 \mu L \dot{m}}{\rho^2 \pi C \Delta T D^4} \quad [7.1.6]$$

When evaluating R_{store} fluid mass flow rate for a given rate of energy storage is determined using equation [7.1.5]. Pipe diameter and flow-loop length are then chosen based on system design criteria.

Figure 7.4 offers a comparison between several candidate storage fluids. Figure 7.4(a) shows the results for the case where diameter was chosen to achieve a uniform fluid velocity in the pipe for all fluids. Figure 7.4(b) shows R_{store} for the case where pipe diameter remained constant for all fluids. *L* was chosen to normalize results relative to Therminol®VP-1 ($R_{store}=1$). A storage system operating range of 300-400ºC was used in order to be indicative of current generation parabolic-trough systems using Therminol®VP-1 as the solar field heat transfer fluid. The molten salt storage fluids (Hitec XL, Nitrate Salt) analyzed showed pumping loads an order-of-magnitude larger than the thermal oils in the 300-400ºC temperature range. This characteristic of the molten salts in this temperature range should be considered when designing indirect storage systems for use in Therminol®VP-1 based parabolic trough power systems.

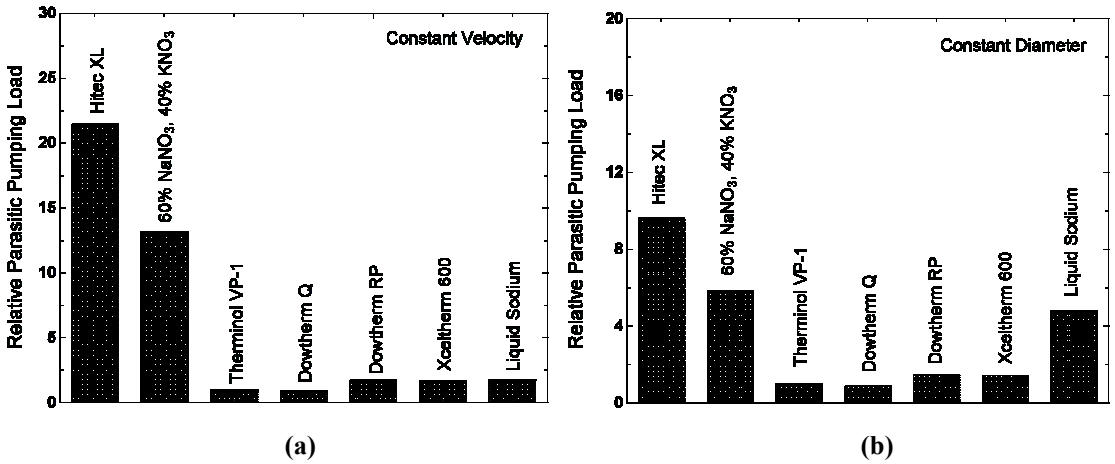

Figure 7.4: Relative parasitic pumping power per unit thermal energy stored over a 300ºC-400ºC storage temperature gradient. Results normalized to Therminol®VP-1 = 1.

Figure 7.5 shows that the storage pumping load relative to Therminol®VP-1 improves dramatically as storage system operating temperature increases because of the strong reduction in viscosity with increasing temperature. The parasitic loads associated with molten salts can be greatly reduced if they are maintained at high temperature.

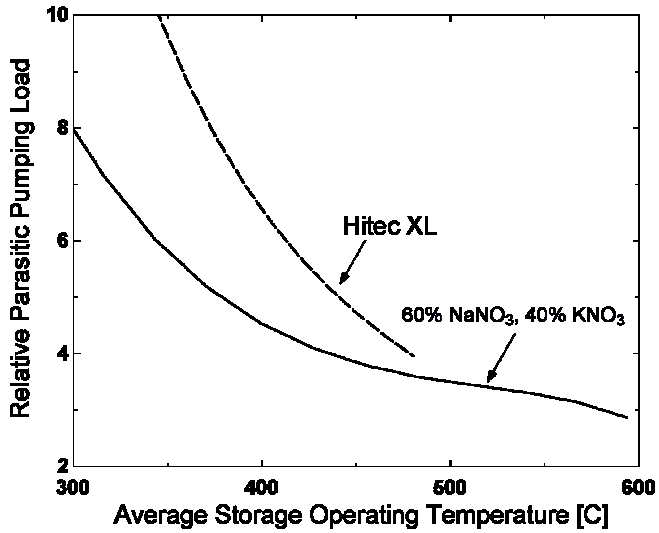

Figure 7.5: Decrease in relative parasitic pumping power with temperature for Hitec XL and Nitrate Salt.

7.2 Storage System Control and Operating Strategies

The presence of a thermal storage system in a solar powerplant requires operating and control strategies to dictate when and how the storage is used. Two storage system control and dispatch strategies are presented in this section. These strategies are derived with a specific focus on two utility pricing schemes. The pricing schemes are: variable and fixed-rate pricing. Note that these strategies are configured for daily charge-discharge cycles, no accommodation is made for potentially longer storage terms.

In the case of variable pricing the price the utility is willing to pay for electricity delivered to the grid varies through the day. In this case, it is desirable to maximize plant output during the period when electricity has the most value. Storage can be a strategic asset in this situation as the plant's production peak is often separated by several hours from the price peak. Figure 7.6 shows sample average real-time pricing data for a summer day in California [Reindl, 2006] compared to average summer insolation from Dagget California [Patnode, 2006].

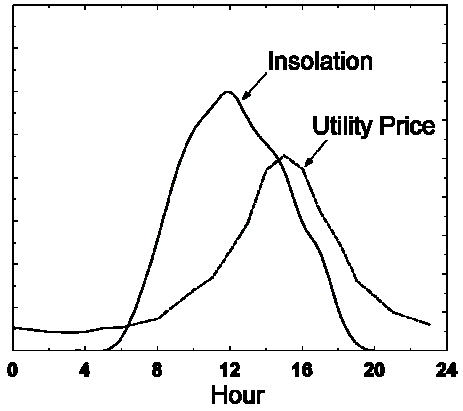

Figure 7.6: Typical time-shift between utility peak rate periods and peak solar insolation in California.

The operating strategy derived based on a fixed-price paid for electricity is different than the variable price case. In the fixed-price case it is desirable to maximize the total electricity output of the system. This can be accomplished by using storage to maintain powerplant operation at its maximum efficiency point. Storage would be used to both maintain the design input to the powerplant during low-insolation periods, and extend the

operation of the powerplant into the evening.

Figure 7.7 and Figure 7.8 show the basic structure of both control strategies. They are both dispatched based on the input from the solar field. If there is positive heat transfer fluid flow from the solar field and it meets some defined temperature specification for storing thermal energy (e.g. T=400ºC) the system enters "charge mode." If this temperature requirement is not met, the system is controlled to enter "discharge mode." Discharge mode is the same for both control strategies, wherein the tank is discharged at some specified rate (by supplying thermal energy to the powerplant) until its charge has been exhausted. It is during "charge mode" that system operation is different for the two control strategies.

In variable-price mode there is a defined "peak" window of time where the price for electricity is high. This strategy is built around focusing plant output during the peak period. During peak periods all resources (solar field flow and storage) are simultaneously focused on power generation by maximizing the fluid delivery rate to the power cycle. During off-peak periods the plant shuts down and all available solar field flow is used to charge storage in anticipation of the peak period. Referring to Figure 7.6, this strategy generally requires storage of thermal energy during the morning hours and then operating the power cycle at peak capacity during the afternoon using a combination of storage discharge and fluid delivered by the solar field.

In fixed-rate mode, storage discharge control is designed to maintain power cycle operation at its maximum efficiency point (constant output). Constant output is achieved by delivering a fixed rate of heat transfer fluid to the power cycle by selectively charging and discharging storage depending on the rate at which heat transfer fluid is provided from the solar field. Heat transfer fluid delivered from the solar field in excess of the requirement of the power cycle is stored. Storage is discharged when heat transfer fluid delivered from the solar field is insufficient to meet the power cycle's demands.

Further details of control strategy implementation are presented in Appendices B and C.

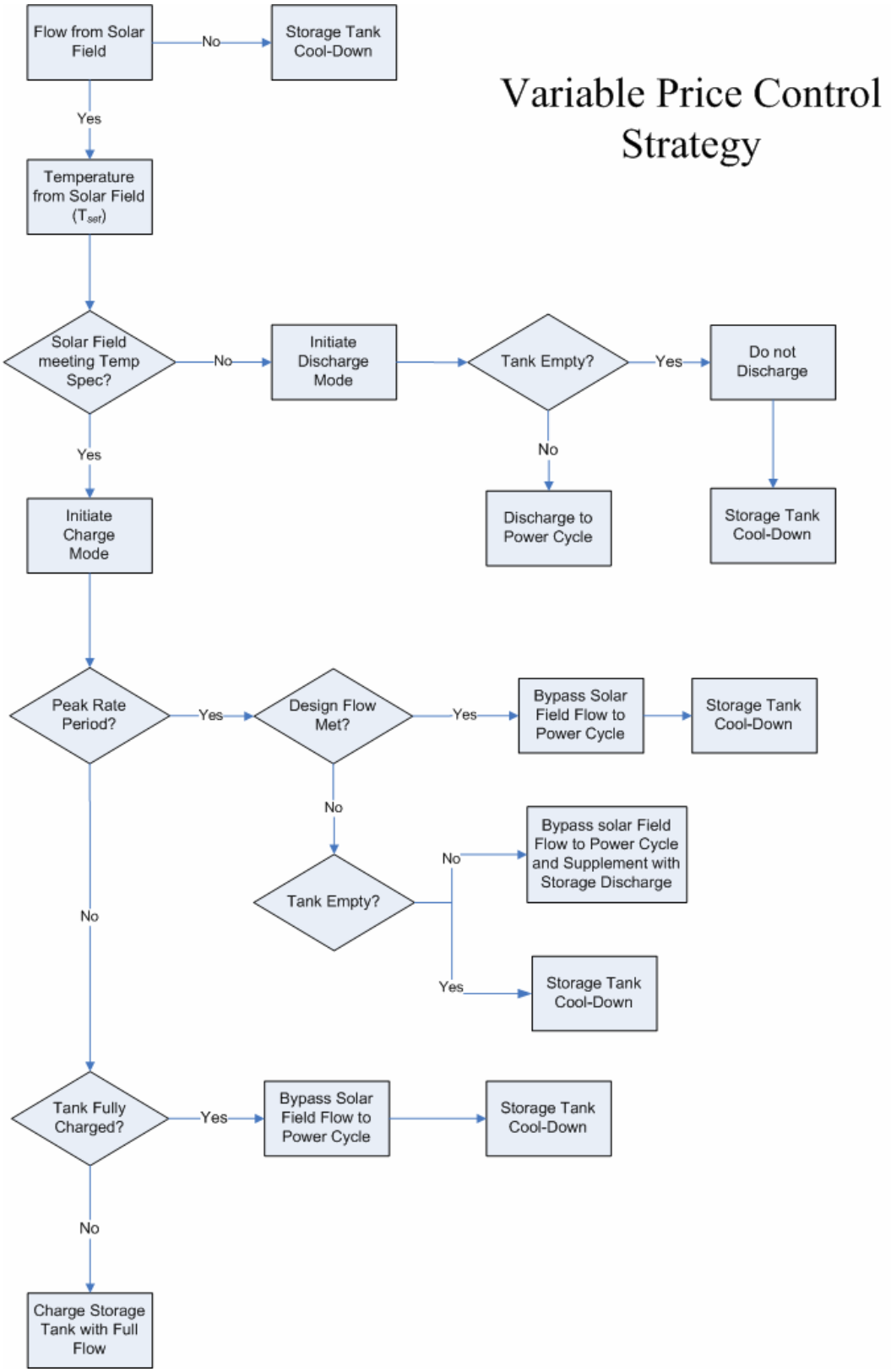

Figure 7.7: Flow-chart describing the storage system control strategy used for variable price operating strategies

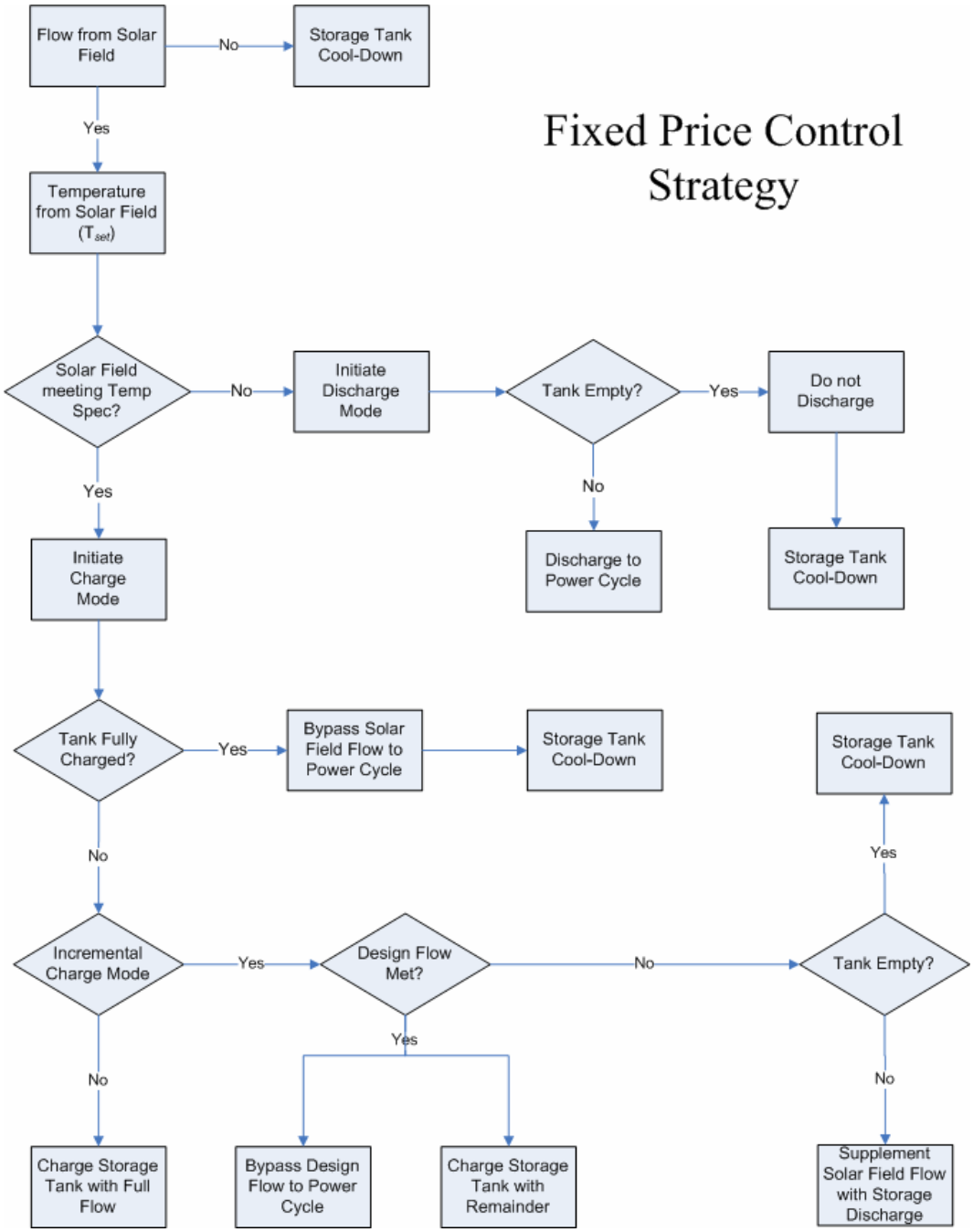

Figure 7.8: Flow-chart describing the storage system control strategy used for fixed-price operating strategies

Storage as Load leveler

One use of storage in a fixed-rate pricing structure is to maintain powerplant operation at its maximum efficiency point throughout the solar day. In order to investigate the possible advantages of this operating strategy, the simulation models of both the APS ORC plant presented in this thesis and the SEGS VI plant developed by Patnode [2006] were run to examine the variation in plant efficiency at constant HTF supply temperature for varying flow rates. The results are shown in Figure 7.9 where reduced efficiency is the ratio of efficiency to full-load efficiency and reduced mass flow rate is the ratio of mass flow to full-load mass flow.

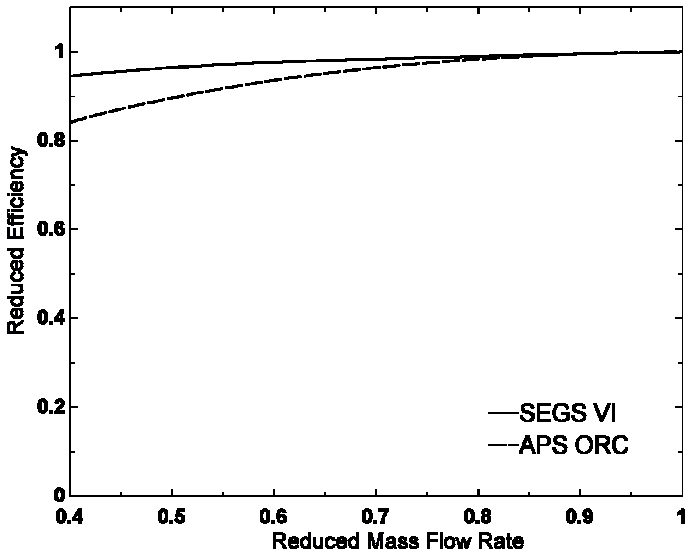

Figure 7.9: The change in cycle efficiency as a function of HTF flow rate for the SEGS VI and APS solar-thermal powerplants.

The benefit of a load-leveling operating strategy depends on plant efficiency being a strong function of load (HTF flow rate). That is, the gain in plant efficiency from load-leveling must offset storage system cost. In the case of both plants, efficiency is a weak function of HTF flow rate indicating that with the exception of extremely low HTF flow rates there is no intrinsic advantage to maintaining a constant power cycle operating point. The apparent independence of cycle efficiency and part-load HTF flow rate is driven by competing effects which cancel one another. As HTF flow rate decreases, turbine efficiency decreases while heat exchanger effectiveness increases.

This analysis suggests that there is not a significant benefit from using storage in a solar powerplant operating in a fixed-rate pricing structure. In general this appears to be true; however an alternative case for using storage in a system operating within a fixed-rate pricing structure has been proposed [Price, 2006]. It suggested that thermal-energy storage be used as a retrofit to an existing plant, in combination with additional solar field, to extend the operating interval of an existing powerplant. In this case, the existing power cycle could not handle the increased thermal output of the expanded solar field. Storage would then be used to capture this excess thermal energy for use during periods of lower insolation.

7.3 Sample TRNSYS Simulations

TRNSYS is the simulation environment of choice for solar energy technologies. In this section the basic layout and use of TRNSYS employing the models developed in this thesis is presented.

The simulation of a solar-thermal powerplant with storage in TRNSYS is based on 5 core TRNSYS component models. Type 805 is a parabolic-trough solar field model developed by Patnode [2006]. Type 811 is a Rankine cycle powerplant model based on SEGS VI, also developed by Patnode [2006]. Type 994 is the packed-bed stratified storage model developed in this thesis, described in Appendix B. Type 998 is a heat exchanger model developed specifically for the simulation of indirect storage systems. Type 998 is described in detail in Appendix C.

Figure 7.10 and Figure 7.11 show the layout of a parabolic-trough Rankine cycle powerplant with direct and fully-indirect storage in the TRNSYS Simulation Studio [Klein et al, 2006].

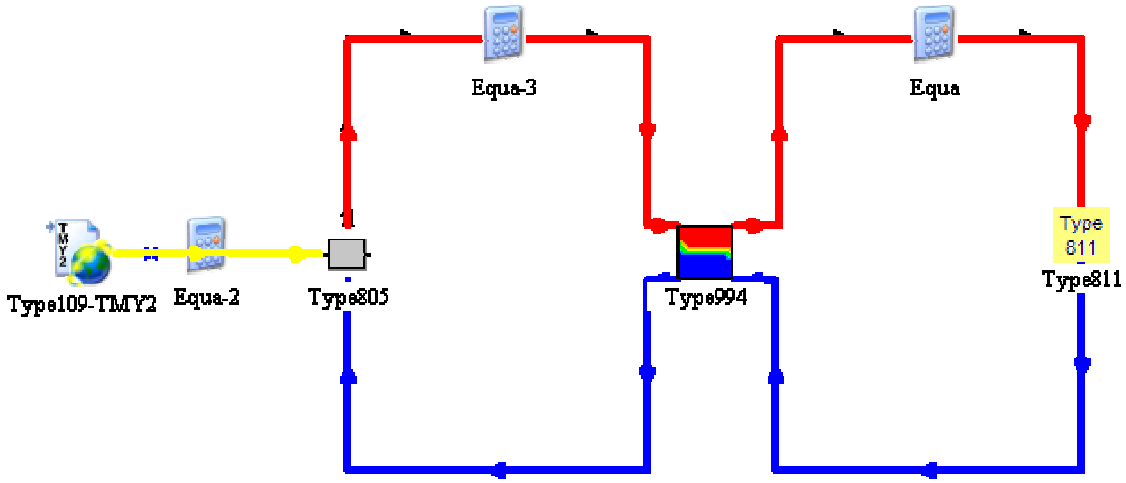

Figure 7.10: TRNSYS Simulation Studio representation of a direct storage system

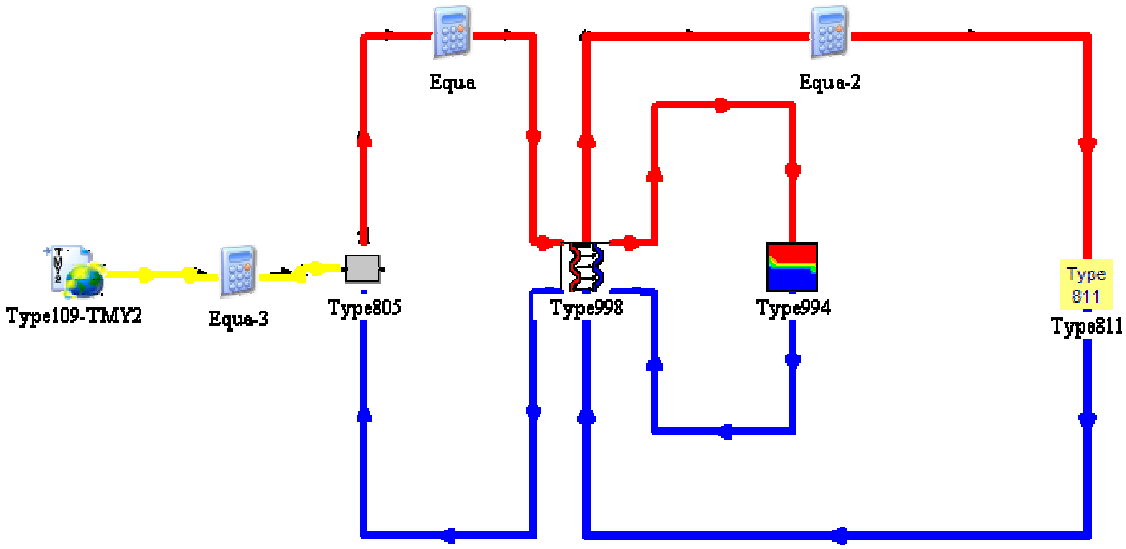

Figure 7.11: TRNSYS Simulation Studio representation of a fully-indirect storage system

Control strategy simulation

Figure 7.12 shows the results single-day direct storage simulation using the control strategies described in section 7.2. The variable-price control strategy uses storage to produce peak output over a five-hour period (shifted roughly three hours past solar noon). The fixed-rate control strategy results in less instantaneous power output, but electricity is produced over a period that extends past sunset.

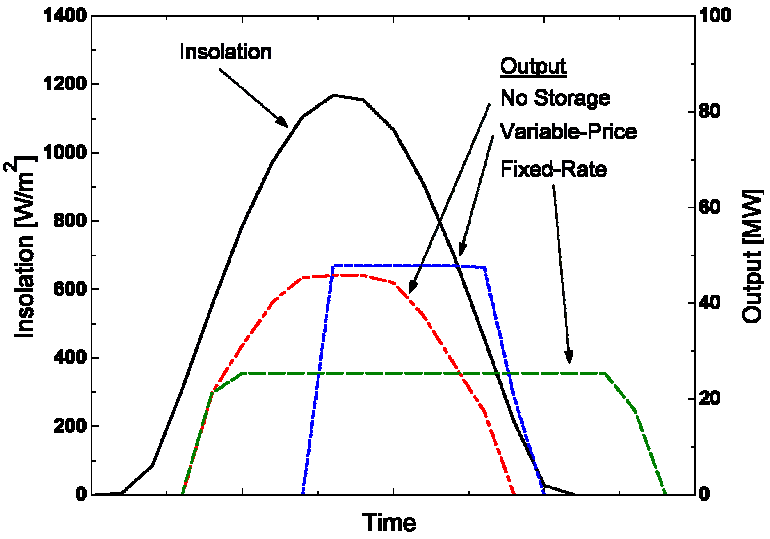

Figure 7.12: TRNSYS simulation output for a single day using no storage, the variable-price control strategy, and the fixed-rate control strategy.

The total energy outputs for the operating strategies shown in Figure 7.12 are shown in Table 7.1:

Table 7.1: TRNSYS Simulation Summary

Operating Mode	Integrated Output (MW-hr)
No Storage	349
Variable-Rate	329
Fixed-Rate	369

The variable-rate control strategy produces less energy than the no-storage case because at very large flow rates the power cycle is able to absorb less of the energy delivered to it. These high flow rates then result in higher solar field return temperatures and larger solar field losses. The fixed-rate control strategy produces more energy than the no-storage case because the plant was operated continuously at an output where cycle efficiency was high and solar field return temperatures were low. This creates a balance between solar field and power cycle efficiency, discussed in detail in chapter 5.

Indirect Storage System Performance

The efficiency of an indirect storage system is coupled directly to the effectiveness of the indirect heat exchanger, and the ability to match hot and cold fluid capacitance rates. Section 7.1 shows how system performance is theoretically coupled with heat exchanger

NTU. TRNSYS is used here to examine the compounding impact of this coupling over a longer period and subject to weather variation. The indirect heat exchanger (Type 998) calculates storage fluid flow rate such that the capacitance rates of the fluids in the heat exchanger are approximately matched.

Figure 7.13 shows the results of a three-day simulation of a solar powerplant with fully indirect stratified storage using the fixed-rate control strategy. Integrated system output and system efficiency are reported as a function of heat exchanger *UA*. Efficiency in this case is the ratio of integrated output and the integrated output achieved with a perfect heat exchanger. *UA* is used as the independent variable rather than *NTU* because fluid flow rates vary as dictated by the control strategy and available insolation. This variation in flow implies that *NTU* also varies during a given simulation run. Heat exchanger *UA* was taken to be a constant in this case. However, during normal simulation *UA* will vary with fluid flow rate as described in Appendix C.

System output and efficiency are shown in Figure 7.13 to degrade with reductions in heat exchanger *UA*. This is a result of two phenomena: low heat exchanger *UA* results in more heat exchanger availability destruction (see section 7.1) as well as leading to higher average solar field operating temperatures during charging which increases solar field losses. The low heat transfer fluid temperatures produced by low *UA* heat exchangers also results in decreased power cycle efficiency.

Unlike the curves shown in Figures 7.2 and 7.3 which decrease rapidly at very low values of *NTU*, system efficiency in the simulation limits to a value of ~70%. This limit is a product of the fixed-rate control strategy. In fixed-rate operation a large amount of heat transfer fluid is diverted directly from the solar field to the power cycle and is unaffected by storage system inefficiencies. The limit observed in Figure 7.13 indicates the point where storage system efficiency has gone to zero and remaining output is due solely to fluid diverted directly from the solar field.

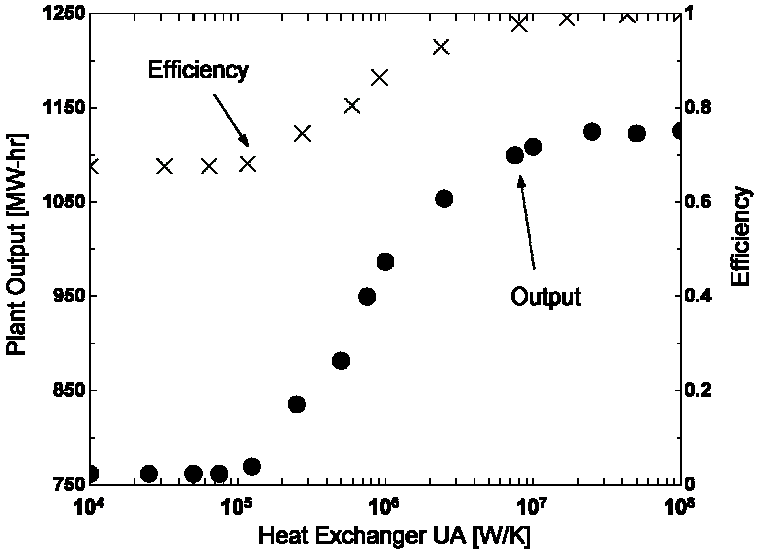

Figure 7.13: Variation in total system output as a function of heat exchanger *UA* for a three day period using the fixed-rate control strategy.

8 Conclusions and Recommendations

Summary and Conclusions

The properties of organic Rankine cycles make them attractive for application in the expanding low-cost, small-scale parabolic-trough solar power market. They offer a simple cycle design, which enables unattended operation, reduced production cost and reduced complexity. In addition, they support efficient operation at lower solar field operating temperatures making it possible for *direct* thermal energy storage technologies to be considered. *Direct* thermal energy storage offers a significant cost and performance advantage over the indirect systems proposed for use in the high-temperature SEGS systems. These advantages make organic Rankine cycles particularly attractive for off-grid or remote power applications, in addition to use with lower-cost and lower-temperature solar collector designs.

A detailed model of the APS Saguaro 1 MW organic Rankine cycle was developed and validated against manufacturer's data. The model was integrated into TRNSYS, creating a valuable tool for investigating the long-term performance of organic Rankine cycles in solar-thermal applications. The model was used to demonstrate that organic Rankine cycles are capable of matching the efficiency of a steam Rankine cycle operating between shared thermal boundary conditions of 358°C and 40°C (conditions observed at the SEGS VI solar-thermal powerplant). However, few organic fluids are able to operate at

these high temperatures, and those that can sacrifice many of the advantages that make organic Rankine cycles attractive. Organic Rankine cycles are thus better suited for small-scale applications where the reduced O&M and the ability to operate unattended are of higher value than efficiency.

While organic Rankine cycle technology shows great potential, current cycle design practice is not optimized for use with a solar-thermal resource. Using a methodology based on the finite-time thermodynamic analysis, a capital-cost optimization of the APS Saguaro plant showed opportunity for a significant (17%) reduction in capital cost while maintaining design output. The optimized design was achieved by increasing investment in plant heat exchanger area to improve cycle efficiency. The increased cycle efficiency reduced the size of the solar field for the same design power output. The economic viability of organic Rankine cycle solar power systems is dependent on optimizations of this nature.

The flexibility of all solar technologies is limited by the natural diurnal variation in insolation. Thermal energy storage represents the most likely near-term option for de-coupling the electric output of parabolic-trough powerplants (both steam and organic Rankine cycle based) from variation in solar radiation. Among the technically feasible thermal energy storage concepts, the single-tank packed-bed thermocline is considered the most attractive compromise between cost and performance. A model of these packed-bed thermocline systems was developed enabling rapid annual simulations while accurately representing performance observed on the Solar One thermocline system. The capacity to consider both *direct* and *indirect* storage systems is built into the model. Integrated into TRNSYS, the model provides a valuable tool in analyzing storage system design and control.

Optimal integration and control of a storage system is a complex function of many variables including end-user demand, part-load power cycle performance, operating temperatures and fluid stability limits. The number of constraints makes it difficult to draw any general conclusions about optimal storage system integration. To demonstrate

model capability in TRNSYS, two conceivable control strategies are considered: a variable-rate control strategy that maximizes output during a "peak-rate" window, and a fixed-rate control strategy that extends power production as long as possible. The fixed-rate strategy proves the most efficient from an energy perspective, by operating the power cycle for a longer period at its design point.

There is little to be gained in overall system solar-to-electric efficiency by using storage as a thermal capacitor to maintain power cycle operation at its optimal point. This observation makes the economics of thermal storage (*direct* or *indirect*) tenuous at best. Utility market forces must strongly favor the flexibility offered by storage in order to offset its substantial cost.

Recommendations for future work

The optimization of the APS Saguaro plant presented in this thesis identifies the opportunity to improve overall plant performance, but the equipment cost functions are only approximate. More detailed power cycle and solar field cost estimation is essential for putting this optimal design strategy into practice. To accomplish this, more powerplant cost data needs to be obtained and compared with both the cost functions used in this thesis as well as other cost functions in order to establish a validated reference for not only capital cost variation but also the absolute costs required to perform useful economic analyses. In particular, in the power cycle model, independent cost weightings for different heat exchanger types (boiler, condenser, recuperator) need to be identified. A more accurate baseline cost of the solar field should also be established, as the relative weighting between solar field and power cycle cost is the principle factor in determining the optimum power cycle operating point.

Using validated cost functions, the optimization methodology as a whole could be tested against a variety of power cycle designs – both solar-thermal and traditional.

The storage simulation models developed in this thesis agree with existing analytical models of packed-bed thermocline storage systems. However, storage system performance alone is not sufficient to determine optimal strategies for designing and controlling these storage systems. More elaborate control strategies than those considered in this thesis should be developed for simulations in order to determine both the market conditions (if any) that make thermal energy storage an attractive option for utility scale generation, as well as how to operate the storage system in those market conditions. Operating strategies should also be considered for remote or off-grid applications where specific end-user demands dictate plant operation rather than market conditions.

Optimization studies that focus just on the storage system, rather than its integration into the powerplant, could also be performed. There are a number of competing factors that could be considered: packing material cost, storage fluid cost, tank cost, total system thermal capacity, charge/discharge rate, pressure drop (pumping loads), tank aspect ratio, and convective losses (insulation). Considered together, along with readily available candidate materials and fluids, economically optimal storage systems could be designed for specific sets of system requirements.

APPENDIX A

TRNSYS Listing: Type 996 (APS ORC Power Cycle Model)

General Description

Type 996 models the performance of a 1-MW organic Rankine cycle powerplant that uses n-pentane as the power cycle working fluid and Radco Industries XCELTHERM®600 as the solar field heat transfer fluid.

Type 996 is a linear regression of a detailed power cycle model developed using EES [Klein, 2006]. A regression, rather than the detailed model is used because repeated solving of the detailed model would be computationally prohibitive in a simulation. A detailed description of the power plant as well as modeling techniques and validation are presented by McMahan [2006]. The EES files used to develop Type 996 are included with this thesis. This EES model can be used to recalculate the linear regression parameters allowing the consideration of varied plant operating parameters.

Nomenclature

a_0-a_9 = Linear regression coefficients for equation A.1 [-]
b_0-b_9 = Linear regression coefficients for equation A.2 [-]
$\dot{m}_{HTF}$ = Heat transfer fluid mass flow rate [kg/s]
$\dot{m}_{HTF,max}$ = Maximum heat transfer fluid mass flow rate [kg/s]
$\dot{m}_{HTF,min}$ = Minimum heat transfer fluid mass flow rate [kg/s]
Net_Power = Net power produced by the power cycle [kW]
Plant_Size = Capacity of plant being simulated (scaling factor for model) [kW]
$T_{\_WF\_min}$ = Minimum power cycle working fluid temperature [C]
$T_{\_HTF\_in}$ = Heat transfer fluid power cycle inlet temperature [C]
$T_{\_HTF\_max}$ = Maximum heat transfer fluid power cycle inlet temperature [C]
$T_{\_HTF\_min}$ = Minimum heat transfer fluid power cycle inlet temperature [C]
$T_{\_HTF\_out}$ = Heat transfer fluid power cycle outlet temperature [C]

Mathematical Description

All outputs are correlated as functions of powerplant thermal boundary conditions: minimum working fluid temperature, heat transfer fluid inlet temperature and heat transfer fluid flow rate. The minimum working fluid temperature is specified by the user, either with arbitrary inputs or outputs from another component representing cooling system performance. This enables the incorporation of seasonal variation in cooling performance as well as the flexibility to consider a variety of cooling technologies and scenarios into simulations. The default minimum working fluid temperature is based on 250 kg/s of cooling water delivered at 20ºC.

The correlation for net power cycle output is of the following form:

$$Net\_Power = a_0 + a_1 \cdot T_{HTF,in} + a_2 \cdot T_{HTF,in}^{\ 2} + a_3 \cdot \dot{m}_{HTF} + a_4 \cdot \dot{m}_{HTF}^{\ 2} + a_5 \cdot T_{WF,min} + a_6 \cdot T_{WW,min}^{\ 2} + a_7 \cdot T_{HTF,in} \cdot \dot{m}_{HTF} + a_8 \cdot T_{HTF,in} \cdot T_{WF,min} + a_9 \cdot \dot{m}_{HTF} \cdot T_{WF,min} \quad [A.1]$$

The correlation for net heat transfer fluid output temperature is of the following form:

$$T_{HTF,out} = b_0 + b_1 \cdot T_{HTF,in} + b_2 \cdot T_{HTF,in}^{\ 2} + b_3 \cdot \dot{m}_{HTF} + b_4 \cdot \dot{m}_{HTF}^{\ 2} + b_5 \cdot T_{WF,min} + b_6 \cdot T_{WF,min}^{\ 2} + b_7 \cdot T_{HTF,in} \cdot \dot{m}_{HTF} + b_8 \cdot T_{HTF,in} \cdot T_{WF,min} + b_9 \cdot \dot{m}_{HTF} \cdot T_{WF,min} \quad [A.2]$$

The coefficients for each correlation derived for the APS plant are listed as the default values in the *Parameters* table.

Maximum and minimum heat transfer fluid flow rates and temperatures are provided as parameters. If heat transfer fluid flow rate or temperature exceeds the maximum values then the power cycle is bypassed. Likewise, the power cycle is bypassed if heat transfer fluid flow or temperature is less than the minimum value. The default maximum and minimum values for the heat transfer fluid are estimated from plant documentation [Price, 2006].

Type 996 is configured to allow simulation of larger powerplants by scaling the performance of the 1-MW design case. To demonstrate this, consider setting the *Plant_Size* parameter to 5,000 kW (5 times the design size). It follows that the expected heat transfer fluid flow rate would be 5 times larger in order to deliver sufficient thermal energy to the power cycle. To accommodate this larger flow rate with the 1,000 kW model, the heat transfer fluid mass flow rate is scaled linearly with plant size in the following manner:

$$\dot{m}_{HTF,in} = \frac{\dot{m}_{HTF,in}}{(Plant\_Size / Plant\_Size_{DEFAULT})} \quad [A.4]$$

Note that as plant size scales, so too will the cooling load. Thus, in the 5,000 kW case the default plant would require 1,250 kg/s of cooling water rather than 250 kg/s.

Parameters

	Name	Dimension	Unit	Type	Range	Default
1	*Plant_Size*	Power	[kW]	real	[-inf;inf]	1000
2	a_0	Dimensionless	[-]	real	[-inf;inf]	479.2416
3	a_1	Dimensionless	[-]	real	[-inf;inf]	-4.892304
0.	a_2	Dimensionless	[-]	real	[-inf;inf]	0.01149868
5	a_3	Dimensionless	[-]	real	[-inf;inf]	-63.54109
6	a_4	Dimensionless	[-]	real	[-inf;inf]	-1.057854

7	a_5	Dimensionless	[-]	real	[-inf;inf]	6.485757
8	a_6	Dimensionless	[-]	real	[-inf;inf]	0.003776489
9	a_7	Dimensionless	[-]	real	[-inf;inf]	0.605649
10	a_8	Dimensionless	[-]	real	[-inf;inf]	-0.03548787
11	a_9	Dimensionless	[-]	real	[-inf;inf]	-0.3570907
12	b_0	Dimensionless	[-]	real	[-inf;inf]	-13.46833
13	b_1	Dimensionless	[-]	real	[-inf;inf]	0.5829432
14	b_2	Dimensionless	[-]	real	[-inf;inf]	-0.001085932
15	b_3	Dimensionless	[-]	real	[-inf;inf]	6.61631
16	b_4	Dimensionless	[-]	real	[-inf;inf]	-0.084561490
17	b_5	Dimensionless	[-]	real	[-inf;inf]	-0.01728301
18	b_6	Dimensionless	[-]	real	[-inf;inf]	0.000079494
19	b_7	Dimensionless	[-]	real	[-inf;inf]	-0.005809497
20	b_8	Dimensionless	[-]	real	[-inf;inf]	0.001949139
21	b_9	Dimensionless	[-]	real	[-inf;inf]	-0.012579470
32	*mdot_HTF_max*	Flow Rate	[kg/s]	real	[-inf;inf]	14
33	*mdot_HTF_min*	Flow Rate	[kg/s]	real	[-inf;inf]	6
34	*T_HTF_max*	Temperature	[C]	real	[-inf;inf]	310
35	*T_HTF_min*	Temperature	[C]	real	[-inf;inf]	190

Inputs

	Name	Dimension	Unit	Type	Range	Default
1	$T_{HTF,in}$	Temperature	[C]	real	[-inf;inf]	300
2	$T_{WF,min}$	Temperature	[C]	real	[-inf;inf]	22.3
3	$\dot{m}_{HTF,in}$	Flow Rate	[kg/s]	real	[-inf;inf]	11.75

Outputs

	Name	Dimension	Unit	Type	Range	Default
1	*Net_Power*	Power	[kW]	real	[-inf;inf]	1000
2	$T_{HTF,out}$	Temperature	[C]	real	[-inf;inf]	120

Information Flow Diagram

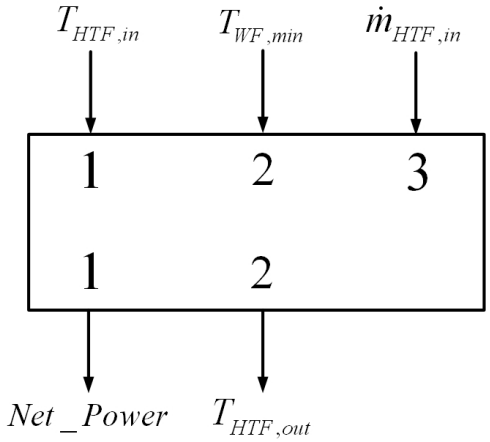

APPENDIX B

TRNSYS Listing: Type 994 (Packed-Bed Stratified Storage)

General Description

Type 994 models a stratified fluid storage tank with a solid material added for additional thermal capacitance. Type 994 differs from Type 10 by including fluid thermal capacitance and incorporating some control and dispatch capability designed to aide simulation of solar-thermal powerplants. Type 994 consists of two separate heat transfer models that are internally selected based on the operating condition of the storage system in a given time step. One model represents the charging and discharging of the system (a non-zero fluid mass flow), and the other models long-term idle periods (zero fluid mass flow).

The Schumann model is a formulation of the one-dimensional governing heat transfer equation for a fluid flowing through a packed bed. It is used in Type 994 to represent charging and discharging storage system operation. The Schumann model neglects viscous dissipation, axial conduction and temperature gradients within the solid particles. With these assumptions the coupled governing partial differential equations take the form:

$$\frac{\partial T_f}{\partial t} + v\frac{\partial T_f}{\partial x} = \frac{-h(V/A)}{\rho_f C_f \varepsilon}\cdot(T_f - T_s) \qquad \text{[B.1]}$$

$$\frac{\partial T_s}{\partial t} = \frac{h(V/A)}{\rho_s C_s (1-\varepsilon_b)}\cdot(T_f - T_s) \qquad \text{[B.2]}$$

These equations can also be shown as differential control volume energy balances:

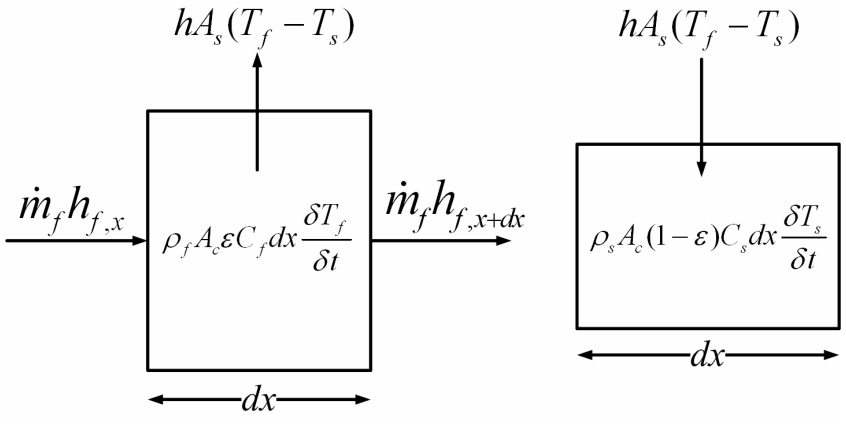

Figure B.1 1-D fluid and solid differential control volume energy balances from the Schumann equations for the (a) fluid and (b) solid constituents.

Equations [B.1] and [B.2] require fluid inlet and initial solid temperature boundary conditions. Type 994 also makes the "*infinite-NTU*" assumption. That is, the fluid-solid heat transfer coefficient is sufficiently large that at any time *t* and location *x*, the fluid and solid are in thermal equilibrium. This was shown to be an appropriate assumption for thermal storage systems by McMahan [2006].

When the storage tank is idle the fluid-solid constituents are treated as a continuum and are governed by equation [B.3], with corresponding energy flows shown in figure B.2:

$$(\rho_f \varepsilon C_f + \rho_s (1-\varepsilon) C_s) A_c \frac{dT}{dt} = k_{eff} A_c \frac{\partial^2 T}{\partial x^2} - h_{loss,w} A_w (T - T_{amb}) \qquad [B.3]$$

where;

$$K_{eff} = \varepsilon K_f + (1-\varepsilon) K_s \qquad [B.4]$$

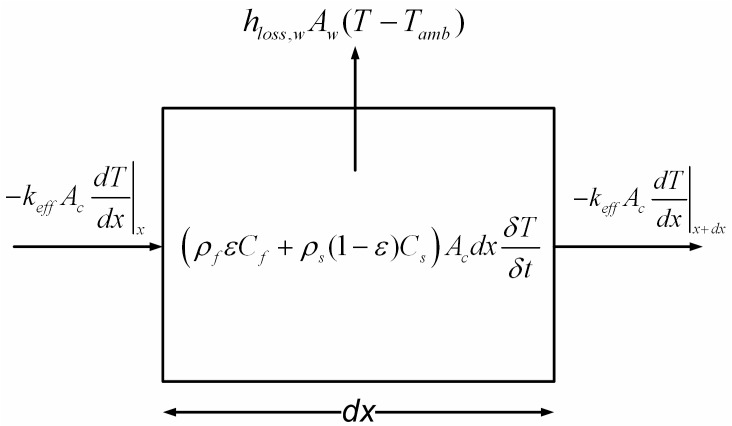

Figure B.2 1-D fluid-solid continuum differential energy balance for long-term idle loss simulation

The boundary conditions for equation [5.2.14][B.3] are:

$$-k_{eff} A_c \left.\frac{dT}{dx}\right|_{x=0} = h_{loss,top} A_{top} (T|_{x=o} - T_{amb}) \qquad [B.5]$$

$$-k_{eff} A_c \left.\frac{dT}{dx}\right|_{x=L} = h_{loss,bot} A_{bot} (T|_{x=L} - T_{amb}) \qquad [B.6]$$

Nomenclature

A_s	= Total solid-fluid heat transfer surface area [m^2]
A_c	= cross-sectional area in the direction of flow [m^2]
A_{node}	= heat transfer surface area in a numerical control volume [m^2]
A_{bot}	= bottom loss heat transfer surface area [m^2]
A_{top}	= top loss heat transfer surface area [m^2]
A_w	= wall loss heat transfer surface area [m^2]
C_f	= fluid specific heat [J/kg-K]

C_s = solid specific heat [J/kg-K]
FluidNumber = integer representing a specific fluid for obtaining properties [-]
h = solid-fluid heat transfer coefficient [W/m^2-K]
$h_{loss,top}$ = (*Top_loss*) top loss heat transfer coefficient [W/m^2-K]
$h_{loss,bot}$ = (*Bottom_Loss*) bottom loss heat transfer coefficient [W/m^2-K]
$h_{loss,w}$ = (*Loss_Coefficient*) wall loss heat transfer coefficient [W/m^2-K]
i = temperature node number in numerical model [-]
idle_timestep = time step used by the long-term idle model [s]
k_f = fluid thermal conductivity [W/m-K]
k_s = solid thermal conductivity [W/m-K]
k_{eff} = fluid-solid continuum effective thermal conductivity [W/m-K]
InternalNodes = number of numerical control volumes [-]
LossCoeff = wall loss coefficient [W/m^2-K]
m_f = fluid mass flow rate [kg/s]
$\dot{m}_{discharge}$ = heat transfer fluid flow rate supplied to the power cycle during discharge mode and constant output mode [kg/s]
$\dot{m}_{peak}$ = heat transfer fluid flow rate supplied to the power cycle during peak-period discharge [kg/s]
$\dot{m}_{in,top}$ = fluid mass flow inlet while charging [kg/s]
$\dot{m}_{in,bottom}$ = fluid mass flow inlet while discharging [kg/s]
$\dot{m}_{out,top}$ = fluid mass flow outlet while discharging [kg/s]
$\dot{m}_{out,bottom}$ = fluid mass flow outlet while charging [kg/s]
Output_Code = Output used to indicate tank status (1=normal, 2=full, 3=empty) to other simulation components [-]
Peak_Start = Start time of peak rate period [hr]
Peak_Length = Length of peak period [hrs]
RateMode = indicates rate schedule allowing selection of control strategies based on fixed-rate and variable rate structures [-]
StorageSize = storage system design capacity [kWh]
StorageMode = Storage operating mode [-]
SolidNumber = integer representing a specific solid for obtaining properties [-]
t = time [s]
TankDiameter = storage tank diameter, height is calculated based on storage size [m]
$T_{in,top}$ = fluid inlet temperature while charging [C]
$T_{in,bottom}$ = fluid inlet temperature while discharging [C]
$T_{out,top}$ = fluid outlet temperature while discharging [C]
$T_{out,bottom}$ = fluid outlet temperature while charging [C]
T_f = Fluid Temperature [C]
T_s = Solid Temperature [C]
$T_{\_hot\_design}$ = design "hot" storage temperature, used to calculate tank capacity [C]
$T_{\_cold\_design}$ = design "cold" storage temperature, used to calculate tank capacity [C]
$T_{f,i}$ = Fluid Temperature at node i [C]
$T_{s,i}$ = Solid Temperature at node i [C]

T_o = Initial System Temperature (fluid and solid assumed in equilibrium) [C]
$T_{\_min\_charge}$ = minimum temperature accepted by the storage unit for charging. This parameter allows low temperatures to be rejected and prevent de-stratification. [C]
$T_{\_min\_discharge}$ = minimum temperature accepted for discharge. This parameter allows low temperatures to be rejected for power generation.
$T_{breakthrough}$ = Maximum temperature difference between the initial storage system temperature and fluid temperature allowed at the cold end of the tank. This indicates the thermocline "breaking through" and the tank being completely full. [C]
V = Total system volume [m^3]
v = fluid velocity [m/s]
$VoidFraction$ = ratio of fluid volume to total storage system volume [m^3/m^3]

Greek
Δx = numerical distance step [m]
Δt = numerical time step [s]
ε = system void fraction [m^3/m^3]
ρ_f = fluid density [kg/m^3]
ρ_s = solid density [kg/m^3]

Superscripts

+ = indicates value at the beginning of the next time step

Mathematical Description

Charge-Discharge

Equations [B.1]-[B.2] are solved numerically using an time-explicit technique. The storage tank is first separated into a grid of axial control volumes as shown in Figure B.3:

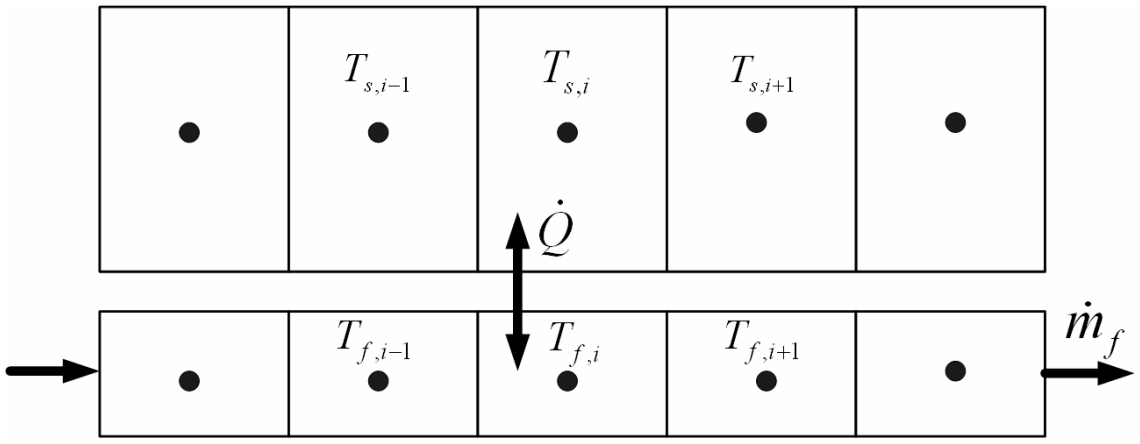

Figure B.3 Numerical grid used for finite-difference solution of equations B.1-B.2

The explicitly discretized versions of equations B.1 and B.2 can be simplified by adding the following constraint:

$$\Delta t = \frac{\rho_f A_c \varepsilon \Delta x}{\dot{m}_f} = \frac{m_f}{\dot{m}_f} \quad [B.7]$$

Constraining the time step in this way has the effect of eliminating the convective energy transfer terms from the energy balance. The details of this derivation are shown by McMahan [2006]. Equations [B.1], [B.2] and [B.7] yield fluid and solid nodal energy balances of the following form:

$$T_{f,(i,t+\Delta t)} = T_{f,(i-1,t)} - \frac{hA_{node}(T_{f,(i-1,t)} - T_{s,(i,t)})}{\dot{m}_f C_f} \quad [B.8]$$

$$T_{s,(i,t+\Delta t)} = T_{s,(i,t)} + \frac{hA_{node}\Delta t(T_{f,(i-1,t)} - T_{s,(i,t)})}{m_s C_s} \quad [B.9]$$

Type 994 further simplifies equations [B.8] and [B.9] by assuming an effectively infinite overall fluid-solid heat transfer coefficient. That is, the fluid and solid are in thermal equilibrium at every point in the computational domains: $T_{f,(i+1,t+\Delta t)} = T_{s,(i,t+\Delta t)}$. With this simplification equations [B.8] and [B.9] become a single equation:

$$T_{f,(i,t+\Delta t)} = T_{s,(i-1,t+\Delta t)} = \frac{T_{f,(i-1,t)}\dot{m}_f C_{p,f}\Delta t + T_{s,(i,t)} m_s C_{p,s}}{\dot{m}_f C_{p,f}\Delta t + m_s C_{p,s}} \quad [B.10]$$

Equation [B.10] is then integrated forward in time to determine temperature as a function of location and time within the storage system. Equation B.7 requires that Type 994 operate on a different timescale than TRNSYS. In order to accommodate these disparate time steps, the number of time steps taken by Type 994 (*InternalTimesteps*) during each TRNSYS time step is defined by the following expression:

$$InternalTimesteps = \frac{\Delta t_{TRNSYS}}{\Delta t_{994}} \quad [B.11]$$

To accommodate the different time steps used by Type 994 and TRNSYS the outputs returned to TRNSYS are the integrated averages over the smaller time steps taken by Type 994.

Material and transport properties are based on user input. Temperature-correlated properties that are calculated at each node and time step are available for a number of potential storage fluids:

FluidNumber

1	Nitrate Salt
2	Caloria™ HT-43
3	Hitec XL
4	Therminol VP-1
5	Hitec
6	Dowtherm Q
7	Dowtherm RP
8	Xceltherm®600

9	User-defined, constant properties

The properties of the solid media are constant independent of temperature, based on input parameters.

Long-term idle

Equations [B.3]-[B.6] are solved numerically using an implicit technique to guarantee stability. The storage tank is first separated into a grid of axial control volumes as shown in Figure B.4:

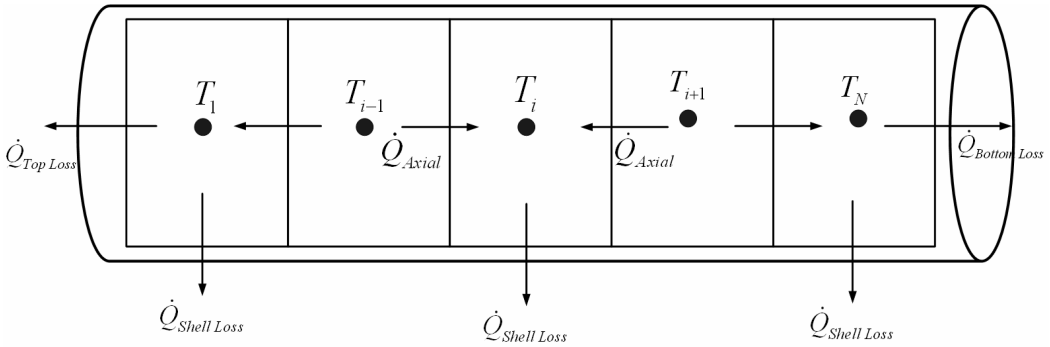

Figure B.4: Numerical grid used for the long-term simulation of packed-bed stratified storage systems

For convenience a total nodal thermal capacitance is defined as follows:

$$(mC)_T = \left(\rho_f C_f \varepsilon + \rho_s C_s (1-\varepsilon)\right) A_c \Delta x \qquad [B.12]$$

Fluid specific heat and thermal conductivity are computed at every node as functions of temperature, as with the charge/discharge model. Fluid-solid density is assumed to be constant for the duration of the simulation period.

Equation [B.3] is discretized implicitly for all internal tank nodes:

$$(mC)_T \left[\frac{T_{i,t+\Delta t} - T_{i,t}}{\Delta t}\right] = \frac{k_{eff} A_c}{\Delta x}\left(T_{i-1,t+\Delta t} - T_{i,t+\Delta t}\right) + \frac{k_{eff} A_c}{\Delta x}\left(T_{i+1,t+\Delta t} - T_{i,t+\Delta t}\right) - h_{loss,w} A_w (T_{i,t+\Delta t} - T_{amb}) \qquad [B.13]$$

Likewise for the bottom of the tank, incorporating boundary condition [B.5]:

$$(mC)_T \left[\frac{T_{n,t+\Delta t} - T_{n,t}}{\Delta t}\right] = \frac{k_{eff} A_c}{\Delta x}\left(T_{n-1,t+\Delta t} - T_{n,t+\Delta t}\right) - h_{loss,w} A_w (T_{n,t+\Delta t} - T_{amb}) - h_{loss,bot} A_{bot} (T_{n,t+\Delta t} - T_{amb}) \qquad [B.14]$$

And for the top of the tank, incorporating boundary condition [B.4]:

$$(mC)_T \left[\frac{T_{1,t+\Delta t} - T_{1,t}}{\Delta t}\right] = \frac{k_{eff} A_c}{\Delta x}\left(T_{2,t+\Delta t} - T_{1,t+\Delta t}\right) - h_{loss,w} A_w (T_{1,t+\Delta t} - T_{amb}) - h_{loss,top} A_{top} (T_{1,t+\Delta t} - T_{amb}) \qquad [B.15]$$

Equations [B.13] through [B.15] form a tri-diagonal system of equations of the form $Ax=B$ where A has the dimensions NxN and B is $Nx1$. The system of equations is solved at each time step and then integrated forward in time. The timestep used to solve [B.13]

through [B.15] is a fixed value (*idle_timestep*). *idle_timestep* should be a multiple of the TRNSYS time step to minimize error.

Storage size calculations

Shown below are the calculations involved in determining system simulation parameters based on the user-specified storage capacity.

The required tank volume is calculated based on the design temperature difference and storage capacity as:

$$V_{tank} = \frac{StorageSize}{(1-\varepsilon)\rho_s C_s (T_{hot\_design} - T_{cold\_design}) + \varepsilon\rho_f (h_f\big|_{T\_hot\_design} - h_f\big|_{T\_cold\_design})} \quad [B.16]$$

The tank height is then calculated based on the specified tank diameter:

$$H_{tank} = \frac{4V_{tank}}{\pi \cdot TankDiameter^2} \quad [B.17]$$

Tank top, bottom and wall surface area are then calculated:

$$A_w = \pi \cdot TankDiameter \cdot H_{tank} \quad [B.18]$$

$$A_{top}, A_{bot} = \frac{\pi \cdot TankDiameter^2}{4} \quad [B.19]$$

Systems Integration information

The *Storage_Mode* parameter determines how Type 994 will interact with all balance-of-system TRNSYS components. The three available storage modes are:

Storage_Mode

1	Direct
2	Indirect
3	Control System Bypass

In direct mode the storage system is should be directly connected to the solar field for charging and the power cycle for discharging. It is important in this mode to ensure that Type 994 is using the same fluid as other TRNSYS components. In direct mode the dispatch and control strategies are administered directly from Type 994 (details follow).

Storage mode 2 (indirect) is designed to interface with Type 998. Type 998 models the heat exchanger that interfaces the solar field and power cycle heat transfer fluid loops. In Storage mode 2 the control strategies are administered from Type 998. See Type 998 documentation for further details. The *OUTPUT_CODE* output of Type 994 is used to signal tank status to Type 998 (or other TRNSYS types). The *OUTPUT_CODE* is defined such that:

OUTPUT_CODE

1	Normal
2	Full
3	Empty

Storage mode 3 bypasses the built-in control strategies. This mode allows Type 994 to be used with control strategies or in simulations developed by the user. In Storage mode 3, Type 994 is used by dictating mass-flow inputs similar to Type 10. If $\dot{m}_{in,top}$ is positive, charging is modeled. If $\dot{m}_{in,bottom}$ is positive, discharging is modeled. If both input mass flows are zero, then long-term idle operation is modeled. Take care that both input mass flows are not greater than zero; this will result in an error.

Built-in Control Strategies

When operating in *Storage_Mode* 1, the built-in control strategies are used. The built-in control strategies were developed specifically for simulating parabolic-trough solar-thermal powerplants. Two general control strategies included, each designed around a commonly proposed utility pricing structure. The first pricing structure is variable, or real-time, pricing where the price of electricity is a function of grid demand. The second structure is fixed-rate pricing. The *Rate_Mode* parameter is used to select the rate schedule being considered:

Rate Mode

1	Variable Pricing
2	Fixed-Rate Pricing

Figures B.5 and B.6 show flow diagrams corresponding to the strategies for each pricing structure. The variable price control strategy is designed to maximize output during the peak-rate period. The fixed-rate price control strategy is designed to maintain a constant output over a longer period, maximizing overall powerplant efficiency and capacity.

Both control strategies are driven first by the input from the solar field. In the absence of positive flow from the solar field, the Type 994 goes into idle mode. If there is positive heat transfer fluid flow from the solar field, the temperature of the heat transfer fluid is then evaluated. If the flow is greater than or equal to the temperature deemed sufficient for charging (*T_min_charge*) then the storage system enters "charge mode." If not, it enters "discharge mode." Discharge mode is the same for both control strategies, the tank discharges at a pre-determined rate ($\dot{m}_{discharge}$) until its charge has been exhausted (*T_out_top* < *T_min_discharge*). "Charge mode" operation is different for each control strategy.

In variable-price mode (*Rate_Mode =1*) there is accommodation for a "peak" period where the price for electricity is high. This strategy is built around focusing plant output over a relatively short time-band where plant output is much more valuable. During peak periods all resources (solar field flow and storage) are simultaneously focused on power

generation at a user-defined maximum flow rate ($\dot{m}_{peak}$). During off-peak periods all available solar field flow is used to charge storage so that it is available during the peak period.

In fixed-rate mode (*Rate_Mode =2*) there is accommodation for constant-output operation. Constant output is achieved by setting a design delivery rate of heat transfer fluid to the power cycle ($\dot{m}_{discharge}$). All solar field flow in excess of $\dot{m}_{discharge}$ is diverted to storage. Likewise, if solar field flow is less than $\dot{m}_{discharge}$ then storage is used to boost solar field flow to the design level (if storage is available).

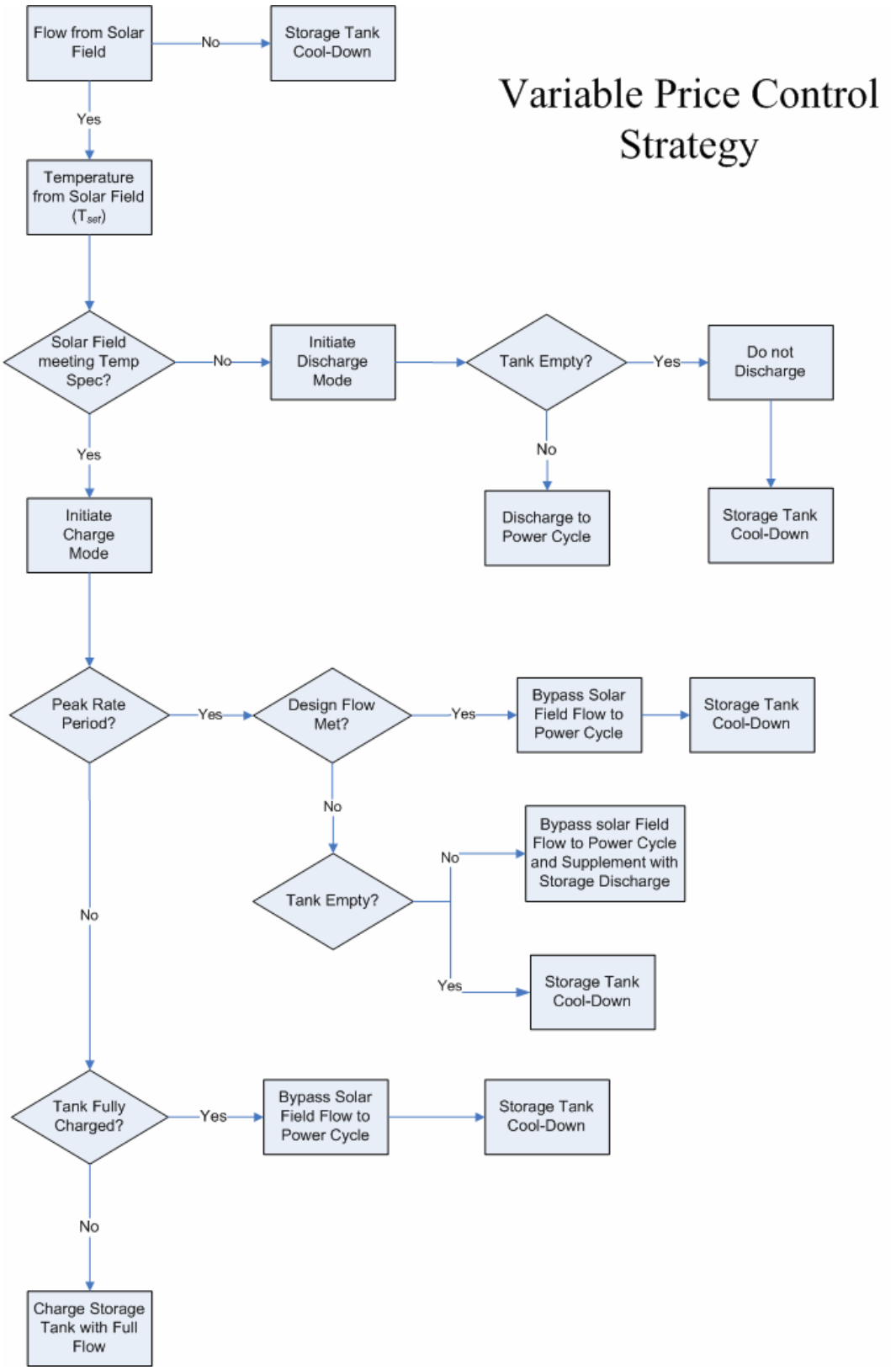

Figure B.5: Variable (real-time) price control strategy for thermal energy storage in solar-thermal powerplants.

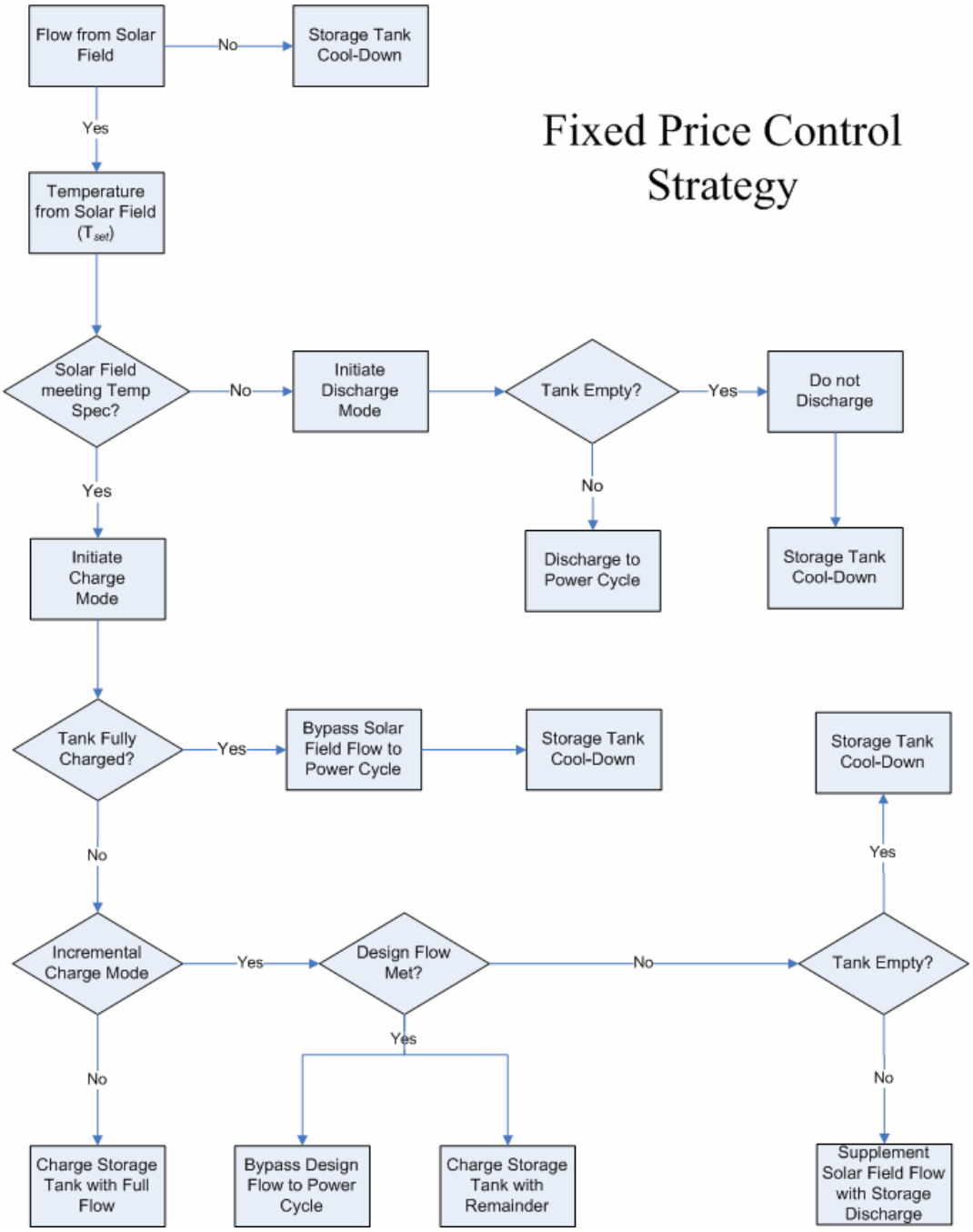

Figure B.6: Fixed-rate price control strategy for thermal energy storage in solar-thermal powerplants.

Parameters

	Name	Dimension	Unit	Type	Range	Default
1	*StorageSize*	Energy	[kWh]	real	[-inf;inf]	120000
2	*LossCoeff*	Heat Transfer Coefficient	[W/m^2-K]	real	[-inf;inf]	0.4
3	*VoidFraction*	Dimensionless	[-]	real	[-inf;inf]	0.25
4	*SolidNumber*	Dimensionless	[-]	integer	[-inf;inf]	1
5	*FluidNumber*	Dimensionless	[-]	integer	[-inf;inf]	1
6	*T_min_discharge*	Dimensionless	[-]	real	[-inf;inf]	350
7	T_o	Temperature	[C]	real	[-inf;inf]	300
8	*T_min_charge*		[C]	real	[-inf;inf]	390
9	*InternalNodes*	Dimensionless	[-]	integer	[-inf;inf]	400
10	C_f	Specific Heat	[J/kg-K]	real	[-inf;inf]	1000
11	C_s	Specific Heat	[J/kg-K]	real	[-inf;inf]	2400
12	ρ_f	Density	[kg/m^3]	real	[-inf;inf]	700
13	ρ_s	Density	[kg/m^3]	real	[-inf;inf]	2400
14	*h_sf*	Heat Transfer Coefficient	[W/m^2-K]	real	[-inf;inf]	100
15	*mdot_Discharge*	Flow Rate	[kg/s]	real	[-inf;inf]	300
16	*T_breakthrough*	Temperature	[C]	real	[-inf;inf]	0
17	*Peak_Start*	Dimensionless	[-]	real	[-inf;inf]	12
18	*Peak_Length*	Dimensionless	[-]	real	[-inf;inf]	0
19	*Top_Loss*	Heat Transfer Coefficient	[W/m^2-K]	real	[-inf;inf]	0
20	*Bottom_Loss*	Heat Transfer Coefficient	[W/m^2-K]	real	[-inf;inf]	0
21	*Tank_Diameter*	Length	[m]	real	[-inf;inf]	0
22	*T_hot_design*	Temperature	[C]	real	[-inf;inf]	400
23	*T_cold_Design*	Temperature	[C]	real	[-inf;inf]	300
24	*k_fluid*	Conductivity	[W/m-K]	real	[-inf;inf]	0.5
25	*k_solid*	Conductivity	[W/m-K]	real	[-inf;inf]	2.5
26	*mdot_peak*	Flow Rate	[kg/s]	real	[-inf;inf]	700
27	*Storage_Mode*	Dimensionless	[-]	integer	[-inf;inf]	1
28	*Rate_Mode*	Dimensionless	[-]	integer	[-inf;inf]	2
29	*idle_timestep*	Time	[s]	real	[-inf;inf]	600

Inputs

	Name	Dimension	Unit	Type	Range	Default
1	$\dot{m}_{in,top}$	Flow Rate	[kg/s]	real	[-inf;inf]	0
2	$T_{in,top}$	Temperature	[C]	real	[-inf;inf]	300
3	$\dot{m}_{in,bottom}$	Flow Rate	[kg/s]	real	[-inf;inf]	0
4	$T_{in,bottom}$	Temperature	[C]	real	[-inf;inf]	300
5	T_{amb}	Temperature	[C]	Real	[-inf;inf]	12

Outputs

	Name	Dimension	Unit	Type	Range	Default
1	$\dot{m}_{out,top}$	Flow Rate	[kg/s]	real	[-inf;inf]	0
2	$\dot{m}_{out,bottom}$	Flow Rate	[kg/s]	real	[-inf;inf]	0
3	$T_{out,top}$	Temperature	[C]	real	[-inf;inf]	300
4	$T_{out,bottom}$	Temperature	[C]	real	[-inf;inf]	300
5	*OUTPUT_CODE*	Dimensionless	[-]	integer	[-inf;inf]	1

Information Flow Diagram

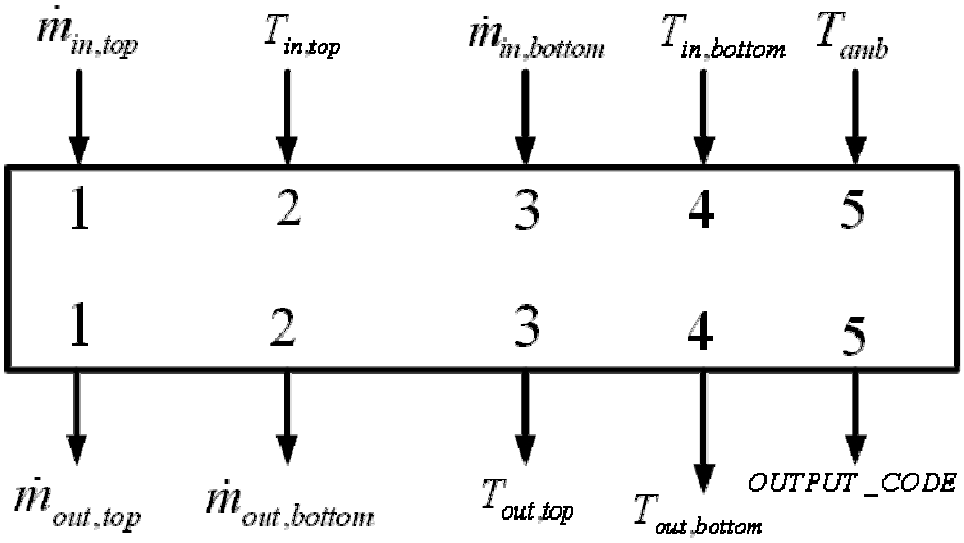

APPENDIX C

TRNSYS Listing: Type 998 (Indirect Storage Heat Exchanger and Dispatch)

General Description

Type 998 models a heat exchanger designed to couple a thermal storage system to a solar-thermal powerplant. In addition to heat exchanger calculations, it provides two basic control strategies that interface a storage system with a power cycle and solar field. Figure C.1 shows the anticipated component configuration:

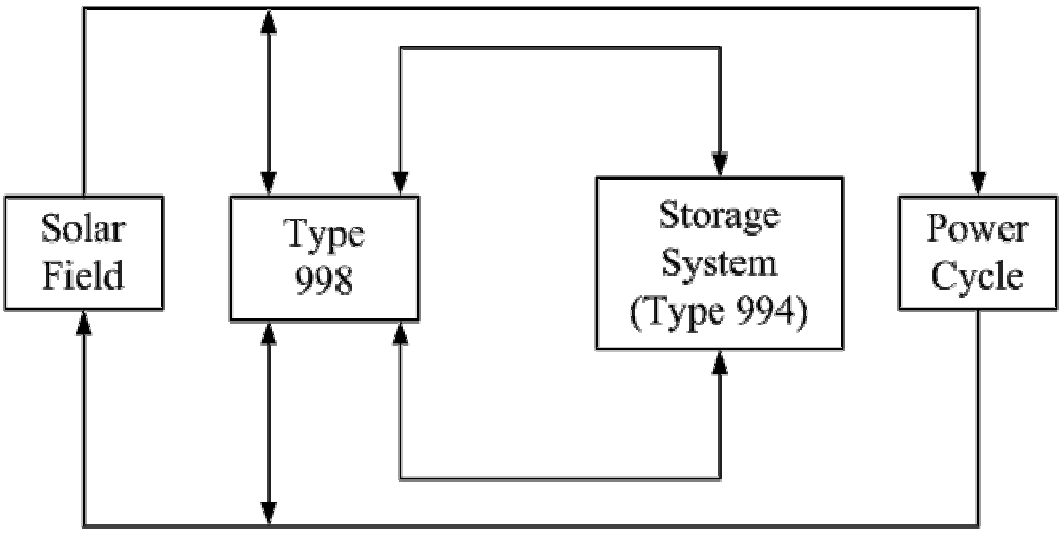

Figure C.1: sample simulation configuration using Type 998as the solar field – storage coupling heat exchanger and controller.

The heat exchanger is modeled using an effectiveness-*NTU* technique. Based on one known flow rate (generally on the solar field side) Type 998 calculates the mass flow rate of the storage system fluid such that the capacitance rates are as closely matched as possible. Matched capacitance rates are chosen in order to maximize heat exchanger (and storage system) performance and minimize required fluid flow rates.

Nomenclature

HTF_Fluid	= integer representing power-cycle side fluid [-]
$\dot{m}_{in,bottom}$	= mass flow input from the power cycle [kg/s]
$\dot{m}_{in,store,bot}$	= mass flow input from the bottom of the storage tank [kg/s]
$\dot{m}_{in,store,top}$	= mass flow input from the top of the storage tank [kg/s]
$\dot{m}_{in,top}$	= mass flow input from the solar field [kg/s]
$\dot{m}_{out,bottom}$	= mass flow output to the solar field [kg/s]
$\dot{m}_{out,store,bot}$	= mass flow output to the bottom of the storage tank [kg/s]

$\dot{m}_{out,store,top}$ = mass flow output to the top of the storage tank [kg/s]
$\dot{m}_{out,top}$ = mass flow output to the power cycle [kg/s]
mdot_Discharge = mass flow used during discharge mode [kg/s]
mdot_peak = maximum mass flow delivered to power cycle during peak periods [kg/s]
Peak_Length = Length of peak period [hrs]
Peak_Start = Start time of peak rate period [hr]
Rate_Mode = Indicates rate schedule allowing selection of control strategies based on fixed-rate and variable rate structures [-]
Storage_Code = Input that indicates storage system status [-]
Storage_Mode = Parameter that indicates storage system operational mode [-]
Store_Fluid = Integer representing storage-side fluid [-]
$T_{in,bottom}$ = Temperature input from the power cycle [C]
$T_{in,store,bot}$ = Temperature input from the bottom of the storage tank [C]
$T_{in,store,top}$ = Temperature input from the top of the storage tank [C]
$T_{in,top}$ = Temperature input from the solar field [C]
$T_{out,bottom}$ = Temperature output to the solar field [C]
$T_{out,store,bot}$ = Temperature output to the bottom of the storage tank [C]
$T_{out,store,top}$ = Temperature output to the top of the storage tank [C]
$T_{out,top}$ = Temperature output to the power cycle [C]
T_min_charge = Minimum temperature acceptable for storage charging [C]
UA = Heat exchanger overall heat transfer coefficient [W/K]

Mathematical Description

The heat exchanger is modeled using an effectiveness-*NTU* technique. Figure C.2 shows the flows through the heat exchanger corresponding to a scenario in which the entire solar field flow is diverted through Type 998 in order to charge the storage system. In this case the flow rate and temperature from the solar field, as well as the inlet temperature from storage are known.

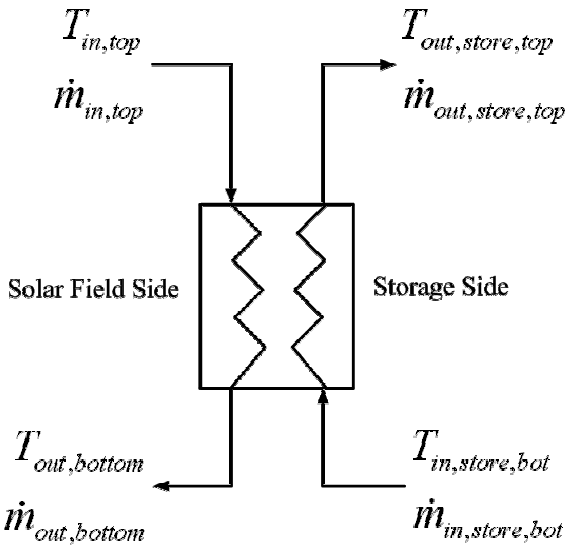

Figure C.2: Sample heat exchanger flows used for sample heat exchanger calculation

An average heat exchanger temperature is calculated based on input temperature. This temperature is used for calculating average heat exchanger fluid properties.

$$\overline{T} = \frac{T_{in,top} + T_{in,store,bot}}{2} \quad [C.1]$$

The solar field side capacitance rate can then be calculated:

$$(\dot{m}C)_{SF} = \dot{m}_{in,top}\, C_{SF}\big|_{\overline{T}} \quad [C.2]$$

Based on the matched capacitance-rate design of the Type 998 heat exchanger, the storage fluid mass flow rate can be calculated:

$$\dot{m}_{in,store,bot} = \frac{(\dot{m}C)_{SF}}{C_{ST}\big|_{\overline{T}}} \quad [C.3]$$

Heat exchanger *NTU* is then calculated:

$$NTU = \frac{UA\left(\frac{\dot{m}_{in,top}}{\dot{m}_{in,top,ref}}\right)^{0.8}}{(\dot{m}C)_{SF}} \quad [C.4]$$

where $\dot{m}_{in,top,ref}$ is the design flow rate corresponding to the user-specified *UA* (the *mdot_SF_ref* parameter). *UA* is always evaluated in terms of the solar field side flow rate as it is always the known flow rate.

With the capacitance rates on both sides of the heat exchanger equal, the effectiveness is calculated in terms of *NTU* as follows [Incropera, 2005]:

$$\varepsilon = \frac{NTU}{1 + NTU} \quad [C.5]$$

The definition of effectiveness then yields the outlet temperatures of both fluids:

$$\varepsilon = \frac{(\dot{m}C)_{SF}(T_{in,top} - T_{out,bottom})}{(\dot{m}C)_{SF}(T_{in,top} - T_{in,store,bot})} = \frac{(\dot{m}C)_{ST}(T_{out,store,top} - T_{in,store,bot})}{(\dot{m}C)_{ST}(T_{in,top} - T_{in,store,bot})} \quad [C.6]$$

This methodology is used also to calculate heat exchanger performance during discharging or partial charging and discharging.

Fluid properties are determined based on the *FluidNumber* parameter with the following definitions:

FluidNumber

1	Nitrate Salt
2	Caloria™ HT-43
3	Hitec XL
4	Therminol VP-1
5	Hitec
6	Dowtherm Q
7	Dowtherm RP
8	Xceltherm®600

Systems Integration

The *Storage_Mode* parameter determines how Type 998 will interact with all balance-of-system TRNSYS components. Currently Type 998 is configured only to work as an indirect heat exchanger for thermal energy storage systems (specifically made for Type 994). To retain a consistent nomenclature between Type 994 and Type 998 *Storage_Mode* is set to 2 by default, indicating indirect coupling with a storage system.

The *Storage_Code* input in Type 998 is designed to receive the *Output_Code* output from Type 994. This allows information about storage tank status (Type 994: 1=Normal, 2=Full, 3=Empty) to be shared by both components. This information is necessary to administer the built-in control strategies.

Built-in Control Strategies

The control strategies administered from Type 998 are identical to those used in Type 994. These control strategies were developed specifically for simulating parabolic-trough solar-thermal powerplants. There are two general control strategies included, each designed around a commonly proposed utility pricing structure. The first pricing structure is variable, or real-time, pricing where the price of electricity is a function of grid demand. This is most common on the open electricity market. The second structure is fixed-rate pricing. This is less common on the open-market, but many utilities interested in increasing their renewable energy portfolio will pay a constant price to providers. The *Rate_Mode* parameter is used to select the rate schedule being considered:

Rate Mode

1	Variable Pricing
2	Fixed-Rate Pricing

Figures C.3 and C.4 show flow diagrams corresponding to the strategies for each pricing structure. The variable price control strategy is designed to maximize output during the peak-rate period. The fixed-rate price control strategy is designed to maintain a constant output over a longer period, maximizing overall powerplant efficiency.

Both control strategies are driven first by the input from the solar field. In the absence of positive flow from the solar field, Type 998 does nothing. If there is positive heat transfer fluid flow from the solar field, the outlet temperature of the solar field is then evaluated. If the temperature of the flow is greater than or equal to the temperature deemed sufficient for charging (*T_min_charge*) then the storage system enters "charge mode." If not, it enters "discharge mode." Discharge mode is the same for both control strategies, the storage system is discharged at a flow rate sufficient to achieve a user-specified delivery of heat transfer fluid to the power cycle ($\dot{m}_{discharge}$) until the storage system has been exhausted (*Storage_Code = 3*). "Charge mode" operation is different for each control strategy.

In variable-price mode (*Rate_Mode =1*) there is accommodation for a "peak" period where the value of output is at a maximum. This strategy is built around focusing plant output over a relatively short time-band where plant output is much more valuable. During peak periods all resources (solar field flow and storage) are simultaneously focused on power generation at a user-defined maximum solar field fluid flow rate ($\dot{m}_{peak}$). During off-peak periods all available solar field flow is used to charge storage so that it is available during the peak period.

In fixed-rate mode (*Rate_Mode =2*) there is accommodation for constant-output operation. Constant output is achieved by setting a design delivery rate of heat transfer fluid to the power cycle ($\dot{m}_{discharge}$). All solar field flow in excess of $\dot{m}_{discharge}$ is diverted to storage. Likewise, if solar field flow is less than $\dot{m}_{discharge}$ then storage is used to boost solar field flow to the design level.

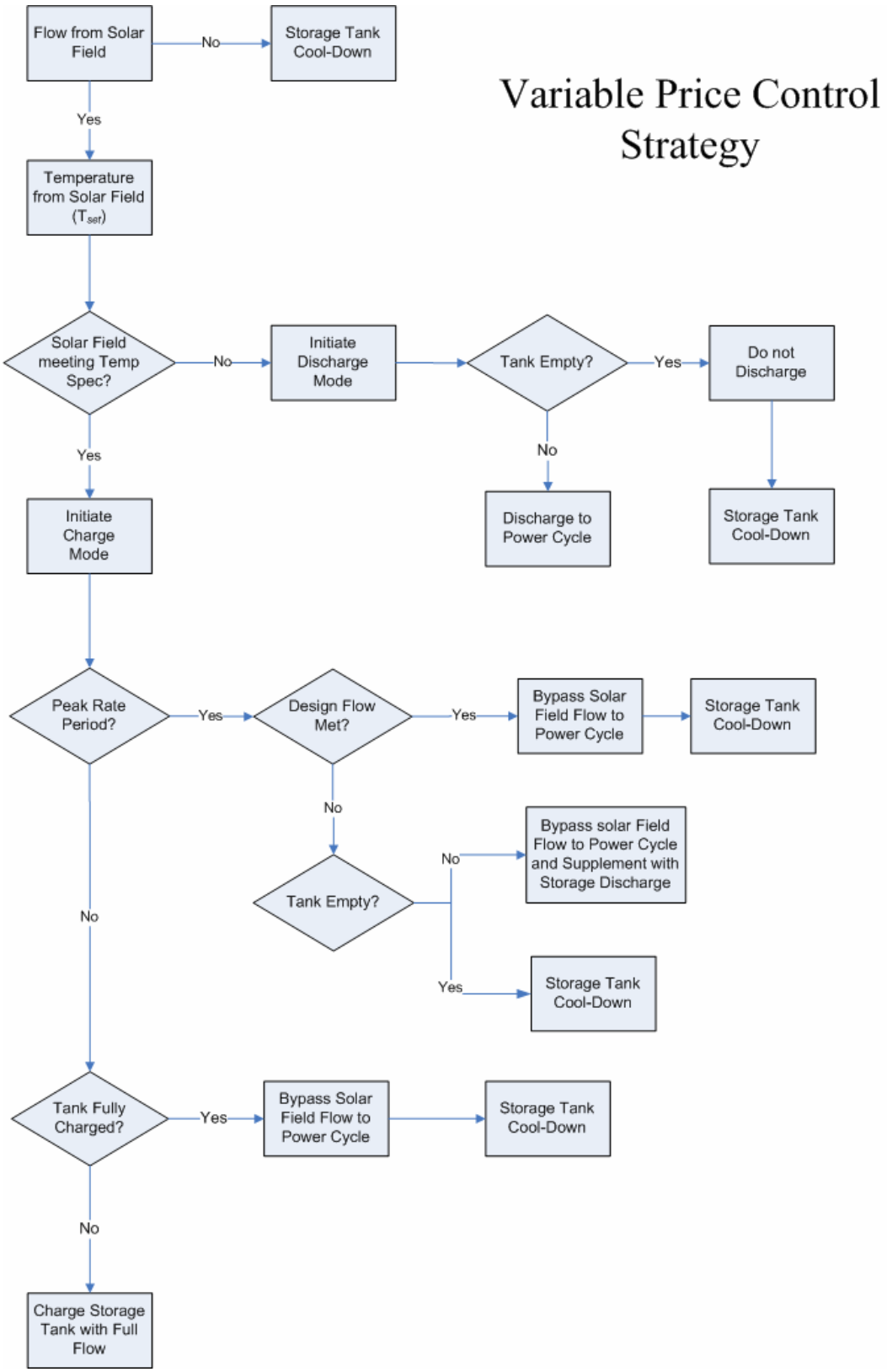

Figure C.3: Variable (real-time) price control strategy for thermal energy storage in solar-thermal powerplants.

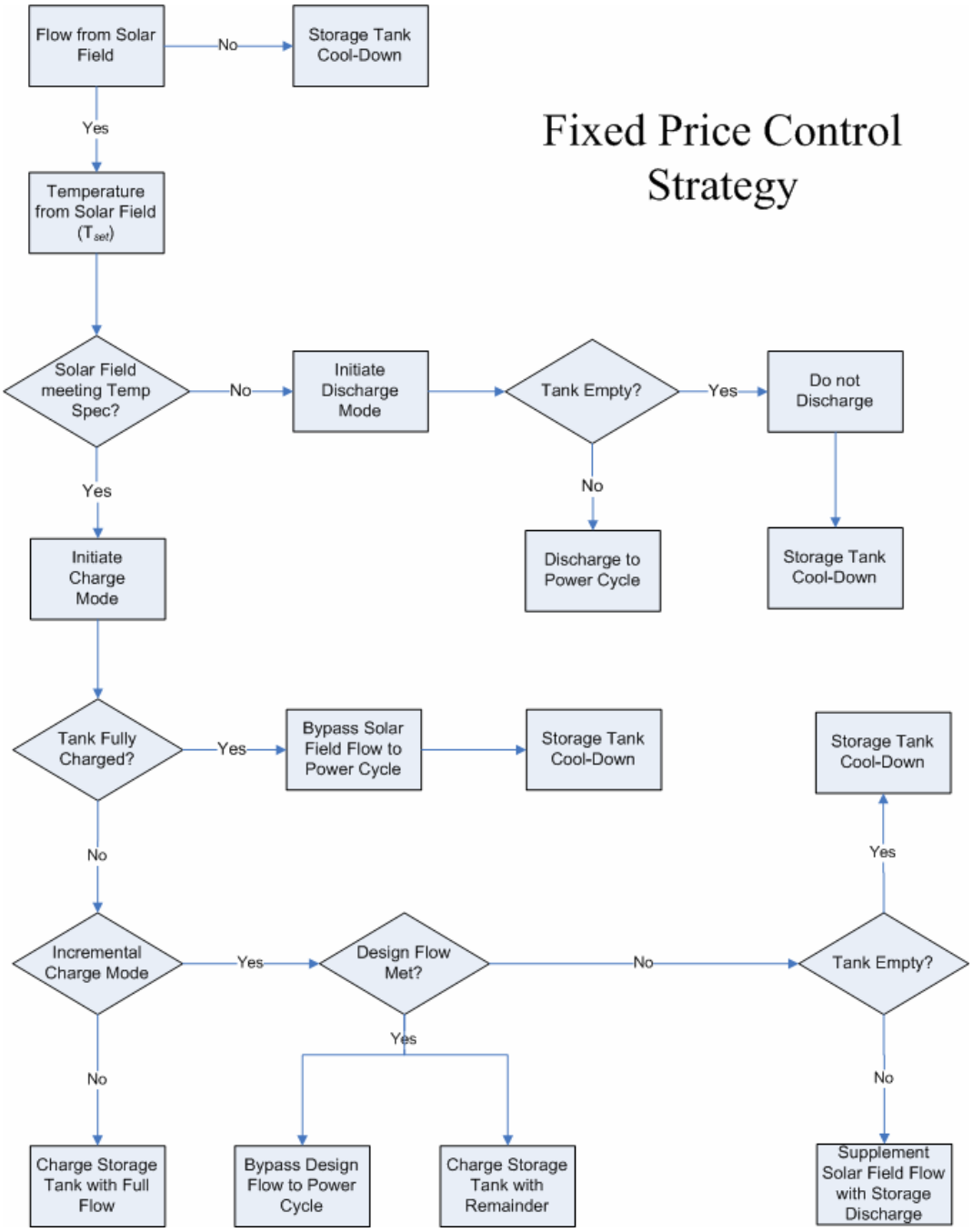

Figure C.4: Fixed-rate price control strategy for thermal energy storage in solar-thermal powerplants.

Parameters

	Name	Dimension	Unit	Type	Range	Default
1	*UA*	Heat Transfer Coefficient	[W/K]	real	[-inf;inf]	100000
2	*Storage_Mode*	Dimensionless	[-]	integer	[-inf;inf]	1
3	*HTF_Fluid*	Dimensionless	[-]	integer	[-inf;inf]	1
4	*Store_Fluid*	Dimensionless	[-]	integer	[-inf;inf]	1
5	*Peak_Start*	Dimensionless	[-]	real	[-inf;inf]	12
6	*Peak_Length*	Dimensionless	[-]	real	[-inf;inf]	0
7	*mdot_Discharge*	Flow Rate	[kg/s]	real	[-inf;inf]	300
8	*mdot_peak*	Flow Rate	[kg/s]	real	[-inf;inf]	450
9	*Rate_Mode*	Dimensionless	[-]	integer	[-inf;inf]	1
10	*mdot_SF_ref*	Flow Rate	[kg/s]	real	[-inf;inf]	350
11	*T_min_charge*	Temperature	[C]	real	[-inf;inf]	380

Inputs

	Name	Dimension	Unit	Type	Range	Default
1	$T_{in,top}$	Temperature	[C]	real	[-inf;inf]	0
2	$\dot{m}_{in,top}$	Flow Rate	[kg/s]	real	[-inf;inf]	0
3	$T_{in,bottom}$	Temperature	[C]	real	[-inf;inf]	0
4	$\dot{m}_{in,bottom}$	Flow Rate	[kg/s]	real	[-inf;inf]	0
5	$T_{in,store,top}$	Temperature	[C]	real	[-inf;inf]	0
6	$\dot{m}_{in,store,top}$	Flow Rate	[kg/s]	real	[-inf;inf]	0
7	$T_{in,store,bot}$	Temperature	[C]	real	[-inf;inf]	0
8	$\dot{m}_{in,store,bot}$	Flow Rate	[kg/s]	real	[-inf;inf]	0
9	*Storage_Code*	Dimensionless	[-]	integer	[-inf;inf]	3

Outputs

	Name	Dimension	Unit	Type	Range	Default
1	$T_{out,top}$	Temperature	[C]	real	[-inf;inf]	0
2	$\dot{m}_{out,top}$	Flow Rate	[kg/s]	real	[-inf;inf]	0
3	$T_{out,bottom}$	Temperature	[C]	real	[-inf;inf]	0
4	$\dot{m}_{out,bottom}$	Flow Rate	[kg/s]	real	[-inf;inf]	0
5	$T_{out,store,top}$	Temperature	[C]	real	[-inf;inf]	0
6	$\dot{m}_{out,store,top}$	Flow Rate	[kg/s]	real	[-inf;inf]	0
7	$T_{out,store,bot}$	Temperature	[C]	real	[-inf;inf]	0
8	$\dot{m}_{out,store,bot}$	Flow Rate	[kg/s]	real	[-inf;inf]	0

Information Flow Diagram

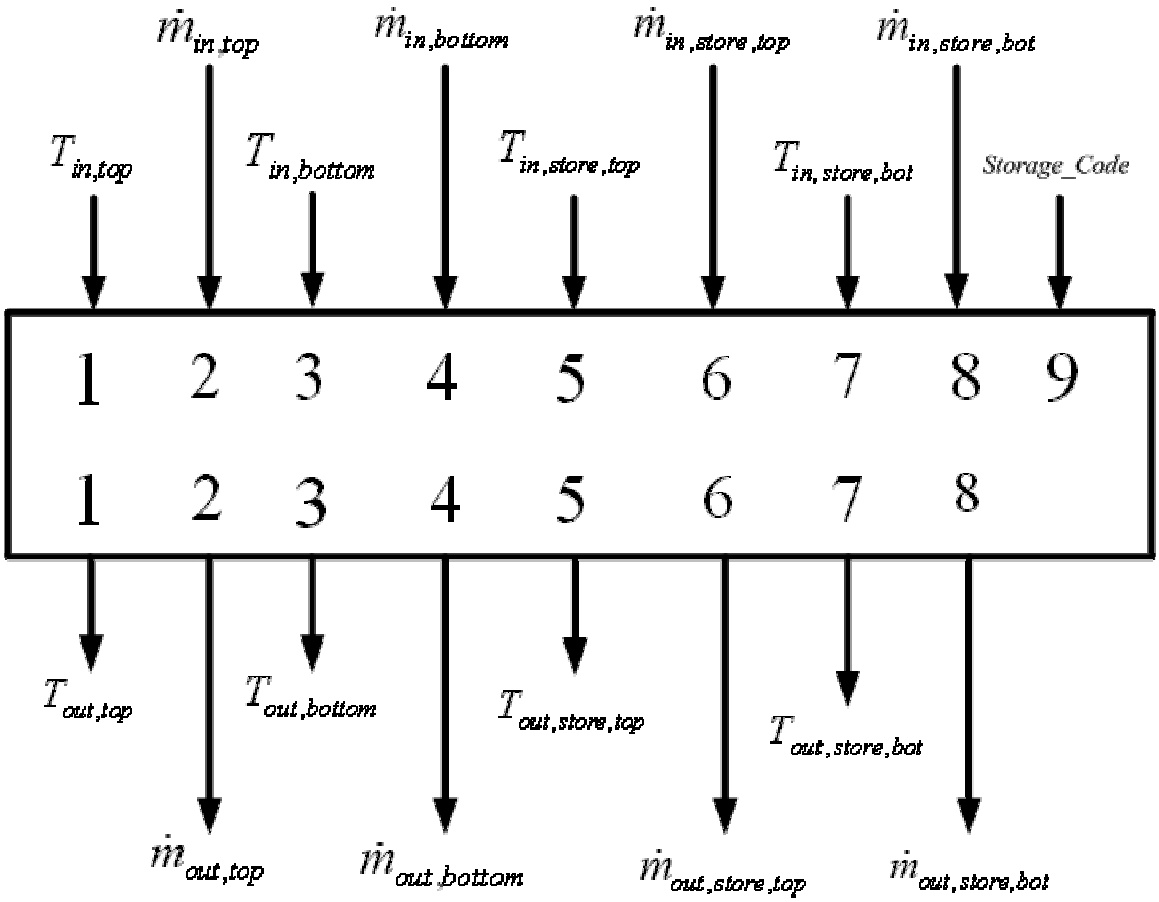

Appendix D

Digital Supplement

This thesis makes use of a series of computer models and programs built for EES as well as TRNSYS. Functional versions of these models as well as source code are included as a digital supplement. The files included on the CD are as follows:

APS Plant EES Models:

APS Saguaro Plant Model.EES

- This is the design case, part-load model

APS Saguaro Plant Model – linear regression.EES

- This is the design case, part-load model version used to create the plant performance correlations used in Type 994.

APS Saguaro Plant Model – FULL-LOAD OPTIMIZED.EES

- This is the optimized full-load APS cycle used in Chapter 5

Type 99x Files (Type 994, 996, 998):

Type 99x.DLL	TRNSYS Library
Type 99x.F90	FORTRAN90 Source Code
Type 99x.TMF	TRNSYS Studio *TYPE* File
Type 99x.BMP	TRNSYS Studio icon
Type 99x.DSP	Visual Studio Project File
Type 99x.DSW	Visual Studio Project Workspace

TRNSYS Sample Simulations:

Direct Storage.TPF	TRNSYS Simulation Studio File
Indirect Storage.TPF	TRNSYS Simulation Studio File
APS Saguaro.TPF	TRNSYS Simulation Studio File

References

Adam, Warren A. *Organic Rankine Engines*. Encyclopedia of Energy Technology, v.3, pp.2157-2161.

Andersen, W.C., Bruno, T.J. *Rapid Screening of Fluids for Chemical Stability in Organic Rankine Cycle Applications*. Ind. Eng. Chem. Res., v. 44 (2005) pp. 5560-5566.

Angelino, G., Colonna diPaliano, P. *Organic Rankine Cycles (ORCs) For Energy Recovery From Molten Carbonate Fuel Cells*. Proceedings of 35th Intersociety Energy Conversion Engineering, Las Vegas Nevada, (2000)

Angelino, G., Invernizzi, C. *Cyclic Methylsiloxanes as Working Fluids for Space Power Cycles*. Transactions of the ASME v. 115 (1993) pp.130-137

Angelino, G., Colonna diPaliano, P. *Multicomponent working fluids for Organic Rankine Cycles (ORCs)*. Energy v.23, no. 6 (1998) pp.449-463

Angelino, G., Colonna diPaliano, P. *Air Cooled Siloxane Bottoming Cycle For Molten Carbonate Fuel Cells*. Proceedings of 2000 Fuel Cell Seminar, Portland Oregon, October (2000)

Badr, O., O'Callaghan, P.W., Probert, S.D. *Rankine-Cycle Systems for Harnessing Power from Low-Grade Energy Sources*. Applied Energy, v.36 (1990) pp.263-292

Badr, O., Probert, S.D., and O'Callaghan, P.W. *Selecting A Working Fluid for a Rankine-Cycle Engine*. Applied Energy, v.21 (1985) pp.1-42

Barber, R.E. *Solar-Powered Rankine Cycle engines – Characteristics*. Proceedings of the 1976 IECEC, No. 769200 (1976)

Bartlett, Robert. *Steam Turbine Performance and Economics*. McGraw-Hill Inc., New York (1958)

Bassily, A.M. *Modeling, numerical optimization, and irreversibility reduction of a dual-pressure reheat combined-cycle*. Applied Energy, v. 81 (2005) pp. 127-151

Beckman, W.A., Duffie, J.A. *Solar Engineering of Thermal Processes*. John Wiley & Sons, New York (1991)

Bejan, Adrian. *Advanced Engineering Thermodynamics*. John Wiley & Sons, New York (1988)

Bliem, C.J. *Zeotropic Mixtures of Halocarbons as working fluids in Binary Geothermal Power Generation Cycles*. Proceedings of the 22nd IECEC, American Institute of Aeronautics and Astronautics. v. 2 (1987)

Bliem, C.J., Mines, G.L. *Relative Performance of Supercritical Binary Geothermal Power Cycles with In-Tube Condensers in Different Orientations.* Proceedings of the 24th IECEC, IEEE. Vol. 5 (1989)

Bliem, C.J. *Aspects of the Kalina Technology Applied to Geothermal Power Production*. Idaho National Engineering Laboratory, September (1989)

Bliem, C.J., Mines, G.L. *Advanced Binary Geothermal Power Plants: Working Fluid Property Determination and Heat Exchanger Design*. Idaho National Engineering Laboratory, December (1989)

Bliem, C.J., Mines, G.L. *Second Law Analysis of Advanced Power Generation Systems Using Variable Temperature Heat Sources*. Idaho National Engineering Laboratory, November (1990)

Bliem, C.J., Mines, G.L. Advanced *Binary Geothermal Power Plants: Limits of Performance*. EG&G Idaho, Inc. January (1991)

Boehm, R.F. *Design Analysis of Thermal Systems*. John Wiley & Sons, New York (1987)

Brosseau, Doug, et al. *Testing of thermocline Filler Materials and Molten-Salt Heat Transfer Fluids for Thermal Energy Storage Systems in Parabolic Trough Power Plants*. Solar Energy Engineering, v. 127 (2005) pp. 109-116

Brugman, J., Hattar, M., Nichols, K., Esaki, Y. *Next Generation Geothermal Power Plants*. Report prepared for the United States Department of Energy, TR-106223 (1996)

Cable, R.G., et al. *SEGS plant performance 1989-1997*. Proceedings of Solar 98: Renewable Energy for the Americas, Albuquerque, NM, p. 445-452 (1998)

Casals, X.G. *Overall Energetic Comparison of Direct Steam Generation and Oil-Based Parabolic Trough Systems with Rankine Cycles for Electricity Generation*. Internal Report, University Comillas, Madrid. February (2000)

Chambadal, P. *Le choix du cycle thermique dans une usine generatrice nucleaire*. Rev Gen Elect Vol 67 (1958) p. 332-345

Chaudoir, D.W., Havens, V.N., Heidenreich, G.R. *Technology Update: Solar Dynamic Organic Rankine Cycle Power System*. Proceedings of the 10th Annual ASME Solar Energy Conference, Denver, Colorado (1988).

Cheek, R.M., Lacey, P.D. *600 kW Organic Rankine Cycle waste Heat Power Conversion System*. Transactions of the 12th IECEC, 1977, pp.1095-1099.

Chen, J., et al. *On the Curzon-Ahlborn efficiency and its connection to with the efficiencies of real heat engines*. Energy Conversion and Management v.42 (2001) p. 173-181

Cheng, L., Tingkuan, C. *Comparison of Six Typical Correlations for Upward Flow Boiling Heat Transfer with Kerosene in a Vertical Smooth Tube*. Heat Transfer Engineering, v. 21 no. 5 (2000) pp. 27-34

Curran, H.M. *Use of Organic Working Fluids in Rankine Engines*. Energy, v.5 no.2 (1981) pp.218-223

Curzon, F.L., Ahlborn, B. *Efficiency of a Carnot engine at maximum power output*. Am J Phys, Vol. 43 (1975) p. 22-24

Demarchi, D.P., Gaia, M. *Performance Analysis of innovative collector fields for solar-electric plants*. Proceedings of Intersociety Energy Conversion Engineering Conference, San Francisco (1984)

Demuth, O.J. *Analysis of Mixed Hydrocarbon Binary Thermodynamic Cycles For Moderate Temperature Geothermal Resources*. Proceedings of the 16th Intersociety Energy Conversion Engineering Conference, (1981) pp.1316-1321

Demuth, O.J. *Preliminary Assessment of Condensation Behavior for Hydrocarbon vapor expansions which cross the saturation line near the critical point.* Proceedings of the 18th IECEC, American Institute of Chemical Engineers. v. 1 (1983)

Demuth, O.J., Kochan, R.J. *Analysis of mixed hydrocarbon binary thermodynamic cycles for moderate temperature geothermal resources using regenerative techniques*. Proceedings of the 17th IECEC, IEEE. v.2 (1982)

Durmayaz, A., Sogut, O.S., Sahin, B., Yavuz, H. *Optimization of thermal systems based on finite-time thermodynamics and thermoeconomics*. Progress in Energy and Combustion Science, v. 30 (2004) p. 175-217

Dickson, James. *Feasibility of Using Kalina Cycles in Modular Solar Trough Systems*. Internal Presentation, Exergy, Inc. June (2000)

El Chammas, R., Clodic, D. *Combined Cycle for Hybrid Vehicles*. SAE International, 05P-124 (2004)

El-Wakil, M.M. *Poweplant Technology*. McGraw-Hill, Inc., New York (1984)

Eldighidy, S.M., Taha, I.S. *Optimum Mass Flow Rate of Water In A Flat Plate Solar Collector Coupled With A Storage Tank And An Organic Rankine Cycle Power Loop*. Solar Energy, v.31, no. 5 (1983) pp.455-461

Engelbrecht, K.L., Nellis, G.F., Klein, S.A. *The Effect of Internal Temperature Gradients on Regenerator Matrix Performance.* Accepted for publication, Journal of Heat Transfer, February (2006)

Faas, S.E., et al. *10 MWe Solar Thermal Central Receiver Pilot Plant: Thermal Storage Subsystem Evaluation – Final Report*. Sandia Report SAND86-8212 (1986)

Fenton, Donald L., et al. *Operation and Evaluation of the Willard Solar Thermal Power Irrigation System*. Solar Energy, v.32, no.6 (1984) pp.735-751

Forristall, R. *Heat Transfer Analysis and Modeling of a Parabolic Trough Solar Receiver Implemented in Engineering Equation Solver.* NREL/TP-550-34169, October (2003)

Gawlik, K., Hassani, V. *Advanced Binary Cycles: Optimum Working Fluids*. Proceedings of Geothermal Resources Council, San Diego, CA (1998)

Goktun, Selahattin. *Design Parameters of a Solar-Driven Heat Engine*. Energy Sources, v.18 (1996) pp.37-42

Gurgenci, Halim. *Performance of Power Plants with Organic Rankine Cycles Under Part-Load and Off-Design Conditions*. Solar Energy, v.36, no.1 (1986) pp.45-51

Gyftopoulos, E.P. *On the Curzon-Ahlborn efficiency and its lack of connection to power producing processes*. Energy Conversion and Management v.43 (2002) p. 609-615

Herrmann, U., Kearney, D.W. *Survey of Thermal Energy Storage for Parabolic Trough Power Plants*. Solar Energy Engineering, v. 124 (2002) pp. 145-152

Herrmann, Ulf, et al. *Two-tank molten salt storage for parabolic trough solar power plants*. Energy, v. 29 (2004) pp. 883-893

Hollands, K.G.T., Sullivan, H.F. *Pressure drops across rock bed thermal storage systems*. Solar Energy, v. 33, No. 2 (1984) pp. 221-225

Hung, T.C. *Waste heat recovery of organic Rankine cycle using dry fluids*. Energy Conversion and Management, v.42 (2001) pp.539-553

Hung, T.C., Shai, T.Y., and Wang, S.K. *A Review of Organic Rankine Cycles (ORCs) For the Recovery of Low-Grade Waste Heat*. Energy v.22, no. 7 (1997) pp. 661-667

Ibrahim, O.M. *Evaluation and Design of Absorption Power Cycles*. PhD Thesis, University of Wisconsin-Madison (1991)

Ibrahim, O.M., Klein, S.A. *High-Power Multi-Stage Rankine Cycles*. Transactions of the ASME, v.117 (1995) pp.192-196

Incropera, F.P., DeWitt, D.P. *Fundamentals of Heat and Mass Transfer, 5th edition*. John Wiley & Sons, New York (2002)

Iqbal, K.Z., Fish, L.W., Starling, K.E. *Development of a geothermal binary cycle simulator*. Proceedings of the Oklahoma Academy of Sciences meeting. v. 57 (1977) pp.122-130

Jeffreson, C.P. *Prediction of Breakthrough Curves in Packed Beds: Applicability of Single Parameter Models*. AlChE Journal, v. 18, No. 2 (1972), pp. 409-416

Kalina, A.I., Leibowitz, H.M. Application of the Kalina Cycle Technology to Geothermal Power Generation. Transactions of the Geothermal Resources Council, v. 13 (1989) pp.605-611

Kane, M., et al. *Small hybrid solar power system*. Energy, v.28 (2003) pp.1427-1443

Kays, W.M., Crawford, M.E. *Convective Heat and Mass Transfer, Fourth Edition*. McGraw-Hill, New York (2005)

Kearny, D., et al. *Assessment of a Molten Salt Heat Transfer Fluid in a Parabolic Trough Solar Field.* Transactions of the ASME, v. 125 (2003), pp. 170-176

Kiselev, S.B., Ely, J.F. *Generalized corresponding states model for bulk and interfacial properties in pure fluids and fluid mixtures*. Journal of Chemical Physics. v. 119, no. 16 (2003) pp.8645-8661

Khaliq, Abdul. *Finite-time heat-transfer analysis and generalized power-optimization of an endoreversible Rankine heat-engine*. Applied Energy, v. 79 (2004) pp. 27-40

Klein, S.A. *Engineering Equation Solver (EES)*. F-Chart Software, http://www.fchart.com (1992-2006)

Klein, S.A., et al. TRNSYS 16: a TRaNsient System Simulation program. Solar Energy Laboratory, University of Wisconsin-Madison, http://sel.me.wisc.edu/trnsys (2006)

Kohler, S., Saadat, A. *Thermodynamic Modeling of Binary Cycles Looking for Best Case Scenarios*. International Geothermal Conference, Reykjavik, September (2003)

Kolb, G.J., Hassani, V. *Performance Analysis of Thermocline Energy Storage Proposed For The 1 MW Saguaro Solar Trough Plant*. Proceedings of ISEC 2006, Denver, Colorado (2006)

Kuo, C.H., et al. *Solar-Powered Organic Rankine System For Domestic Electric-Power Generation*. Proceedings of the Second Trabzon International Energy and Environment Symposium, Turkey, July (1998)

Larson, Dennis L. *Operational Evaluation of the Grid-Connected Coolidge Solar Thermal Electric Power Plant*. Solar Energy, v.38, no.1 (1987) pp.11-24

Leff, H.S. *Thermal Efficiency at Maximum Work Output: New Results for Old Heat Engines*. American Journal of Physics, v.55 no.7 (1987)

Linne, Diane L., et al. *Evaluation of Heat Transfer and Thermal Stability of Supercritical JP-7 Fuel*. Proceedings of the 33rd Joint Propulsion Conference, Seattle, Washington. NASA TM-107485 (1997)

Lippke, Frank. *Simulation of the Part Load Behavior of a 30MWe SEGS Plant*. Prepared for Sandia National Laboratories, Albuquerque, NM, SAND95-1293. June (1995)

Luettmer-Strathmann, J., Sengers, J.V. *The transport properties of fluid mixtures near the vapor-liquid critical line*. Journal of Chemical Physics. Vol. 104, no. 8 (1996) pp. 3026-3042

Manco, S., Nervegna, N. *Working Fluid Selection Via Computer Assisted Analysis of ORC Waste Heat Recovery Systems*. Proceedings of the 20th Intersociety Energy Conversion Engineering Conference, pp.3.72-3.83, 1985

Maizza, V., Maizza, A. *Unconventional working fluids in organic Rankine-cycles for waste energy recovery systems*. Applied Thermal Engineering, v.21 (2001) pp.381-390

McDonnell Douglas Astronautics Company. *10 MWe Solar Thermal Central Receiver Pilot Plant Mode 5 (Test 1150) and Mode 6 (Test 1160) Test Report*. Sandia Contractor Report SAND86-8175 (1986)

McLinden, M.O. *Thermodynamic evaluation of refrigerants in the vapor compression cycle using reduced properties*. International Journal of Refrigeration, v. 11 (1988) pp. 134-143

Moens, Luc, et al. *Advanced Thermal Storage Fluids for Solar Parabolic Trough Systems*. Transactions of the ASME, v. 125 (2003), pp. 112-116

Mohanty, B., Paloso Jr., G. *Economic Power Generation From Low-Temperature Geothermal Resources Using Organic Rankine Cycle Combined With Vapour Absorption Chiller*. Heat Recovery Systems & CHP, v.12, no.2 (1992) pp.143-158

Monahan, J., McKenna, R. *Development of a 1-kW Organic Rankine Cycle*. Proceedings of the 1976 IECEC, No. 769199 (1976)

Moran, M.J., Shapiro, H.N. *Fundamentals of Engineering Thermodynamics, 4th edition*. John Wiley & Sons, New York (2000)

Mostert, R., et al. *The thermal conductivity of ethane in the critical region*. Journal of Chemical Physics, v.92, no. 9 (1990) pp.5454-5462

Nellis, G.F., Klein, S.A. *Regenerative Heat Exchangers with Significant Entrained Fluid Heat Capacity*. International Journal of Heat and Mass Transfer, v. 49 (2006) pp. 329-340

Novikov II. *The efficiency of atomic power stations (a review)*. Journal of Nuclear Energy (1958) p. 125-128

Pacheco, J.E., et al. *Development of a Molten-Salt Thermocline Thermal Storage System for Parabolic Trough Plants*. Solar Energy Engineering, v. 124 (2002) pp. 153-159

Patnode, A.M. *Simulation and Performance Evaluation of Parabolic Trough Solar Power Plants*. M.S. Thesis, University of Wisconsin at Madison (2006)

Pilkington. *Solar Steam System Investment Cost*. USA Trough Initiative (2000)

Pope, W.L., et al. *The Importance of the Specific Heat Anomaly in the Design of Binary Rankine Cycle Power Plants*. Transactions of the Geothermal Resources Council. v. 4 (1980) pp.523-526

Prabhu, Edan. *Solar Trough Organic Rankine Electricity System (STORES) Stage 1: Power Plant Optimization and Economics*. NREL subcontract no.NAA-1-30441-05, July (2004)

Price, H., Kearney, D. *Parabolic Trough Technology Roadmap*. NREL internal document, January (1999)

Price, H.W., Carptenter, S. *The Potential for Low-Cost Concentrating Solar Power Systems*. Proceedings of the Intersociety Energy Conversion Engineering Conference, Vancouver, August (1999)

Price, Hank and Hassani, Vahab. *Modular Trough Power Plant Cycle and Systems Analysis*. NREL/TP-550-31240, January (2002)

Price, H. *A Parabolic Trough Solar Power Plant Simulation Model.* Proceedings of ISES 2003: Solar Energy Conference. March (2003)

Price, Henry. *personal communication*. March (2006)
Reindl, D.T. *personal communication*. May (2006)

Rohsenow, W.M., Hartnett, J.P., Cho, Y.I. *Handbook of Heat Transfer*. McGraw-Hill, Inc., New York (1998)

Sargent and Lundy LLC. *Assessment of Parabolic Trough and Power Tower Solar Technology cost and performance forcasts*. October, 2003.

Schumann, T.E.W. *Heat Transfer: A Liquid Flowing Through a Porous Prism*. Journal of the Franklin Institute, v. 208 (1929), pp. 405-416

Sogut, O.S., Durmayaz, A. *Performance optimization of a solar driven heat engine with finite-rate heat transfer*. Renewable Energy, v. 30 (2005) pp. 1329-1344

Steinmann, W.D., Eck, M., Laing, D. *Solarthermal parabolic trough power plants with integrated storage capacity*. International Journal of Energy, Technology and Policy, v. 3 (2005) pp. 123-135

Shitzer, A., Levy, M. *Transient Behavior of a Rock-Bed Thermal Storage System Subjected to Variable Inlet Air Temperatures: Analysis and Experimentation*. Transactions of the ASME, v. 105 (1993) pp. 200-206

Tamme, R., Laing, D., Steinmann, W.D. *Advanced Thermal Energy Storage Technology for Parabolic Trough*. Transactions of the ASME, v. 126 (2004) pp. 794-800

Vijayaraghavan, S., Goswami, D.Y. *Organic Working Fluids for a Combined Power and Cooling Cycle*. Energy Resources Technology, v.127 (2005) pp.125-130

Wali, Ezzat. *Optimum Working Fluids For Solar Powered Rankine Cycle Cooling of Buildings*. Solar Energy, v.25 (1980) pp. 235-241

White, Frank M. *Fluid Mechanics, fifth edition*. McGraw-Hill, Inc., New York, 2003.

Yamamoto, Takahisa, et al. *Design and testing of the Organic Rankine Cycle*. Energy, v.26 (2001) pp.239-251

Yilmaz, T. *A new performance criterion for heat engines: efficient power*. Journal of the Energy Institute, v. 79, No. 1 (2006) pp. 38-41

Zarty, O., Juddaimi, A.E. *Computational Models of a Rock-Bed Thermal Storage Unit*. Solar & Wind Technology, v. 4, No. 2 (1987) pp. 215-218